SPATIAL VARIABILITY IN SOILS:

STIFFNESS AND STRENGTH

A Thesis
Presented to
The Academic Faculty

by

Hyunki Kim

In Partial Fulfillment
of the Requirements of the Degree
Doctor of Philosophy in Civil and Environmental Engineering

Georgia Institute of Technology

August, 2005

SPATIAL VARIABILITY IN SOILS:

STIFFNESS AND STRENGTH

Approved by:

J. Carlos Santamarina, Adviser
Professor, CEE,
Georgia Institute of Technology

J. David Frost
Professor, CEE,
Georgia Institute of Technology

Paul W. Mayne
Professor, CEE,
Georgia Institute of Technology

Glenn J. Rix
Professor, CEE,
Georgia Institute of Technology

Carolyn D. Ruppel
Professor, EAS,
Georgia Institute of Technology

Date Approved: May 24, 2005

To my families

ACKNOWLEDGEMENT

PhD program at Georgia Tech in the past several years was a truly exceptional experience in my life. However, I could not achieve this work without the supports of my near and dear ones.

It was honestly fortunate that Professor J. Carlos Santamarina was my adviser. His profound understanding and insight about soils is the most important driving force that encourages me to progress this research during the four years. Our time spent together was not only a chance for sharing technical information but for learning his philosophy and passion for life. Additionally, I should also appreciate kind cares of his and his family about my wife and me who were not used to living in the United States.

I thank the members of the Particulate Media Research Laboratory for encouragement, assistance and discussion. They are truly good friends, fellows and professionals. The members of the Korean student community in geosystem engineering are truly grateful persons to me during the whole period in Georgia Tech.

I give thanks to the Georgia Institute of Technology and the National Science Foundation for providing funds for this research. I am thankful to my committee members for the thesis and my former advisers in Seoul National University for their valuable pieces of advice and comments: Dr. J.D. Frost, Dr. P.W. Mayne, Dr. G.J. Rix, Dr. C.D. Ruppel, Dr. Myoungmo Kim, Dr. Choongki Chung and Dr. Junboum Park.

Finally, I specially thank my wife Jooyun and all the other family members for their greatest trust and supports on me. I do not believe that I could finish my work without their helps. As everything went on down to this day, I hope everything that I will do to be within my Lord.

TABLE OF CONTENTS

LIST OF TABLES

LIST OF FIGURES

SUMMARY

Geotechnical properties vary in space. Statistical parameters such as mean, deviation, and correlation length are characteristics for each sediment and formation history. The effects of spatial variability on the macro-scale mechanical properties of soils are investigated using Monte Carlo non-linear finite element simulations. Boundary conditions include 1) isotropic loading, 2) zero-lateral strain loading, 3) drained and undrained deviatoric loading, and 4) small-strain wave propagation. Emphasis is placed on identifying the effects of spatial variability on the stiffness and strength of soils, recognizing emergent phenomena, and creating the background for new geotechnical design methods that take into consideration spatial variability.

The arithmetic mean of soil properties cannot be used to estimate the stiffness or strength of heterogeneous soils. Greater deviation and longer relative correlation length in the spatial distribution of soil properties yield a softer and weaker mechanical response. Load transfer concentrates along stiffer zones, leading to stress-focusing and lower K_0 values. Drained loading promotes internal homogenization. Undrained deviatoric loading can cause percolation of internal weakness and shear strain localization. Spatial heterogeneity adds complexity to elastic wave propagation. Heterogeneous soil mixtures can be engineered to attain unique macroscale behavior.

CHAPTER I

INTRODUCTION

Soils are inherently heterogeneous. At the microscale, soils are multiphase, and include minerals, water, gasses and other non-miscible fluids, ions, and micro-organisms. At the macroscale, soil heterogeneity reflects spatially varying geological processes involved in soil formation such as deposition, physical, chemical and biological weathering, desiccation, consolidation, diagenesis, cementation, leaching, and so on. The resulting multi-scale heterogeneity is denoted in Figure 1.1.

Inherent spatial variability brings unavoidable uncertainty in design (Einstein and Barcher, 1982-See Lacasse and Nadim, 1996). Furthermore, variability leads to unexpected soil response and even emergent phenomena.

Several studies have investigated inherent uncertainty in natural soil properties (Lumb, 1966; Asaoka and A-Grivas, 1982; Spry et al., 1988; Orchant et al., 1988; Filippas et al., 1988; Soulie et al, 1990; Kulhawy et al., 1992; Chaisson et al., 1995; Phoon et al., 1995). Others have attempted to predict the corresponding global soil response: deformation (Baecher and Ingra, 1981; Zeitoun and Baker, 1992; Paice et al., 1994, Paice et al., 1996), strength (Griffiths and Fenton, 2000; Griffiths and Fenton, 2001; Griffiths, 2000; Griffiths and Lane, 1999; Griffiths et al, 2002), conduction (Dagan, 1989; Rubin and Gómez-Hernández, 1990; Fenton and Griffiths, 1993; Neuman and Orr, 1993), and diffusion (Hwang and Witczak, 1984; Nishimura et al., 2002).

(a)

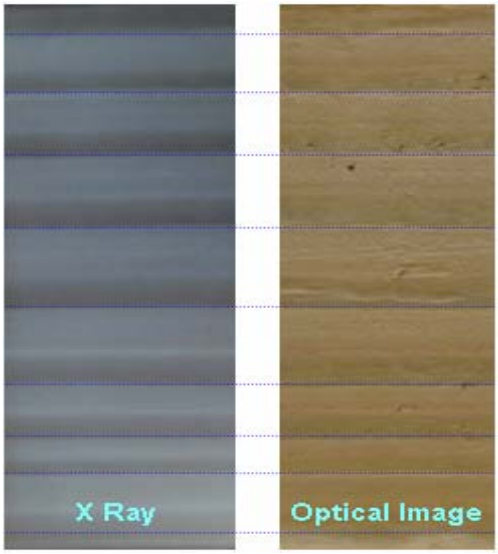

(b)

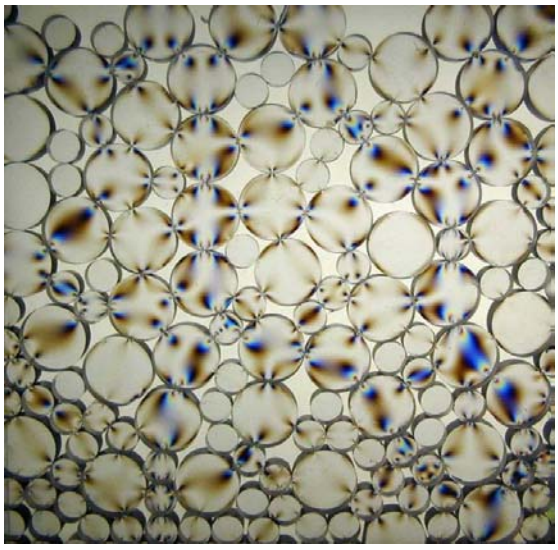

(c)

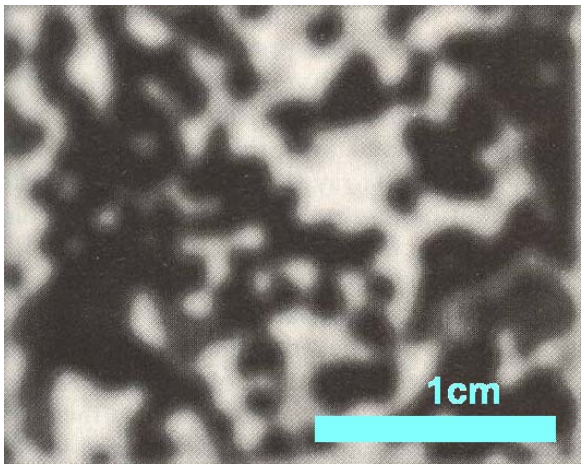

(d)

Figure 1.1 Spatial variability in soils - Multiple scales: (a) Macro-scale variability (Black Canyon in Colorado, from http://geology.asu.edu). (b) Meso-scale layering (Cross-section of varved clay, from Lee, 2003). (c) Particle-scale variability (Photoelastic disks under K_0 loading, from Santamarina et al., 2001). (d) Variability within a particle (X-ray image of density distribution in 2D sliced limestone, from Luset, 1989-See Mukerji et al., 1995).

The current design codes partially consider spatial variability within the latitude provided by the ultimate limit state approach (See Kulhawy and Phoon, 2002; Phoon, 2004; Zhang and NG, 2005): OHBDC3, Ministry of Transportation Ontario, 1992; EPRI, Phoon et al., 1995; Building Code of Canada, Becker, 1996; Eurocode 7, CEN, 2001; AASHTO LRFD Bridge Code, AASHTO, 2002; Geo-code 21 of Japan, Honjo and Kusakabe, 2002; Chinese code for the design of building foundation, MOC, 2002.

This study has three major goals: first, to identify the effects spatial variability on global soil properties; second, to identify emergent phenomena; and third, to provide pertinent information that can be used to develop geotechnical design guidelines that take spatial variability into consideration. The thesis is organized into seven chapters:

- Chapter 2: Definitions and numerical modeling of spatial variability in soils.
- Chapter 3: Numerical simulation studies on the mechanical response of heterogeneous soils under isotropic and K_0 loading conditions.
- Chapter 4: Numerical simulation studies designed to explore the effect of spatial variability on drained and undrained strength.
- Chapter 5: Numerical simulation studies on small strain wave propagation in heterogeneous soils.
- Chapter 6: Mechanical behavior of granular mixtures consisting of small hard grains and large-soft grains. Such mixtures are investigated as an engineering application of spatial variability control. Both numerical and experimental methods are implemented in this chapter.
- Chapter 7: Summary of salient conclusions.

CHAPTER II

SPATIAL VARIABILITY AND CORRELATED RANDOM FIELDS

This chapter introduces statistical models to characterize soil heterogeneity, and describes the numerical reconstruction of heterogeneous fields in view of numerical studies designed to explore the effects of spatial variability on geotechnical parameters.

2.1 UNCERTAINTY IN GEOTECHNICAL ENGINEERING

There are three primary sources of uncertainty in geotechnical design parameters: inherent soil variability, measurement error, and transformation uncertainty (Figure 2.1). Inherent variability is the consequence of natural geologic processes that continually modify the soil mass in situ. Measurement error results from equipment, test-operators, and random test effects during measurements. Statistical uncertainty results from limited amount of information, and can be reduced by extracting more samples (Kulhawy, 1992). On the other hand, the systematic bias caused by the process of sampling and measurement cannot be removed by statistics and requires additional proper correction. Transformation uncertainty is introduced when field or laboratory measurements are "transformed" into design soil properties with empirical or other correlation models. Among these three sources of uncertainty, only the inherent soil variability is taken into consideration in this study.

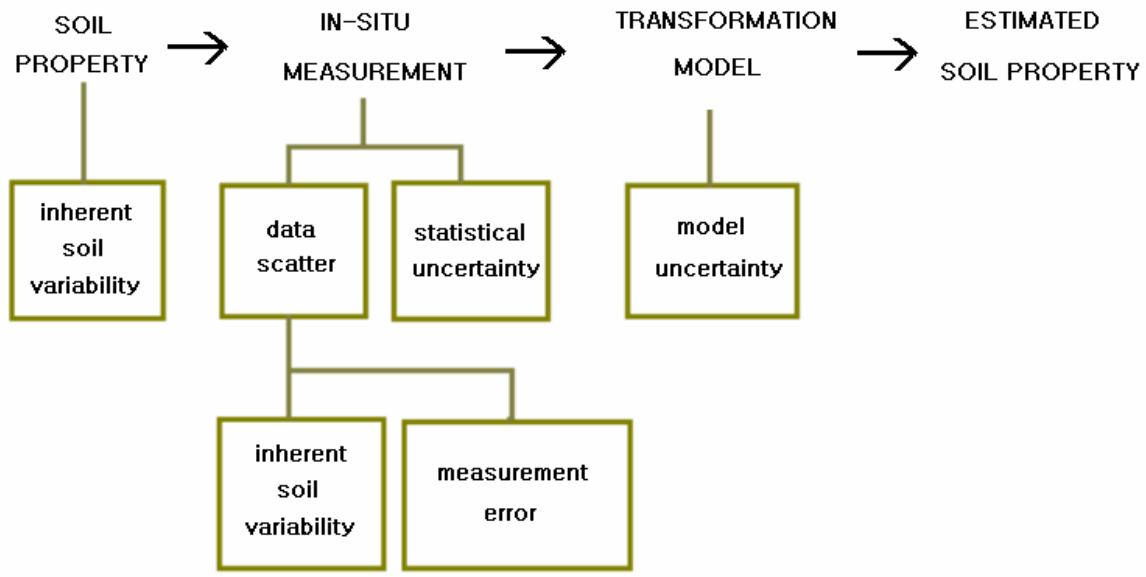

Figure 2.1 Uncertainty in soil property estimates (Kulhawy, 1992).

The field of geostatistics provides the mathematical tools needed to estimate spatially or temporally correlated data from sparse sample data. It was originally developed to examine the spatial variation in crop yield (Mercer and Hall, 1911 - See Webster and Oliver, 2001). The main geostatistical terms such as spatial dependence, correlation range, nuggets, blocking, spatial lag and so on were established between 1920's and 1940's (Fisher, 1925; Youden and Mehlich, 1937; Kolomogorov, 1941 - See Webster and Oliver, 2001). "Kriging" is the standard process that is used to estimate unknown information in geostatistics, and was initiated by Krige (1966) to improve the precision of estimating concentration of gold and other metals in ore bodies. Frequently encountered terms in geostatistics are reviewed in Table 2.1.

Table 2.1 Basic glossary in spatial analysis (Clark, 1979; Wackernagel, 1995; Webster and Oliver, 2001; www.u.arizona.edu/~donaldm/)

terms	description
Drift	The representative quantity of a random function. If a random function is stationary, the drift must be a constant.
Ergodic	When the moments of the single observable realization in space approach those of the ensemble as the regional bounds expand toward infinity.
Kriging estimator	While the estimator may be a linear or a non-linear function of the data, the weights in the estimator are determined by requiring the estimator to be unbiased and have minimum error variance.
Nugget	The magnitude of the discontinuity in the variogram at the origin.
Posting	To plot the sampling points on a map.
Quasi-stationary	When the variogram is of local interest only very locally.
Range	The distance at which the variogram becomes a constant. The power model does not have a finite range. The exponential and Gaussian models have only an apparent range
Sill	The value of the variogram for distances beyond the range of the variogram. The power model does not have a sill
Spatial correlation	Used both as a generic term to denote that data at two locations is correlated in some sense as a function of their locations and also to denote the value of a spatial structure function such as variogram or autocovariance for a pair of locations.
Stationarity	The distribution of the random process has certain attributes that are the same everywhere

2.2 INHERENT SOIL VARIABILITY

Figure 2.2 shows a data set obtained during CPT field testing. Conventionally, the soil profile is classified into several layers, and dominant linear trends or average values are used to estimate the design parameters. Indeed, spatial variability is ignored in current design.

However, variability can be taken into consideration using several statistical parameters (Vanmarke, 1977; Kulhawy and Phoon, 1996; Phoon and Kulhawy, 1999). The most important parameters that characterize the spatially varying soil properties are the central trend, the coefficient of variation (COV), the correlation length L, and anisotropy in variability distributions (Figure 2.3).

2.2.1 Soil Profile

The spatial variation in property X with depth z can be decomposed into a trend function t and a fluctuating component w (Figure 2.3).

$$X(z) = t(z) + w(z) \tag{2.1}$$

If *w(z)* is considered to be statistically homogeneous, the mean and variance of *w(z)* are independent of depth, and the correlation of *w(z)* signals at two different depths is a function of their spatial separation rather than their absolute locations (Vanmarcke, 1984).

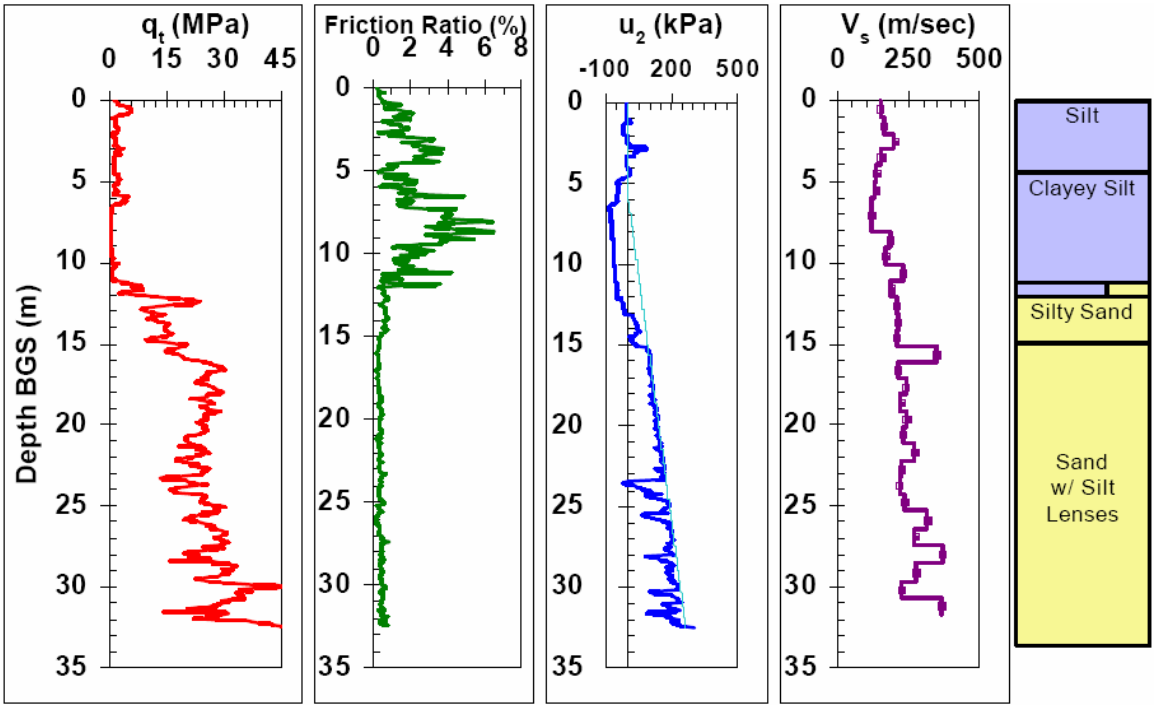

Figure 2.2 Example of soil profile by SCPT testing (Blytheville, AR; from Schneider and Mayne, 2000).

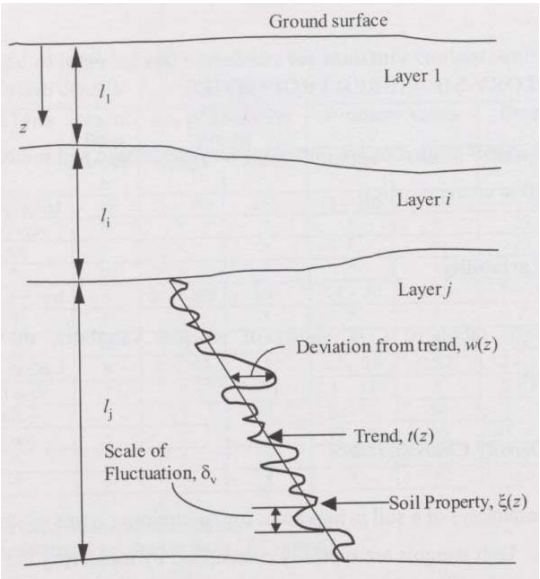

Figure 2.3 Schematic diagram of inherent soil variability (Kulhawy, 1992).

2.2.2 Coefficient of Variation

The standard deviation of inherent soil variability for a statistically homogeneous variability function *w(z)* is defined for *n* data points as:

$$\sigma_{wi} = \sqrt{\frac{1}{n-1}\sum_{k=1}^{n}[w_k(z_i)]^2} \tag{2.2}$$

A useful dimensionless ratio can be calculated by normalizing σ_{wi} with respect to the "local" mean soil property t_i obtained from the trend function *t(z)*. This ratio is called the coefficient COV_{wi},

$$COV_{wi} = \frac{\sigma_{wi}}{t_i} \tag{2.3}$$

The reported COV may be considerably larger than the actual inherent soil variability because of four potential effects (Phoon and Kulhawy, 1999): (1) soil data from different geologic units are mixed, (2) equipment and procedural controls are generally insufficient, (3) deterministic trends in the soil data are not properly removed, and (4) soil data are gathered over a long period of time with different testing techniques. Typical COV values for various soil properties are summarized in Table 2.2. A more comprehensive listing can be found in Jones et al. (2002).

Table 2.2 Coefficient of variation for soil properties (from Harr, 1987).

Parameter	Coefficient of variation [%]	Source
Porosity	10	Schultze (1972)
Specific gravity	2	Padilla and Vanmarcke (1974)
Water content (Silty clay)	20	Padilla and Vanmarcke (1974)
Water content (Clay)	13	Fredlund and Dahlman (1972)
Degree of saturation	10	Fredlund and Dahlman (1972)
Unit weight	3	Hammitt (1966)
Coefficient of permeability	240 at 80% saturation	Nielsen et al. (1973)
	90 at 100% saturation	Nielsen et al. (1973)
Compressibility factor	16	Padilla and Vanmarcke (1974)
Preconsolidation pressure	19	Padilla and Vanmarcke (1974)
Compression index (Sandy clay)	26	Lumb (1966)
Compression index (Clay)	30	Fredlund and Dahlman (1972)
Standard penetration test	26	Schultze (1972)
Standard cone test	37	Schultze (1972)
Friction angle (Gravel)	7	Schultze (1972)
Friction angle (sand)	12	Schultze (1972)

2.2.3 Scale of Fluctuation

The scale of fluctuation *SOF* provides the spatial range where values of a given property show relatively strong spatial correlation. That scale of fluctuation is calculated as follows (Jones et al., 2002):

1) Calculate the variance of the data series, σ_r^2.
2) Smooth the series by moving average with the window width w_i.
3) Calculate the variance of the windowed series, σ_{wi}^2.
4) Calculate the corresponding scale of fluctuation SOF_i with respect to the window size w_i: $SOF_i = \frac{\sigma_{wi}^2}{\sigma_r^2} \times w_i$
5) Plot SOF_i as a function of window size w_i.
6) Take the peak *SOF* value as an estimate of the scale of fluctuation δ.

A sinusoidal signal with random noise and the computed scale of fluctuation are shown in Figure 2.4.

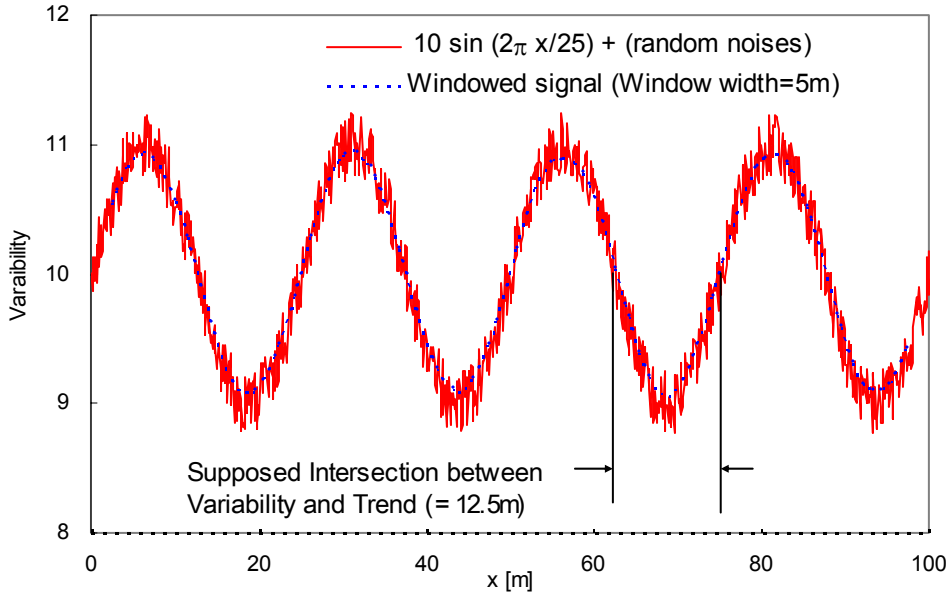

(a)

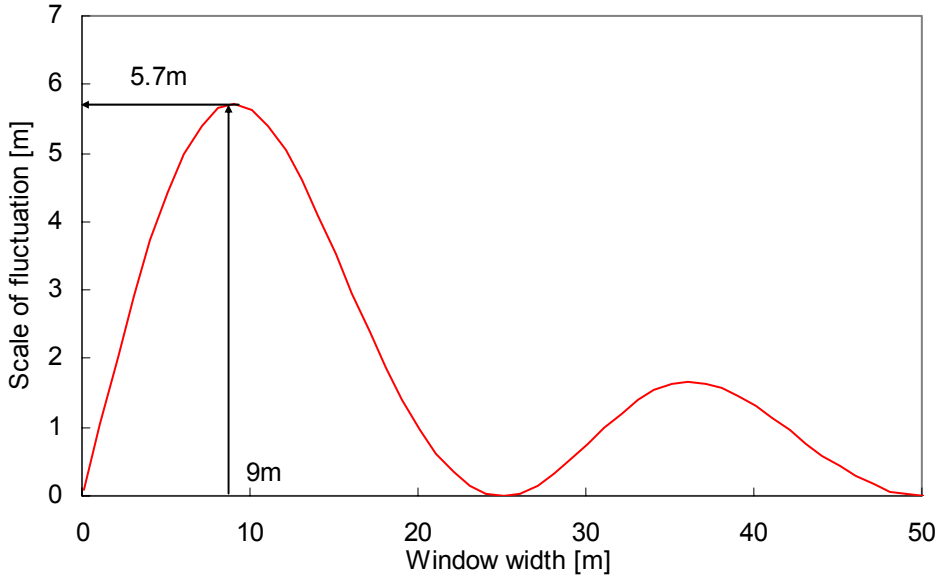

(b)

Figure 2.4 One-dimensional random signal and the corresponding scale of fluctuation (SOF): The maximum value of SOF with respect to the window width is the effective scale of fluctuation. (a) Example of an original random signal and its windowed signal with the width of 10m. (b) Corresponding scale of fluctuation for the signal shown in (a).

2.2.4 Correlation Length

Given a finite random variable X with sample mean $E(X)$ and variance $V(X)$, the autocovariance of X is a function of the data separation distance d

$$\operatorname{cov}(X_i, X_{i+d}) = \frac{\left(\sum_i X_i X_{i+d}\right) - \frac{1}{n-d}\sum_i X_i \frac{1}{n}\sum_i X_{i+d}}{n-d-1} \tag{2.5}$$

where n is the number of data points gathered with a constant sampling interval. The autocorrelation of X, named $C(d)$ is obtained by normalizing the autocovariance with the variance of the variable

$$C(d) = \frac{\operatorname{cov}(X_i, X_{i+d})}{V(X)} \tag{2.6}$$

Many standardized mathematical expressions are proposed for the autocorrelation function in Table 2.3. The corresponding scale of fluctuation is shown in each case.

The correlation length L or autocorrelation length is the distance where the spatial autocorrelation decays by 1/e, about 37%. The scale of fluctuation SOF is usually between 1.4 and 2.0 times the correlation length L for exponential, squared exponential, and spherical autocorrelation functions (Vanmarcke, 1984). Correlation length for various soil properties is summarized in Table 2.4. The correlation length L and the medium size D (side length in a square geometry or the diameter in a circle) are dependent on each other. The correlation length normalized by the medium size is called the relative correlation length L/D in this study.

Table 2.3 Autocorrelation functions and corresponding scale of fluctuation (from Vanmarcke, 1977)

Correlation Function	Scale of fluctuation
$e^{-\lvert d\rvert / L_1}$	$2L_1$
$e^{-(d / L_2)^2}$	$\sqrt{\pi} L_2$
$e^{-\lvert d\rvert / L_3} \cos(d / L_3)$	L_3
$e^{-\lvert d\rvert / L_4}\left[1 + \frac{\lvert d\rvert}{L_4}\right]$	$4L_4$

Note: L_1, L_2, L_3 and L_4: corresponding correlation scales; d: spatial distance between points.

Table 2.4 Correlation lengths for various soil properties (Compiled by DeGroot 1996 and Lacasse et al. 1996)

Soil Property	Soil	Direction	Autocorrelation distance [m]	Reference
SPT N value	Dune sand	Horizontal	20	Hilldale-Cunningham (1971)
	Alluvial sand		17	DeGroot (1996)
DMT P_0	Varved clay	Vertical	1	DeGroot (1996)
FVT S_u	Sensitive clay	Horizontal	23	DeGroot and Baecher (1993)
	Clay	Vertical	1 ~ 3	Asaoka and A-Grivas (1982)
	Sensitive clay		1	Baecher (1982)
	Sensitive clay		2	Chaisson et al. (1995)
Laboratory S_u	Chicago clay	Vertical	0.5 (Unconfined compression test)	Wu (1974)
	Offshore sites		0.3 ~ 0.6 (Triaxial loading test and DSS)	Keaveny et al. (1989)
Hydraulic Conductivity	Salt dome	Horizontal	1500	Ditmars et al. (1988)
	Compacted clay		0.5 ~ 2	Benson (1991)
	Sand aquifer		1 ~ 2.5	Bjeng et al. (1992)

Notations: SPT, Standard Penetration Test; DMT, Dilatometer Test; FVT, Field Vane Test; DSS, Direct Simple Shear test

Table 2.4 Correlation lengths for various soil properties (continued)

Soil Property	Soil	Direction	Autocorrelation distance [m]	Reference
CPT tip resistance	Offshore soils	Horizontal	30	Hoeg and Tang (1976), Tang (1979)
	Offshore sand		14 ~ 38	Keaveny et al. (1989)
	Silty clay		5 ~ 12	Lacasse and Lamballerie (1995)
	Clean sand	Vertical	3	Alonzo and Krizek (1975)
	Mexico clay		1	Alonzo and Krizek (1975)
	Clay		1	Vanmarcke (1977)
	Sensitive clay		2	Chaisson et al. (1995)
	Silty clay		1	Lacasse and Lamballerie (1995)
	Copper tailings		0.5	Baecher (1979)
	Clean sand		1.6	Kulatilake and Ghosh (1988)

2.3 CORRELATED RANDOM FIELDS – NUMERICAL GENERATION

The generation of multidimensional correlated random fields typically follows three steps. First, generate a 2D array $\underline{\underline{u}}$ of uniform distributed random numbers using conventional built-in functions in numerical codes. Second, convert this array into an array $\underline{\underline{\varepsilon}}$ of Gaussian distributed random numbers using numerical methods such as the Box-Muller method (Table 2.5; Box and Muller, 1958 - See Press et al, 1992). Finally, transform the uncorrelated array $\underline{\underline{\varepsilon}}$ into a correlated field $\underline{\underline{g}}$.

Several methods have been developed to perform the third step. The following selected methods are explained herein:

1) Table 2.6: Method by Mejía and Rodríguez
2) Table 2.7: Turning Bands Method
3) Table 2.8: Method by Ehlschlaeger and Goodchild
4) Table 2.9: Matrix Decomposition Technique

The Mejía and Rodríguez's method and the Turning Bands method were developed to simulate randomized rainfall distribution. The random fields generated by these methods exhibit "spatially centralized" randomness, as shown in Figure 2.4(b). The Ehlschlaeger and Goodchild's method provides time-efficient generation of multi-dimensional correlated random fields with statistically homogeneous distributions throughout the medium (Figure 2.4c). However, the correlation length and the coefficient of variation are not specified in this method. The matrix decomposition technique can model the

statistically homogeneous correlated random field with very clear relationships between the given statistical parameters and the corresponding random field, including a preselected correlation length (Figure 2.4d). Therefore, the matrix decomposition technique is chosen to generate correlated random fields in this research.

Table 2.5 Description of the Box-Muller method

Name	Box-Muller method
Reference	Box, G.E.P. and Muller, M.E., (1958),
Description	Generation of an array $\underline{\varepsilon}$ of Gaussian distributed random numbers from an array $\underline{u}$ of uniform distributed random numbers
Procedure	1) Pick two random numbers (u_1, u_2) from the array of $\underline{u}$ of uniform distribution (between zero and one) 2) Generate the Gaussian distributed random numbers (ε_1, ε_2) as $\varepsilon_1 = \sqrt{-2\ln r_1}\cdot\cos(2\pi\cdot r_2)$ $\varepsilon_2 = \sqrt{-2\ln r_1}\cdot\sin(2\pi\cdot r_2)$ The array $\underline{\varepsilon}$ has zero mean and standard deviation one.

Table 2.6 Correlated Gaussian random field generation – Procedure suggested by Mejía and Rodríguez

Name	Mejía and Rodríguez Method
Reference	Mejía, J.M. and I. Rodríguez-Iturbe. (1974)
Description	Analytical solution derived from the given correlation function $\rho(\tau)=e^{-\alpha G\|\tau\|}$ for a certain point
Procedure	1) Generate more than 50 uniform distributed random numbers for each of three parameter *α,β, and δ.* $\alpha_m \sim U(0,1), \beta_m \sim U(0,2\pi), \delta_m \sim U(0,2\pi)$ *(m=1,2,⋯,M, M>50)* 2) Calculate the vector $\underline{W}$ for the given correlation length *L* $W_m = \frac{1}{L}\left[\left(\frac{1}{1-\alpha_m}\right)^2 - 1\right]^{1/2} \qquad m = 1,2,\cdots,M$ 3) Generate the correlated Gaussian random error $\underline{g}$ at one point (x_i, y_j) $g_{ij} = g(x_i, y_j) = \left(\frac{2}{M}\right)^{1/2} \cdot \sum_{m=1}^{M} \cos\left[W_m \cdot (x_i \cdot \sin\beta_m + y_j \cdot \cos\beta_m + \delta_m)\right]$ 4) Go back to step1) for the next point until all the fields are filled. 5) Calculate the correlated Gaussian random field $\underline{\underline{G}}$. $G_{ij} = T_{ij} + g_{ij} \cdot \sigma$ G_{ij} = value of the correlated Gaussian random field at location (x_i, y_j) T_{ij} = trend of G_{ij} at location (x_i, y_j) g_{ij} = value of the Gaussian random error field with correlation length *r* at location (x_i, y_j) σ = target standard deviation

Table 2.7 Correlated Gaussian random field generation by the “Turning Bands Method”

Name	Turning Bands Method
Reference	Mantoglou, A. and Wilson, J.L., (1982)
Description	This method generates the auto-correlated random field from random values simulated along several lines, using a one-dimensional covariance function that corresponds to the given two or three-dimensional one. The weighted sum of the corresponding values of the line processes is assigned at each point of the two-dimensional field.
Procedure	1) Let $\underline{\underline{g}}$ represent the wanted two-dimensional random field 2) Choose an arbitrary origin *O* 3) Generate *N* lines with direction vectors $\underline{v}$, uniformly distributed on the unit circle or unit sphere. 4) Considering each line with index *i*, generate second-order stationary one-dimensional discrete random numbers $g_i(d_{kl})$ with zero mean and standard deviation one, as shown in the Mejía and Rodríguez Method (step 1 ~ 3). d_{kl} is the distance between point *k* and point *l*. 5) Calculate the correlated random number at each point. $$\underline{\underline{g}}(\underline{X}) = \frac{1}{\sqrt{N}} \sum_{i=1}^{N} g_i(\underline{X} \cdot \underline{v}_i)$$ Note that $\underline{X} \cdot v_i$ is the projection of $\underline{X}$ (location vector) in the direction of $\underline{v}_i$.

Table 2.8 Correlated Gaussian random field generation – Procedure suggested by Ehlschlaeger and Goodchild

Name	Ehlschlaeger and Goodchild Method
Reference	Ehlschlaeger, C.R. and Goodchild M.F., (1994)
Description	The method generates a spatially correlated Gaussian distributed random field defined by the available quantitative descriptors of variability.
Procedure	1) Generate an uncorrelated Gaussian distributed random field $\underline{\varepsilon}$ for the given geometry, and define the minimum distance of spatial independence *D* and the distance decay exponent *E*. 2) Calculate the matrix $\underline{w}$ that captures the spatial correlative effect of each point. $$\text{if } d_{ij} < D \text{ then } w_{ij} = \left(1 - \frac{d_{ij}}{D}\right)^{E}, \text{otherwise } w_{ij} = 0$$,where d_{ij} = distance between point *i* and point *j* 3) Calculate the vector of the correlated Gaussian distributed random variability, $\underline{g}$. $$g_i = \frac{\sum_j w_{ij}\varepsilon_j}{\sqrt{\sum_j w_{ij}^2}}$$ g_i = auto-correlated random variability at point *i* w_{ij} = spatial autocorrelative effect between point *i* and point *j* ε_j = Gaussian random variable with zero mean and standard deviation one at point *j* 4) Add the trend $\underline{T}$ to the calculated error vector $\underline{g}$ to get the random field $\underline{G}$ $$G_i = T_i + g_i$$

Table 2.9 Correlated Gaussian random field generation by the “Matrix Decomposition Technique”

Name	Matrix Decomposition Technique
Reference	El-Kadi A.I. and Williams, S.A., (2000)
Description	The method generates a multidimensional array that satisfies the exponentially decaying covariance function with distance between points.
Procedure	1) Assign an index to each location of the target geometry. 2) Generate matrix $\underline{d}$ where d_{ij} is the distance between point *i* and point *j*. 3) Compute the covariance matrix $\underline{A}$ from matrix $\underline{d}$ $$A_{ij} = \sigma^2 e^{-\frac{1}{L}\lvert d_{ij}\rvert}$$ σ = target standard deviation d_{ij} = distance between point *i* and point *j* *L* = correlation length 4) Decompose matrix $\underline{A}$ into matrix $\underline{C}$ so that $$\underline{\underline{A}} = \underline{\underline{C}}\,\underline{\underline{C}}^T$$ $$C_{mm}C_{im} = A_{im} - \sum_{k=1}^{m-1} C_{ik}C_{mk}$$ (Choleski decomposition; Nash, 1979) 5) Generate the uncorrelated Gaussian random field $\underline{\varepsilon}$ 6) Calculate the correlated Gaussian random field $\underline{G}$ $$\underline{G} = \underline{\underline{C}} \cdot \underline{\varepsilon} + \underline{T}$$ T_i = trend value in the random field at point *i* $\underline{\varepsilon}$ = vector of random numbers with Gaussian distribution, *N[0,1]*

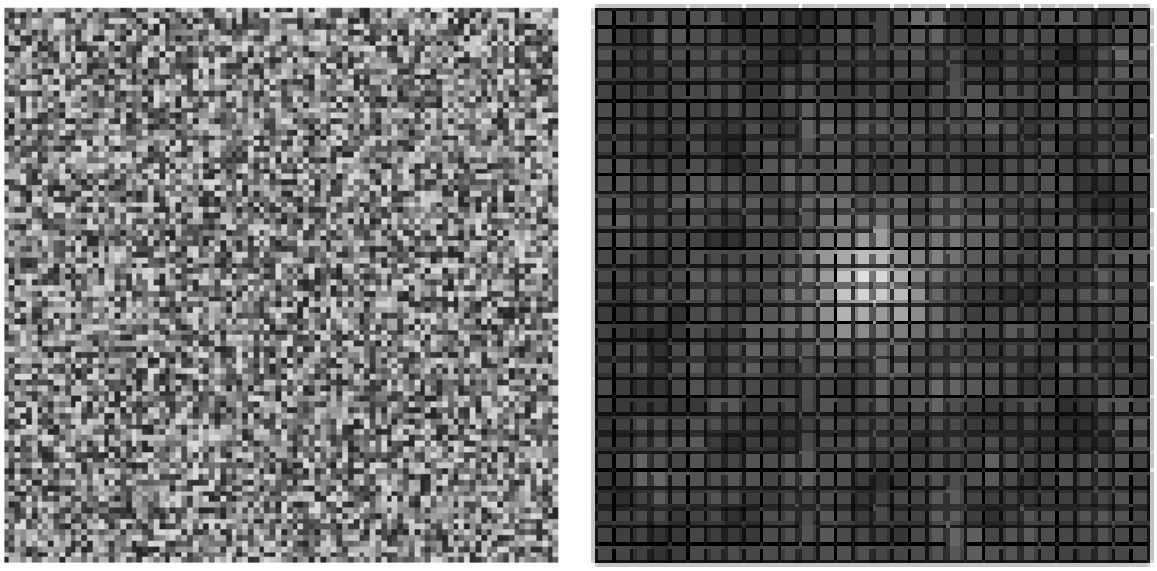

(a) (b)

(c) (d)

Figure 2.5 Examples of the artificial random fields generated with the various methods. (a) Uncorrelated random field by the Box-Muller method. (b) Correlated random field by the Mejía and Rodríguez method. (c) Correlated random field by the Ehlschlaeger and Goodchild method. (d) Correlated random field by the matrix decomposition technique

2.4 PARAMETRIC STUDY

Two preliminary studies are conducted to assess statistical trends in the simulations. The first parametric study explores the number of random numbers that guarantee stable statistical values in a generated domain. Figure 2.6 shows the evolving cumulative average and standard deviation as new random numbers are generated (uniform distribution, μ=0, σ=1). More than 10,000 realizations are needed to attain an estimation error < 1% in the mean and standard deviation. If the random numbers follow the normal distribution, the required number N of realizations for an error < 1% is N=16,641 (Harr, 1987).

The second simulation study is conducted to verify correlated random fields generated with the matrix decomposition technique. One-dimensional 1000-point long correlated random fields are simulated with correlation lengths L= 4, 10, 20, and 40. Twenty realizations are tested in each case, and the correlation length is calculated for each realization. Figure 2.7 shows an example of autocorrelograms that correspond to a one-dimensional random field with correlation length L=20. Figure 2.8 shows the results of the parametric study. The inevitable deviations between the target correlation length L_{target} and the measured correlation length L_{meas} are readily seen. The coefficient of variation in measured correlation lengths increases with the target correlation length. Therefore, a higher number of realizations are required when longer correlation lengths are simulated in order to obtain reasonable spatial statistics from correlated random field realizations.

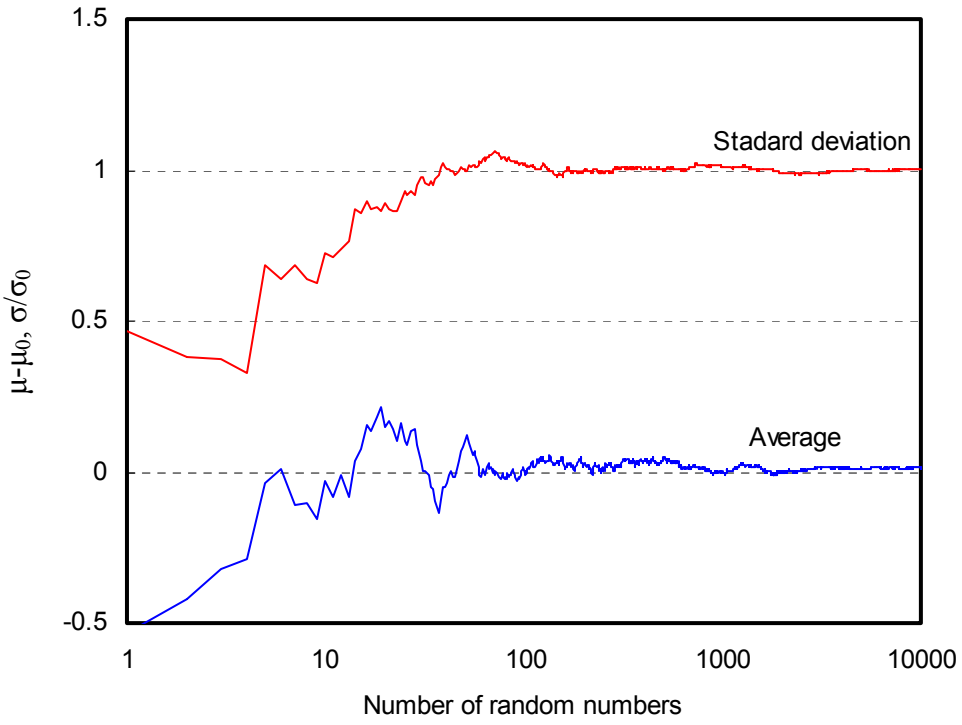

Figure 2.6 Evolving cumulative average and standard deviation. Uniform distributed random numbers with μ=0 and σ=1.

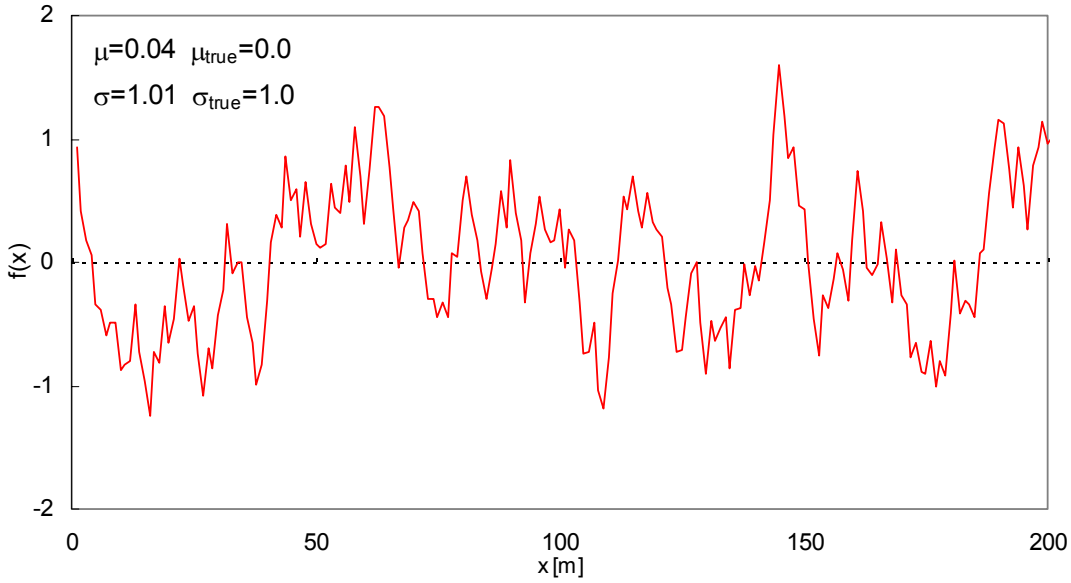

(a)

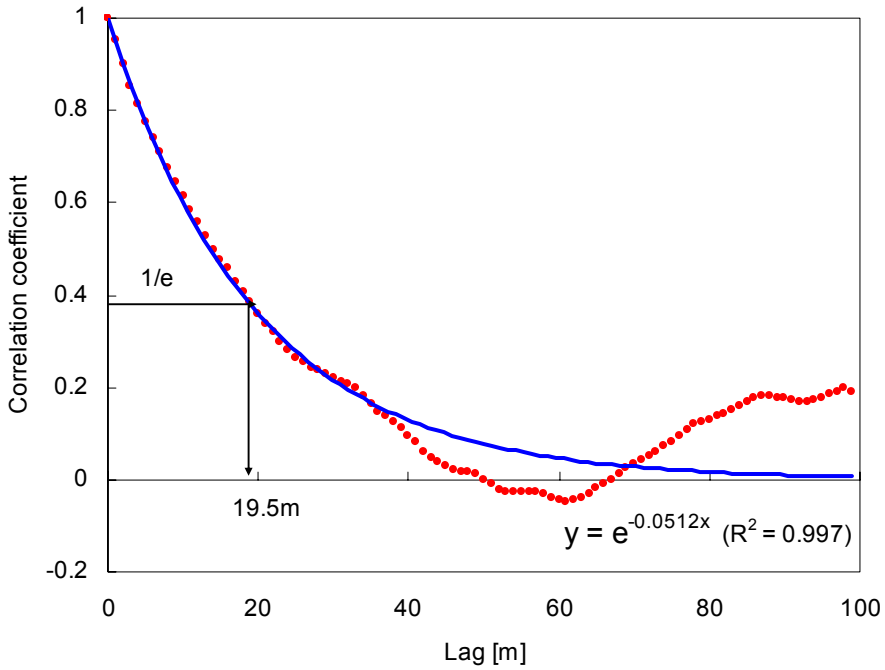

(b)

Figure 2.7 Autocorrelogram and correlation length. (a) One-dimensional correlated random field with L_{target}=20m. (b) The lag where the correlation coefficient drops to 1/e is the effective correlation length; in this simulation, L_{meas}=19.5m.

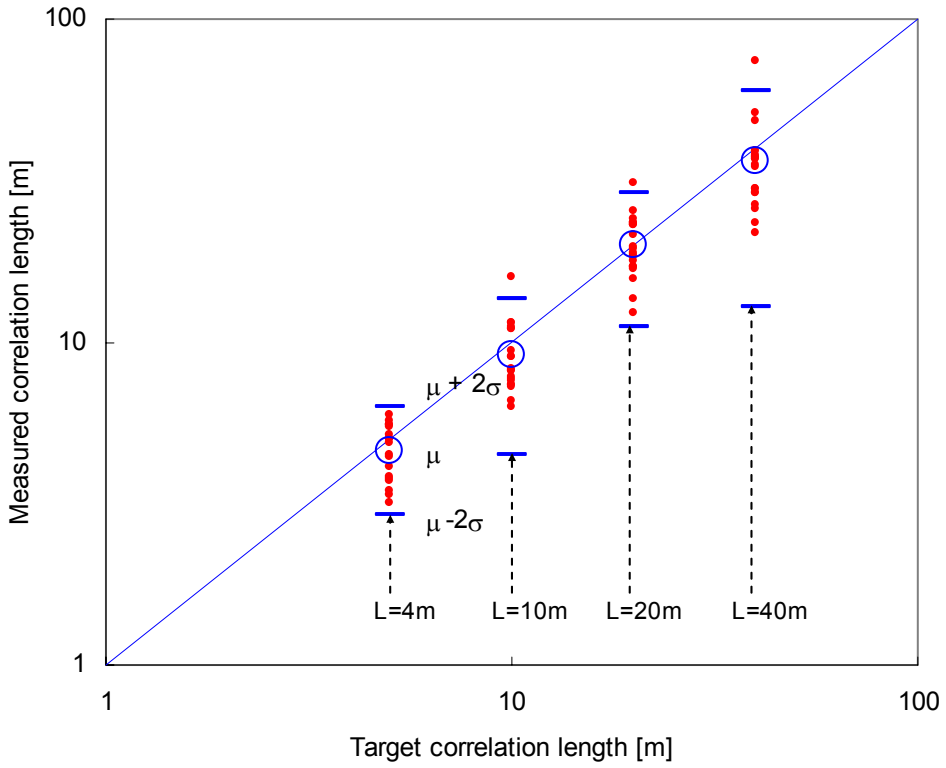

Figure 2.8 Measured correlation lengths vs. target correlation lengths. The target correlation lengths are L_{target}=4m, 10m, 20m and 40m. The mean values and two sigma ranges are shown.

2.5 SUMMARY

- The spatial variability in soil properties can be captured through three main statistical parameters: the mean trend, the deviation from the trend, and the correlation length.
- Ranges of variability parameters are available for various soil properties.
- Several numerical methods have been introduced to reconstruct multidimensional correlated random fields with pre-defined statistical parameters.
- Parametric studies show the adequacy of correlated random fields generated with the matrix decomposition technique.

CHAPTER III

STIFFNESS IN SPATIALLY VARYING MEDIA

The previous chapter discussed the spatial variability in soils, relevant descriptive parameters, and its numerical simulation. This chapter addresses local stiffness variability and its effects on the global mechanical response of spatially varying soils.

3.1 INTRODUCTION

Previous probabilistic studies have treated soils as isotropic linear elastic materials with a spatially varying Young's modulus (Resendiz and Herrera, 1969; Ang and Tang, 1975; Baecher and Ingra, 1981; Harr, 1987; Zeitoun and Baker, 1992; Fenton et al., 1996; Paice et al., 1996). The following observations can be made from these studies:

- The uncertainty in vertical displacement is much less sensitive to Poisson's ratio variability than to Young's modulus variability (Cambou, 1975).
- The expected average elastic settlement increases with increasing values in the coefficient of variation of Young's modulus, COV[E].
- As the correlation length increases, the variance of the expected settlement also increases. On the other hand, if the correlation length becomes much shorter than the loading size, the variation of the settlement is negligible.

- Field data suggest that the correlation length L is longer than the loading size B in most cases; When $L \gg B$, the variance of the settlement estimation is equal to the variance of the modulus.

Several important questions still remain. First, there is no closed form solution or mathematical expressions for effective stiffness that take into consideration the various statistical parameters in spatial variability. Second, statistical parameters such as correlation length are not properly normalized to assess mechanical effects even though spatial scales in load-deformation problems are dependent on each other. Third, the isotropic linear elasticity case has been analyzed to estimate the global deformation of heterogeneous soils in most studies.

3.2 EFFECTIVE MEDIA – EQUIVALENT LINEAR ELASTIC PROPERTIES

The load-deformation response can be obtained with a deterministic approach if accurate and complete geostatistical information is available. However, lack of spatial information leads to probabilistic formulations.

The conventional probabilistic approach considers the arithmetic mean as the representative elastic parameter to estimate the elastic behavior of heterogeneous media. However, different spatial distributions with the same mean can yield different global response. Some analytical solutions for effective elastic modulus corresponding to simple geometries are summarized in Table 3.1.

Table 3.1 (a) Effective modulus in linear elastic heterogeneous media - simple geometries (Qu, 2002).

Minimum Potential Energy Theorem
Among all kinetically admissible displacement fields, the true solution makes the potential energy minimum. The theorem gives the upper bound of effective stiffness in composite materials (Voigt's upper bound). The effective elastic modulus of this spring system is calculated as the arithmetic average of the spring moduli.
Minimum Complementary Energy Theorem
Among all statically admissible stress fields, the true solution makes the complementary energy minimum. The theorem gives the upper bound of effective compliance in composite materials, which is equal to the lower bound of effective stiffness (Reuss' lower bound). The effective elastic modulus of this spring system is calculated as the reciprocal of the average value of the inverse of spring moduli.
Hashin-Strinkman Bounds (Hashin and Strinkman, 1963)
The Hashin-Strinkman bounds give the narrowest possible range without specifying anything about the geometry. The upper bound is realized when the stiffer material forms the shell, and the lower bound is realized when the stiffer material forms the core.
Effective Stiffness of the Heterogeneous Media with Small Volume Fraction of Inclusions
If the inclusion shape is spherical or ellipsoidal, the effective modulus of such a heterogeneous material is calculated by Wu (1966) and Kuster and Toksöz (1974). Both methods are developed under the assumption that the volume fraction of the matrix material is predominant. In self consistent approximation, the effective properties are computed by adding the inclusion properties and the matrix material properties.

Table 3.1(b) Effective modulus in linear elastic heterogeneous media - simple geometries (from Qu, 2002; Mavko et al., 1998).

Minimum Potential Energy Theorem (the Voigt estimate)

$$\overline{L}_{ijkl} \le \frac{1}{D}\int_D L_{ijkl}\,dV \quad \text{, where D is a domain.}$$

Minimum Complementary Energy Theorem (the Ruess estimate; Ruess, 1929)

$$\overline{M}_{ijkl} \le \frac{1}{D}\int_D M_{ijkl}\,dV \quad \text{, where D is a domain.}$$

Hashin- Strinkman Bounds (Hashin and Strinkman, 1963)

$$K^{HS+} = K_1 + \frac{f_2}{(K_2 - K_1)^{-1} + f_1 \cdot (K_1 + \frac{4}{3}\mu_1)^{-1}}$$

$$\mu^{HS+} = \mu_1 + \frac{f_2}{(\mu_2 - \mu_1)^{-1} + \frac{2f_1(K_1 + 2\mu_1)}{5\mu_1(K_1 + \frac{4}{3}\mu_1)}}$$

Those equations are the upper bounds. If index 1 and 2 are exchanged, the lower bounds are obtained. ($K_1>K_2$, $\mu_1>\mu_2$)

Backus' average (Backus, 1962)

$$\overline{L}_{11} = < L_{11} - \frac{L_{13}^{\,2}}{L_{33}} > + < \frac{1}{L_{33}} >^{-1} < \frac{L_{13}}{L_{33}} >^2, \overline{L}_{12} = < L_{12} - \frac{L_{13}^{\,2}}{L_{33}} > + < \frac{1}{L_{33}} >^{-1} < \frac{L_{13}}{L_{33}} >^2$$

$$\overline{L}_{13} = < \frac{1}{L_{33}} >^{-1} < \frac{L_{13}}{L_{33}} >, \overline{L}_{33} = < \frac{1}{L_{33}} >^{-1}, \overline{L}_{44} = < \frac{1}{L_{44}} >^{-1}, \overline{L}_{66} = < L_{66} >$$

Kuster and Toksőz (1974)

$$(\overline{K} - K_m)\frac{(K_m + \frac{4}{3}\mu_m)}{(\overline{K} + \frac{4}{3}\mu_m)} = \sum_i f_i \cdot (K_i - K_m) \cdot P^{mi}$$

$$(\overline{\mu} - \mu_m)\frac{(\mu_m + \xi_m)}{(\overline{\mu} + \xi_m)} = \sum_i f_i \cdot (\mu_i - \mu_m) \cdot Q^{mi}$$

where

$$\xi_m = \frac{\mu_m}{6} \cdot \frac{(9K_m + 8\mu_m)}{(K_m + 2\mu_m)}, P^{mi} = \frac{K_m + \frac{4}{3}\mu_m}{K_i + \frac{4}{3}\mu_m}, Q^{mi} = \frac{\mu_m + \xi_m}{\mu_i + \xi_m}$$

Notations: L (stiffness matrix), M (compliance matrix), f (volume fraction of each material), K (bulk modulus), μ (shear modulus), υ (Poisson's ratio), <> (volume average)
Subscripts: m (matrix material), i (inclusion material)

Table 3.1(b) Effective modulus in linear elastic heterogeneous media - simple geometries (Qu, 2002; Mavko et al., 1998), (continued).

Self-consistent approximation (Wu, 1965)

$$\overline{K} = K_m + f_i \cdot (K_i - K_m) \cdot P^i$$
$$\overline{\mu} = \mu_m + f_i \cdot (\mu_i - \mu_m) \cdot Q^i$$

where

$$P^i = \frac{\overline{K} + \frac{4}{3}\overline{\mu}}{K_i + \frac{4}{3}\overline{\mu}}, \quad Q^i = \frac{\overline{\mu} + \overline{\xi}}{\mu_i + \overline{\mu}}, \quad \overline{\xi} = \frac{\overline{\mu}}{6} \cdot \frac{(9\overline{K} + 8\overline{\mu})}{(\overline{K} + 2\overline{\mu})}$$

The Eshelby estimate (Eshelby, 1957)

$$\overline{\mu} = \mu_m \left\{ 1 - \frac{f_1(\mu_1 - \mu_m)}{\mu_m + 2\delta_m(\mu_1 - \mu_m)} \right\}^{-1}$$
$$\overline{K} = K_m \left\{ 1 - \frac{f_1(K_1 - K_m)}{K_m + 3\gamma_m(K_1 - K_m)} \right\}^{-1}$$

where

$$\gamma_m = \frac{K_m}{3K_m + 4\mu_m} = \frac{1 + \upsilon_m}{9(1 - \upsilon_m)}, \delta_m = \frac{3K_m + 6\mu_m}{15K_m + 20\mu_m} = \frac{4 - 5\upsilon_m}{15(1 - \upsilon_m)}$$

The Mori-Tanaka estimate (Mori and Tanaka, 1973)

$$\overline{\mu} = \mu_m \left\{ 1 - \frac{f_1(\mu_1 - \mu_m)}{\mu_m + 2\delta_m(1 - f_1)(\mu_1 - \mu_m)} \right\}^{-1}$$
$$\overline{K} = K_m \left\{ 1 - \frac{f_1(K_1 - K_m)}{K_m + 3\gamma_m(1 - f_1)(K_1 - K_m)} \right\}^{-1}$$

where

$$\gamma_m = \frac{K_m}{3K_m + 4\mu_m} = \frac{1 + \upsilon_m}{9(1 - \upsilon_m)}, \delta_m = \frac{3K_m + 6\mu_m}{15K_m + 20\mu_m} = \frac{4 - 5\upsilon_m}{15(1 - \upsilon_m)}$$

The Hill's average moduli estimate (Hill, 1952)

$$\overline{K} = \frac{K_{Voigt} + K_{Ruess}}{2}$$

where

$$K_{Voigt} = \sum_{i=1}^{N} f_i K_i, \quad \frac{1}{K_{Ruess}} = \sum_{i=1}^{N} \frac{f_i}{K_i}$$

Notations: L (stiffness matrix), M (compliance matrix), f (volume fraction of each material), K (bulk modulus), μ (shear modulus), υ (Poisson's ratio), <> (volume average)
Subscripts: m (matrix material), i (inclusion material)

Table 3.1(b) Effective modulus in linear elastic heterogeneous media - simple geometries (Qu, 2002; Mavko et al., 1998), (continued).

Winkler (1983): for a random sphere packing

$$\overline{K} = \frac{C(1-\phi)}{12\pi R} S_n, \quad \overline{G} = \frac{C(1-\phi)}{20\pi R}\left(S_n + 1.5 S_\tau\right)$$

where S_n and S_τ are normal and tangential stiffness of a two-sphere combination (Digby, 1981).

$$S_n = \frac{4Gb}{1-\upsilon}, \quad S_\tau = \frac{8Ga}{1-\upsilon}$$

where a is the radius of the contact area

$$b = R\left[d^2 + \left(\frac{a}{R}\right)^2\right]^{1/2}, \text{where } d^3 + \frac{3}{2}\left(\frac{a}{R}\right)^2 d - \frac{3\pi(1-\upsilon)}{2C(1-\phi)}\frac{P}{G} = 0$$

The Hertz-Mindlin model (Mindlin, 1949)

$$\overline{K} = \sqrt[3]{\frac{C^2(1-\phi)^2 G^2}{18\pi^2(1-\upsilon)^2} P}, \quad \overline{G} = \frac{5-4\upsilon}{5(2-\upsilon)} \sqrt[3]{\frac{3C^2(1-\phi)^2 G^2}{2\pi^2(1-\upsilon)^2} P}$$

where P is an applied hydrostatic pressure

The Walton model (Walton, 1987)

$$\overline{K} = \frac{1}{6}\sqrt[3]{\frac{3(1-\phi)^2 C^2 P}{\pi^4 B^2}}, \quad \overline{G} = \frac{3}{5}\overline{K}\frac{5B+A}{2B+A}$$

where

$$A = \frac{1}{4\pi}\left(\frac{1}{G} - \frac{1}{G+\lambda}\right), \quad B = \frac{1}{4\pi}\left(\frac{1}{G} + \frac{1}{G+\lambda}\right),$$

λ is Lamé's coefficient of the grain material.

The Brandt model (Brandt, 1955)

$$K = \frac{2P^{1/3}}{9\phi}\left[\frac{E}{1.75(1-\upsilon^2)}\right]^{2/3} Z - 1.5PZ$$

where

$$Z = \frac{(1+30.75z)^{5/3}}{1+46.13z}, \quad z = \frac{K^{3/2}(1-\upsilon^2)}{E\sqrt{P}},$$

E is Young's modulus of the mineral and K is the fluid bulk modulus.

Notations: Φ (porosity), C (coordination number), R (sphere radius), G (the shear modulus of the grain material), υ (Poisson's ratio of the grain material)

Table 3.1(b) Effective modulus in linear elastic heterogeneous media - simple geometries (Qu, 2002; Mavko et al., 1998), (continued).

The low-frequency Gassmann-Biot theory (Biot, 1956)

$$\frac{K_{sat}}{K_0 - K_{sat}} = \frac{K_{dry}}{K_0 - K_{dry}} + \frac{K_{fl}}{\phi(K_0 - K_{fl})}, \quad \mu_{sat} = \mu_{dry}$$

where

K_{dry}, μ_{dry}=effective bulk and shear modulus of dry rock

K_{sat}, μ_{sat} =effective bulk and shear modulus of the saturated rock

K_0=bulk modulus of mineral material

K_{fl}=effective modulus of pore fluid

Φ=porosity

The Mavko-Jizba squirt relations (Mavko and Jizba, 1991)

$$\frac{1}{K_{uf}} \approx \frac{1}{K_{dry-hiP}} + \left(\frac{1}{K_{fl}} + \frac{1}{K_0}\right)\phi_{soft}, \quad \left(\frac{1}{\mu_{uf}} - \frac{1}{\mu_{dry}}\right) = \frac{4}{15}\left(\frac{1}{K_{uf}} - \frac{1}{K_{dry}}\right)$$

where

K_{uf}, μ_{uf} =effective high-frequency unrelaxed wet frame bulk and shear modulus

K_{dry}, μ_{dry} =effective bulk and shear modulus of dry rock

$K_{dry\text{-}hiP}$ = effective bulk modulus of dry rock at very high pressure

K_0=bulk modulus of mineral material

K_{fl}=effective modulus of pore fluid

Φ_{soft}=soft porosity – the amount of porosity that closes at high pressure

Notations: Φ (porosity), C (coordination number), R (sphere radius), G (the shear modulus of the grain material), υ (Poisson's ratio of the grain material)

Closed-form solutions for simple spring-geometries are summarized in Table 3.2. The following observations can be made:

- The effective modulus of a two-dimensional spring network depend on the rate of shear coupling between spring columns.
- The effective spring constant for a network with perfect shear coupling is the arithmetic mean, and it is the harmonic mean when there is no shear coupling.
- The harmonic mean is a lower bound of the effective modulus.

3.2.2 One-Dimensional Randomly Varying Media

The effective Young's modulus for one dimensional deformation under vertical loading is the harmonic mean of Young's modulus with depth E_z. The effective modulus can be decoupled into the trend part and the random variability part, and the range of random variability is assumed proportional to the trend value when the mean trend of Young's modulus variation with depth $\overline{E}_z$, and the random variability with depth ε_z are assigned as independent variables of each other

$$E_{eff\,(\text{with random variability})} = \frac{1}{\mu\left(\frac{1}{E_z}\right)} = \frac{1}{\mu\left(\frac{1}{\overline{E}_z(1+\varepsilon_z)}\right)} = \frac{1}{\mu\left(\frac{1}{\overline{E}_z}\right)\cdot\mu\left(\frac{1}{1+\varepsilon_z}\right)} \tag{3.5}$$

$$E_{eff\,(\text{without random variability})} = \frac{1}{\mu\left(\frac{1}{\overline{E}_z}\right)} \tag{3.6}$$

Table 3.2 Simplified spatial variability model of 2-dimensional linear elastic fields

Condition	Effective elastic modulus
Generalized 2D elastic model	
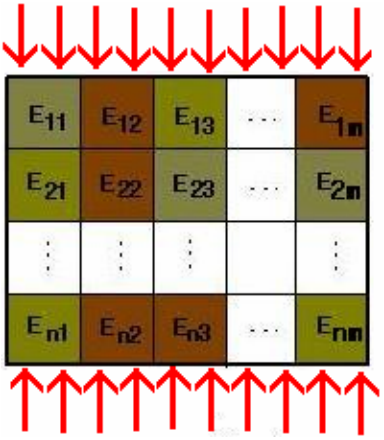	There is no analytic solution for general 2D elastic field. *m* is the number of element in the horizontal direction, and *n* is the number of element in the vertical direction.
"No shear coupling" between spring columns	
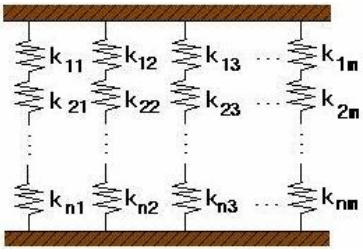	(i) n, m are finite numbers $\bar{k}_{no-coupling} = \frac{1}{m}\sum_{j=1}^{m}\frac{1}{\frac{1}{n}\sum_{i=1}^{n}\frac{1}{k_{ij}}}$ (ii) n, m are infinite numbers $\bar{k}_{no-coupling} = \lim_{m\to\infty}\lim_{n\to\infty}\frac{1}{m}\sum_{j=1}^{m}\frac{1}{\frac{1}{n}\sum_{i=1}^{n}\frac{1}{k_{ij}}} = \lim_{m\to\infty}\lim_{n\to\infty}\frac{1}{m}\cdot\sum_{j=1}^{m}\text{Harmonic Mean}_{\text{j}}\left[k_{ij}\right]$ $= \lim_{m\to\infty}\lim_{n\to\infty}\text{Arithmetic}_{\text{i}}\left[\text{Harmonic}_{\text{j}}\left[k_{ij}\right]\right] \approx (\text{Harmonic mean of } k)$
"Perfect shear coupling" between spring columns	
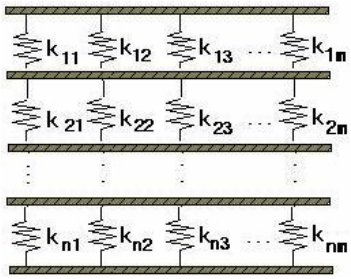	(i) n, m are finite numbers $\bar{k}_{perfect-coupling} = \frac{1}{\frac{1}{n}\sum_{i=1}^{n}\frac{1}{\frac{1}{m}\sum_{j=1}^{m}k_{ij}}}$ (ii) n, m are infinite numbers $\bar{k}_{perfect-coupling} = \lim_{n\to\infty}\lim_{m\to\infty}\frac{1}{\frac{1}{n}\sum_{i=1}^{n}\frac{1}{\frac{1}{m}\sum_{j=1}^{m}k_{ij}}} = \lim_{n\to\infty}\lim_{m\to\infty}\frac{1}{\frac{1}{n}\sum_{i=1}^{n}\frac{1}{\text{Arithmetic}_{\text{i}}\left[k_{ij}\right]}}$ $= \text{Harmonic}_{\text{j}}\left[\text{Arithmetic}_{\text{i}}\left[k_{ij}\right]\right] \approx (\text{Aithmetic mean of } k)$

Note: $\text{Harmonic}_j[A]$ is the harmonic mean value of property A in the column indexed with j, and $\text{Arithmetic}_i[A]$ is the arithmetic mean value of property A in the layer indexed with i.

where $\mu(A)$ is the line average of A. The ratio of the effective modulus with variability to the effective modulus without random variability is:

$$\frac{E_{eff\,(\text{with random variability})}}{E_{eff\,(\text{without random variability})}} = \frac{1 \Big/ \mu\left(\frac{1}{\overline{E}_z}\right) \cdot \mu\left(\frac{1}{1+\varepsilon_z}\right)}{1 \Big/ \mu\left(\frac{1}{\overline{E}_z}\right)} = \frac{1}{\mu\left(\frac{1}{1+\varepsilon_z}\right)} \tag{3.7}$$

The ratio is independent of the mean trend of the modulus, and it depends only on the harmonic mean of the random variability part. Therefore, the effective modulus considering random variability can be estimated by multiplying the expectation of the random variability part and the effective modulus without the random variability:

$$E_{\text{eff (with random variabilities)}} = \frac{1}{\mu\left(\frac{1}{1+\varepsilon_z}\right)} \cdot E_{\text{eff (without random variabilities)}} \tag{3.8}$$

3.2.3 Estimation of the Harmonic Mean of the Random Variability Component

The random variability component can be estimated once the probability distribution is known. Uniform, normal and log-normal distributions are often assumed in geotechnical engineering (Lumb, 1966; Tan et al., 1993; Lacasse and Nadim, 1996). If the random variable is assumed normal distributed, negative and infinitely large positive values are possible, which may not be physically acceptable in many geotechnical parameters such as mass density, elastic modulus and hydraulic conductivity. The log-normal distribution applies to positive random variables, but is biased. Finally, while the uniform distribution may appear less realistic than normal or log-normal distributions,

the uniform distribution assumption can provide reasonable physical restrictions for extreme value management.

The harmonic mean of a random variable $1+\varepsilon_z$ (from Eq. 3.8) is defined as:

$$\frac{1}{\mu\left(\frac{1}{1+\varepsilon_z}\right)} = \frac{1}{\int_{x_{\min}}^{x_{\max}} \frac{1}{1+x} \cdot f(x)dx} \tag{3.9}$$

where ε_z captures the random variability normalized by the trend value, and *f(x)* is the associated probability density function. The value of ε_z has zero mean and must be larger than –1. For example, if random variability follows the uniform distribution, the integration range is $\pm\sqrt{3}\cdot COV$ and the probability density function is $f(x) = 1/[2\sqrt{3}COV]$. Then,

$$\left[\frac{1}{\int_{x_{\min}}^{x_{\max}} \frac{1}{1+x} \cdot f(x)dx}\right]_{\text{Uniform Distribution}} = \frac{1}{\int_{-\sqrt{3}COV}^{\sqrt{3}COV} \frac{1}{1+x} \cdot \frac{1}{2\sqrt{3}COV} dx} = \frac{2\sqrt{3}\cdot COV}{\ln\left(\frac{1+\sqrt{3}\cdot COV}{1-\sqrt{3}\cdot COV}\right)} \tag{3.10}$$

Figure 3.1 shows the estimation of the random variability component (in Eq. 3.8) for uniform, normal and log-normal distributions. The harmonic mean is very sensitive to small values. Therefore, all the generated random numbers are greater than 1% of the selected mean value. All curves in Figure 3.1 show a decrease in harmonic mean with increasing COV, even though the global arithmetic mean remains the same. Differences between the harmonic mean estimation for the different distributions is very small when the variability range is less than 30% of COV. Conversely, the harmonic mean is very sensitive to the distribution for widely varying conditions (Note: USACE, 1995 - See Jones et al., 2002 - suggests guidelines for probabilistic distribution selection).

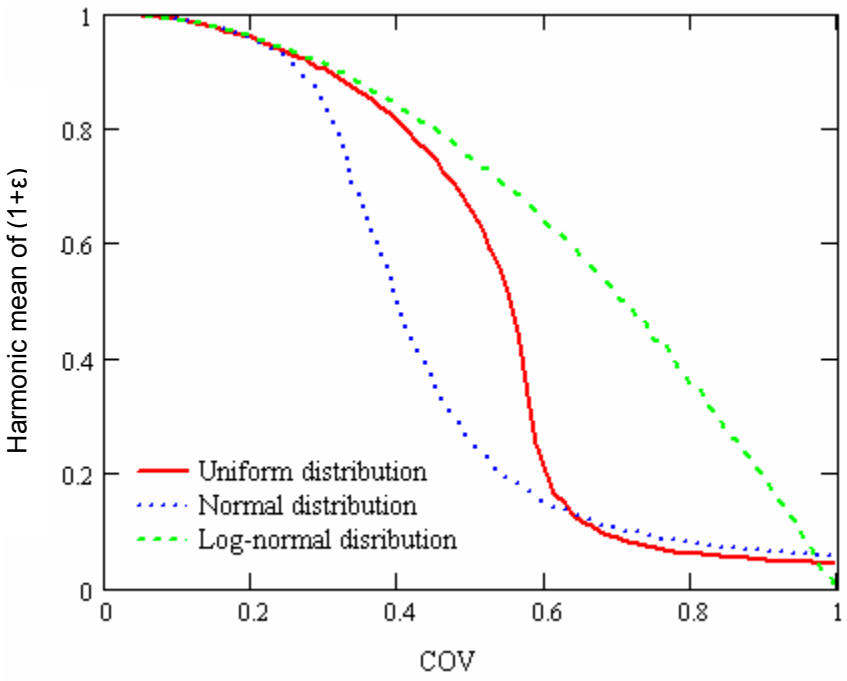

Figure 3.1 Harmonic mean of a random variable (1+ε) – different probability distribution. Note: ε is a random variable with zero mean

3.3 HETEROGENEOUS MEDIA SUBJECTED TO ISOTROPIC LOADING

The internal stress distribution due to isotropic boundary loading is homogeneous when the medium is perfectly homogeneous (Timoshenko and Goodier, 1970). This is not the case in spatially heterogeneous media such as soils.

3.3.1 Material Model Description

The modified Duncan-Chang material model is herein used to describe the nonlinear shear strain-dependent soil behavior. Duncan and Chang (1970) develop the hyperbolic material model to capture soil characteristics such as isotropic stress induced hardening, Mohr-Coulomb strength, hysteresis phenomena, and the difference between the ultimate deviatory stress and the initial yield stress. The modified Duncan-Chang material model involves about thirteen parameters. The mechanical response of cohesionless particulate materials is investigated under primary isotropic or K_0 loading in this study. Model parameters can be limited to several parameters. Other parameters except for the G_{max}-σ' power function parameters α^* and β^* are assumed constant.

The power function exponents α^* and β^* are dependent on each other. Fernandez (2000) summarizes shear wave velocity measurement for the various materials ranging from sands and clays, to lead shot and steel spheres (Table 3.3). The stiffer the particles and the denser the packing, then the higher value of α and the lower value of β are, where $V_s = \alpha \cdot \left(\frac{\sigma_1 + \sigma_3}{2kPa} \right)^{\beta}$. The empirical equation for this relationship is

$$\beta \approx 0.36 - \frac{\alpha}{700} \tag{3.11}$$

If the mass density ρ is assumed constant during loading, the small strain shear modulus parameters α_G^* and β_G^* can be defined from α and β.

$$G_{\max} = \rho \cdot V_s^2 = \rho\alpha^2 \cdot \left(\frac{\sigma_0}{1kPa}\right)^{2\beta} = \alpha_G^* \left(\frac{\sigma_0}{1kPa}\right)^{\beta_G^*} \tag{3.12}$$

Table 3.3 Typical values for α and β (Compiled by Fernandez, 2000)

Theory/Reference	Type of material	α[m/sec]	β
Hertz's theory	Spherical particles		0.250
	Cone to plane contacts		0.167
Sand			
Fam and Santamarina (1996)	Barco sand	91.34	0.250
Sully and Campanella (1995)	Sand	59.23	0.250
Roesler (1979)	Rounded sand	99	0.246
	Rounded sand	106	0.228
Jamiolkowski and Presti (1994)	Ticino sand	88	0.209
Yan and Byrne(1990)	Ottawa sand	55.5	0.276
	Silica sand	112.56	0.176
	Silica sand	106.6	0.22
	Silica sand	67.2	0.285
Stokoe et al. (1991)	Ottawa sand	67.37	0.32
Fine grained soils			
Santamarina et al. (1996)	Lagunillas silt	54.93	0.258
Cascante and Santamarina (1996)	Kaolinite	41.00	0.301
Butcher and Powell (1996)	Holmen sand	28.65	0.32
Cascante and Santamarina (1996)	Silica flour	30.00	0.309
Other granular materials			
Canscante and Santamarina (1996)	Steel spheres	170.74	0.140
	Lead shots	56.95	0.250
	Silica/Kaolin pellets	56.08	0.250

3.3.2 Numerical Experimentation Scheme

A disk with a diameter D is discretized into 1962 four-node plane strain square elements. Two-dimensional correlated random fields are generated with a relative correlation length L/D=0.16. The small-strain shear modulus at 1kPa, α_G^*, is selected as the random variable, and the other properties are assumed constant. Table 3.4 summarizes all the material parameters in this simulation. The assigned mean value of the small-strain shear modulus at 1kPa is α_G^*=102Mpa, and the corresponding β_G^* is computed from Eq. 3.11. The coefficient of variation in the uniform distributed small-strain elastic modulus is COV[α_G*]=0.1. An isotropic loading of 100kPa is applied, and the volumetric stress and strain are analyzed radially from the center to evaluate changes in the local and global mechanical response (Figure 3.2). Numerical simulations are repeated twenty times for each case to obtain statistically meaningful results for correlated random media.

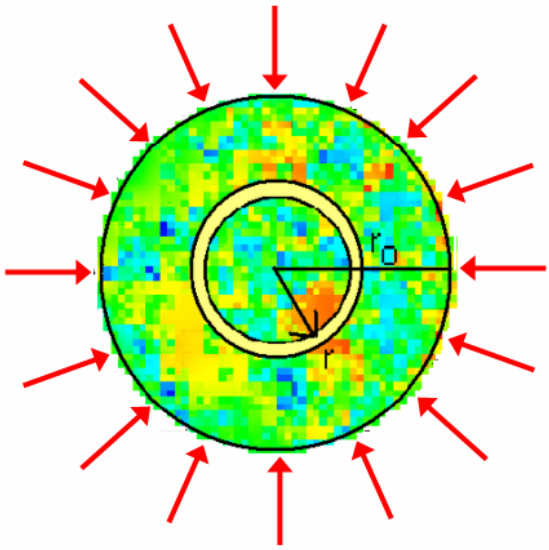

Figure 3.2 Isotropic loading on a heterogeneous medium (1962 four-node plain strain elements). The stress and strain fields are investigated along concentric annular zones.

3.3.3 Reference Case

The reference material corresponds to a dense sand (See Table 3.4). Results are interpreted in terms of statistical parameters defined in Table 3.5.

3.3.3.1 Volumetric Stress Distribution

Figure 3.3 shows the volumetric stress distribution and its variance versus the radial distance from the center of the disk. The measured mean volumetric stress values are normalized by the externally applied isotropic stress to study internal load transfer. Figure 3.3a shows that volumetric stresses near the center are smaller than around the perimeter because stresses are transferred along the correlated stiffer zone.

Figure 3.3b shows the ensemble COV of realizations' mean volumetric stress distribution. The volumetric stress near the boundary is similar to the applied external isotropic stress. The variation in the mean volumetric stress increases toward the center particularly when $r<0.6r_0$.

Figure 3.3c displays the ensemble mean of realizations' COV for volumetric stress versus radial distance.

Table 3.4 Reference material properties of dense sands for the Monte Carlo simulation with the modified Duncan and Chang model

Notation	Property Description	Reference Value
Material Properties		
α_G^*	Mean of small-strain shear modulus at 1kPa for the primary loading	102Mpa
$\alpha_{G\_ul}^*$	Mean of small-strain shear modulus at 1kPa for the unloading and reloading	N/A
α_B^*	Mean of bulk modulus at 1kPa for the primary loading	137Mpa
β_G	Stress exponent of small-strain shear modulus	0.49
β_B	Stress exponent of bulk modulus	0.49
P_a	Atmospheric pressure	100kPa
R_f	Failure ratio	1
c	Cohesion intercept of soil	0
ϕ	Soil friction angle at $\sigma'_3 = P_a$	30^o
$\Delta\phi$	Friction angle reduction factor	0^o
G_i	Mean of Young's modulus for geostatic step	102Mpa
B_i	Mean of bulk modulus for geostatic step	137Mpa
ρ_{dry}	Dry mass density	$16kN/m^3$
Random Variability Characteristics		
COV_E	Coefficient of variation in the initial small-strain elastic modulus distribution	10%
L/D	Relative correlation length	16%

Table 3.5 Parameters used to analyze the results attained with randomly realized media

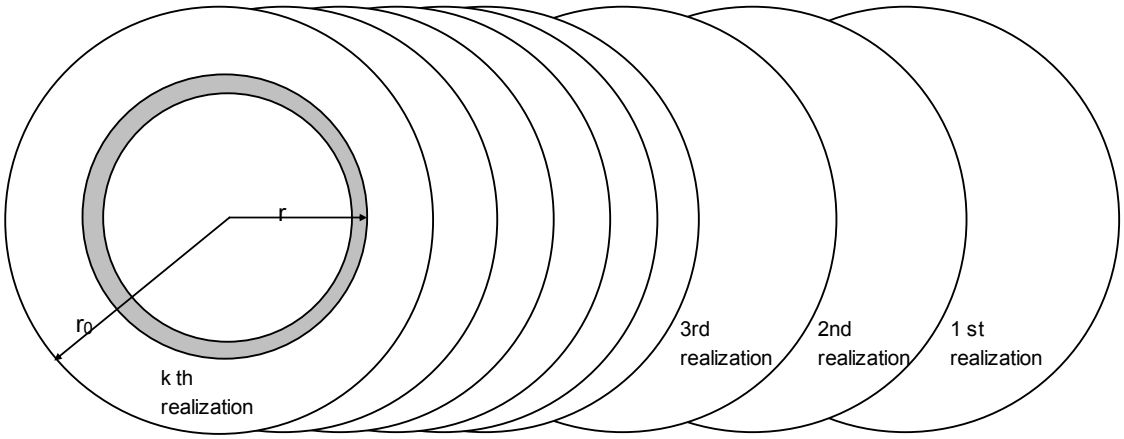

Radial statistics for the k-th realization	Ensemble statistics for k=1-to-K realizations
1) Realization' s mean volumetric stress at radial distance r $\mu_k[J_1(r)] = \frac{\sum_{n=1}^{N(r)} [J_1(r)]_k}{N(r)}$ 2) Realization' s standard deviation for volumetric stress at radial distance r $\sigma_k[J_1(r)] = \sqrt{\frac{\sum_{n=1}^{N(r)} \{[J_1(r)]_k - \mu_k[J_1(r)]\}^2}{N(r)}}$ 3) Realization' s COV for volumetric stress at radial distance r $COV_k[J_1(r)] = \frac{\sigma_k[J_1(r)]}{\mu_k[J_1(r)]}$	1) Ensemble average of realizations' mean volumetric stresses at radial distance r $\mu[\mu_k[J_1(r)]] = \frac{\sum_{k=1}^{K} \mu_k[J_1(r)]}{K}$ 2) Ensemble mean of realization's standard deviations for volumetric stress at radial distance r $\mu[\sigma_k[J_1(r)]] = \frac{\sum_{k=1}^{K} \sigma_k[J_1(r)]}{K}$ 3) Ensemble mean of realizations' COV for volumetric stress at radial distance r $\mu[COV_k[J_1(r)]] = \mu\left[\frac{\sigma_k[J_1(r)]}{\mu_k[J_1(r)]}\right]$ 4) Ensemble standard deviation of the realizations' mean volumetric stress at radial distance r $\sigma[\mu_k[J_1(r)]] = \sqrt{\frac{\sum_{k=1}^{K} \{\mu_k[J_1(r)] - \mu[\mu_k[J_1(r)]]\}^2}{K}}$ 5) Ensemble COV of realizations' mean volumetric stress at radial distance r $COV[\mu_k[J_1(r)]] = \frac{\sigma[\mu_k[J_1(r)]]}{\mu[\mu_k[J_1(r)]]}$

Note: $N(r)$ is the number of elements with radial distance r, and K is the number of realizations, and k is the index for each realization, and $J_1(r)$ is the volumetric stress at radial distance r, and $J_1(r_0)$ is the applied isotropic stress. All relationships are the same for $I_1(r)$, the volumetric strain at radial distance r.

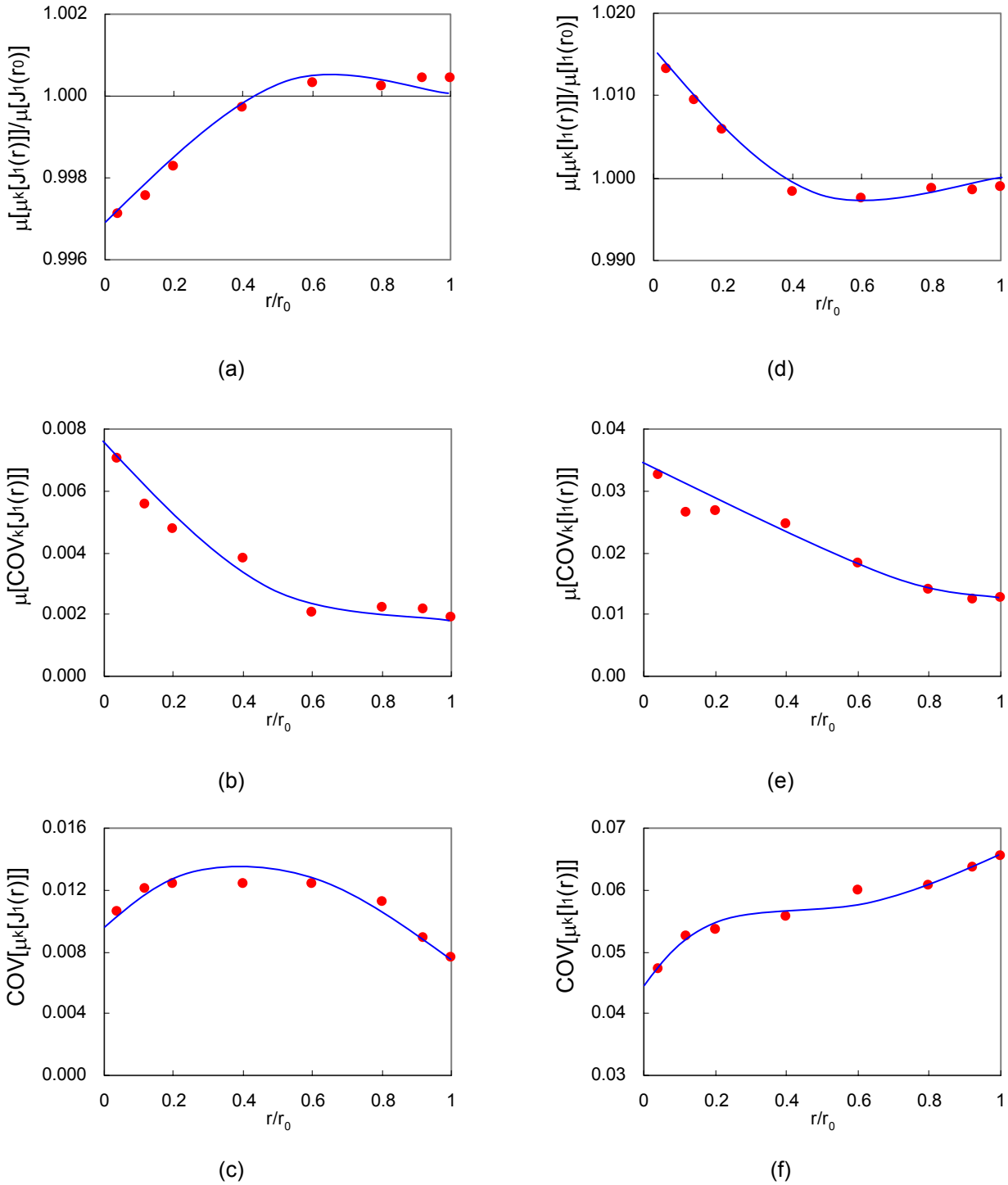

Figure 3.3 Isotropic loading heterogeneous soils in circular geometry. All parameters are for dense sand. (a) Ensemble average of realizations' mean volumetric stresses. (b) Ensemble mean of realizations' COV for volumetric stress. (c) Ensemble COV of realization's mean volumetric stress. (d) Ensemble average of realizations' mean volumetric strains. (e) Ensemble mean of realizations' COV for volumetric strain. (c) Ensemble COV of realization's mean volumetric strain.

3.3.3.2Volumetric Strain Distribution

The radial distribution of the ensemble average of realizations' mean volumetric strains normalized by the global volumetric strain is shown in Figure 3.3d. The volumetric strain increases towards the center. Figure 3.3e shows that the ensemble COV of realizations' mean volumetric strain increases towards the center in agreement with the variability in volumetric stress. Finally, Figure 3.3f shows the ensemble mean of realizations' COV for the volumetric strains at radial distance r. Local deformations are more homogeneous at the center.

3.3.4 Parametric Studies with Different Conditions.

The mechanical response associated to spatial variability with different material models is explored herein. Different assumptions are compared to identify their effects on global material properties:

1) Nonlinear elasticity (reference material) vs. linear elasticity
2) Long correlation length (L/D=0.16; reference material) vs. short correlation length (L/D=0.01)
3) COV[α_G*]=0.1 (reference material) vs. COV[α_G*]=0.2
4) Dense sand (reference material) vs. soft clay
5) Circular shape boundary (reference material) vs. rectangular shape boundary.

3.3.4.1 Linear Elasticity vs. Nonlinear Elasticity

Figure 3.4 shows a comparison between cases. The stress transferred through the center decreases (Figure 3.4a), and the global mechanical response is more variable

(Figures 3.4b and c) when the system is linear. This is in agreement with the stress-induced homogenization phenomenon in non-linear media. Results in Figure 3.4f confirm homogenization effects in terms of the decrease in variance, particularly around the perimeter of the nonlinear heterogeneous medium.

3.3.4.2 Long vs. Short Correlation Length

The physical similarity between contiguous points decreases when the correlated random fields are generated with a short correlation length (L/D=0.01). However, a more statistically homogeneous variability is obtained. The shorter correlation length would lead to lower stress concentration through stiffer zones, and the load transferred through the center of a medium increases with decreasing correlation length (Figure 3.5a). The local variance in the volumetric parameters increases with shorter correlation length (Figure 3.5c, f). However, the variance between realizations decreases (Figure 3.5b, e). The volumetric deformation at the center decreases in short correlated media (Figure 3.5d) because shorter correlation length yields more statistically homogeneous variability in a given local area.

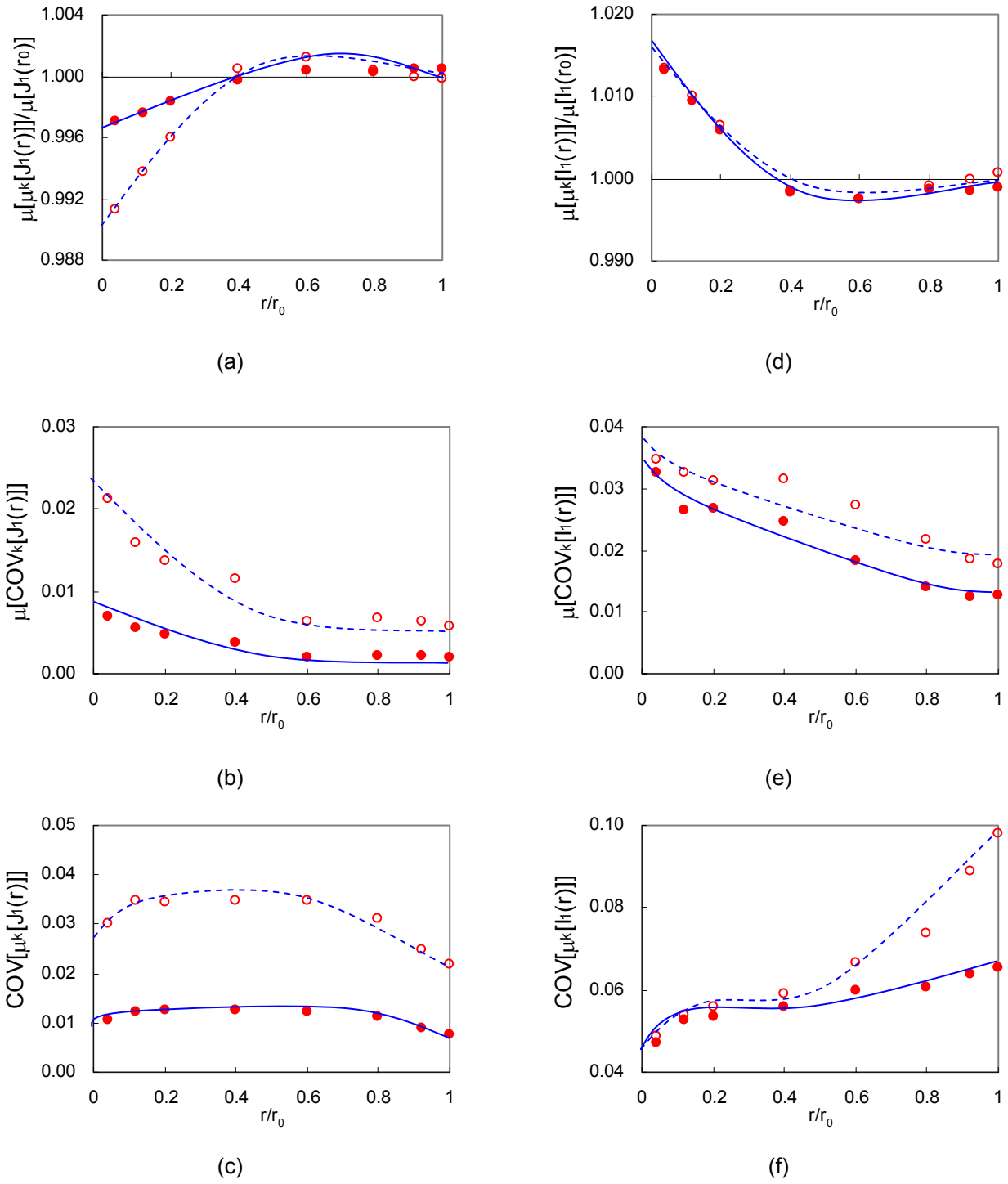

Figure 3.4 Effects of material model on the radial distribution of volumetric stress and strain - Linear elastic material model (hollow dots) versus modified Duncan-Chang material model (solid dots). (a) Ensemble average of realizations' mean volumetric stresses. (b) Ensemble mean of realizations' COV for volumetric stress. (c) Ensemble COV of realization's mean volumetric stress. (d) Ensemble average of realizations' mean volumetric strains. (e) Ensemble mean of realizations' COV for volumetric strain. (c) Ensemble COV of realization's mean volumetric strain.

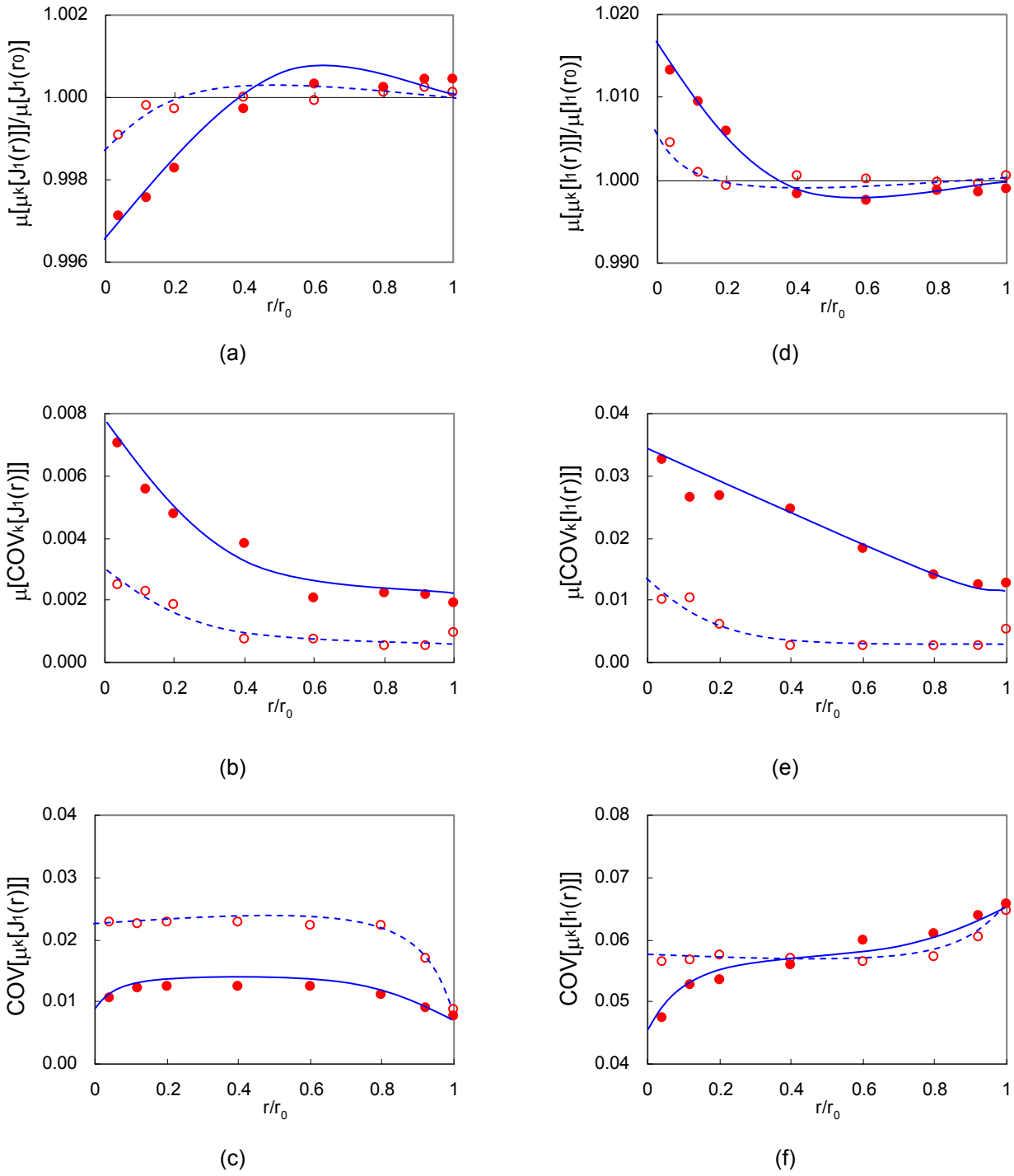

Figure 3.5 Effects of spatial correlation in random variable on the radial distribution of volumetric stress and strain (solid dots, L/D = 16% vs. hollow dots, L/D = 1%). (a) Ensemble average of realizations' mean volumetric stresses. (b) Ensemble mean of realizations' COV for volumetric stress. (c) Ensemble COV of realization's mean volumetric stress. (d) Ensemble average of realizations' mean volumetric strains. (e) Ensemble mean of realizations' COV for volumetric strain. (c) Ensemble COV of realization's mean volumetric strain.

3.3.4.3. Different COV[α_G] in Small Strain Elastic Modulus Parameter*

Two different variations in the small-strain elastic modulus parameter α^* are imposed for the same random media (COV[α_G*] =0.1 and 0.2). The local variation and the variation among realizations increase with COV[α_G*] (Figure 3.6). Higher variability also leads to a reduction to the load transfer through the center, and increases the relative volumetric strain at the center. The increase in stiffness variability decreases the effective global stiffness. Thus, the global volumetric strain in the case with COV[α_G*] =0.2 is greater than in the case with COV[α_G*] =0.1.

3.3.4.4 Dense Sand vs. Soft Clay

The small strain stiffness parameters α_G^* and β_G^* are selected to represent dense sand and soft clay. The assigned mean value of α_G^* for soft clay is $\mu[\alpha_G^*]$=19.6MPa, and the corresponding exponent is β_G^* =0.62. Figure 3.7 shows that the dense sand becomes more homogenized with pressure than the soft clay. Note that the same initial COV[α_G*] causes higher and wider variability in the soft clay because the material nonlinearity with higher β_G^* is more sensitive to the applied stress.

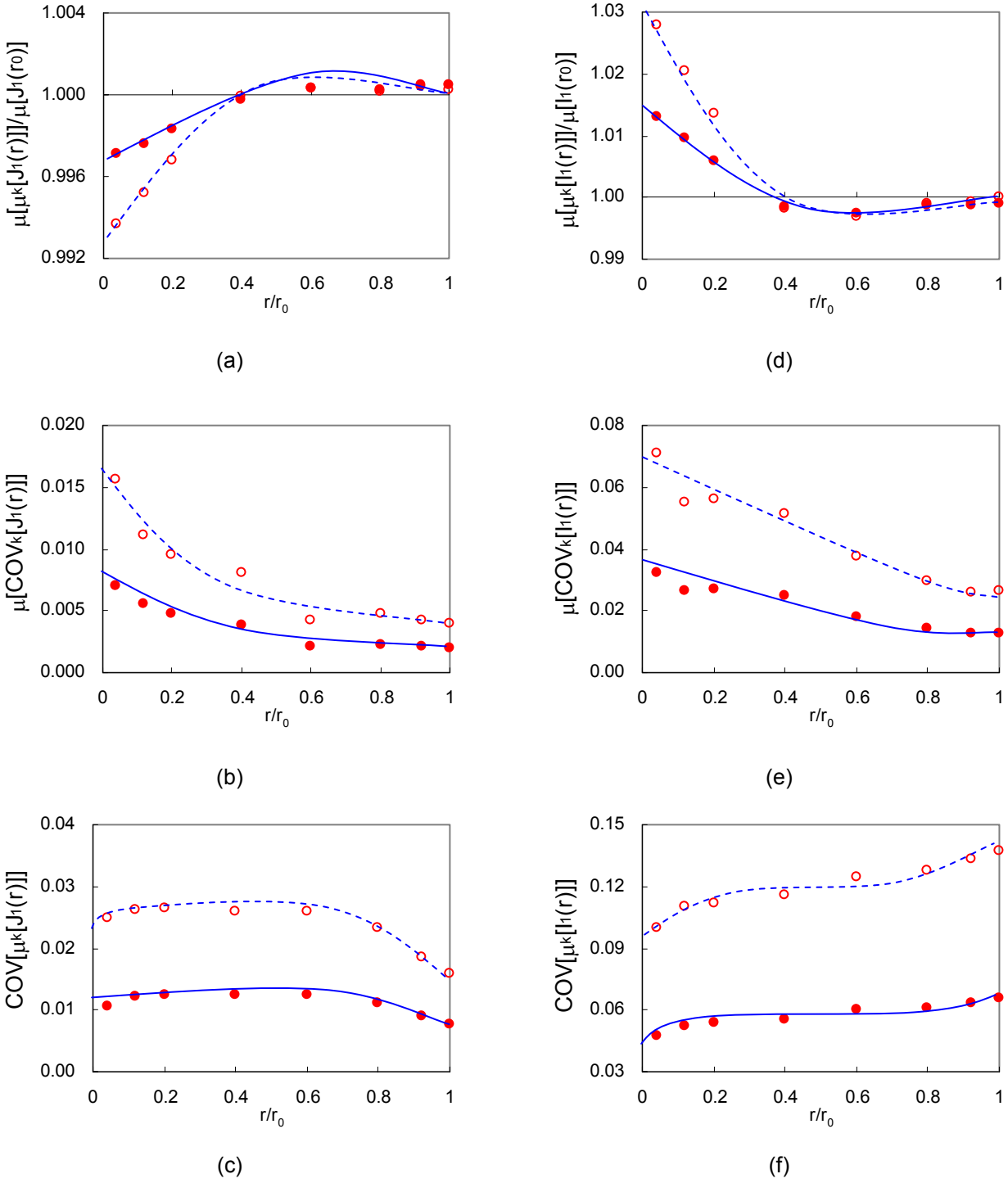

Figure 3.6 Effects of variability in random variables on the radial distribution of volumetric stress and strain (COV 10%-solid dots vs. COV 20%-hollow dots in small strain shear modulus parameter α_G^*). (a) Ensemble average of realizations' mean volumetric stresses. (b) Ensemble mean of realizations' COV for volumetric stress. (c) Ensemble COV of realization's mean volumetric stress. (d) Ensemble average of realizations' mean volumetric strains. (e) Ensemble mean of realizations' COV for volumetric strain. (c) Ensemble COV of realization's mean volumetric strain.

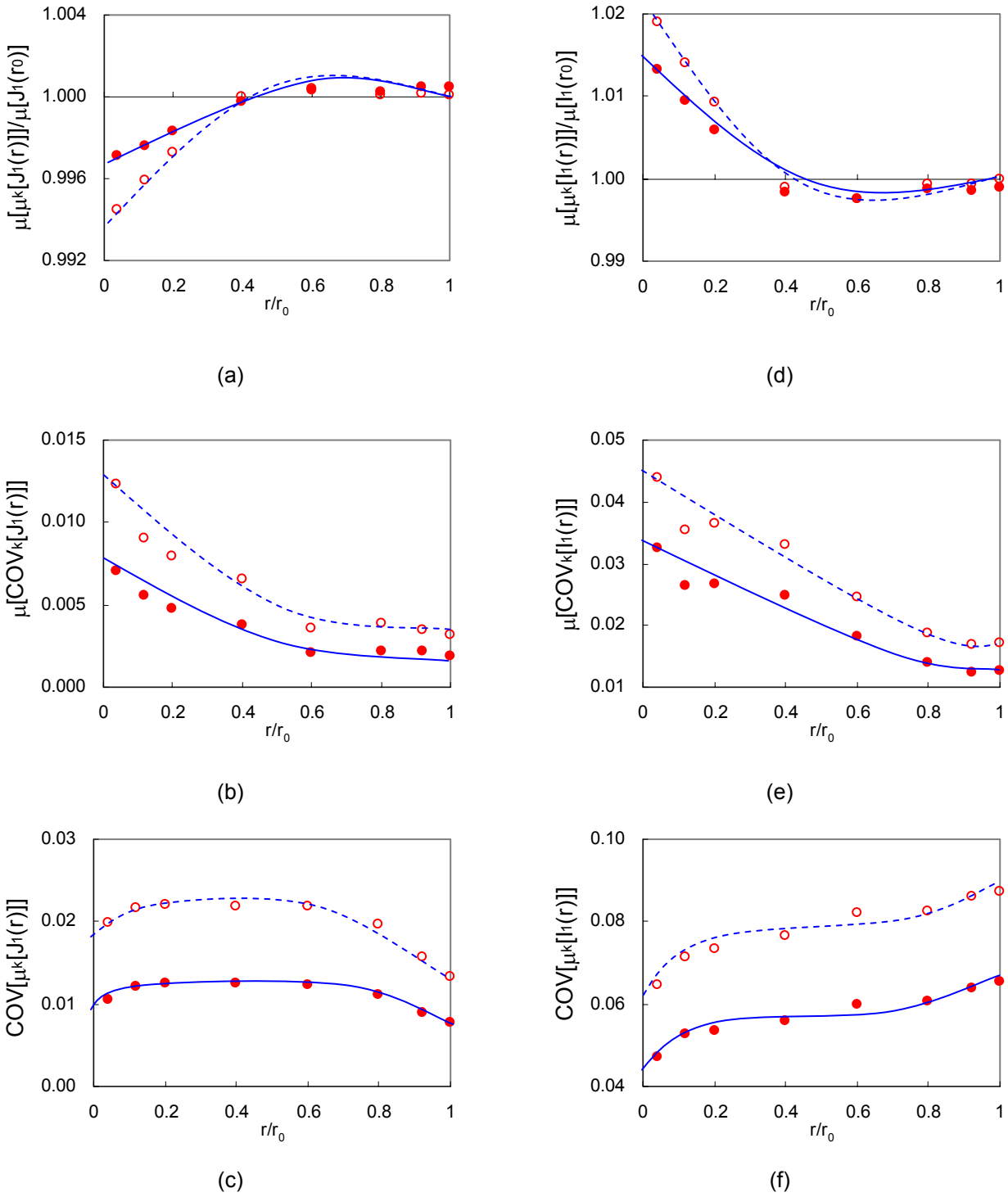

Figure 3.7 Effects of mean material property difference on the radial distribution of volumetric stress and strain: dense sand ($\mu[\alpha_G^*]$=104Mpa, solid dots) vs. soft clay ($\mu[\alpha_G^*]$=19.6Mpa, hollow dots). (a) Ensemble average of realizations' mean volumetric stresses. (b) Ensemble mean of realizations' COV for volumetric stress. (c) Ensemble COV of realization's mean volumetric stress. (d) Ensemble average of realizations' mean volumetric strains. (e) Ensemble mean of realizations' COV for volumetric strain. (c) Ensemble COV of realization's mean volumetric strain.

3.3.4.5 Different Specimen Shape: Circular vs. Square Geometries

Overall, similar global and local responses are obtained with circular and square geometries (Figure 3.8). Slightly greater mean COV in the volumetric stress distribution around the boundary is found in square specimens (Figure 3.8c and f). Boundary shape effects become negligible for $r<0.8\ r_0$.

3.3.5 Summary

The following salient observations are extracted from this study:

- The stress and strain distributions in a heterogeneous medium under isotropic loading are heterogeneous.
- Higher variability develops in internal strain distribution than in internal stress distribution.
- Volumetric stresses near the center are smaller than around the perimeter because stresses are transferred along the correlated stiffer zones.
- Shorter correlation length leads to lower stress concentration through stiffer zones. Conversely, the load transferred through the center decreases with increasing correlation length

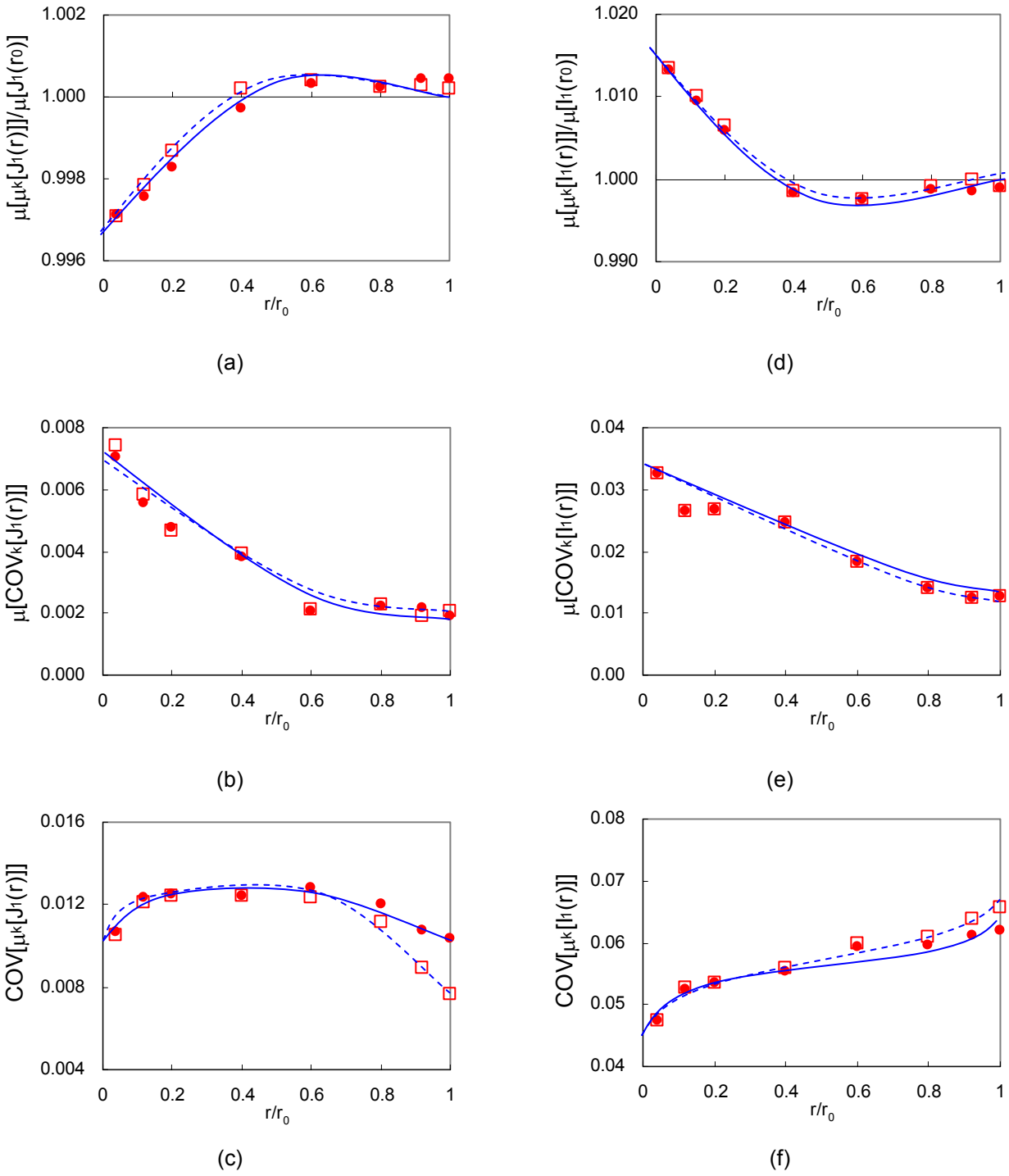

Figure 3.8 Boundary shape effects on the radial distribution of volumetric stress and strain (circular shape boundary-solid dots vs. rectangular shape boundary-hollow dots). (a) Ensemble average of realizations' mean volumetric stresses. (b) Ensemble mean of realizations' COV for volumetric stress. (c) Ensemble COV of realization's mean volumetric stress. (d) Ensemble average of realizations' mean volumetric strains. (e) Ensemble mean of realizations' COV for volumetric strain. (c) Ensemble COV of realization's mean volumetric strain.

3.4 HETEROGENEOUS NONLINEAR MEDIA SUBJECTED TO K_0 LOADING

The local and global mechanical response of heterogeneous soils subjected to K_0 loading is investigated in this section using Monte-Carlo simulations of correlated random heterogeneous media.

3.4.1 Numerical Model

The square medium is discretized into 100x 100 four-node plane strain elements. A zero horizontal displacement condition is imposed on lateral boundaries. The top and bottom plates are rigid but free to move vertically (Figure 3.9). Mesh discretization effects and the implications of random variable distribution assumption are explored in Appendices C and D.

The modified Duncan and Chang material model used in the previous section is involved in this study. This is an isotropic nonlinear elastic material model with isotopic stress-induced stiffness hardening and deviatoric strain-induced hyperbolic shear stiffness degradation. The small-strain stiffness at σ_0'=1kPa α_G^* is the only random variable for Monte Carlo simulations in this study. Other material properties such as Poisson's ratio and mass density are assumed constant (Table 3.4).

The selected mean and coefficient of variation for the random variable α_G^* are $\mu[\alpha_G^*]$=102Mpa and COV[α_G^*]=0.3. The random variable α_G^* is assumed uniform distributed between [49Mpa, 155Mpa]. Soils with relative correlation lengths L/D=0.01, 0.02, 0.04, 0.08, 0.10, 0.14, and 0.20 are simulated. Twenty different random fields are generated for each correlation length.

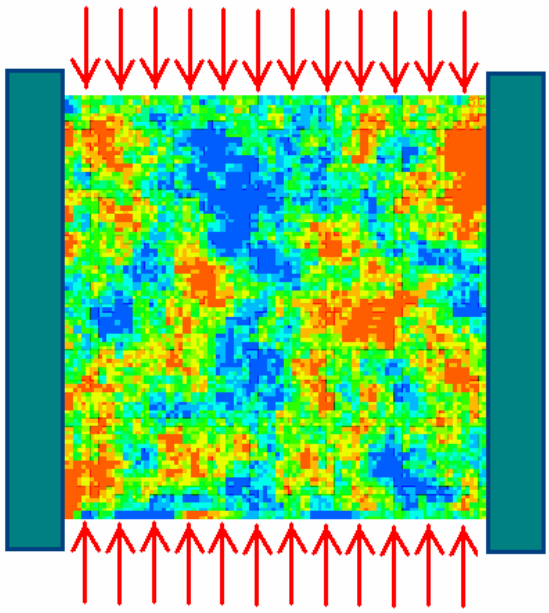

Figure 3.9 Loading and boundary condition for numerical simulations under K_0 loading. The random field shown has a relative correlation length L/D=0.10.

3.4.2 Numerical Results

3.4.2.1 Mean In-plane Principal Stress

The internal distribution of the mean principal stress in each realization as well as ensemble averages and COV are computed at each loading step. Probability density curves for the mean principal stress distribution are shown in Figures 3.10 and 3.11 for different relative correlation lengths. The kurtosis of the distribution increases with the applied vertical stress, which indicates that the corresponding stress distribution becomes homogenized as loading increases. The probability density curves become skewed to the left-hand side with the increase in the applied vertical stress. This indicates that stiffer parts become more homogenized than the softer parts.

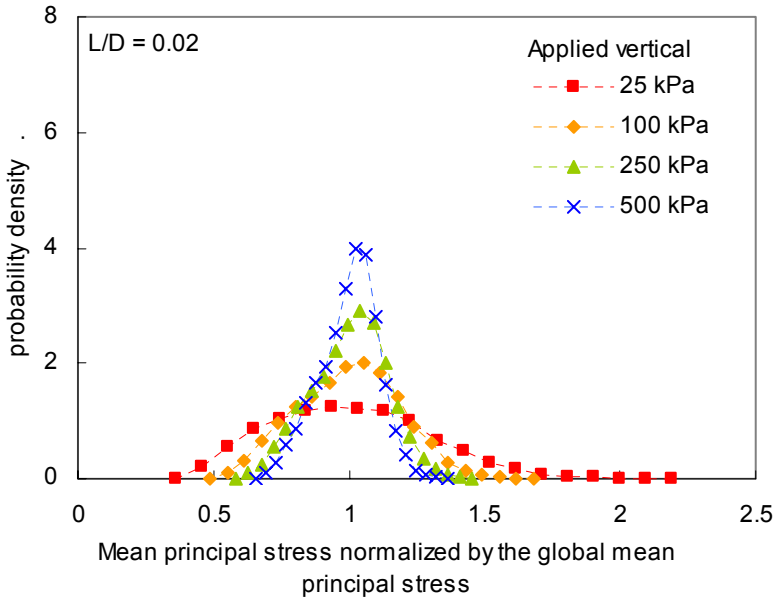

Figure 3.10 Distribution of internal normalized mean principal stress for different values of applied vertical load under K_0 loading (relative correlation length L/D=0.02).

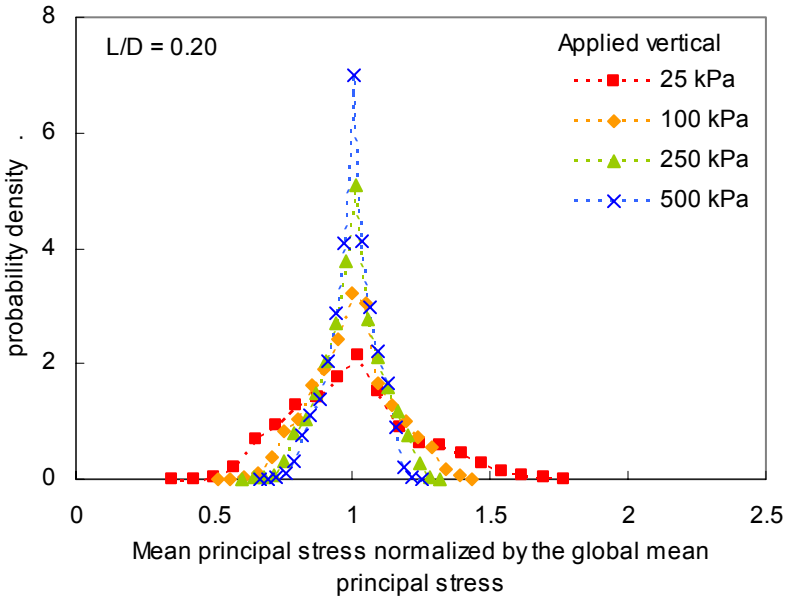

Figure 3.11 Distribution of internal normalized mean principal stress for different values of applied vertical load under K_0 loading (relative correlation length L/D=0.20).

Figure 3.12 shows the ensemble COV for the internal mean principal stresses versus the relative correlation length for different applied vertical stress levels. COV decreases when the applied vertical stress and the relative correlation length increase.

Lines in Figure 3.12 are obtained from a multi-variable linear regression analysis with two independent input variables: the relative correlation length *L/D* and the applied vertical stress $\overline{\sigma}_v$. The predicted COV for the mean principal stress MPS is:

$$COV_{MPS} = C_0 + C_1 \cdot \ln(L/D) + C_2 \cdot \ln(\overline{\sigma_v}/1kPa) \qquad (3.14\text{ a})$$

$$COV_{MPS} = 0.4302 - 0.0073\ln(L/D) - 0.0569\ln(\overline{\sigma_v}/1kPa) \qquad (R^2 = 0.9803) \quad (3.14\text{ b})$$

Note that the computed regression coefficient for the applied stress C_2=-0.0569 is about eight times greater than the coefficient for the relative correlation length C_1=-0.0073.

3.4.2.2 Distribution of Stress-induced Young's modulus

Load-induced internal homogenization is explored again, this time under K_0 condition. Figure 3.13 shows the ensemble COV in the distribution of ln(*E*). A multivariable linear regression analysis leads to:

$$COV_{\ln(E)} = 0.2135 - 0.0045\ln(L/D) - 0.0326\ln(\overline{\sigma_v}/1kPa) \quad (R^2 = 0.9893) \quad (3.15)$$

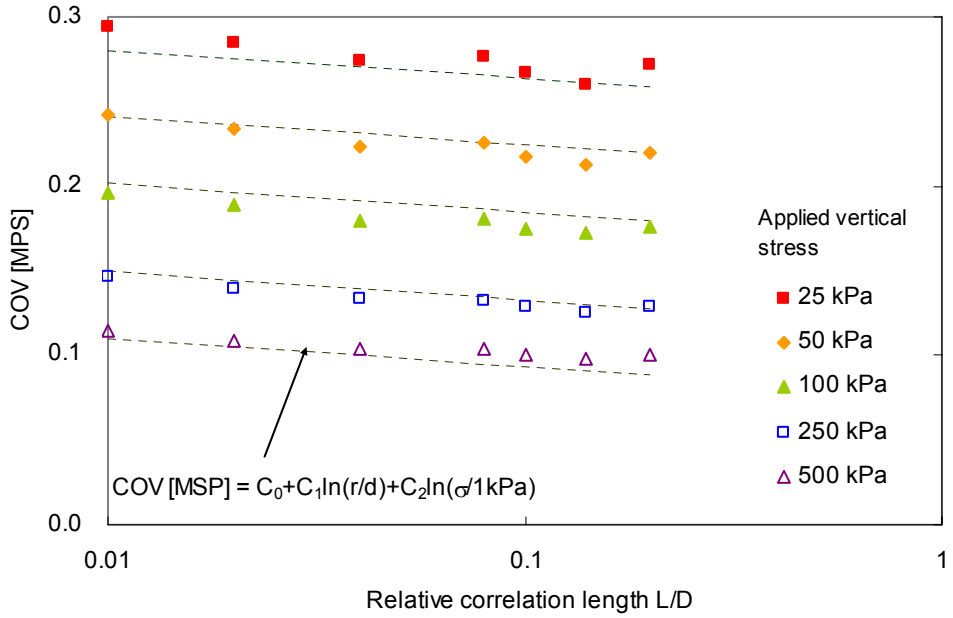

Figure 3.12 Ensemble mean of COV for mean principal stress vs. relative correlation length.

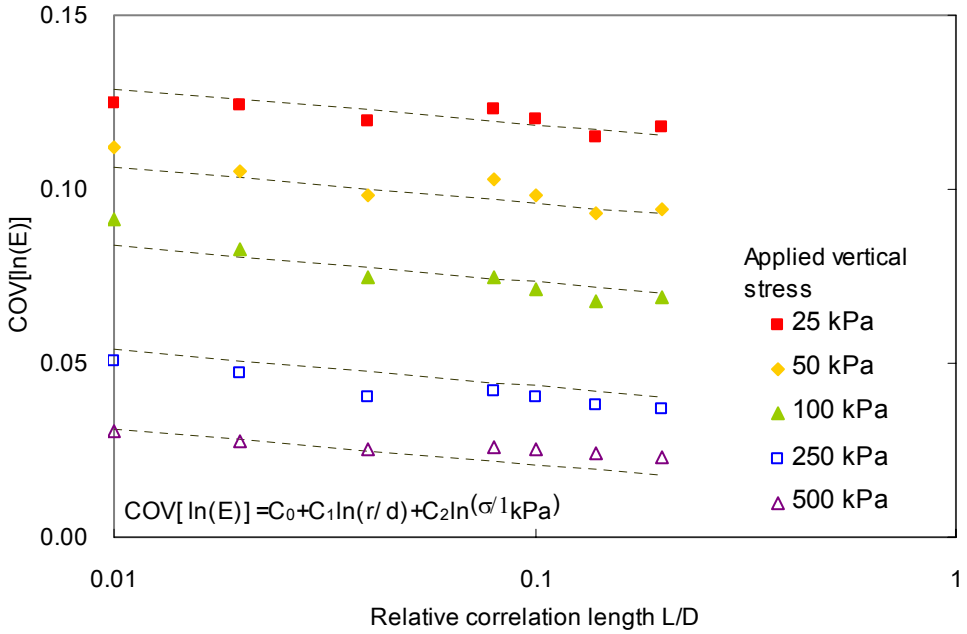

Figure 3.13 Ensemble mean of COV for ln(elastic modulus) vs. relative correlation length.

3.4.3 Local Stress Concentration Under K_0 Loading

Simulations are repeated for correlated heterogeneous media with the same boundary configuration and the same spatial distribution, but with different variability in the initial small-strain modulus distribution at 1kPa of initial loading: COV[α_G^*]=0.1 (Figure 3.14a), COV[α_G^*]=0.3 (Figure 3.15c), and COV[α_G^*]=0.5 (Figure 3.14e). Figure 3.14a, c and e show the vertical stress distribution under σ_v'=100kPa of K_0 loading in each case. Darker areas correspond to lower stress. Media with higher heterogeneity show the clear contrast in internal vertical stress distribution. Thresholded Figures 3.14b, d and f show in black the elements that experience the highest vertical stresses so that their summation justifies 50% of the applied vertical load. Black-colored elements cover 48.12% of the area when COV[α_G^*]=0.1, 43.84% when COV[α_G^*]=0.3, and 37.02% when COV[α_G^*]=0.5. This shows that there is higher vertical stress concentration in media with higher internal heterogeneity.

3.4.4 Effect of Spatial Variability on K_0 Coefficient

Figure 3.15 shows the lateral stress coefficient at rest K_0 versus the area ratio responsible for 50% of the vertical load, for simulations with relative correlation lengths *L/D*=0.005, 0.04, 0.10 and 0.20. All the simulations have the same coefficient of variation COV[α_G^*]=0.3 in the initial small-strain shear modulus distribution. It is observed that the cases with short correlation length yield higher stress concentration and smaller horizontal load transfer than cases with long correlation length.

	σ_v distribution	Area carrying 50% of vertical load
COV[α_G*]=0.1	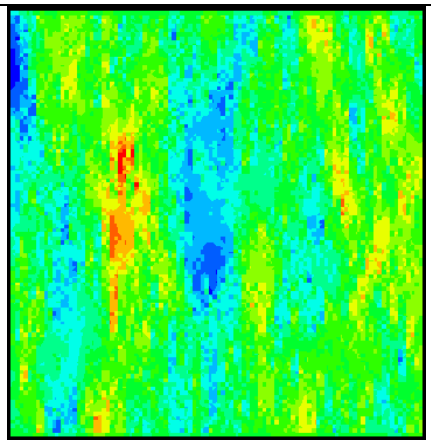 (a)	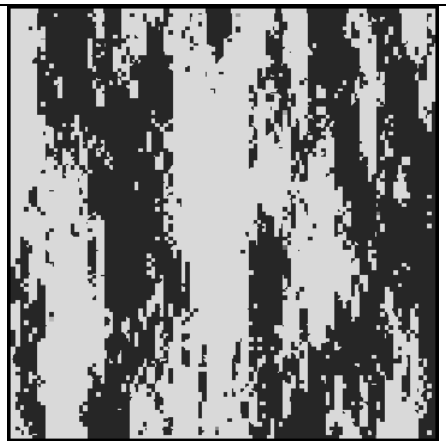 (b)
COV[α_G*]=0.3	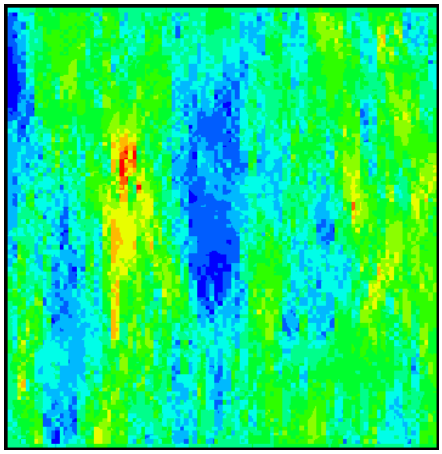 (c)	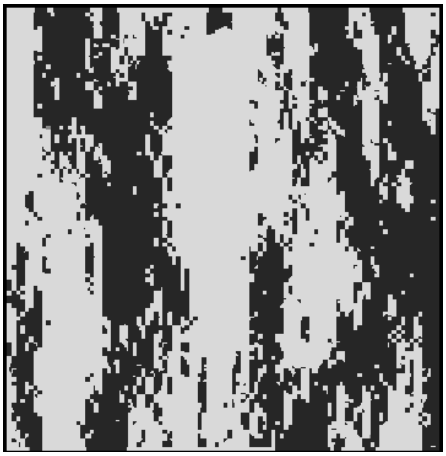 (d)
COV[α_G*]=0.5	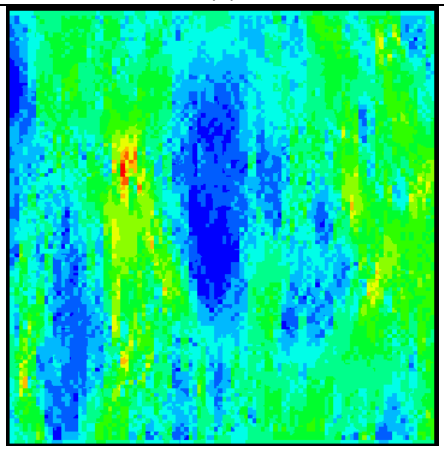 (e)	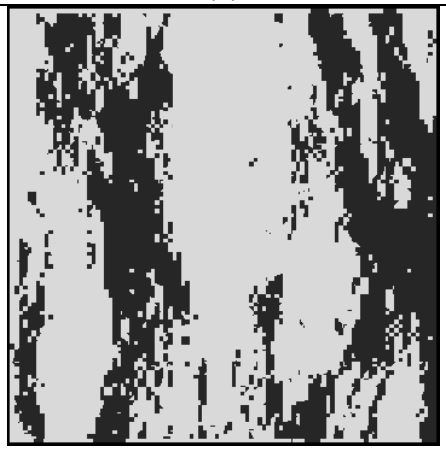 (f)

Figure 3.14 The effect of variability in α_G^* on local stress concentration - different COV[α_G*] but constant spatial correlation L/D=0.1. The initial spatial distribution of α_G^* is shown in Figure 3.10. The dark-colored in the right side figures denote the area that carrying 50% of the vertical load.

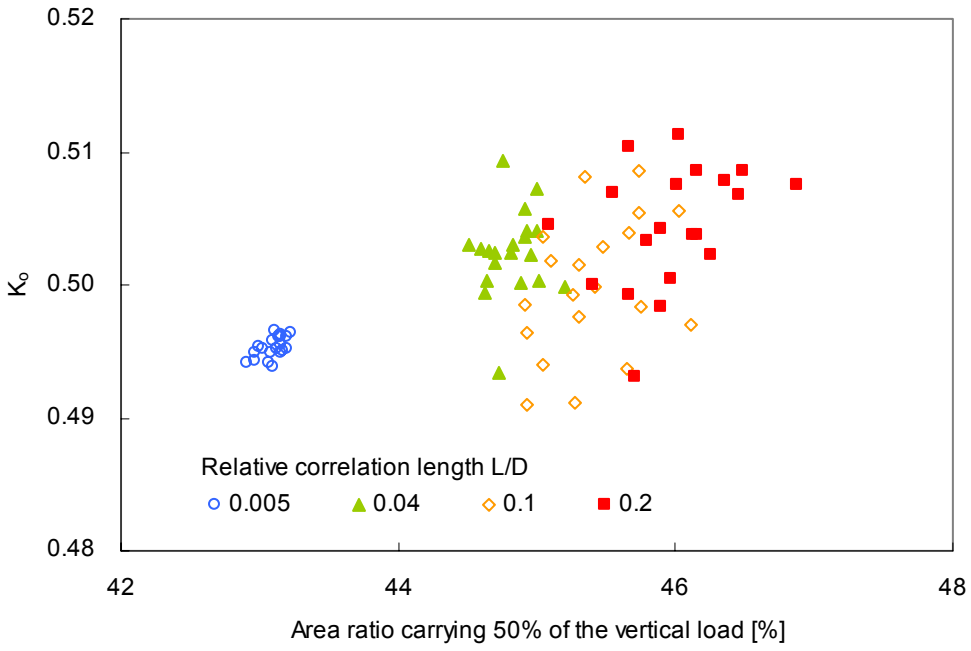

Figure 3.15 K_0 vs. area-ratio that carries 50% of the vertical load for different spatial correlations - COV[(G*]=0.3.

Figure 3.16 shows K_0 coefficients versus load concentration for a short relative correlation length L/D=0.005. The area ratio that carries 50% of the load is 47.86% when COV[α_G^*]=0.1, 45.61% when COV[α_G^*]=0.2, 43.10% when COV[α_G^*]=0.3, 40.16% when COV[α_G^*]=0.4, and 36.38% when COV[α_G^*]=0.5. Once again, stress concentration is enhanced when COV[α_G^*] increases. Furthermore, the data show that K_0 decreases with increasing COV[α_G^*]. Note that higher heterogeneity renders more scattered K_0 values.

Additional simulations are conducted to further assess the effects of the relative correlation length and the initial small-strain shear modulus variability by combining various COV[α_G^*] values (COV[α_G^*]=0.1, 0.3, and 0.5), and relative correlation lengths (short L/D=0.005, long L/D=0.20). Results are summarized in Figure 3.17. It can be concluded that K_0 decreases with increasing variability in the initial G_{max} at 1kPa, and the variability in K_0 is determined by the correlation length.

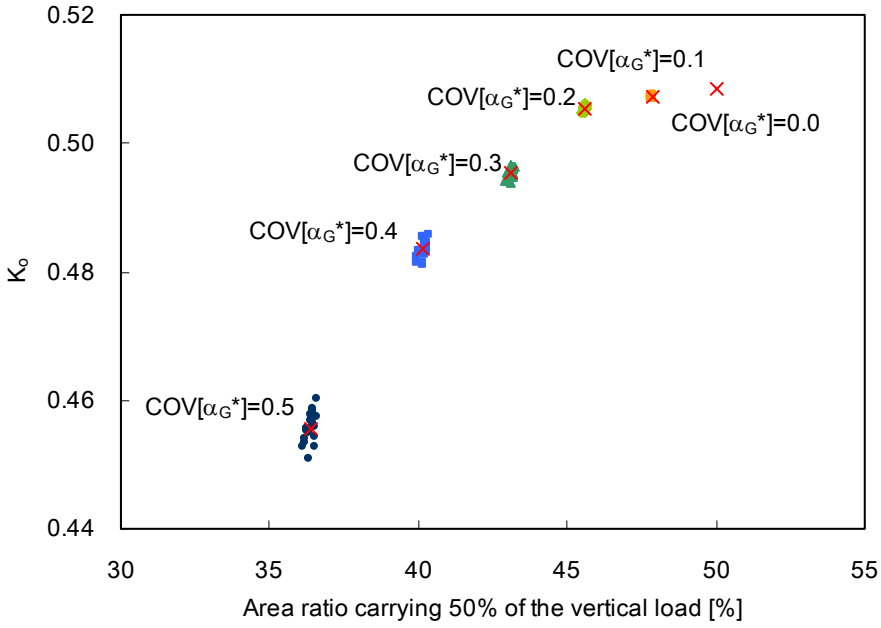

Figure 3.16 K_0 vs. area ratio that carries 50% of the vertical load with different COV[(G*] - Short correlation length (L/D=0.005).

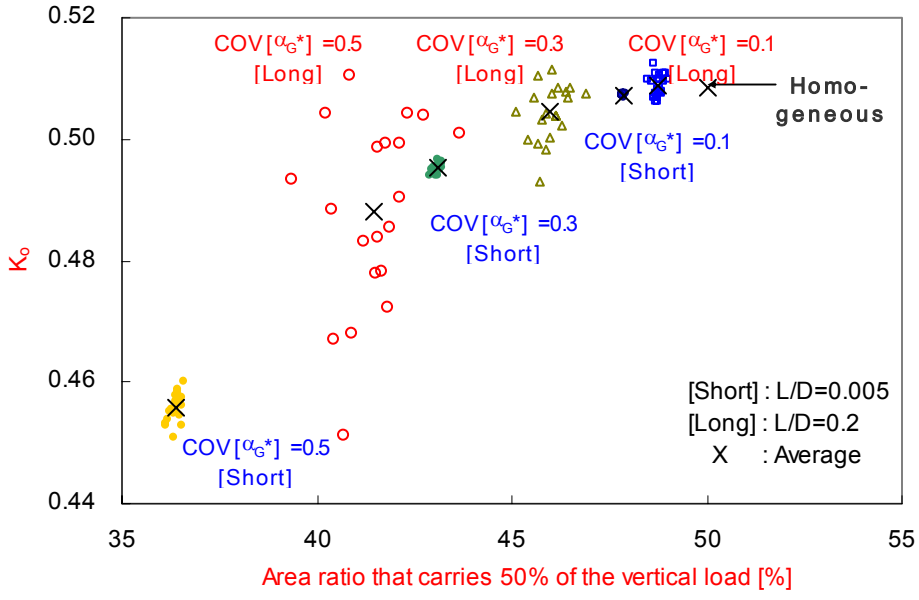

Figure 3.17 K_0 vs. area ratio that carries 50% of the vertical load for different correlation lengths and COV[(G*] values.

3.4.4 Effects of Internal Variability on Global Compressibility under K_0 Loading

The effects of internal variability on the global compressibility of linear and nonlinear elastic media under K_0 loading are investigated through numerical simulations performed with correlated random media. Numerical simulations are repeated twenty times for each case.

3.4.4.1 Effects of COV[*E*] *and L/D in Linear Elastic Media*

Consider heterogeneous linear elastic media where the spatial elastic modulus E distribution has a relative correlation length *L/D*=0.005 (the elastic modulus has a uniform distribution). Several cases are simulated with COV[*E*]= 0.0 (homogeneous), 0.1, 0.2, 0.3, 0.4, and 0.5. Figure 3.18a shows the increments in the ensemble average of normalized vertical strains with respect to COV[*E*]. The trend satisfies a power function:

$$\Delta\varepsilon_v \approx 0.74 \cdot \left(COV[E]\right)^{2.2} \qquad (R^2=0.999) \tag{3.16a}$$

This relation predicts $\Delta\varepsilon_v$=0.11 for COV[*E*]=0.42 (similar to results in Paice et al., 1996). The corresponding reduction in the effective elastic modulus due to COV[*E*] is also expressed as a power function (Figure 3.18b).

$$\Delta E / \mu[E] \approx -0.62 \cdot \left(COV[E]\right)^{2.11} \qquad (R^2=1.000) \tag{3.16b}$$

The following simulation is conducted with a fixed COV[*E*]=0.3, but varying the relative correlation length *L/D*=0.0 (homogeneous), 0.005, 0.04, 0.10, and 0.20. The effective elastic modulus decreases as the relative correlation length increases as displayed

in Figure 3.19. The normalized reduction in stiffness is a power function of the relative correlation length L/D:

$$\Delta E/\mu[E] \approx -0.08 \cdot (L/D)^{0.09} \qquad (R^2=0.997) \qquad (3.18)$$

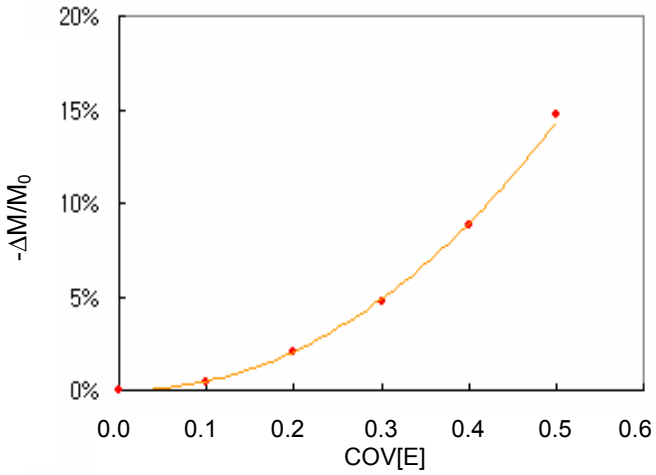

Figure 3.18 Effects of COV[*E*] for linear elastic modulus distribution with short correlation length (*L/D*=0.005) on stiffness softening under K_0 loading.

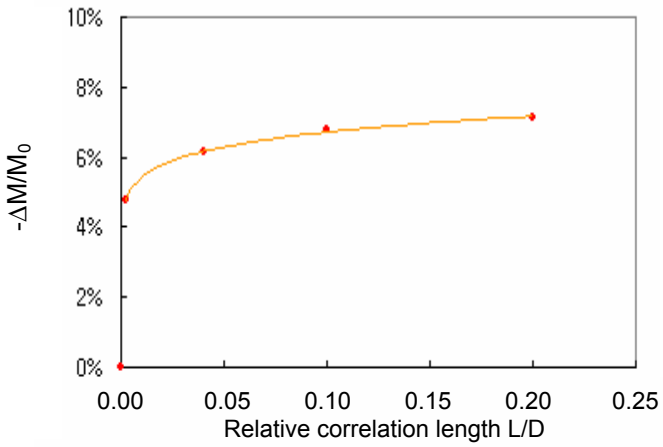

Figure 3.19 Effects of relative correlation length for linear elastic modulus distribution with COV[*E*]=0.3 on stiffness softening $-\Delta M/M_0$ under K_0 loading.

3.4.4.2 Effects of COV[α_G^*] *and L/D in Non-linear Elastic Media*

A new set of K_0 loading simulations is conducted to study the nonlinear load-deformation response of the spatially varying media. The modified Duncan-Chang model is used to reflect nonlinear soil behavior. Basic material properties are shown in Table 3.4. Correlated heterogeneous media are constructed with a short correlation length L/D=0.005, and the different COV[α_G^*] in initial elastic modulus distribution COV[α_G^*]=0.0, 0.1, 0.2, 0.3, 0.4, and 0.5. Figure 3.20 shows load-deformation curves. The computed vertical strains are normalized by the vertical strain obtained in the homogeneous case for the same stress level; this ratio is equivalent to the ratio of the constraint modulus M_{hetero} for the homogeneous medium by M_{homo} for the heterogeneous medium, M_{hetero}/M_{homo} (Figure 3.21). A heterogeneity of COV[α_G^*]=0.5 causes about 25% higher vertical deformation compared to the homogeneous case with stiffness equal to the arithmetic mean of the initial elastic modulus distribution. Trends in Figure 3.21 show a gradual decrease in relative modulus with load as a result of stress-induced homogenization.

The effect of the relative correlation length *L/D* is explored with a complementary set of simulations, and results are shown in Figures 3.22 and 3.23. The impact of relative correlation length is very small for the selectied variability (COV[α_G^*]=0.3).

The relative correlation length has a small effect on the expected vertical modulus, but it determines the variance of the computed effective *M*. In turn, the variance in *M* determines the reliability in settlement estimations. Figure 3.24 shows the two-sigma ranges in M_{homo}/M_{hetero} (the two-sigma range covers about 95% of possible occurrences under the assumption of a normal distribution).

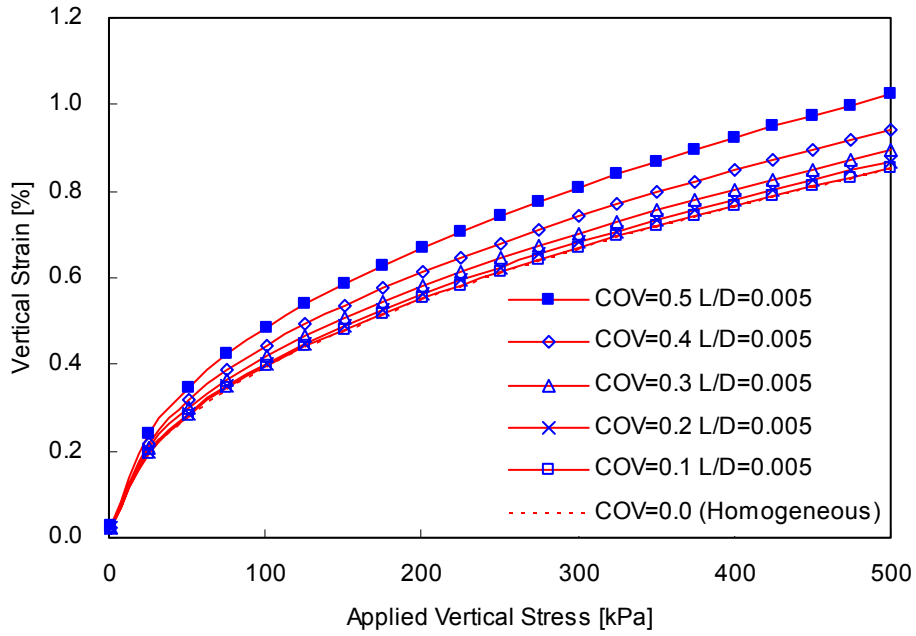

Figure 3.20 Stress-strain curves with different COV[α_G*] in initial elastic modulus distribution under K_0 loading.

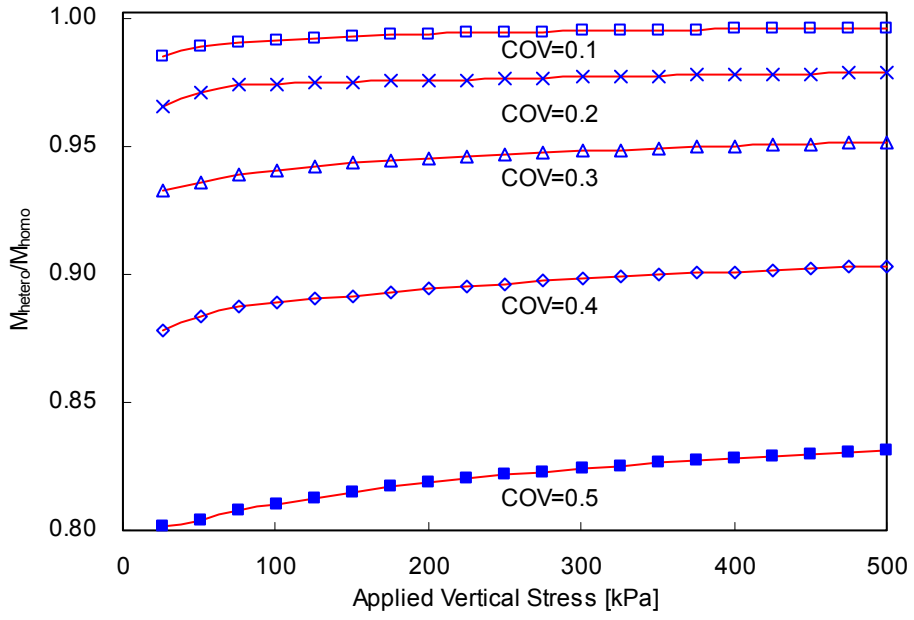

Figure 3.21 M_{hetero}/M_{homo} versus stress for different variability in initial elastic modulus α_G*, COV[α_G*]. The relative correlation length is constant L/D=0.005.

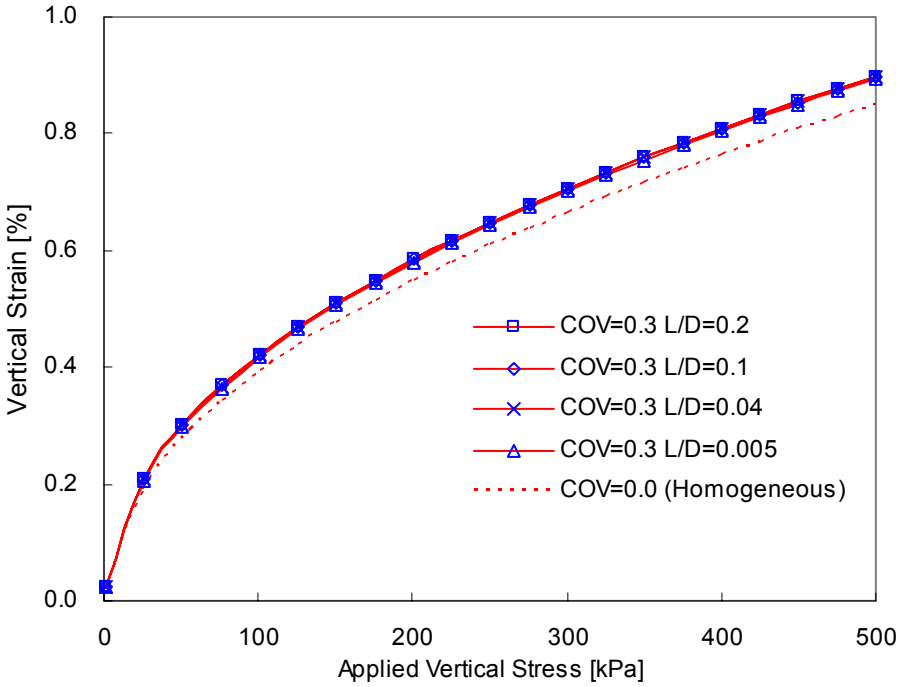

Figure 3.22 Stress-strain curves with different correlation lengths in media with COV[α_G*]=0.3 under K_0 loading.

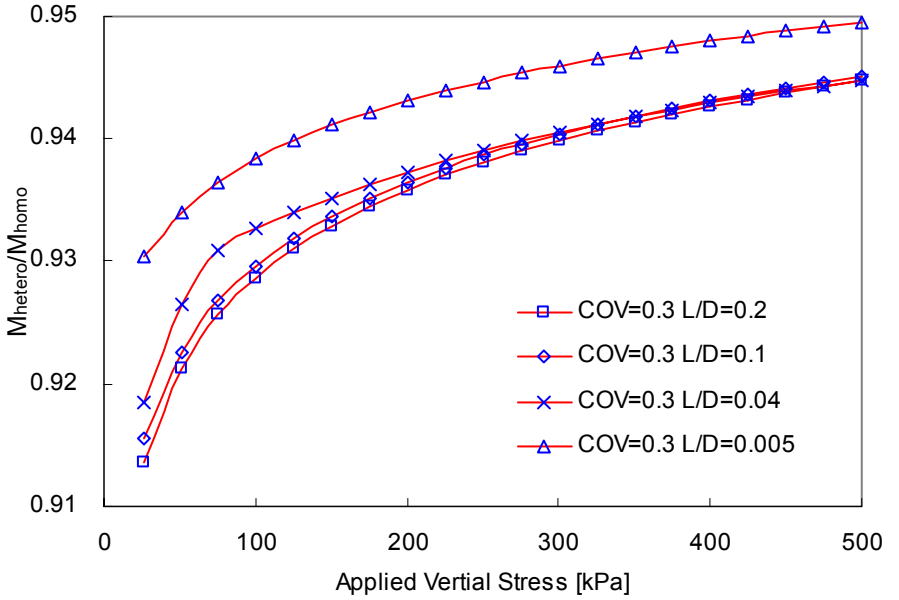

Figure 3.23 Normalized stress-strain curves with different correlation lengths in media with COV[α_G*]=0.3 under K_0 loading.

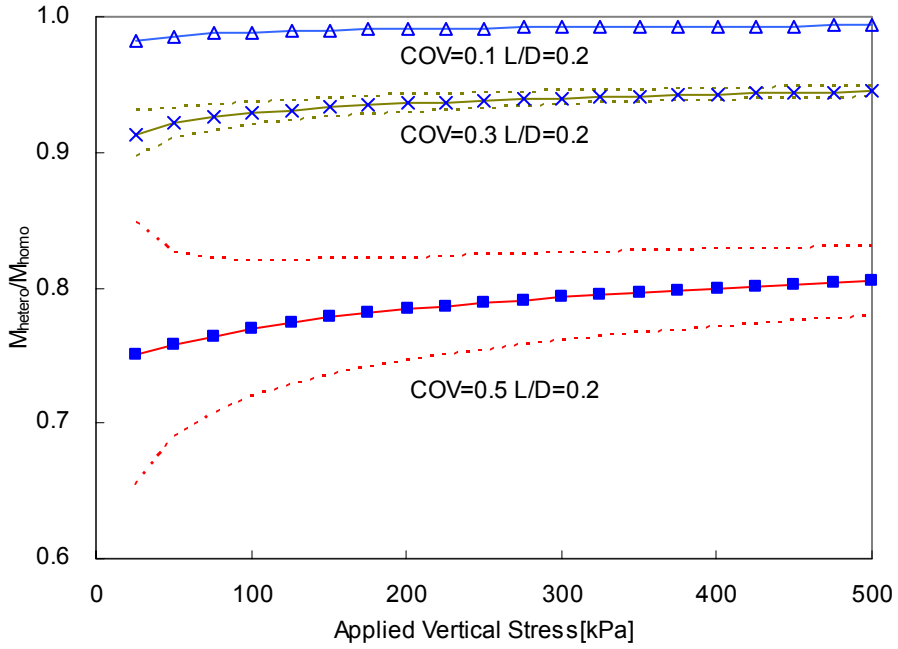

Figure 3.24 Mean and two-sigma range for the normalized constraint modulus M_{hetero}/M_{homo} versus applied vertical stress. Cases corresponds to different variability COV[α_G*]. The case of COV[α_G*]=0.1 and *L/D*=0.2 has too small variance (COV[M_{hetero}/M_{homo}]<0.01).

These results suggest that the variance in *M* due to *L/D* can be ignored in media with short correlation length. The variance of the effective modulus *M* is significant in heterogeneous media with high COV[α_G^*] and long relative correlation length (COV[α_G^*]=0.5, *L/D*=0.2)

3.5 SUMMARY AND CONCLUSIONS

Analytical and numerical results permit drawing the following conclusions about mechanical response of heterogeneous media subjected to isotropic and K_0 loading.

- Spatial variability yields a non-homogeneous stress distribution inside the soil. Load transfer concentrates along stiffer zones. The formation of load carrying columns or "stress-focusing" is a salient phenomenon in K_0 loading of linear and nonlinear elastic media. Stress focusing is more pronounced in media with higher variability in initial stiffness COV[α_G^*].

- Stress-induced stiffness homogenization develops in non-linear media.

- Stress focusing leads to lower K_0 coefficients.

- Local stress and strain variations vanish for very short *L/D.*

- The distribution of the effective constraint modulus M is determined by the variability in the distribution of local stiffness, COV[α_G^*], and the relative correlation length L/D: the higher COV[α_G^*] the lower M_{hetero}/M_{homo} is, and the higher L/D the wider the spread in M_{hetero}/M_{homo}..

CHAPTER IV

STRENGTH IN SPATIALLY VARYING MEDIA

The effects of spatial variability on the drained and undrained deviatory loading response are investigated in this chapter using numerical parametric studies with selected geostatistical parameters.

4.1 INTRODUCTION

Spatial variability in soil parameters such as the distribution of strength itself, variation in soil indices related to strength (void ratio and relative density) and in-situ test data (SPT resistance and cone tip resistance) points to potential effects of soil variability on strength (Tang, 1979; Harr, 1987; Ravi, 1992; Kulhawy 1992; DeGroot and Baecher, 1993; Lacasse and Nadim, 1996; Hegazy et al., 1996; Phoon and Kulhawy, 1999). High resolution techniques also show spatial variability even at the particle scale: liquid/helium porosimetry (Aydin, 1978), mercury porosimetry (Lapierre et al., 1990), petrographic image analysis (Antonellini et al., 1994a), X-ray computerized tomography (Antonellini et al., 1994b), imaging technique with impregnated soils (Jang et al., 1999), and needle probe technique (Cho et al., 2004). Fabric formation and variability are determined by soil formation in nature, and specimen preparation techniques in the laboratory. Implications on the quasi-static loading resistance (Yoshida et al., 1993; Vaid et al., 1995; Hoeg et al, 2000; Vaid and Sivathayalan, 2000) and the dynamic loading loading resistance are

extensively documented (Ladd, 1974; Mulilis et al. 1975; Townsend 1978; Ishihara, 1993; Miura and Yagi, 2002).

Conventional probabilistic approaches such as First Order Second Moment method (FOSM) and Point Estimation Method (PEM) can be applied to obtain simple estimates of the effective shear strength (Ang and Tang, 1975; Harr, 1987). Effective Mixture models for non-linear materials are summarized in Table 4.1. Conventional approaches do not account for the localized deformation of correlated weakness that is observed in heterogeneous material under deviatory loading (Griffiths et al., 2002). Furthermore, the ultimate shear strength decreases dramatically with increasing COV_q for strength (Griffiths et al., 2002 – correlated random fields made of the linearly elastic-perfectly plastic material). This elasto-plastic model is simple and useful, but it cannot properly simulate the real soil response such as stress dependent strength, prefailure plastic strain, and pore water pressure generation. The effects of soil variability on liquefaction potentials are reported in Popescu (1995) and Popescu et al. (1996, 2005). They show that the buildup of excessive pore water pressure in heterogeneous media is higher than in homogeneous media, and that presence of loose pockets is essential to initiate liquefaction. Additionally, they show that consideration of 3D effects is not essential to evaluate Δu_{ex}.

Localization is often associated with stress-softening, and the formation of thin localized shear zones which are about 10 to 25 times d_{50} thick (Arthur et al., 1977; Vardoulakis, 1980; Desrues et al., 1985; Desrues at al., 1996; Yoshida et al., 1994; Finno et al., 1996; Finno et al., 1997).

Table 4.1 Effective mixture theory for nonlinear materials (modified from Zaoui, 2002).

Material nonlinearity	Description
Rate-dependent elastoplasticity	• Kröner (1961): self-consistent prediction of the overall elastoplastic response of polycrystals on the basis of Eshelby's solution of the inclusion problem. • Hill (1965): Alternative use of Eshelby's solution by linearization of the constitutive equations of elastoplasticity and use of the tangent local and global instantaneous moduli. • Kröner model (Kröner, 1961) is improved by others (Hutchinson, 1970; Iwakuma and Nemat-Nasser, 1984; Lipinski et al., 1990).
Nonlinear elasticity and viscoplasticity	• Hutchinson (1976): the overall creep response of viscoplastic polycrystals with Hill's self-consistent scheme. • Molinari (1987), Lebensohn and Tomé (1993), Zaoui and Masson (2001) and Masson et al. (2000): "tangent model," This model approximates the nonlinear local behavior by a linear relation between the stress and the strain rate tensors by using the tangent creep compliances. • New Hashin-Strinkman type bounds for the effective dissipation potential of viscous materials (Talbot and Willis, 1985; Ponte Castañeda, 1991; Suquet, 1993; Willis, 1994).
Nonlinear viscoelasticity and elastoviscoplasticity	• Rougier et al. (1993), Beurthey and Zauoi (2000): two-phase material viscosity is modeled with the viscoelastic nature of the mechanical interactions between the constituents. • Rate-dependent elastoplasticity by modifying Kröner model: Weng (1981), Nemat-Nasser and Obata (1986), Harren (1991) • Rate-dependent elastoplasticity by modifying linear self-consistent model: Rougier et al. (1994), Masson and Zauoi (1999), Pouya and Zauoi (1999) and Masson et al. (2000).

While numerical methods are used to study the localization phenomena using conventional continuum material models (Table 4.2), artificial weak points must be included in the mesh and, the thickness of the shear zone depends on the element size, so the shear zone becomes narrower when a finer mesh is used. Alternative approaches include the softening polar elasto-plastic model (Borst, 1991; Tejchman et al., 1993), the softening polar hypoplastic model (Tejchman et al., 1996), hypoplasticity with multiple plastic mechanisms (Desrues et al., 1996; Desrues and Chambon, 2002), and combined localization mode plasticity (Borja and Aydin, 2004). Note that localization phenomena identified in this chapter is the direct consequence of spatial variability rather than strain-softening local response.

Table 4.2 Localized shear zone analysis with conventional continuum material models (after Tejchman et al., 1999; Tejchman et al., 2001)

Continuum Material Model	References
Softening elasto-plastic model	Shuttle and Smith (1988) Needleman and Tvergard (1992)
dual-yield hardening elasto-plastic model	Ramakrishnan and Atluri (1994) Hicks (1998)
hardening elasto-plastic model with enriched shape function	Leroy and Ortiz (1989)
hardening and softening elasto-plastic model with bifurcation analysis	Borst (1988)
Hardening elasto-plastic model with remeshing	Hicks (1998)
softening visco-plastic model	Loret and Prevost (1991) Belytschko et al. (1994)
softening elasto-plastic model with higher-order gradients	Borst et al. (1992)

4.2 NUMERICAL METHOD AND MATERIAL MODEL

The goal of this study is to gain new understanding into the effect of spatial variability on the drained and undrained strength of soils. The research is implemented using the finite element program ABAQUS/Standard (2001). Figure 4.1 shows the loading and boundary conditions for this simulation. The mesh consists of 100x 100 four-node plain strain elements.

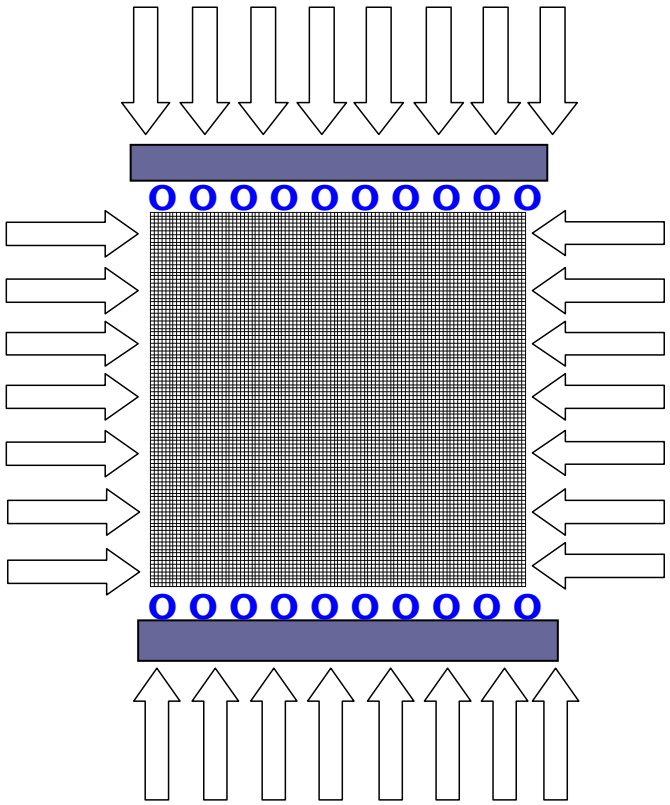

Figure 4.1 Initial mesh shape and boundary conditions – Biaxial loading.

The mesh is square to minimize geometric effects related to the generation of correlated random fields. The plain strain biaxial compression condition is simulated by applying strain-control loading in the vertical direction. The free horizontal displacements of top and bottom nodes simulate frictionless boundary plates. The drainage condition is determined at boundary nodes. The 2D correlated random fields are generated using the matrix decomposition technique (See Chapter II). Multiple realizations of each case are generated at random, and ensemble statistics are analyzed to determine the effects of spatial variability on soil strength. Once a realization is generated, a confining stress σ_0'=100kPa is imposed and followed by deviatoric loading. Mesh discretization effects and the implications of random variable distribution assumption are explored in Appendices C and D.

4.2.1 Material Model

The modified cam clay material model is selected in this study (Roscoe et al., 1958; Roscoe et al., 1963; Roscoe and Burland, 1968). This model simultaneously accommodates consolidation and shearing by introducing prefailure plastic strains using separate yield and failure surfaces. There are five input parameters: the consolidation parameters (logarithmic plastic bulk modulus λ, logarithmic elastic bulk modulus κ and specific volume V_1), the drained strength parameter (stress ratio at critical state M), and the elastic parameter at initial condition (Poisson's ratio ν or elastic shear modulus G). Typical published values are summarized in Tables 4.3(a) & (b). Conventional values for soft clay soils are selected: λ= 0.174; κ=0.026; V_1=2.824 (where $V_1=1+e_0$ at 1kPa); M=1.0; ν_{1kPa}

(Poisson's ratio at 1kPa)=0.3. The void ratio and the shear resistance at a confining stress of σ_0=100kPa are e=0.9 and q_f=113.6kPa. Random variability is imposed on the initial void ratio at σ_0'=100kPa.

Table 4.3 Typical soil parameters for modified cam clay model (Table 4.3a from Atkinson, 1993)

a) Soils	LL	PL	λ	Γ	*N*	*M*	*Φ'*	κ/λ
Fine-grained clay soils								
London clay	75	30	0.16	2.45	2.68	0.89	23°	0.39
Kaolin clay	65	35	0.19	3.14	3.26	1.00	25°	0.26
Glacial clay	35	17	0.09	1.81	1.98	1.18	29°	0.16
Coarse-grained soils								
River sand			0.16	2.99	3.17	1.28	32°	0.09
Decomposed granite			0.09	2.04	2.17	1.59	39°	0.06
Carbonate sand			0.34	4.35	4.80	1.65	40°	0.01

b) Soils	λ	κ	Γ	*M*	*Φ'*	*G'* [kPa]	*k* [m/s]
Soft clay (Wood, 1990)	0.25	0.05	2.5	0.898	23°	500	
Weald clay (Carter, 1982)	0.088	0.031	2.06	0.882	22.6°	3000	1.27×10^{-12}
Kaolin (Almeida, 1986)	0.25	0.05	3.44	0.9	23°	75σ'	2.65×10^{-9}
Gault clay (Almeida, 1986)	0.219	0.035	2.96	1.0	25.4°	2250	0.937×10^{-9}

4.3. UNDRAINED RESPONSE

This section describes the results of numerical simulations conducted to investigate the undrained stress-strain relationships of spatially varying media subjected to undrained deviatory loading.

4.3.1 Uncorrelated Bimodal Mixture

The case of a random bimodal mixture of a strong and a weak material is studied first. The strong medium has the previously selected material properties (λ=0.17; κ=0.026; V_1=2.824; M=1.0; ν_{1kPa}=0.3). The properties of the weak material at σ_0'=100kPa are e_0=1.0 and q_f=63.1kPa.

The area faction of the weak material is varied: V_{weak}=0% (strong material only), 10%, 20%, 30%, 40%, 50%, 70%, 90%, and 100% (weak material only). Weak elements are positioned with a very short relative correlation length L/D=0.005. Figure 4.2a shows the resulting stress-strain curves. Three homogeneous cases are superimposed on the figure corresponding to e_0=0.90, 0.95, and 1.00. Note that a homogeneous medium with initial void ratio e_0=0.95 overestimates the shear strength of 50:50 heterogeneous media with the same mean void ratio. Figure 4.2b shows the one-sigma ranges of the mixture shear strength normalized by the shear strength of the weak material. Mixture models and the strength for homogeneous materials with different initial void ratios are superimposed. It can be concluded that the undrained strength of uncorrelated random mixtures (i.e., very short L/D) is lower than the strength of homogeneous media with the same mean void ratio, but similar to the strength predicted by the harmonic mean of the local strengths. Therefore,

the effective shear resistance of heterogeneous media should not be estimated by the arithmetic mean strength.

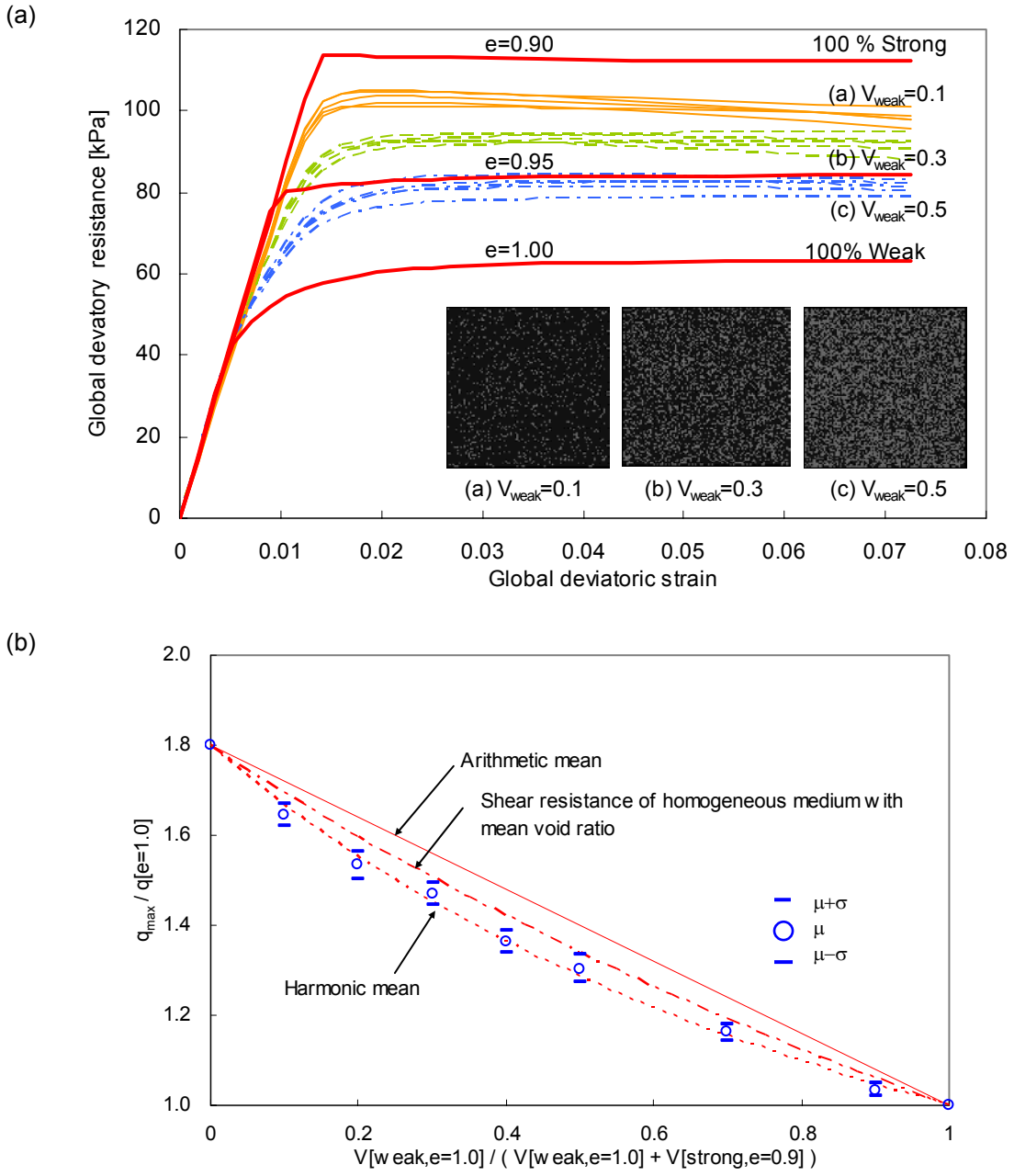

Figure 4.2 Maximum undrained shear strength in binary mixtures. (a) Stress-strain curves of 20 random realizations for each volume fraction of weak material V_{weak}. (b) One-sigma range of maximum undrained shear strength normalized by the weak inclusion strength. The shear strength of the strong component is q_u=113.6kPa, and that of the weak component is q_u=63.1kPa under 100kPa. The solid curves in figure a correspond to homogeneous media.

4.3.2 Correlated Random Media

Deviatory loading simulations are conducted in media with long relative correlation length (L/D=0.10; Figure 4.3a & b) and short relative correlation length (L/D=0.005; Figure 4.3c & d). The initial void ratio range at σ_0'=100kPa is e_0=0.8 to 1.0 with a uniform distribution, and the corresponding shear resistance range varies between 201.3kPa (e=0.8) and 63.1kPa (e=1.0). Figures 4.3b & d display the twenty stress-strain curves for each correlation case. The stress-strain curves for homogeneous cases at various e_0 values are also presented. The strongest or weakest cases are highlighted. The following observations can be drawn from these figures:

- Media with short L/D show greater shear resistance than media with long L/D.
- Media with long L/D show greater variation in shear resistance than media with short L/D.
- Media with long L/D show more pronounced post-peak softening behavior than media with short L/D.

4.3.3 Localization of Shear Strain

Figure 4.4a shows the initial void ratio distribution in one realization with L/D=0.10. The brighter zones indicate higher initial void ratio and lower shear resistance. Frames i, j, k, and l show the shear strain fields, and frames e, f, g, and h show the corresponding excess pore water pressure fields at different global vertical strains. The analysis of this and similar sequences reveals the following evolution of strain localization in heterogeneous media during undrained deviatoric loading:

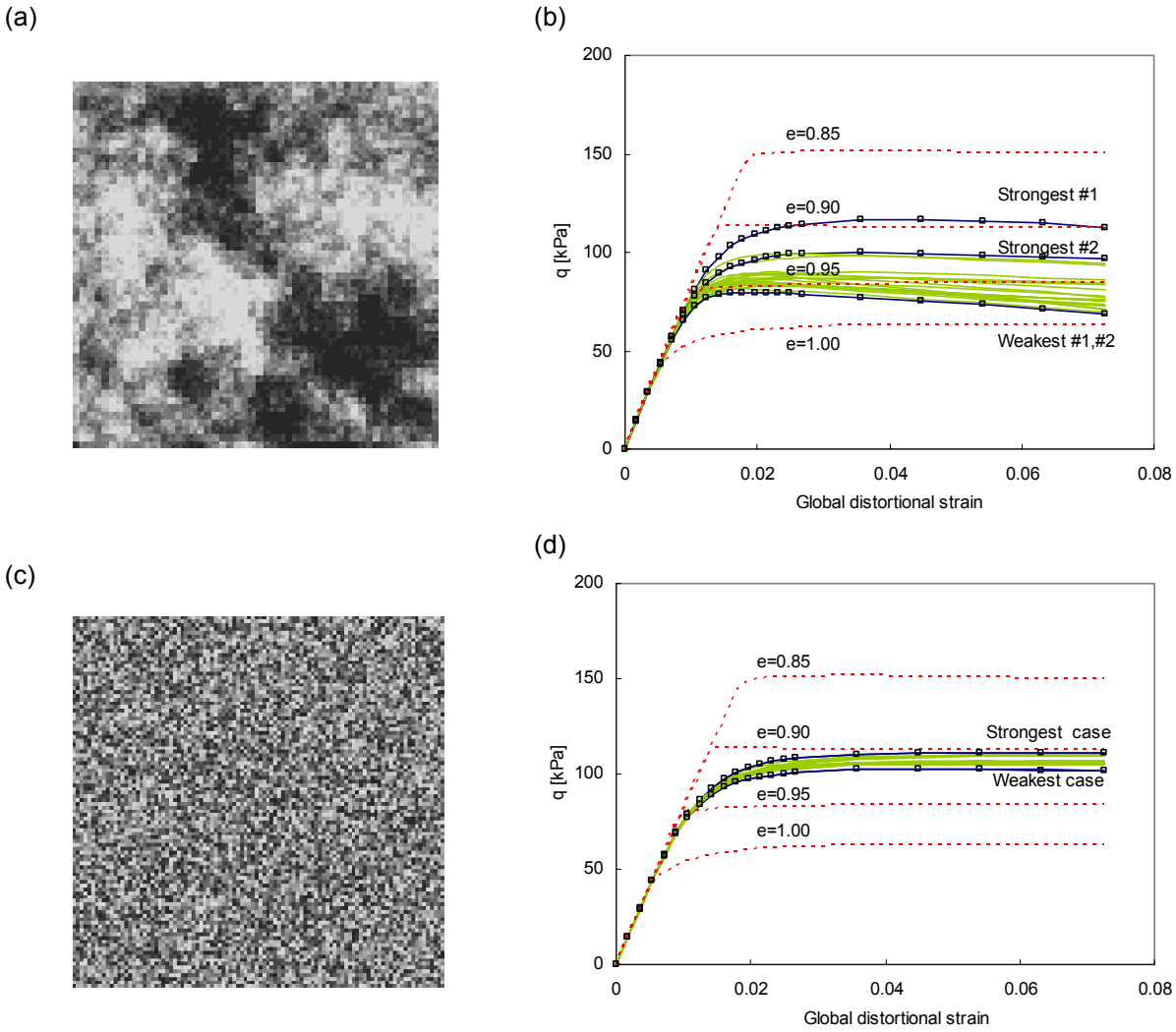

Figure 4.3 The effect of correlation length – undrained deviatoric loading. (a) Random medium with long correlation length *L/D*=0.10. (b) Stress-strain curves for long correlated random cases (μ[e_0]=0.9, COV[e_0]=0.06, *L/D*=0.10), (c) Random medium with short correlation length *L/D*=0.005, (d) Stress-strain responses for short correlation length (COV[e_0]=0.06, *L/D*=0.005).

ε_a	J_2 field	Excess pore pressure field	Shear strain field
ε_a=0.5 %	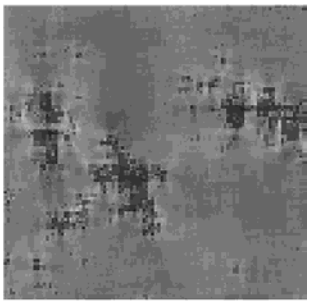 (a)	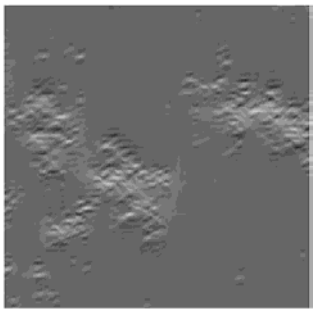 (e)	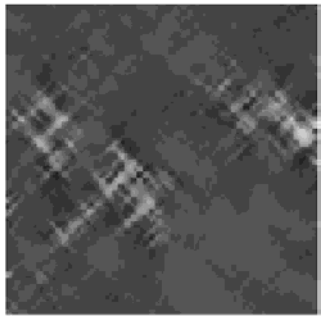 (i)
ε_a=1.0 %	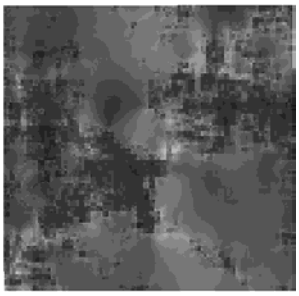 (b)	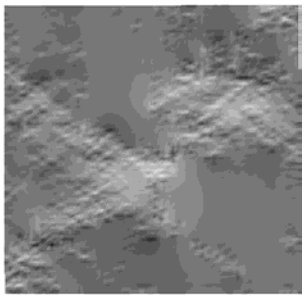 (f)	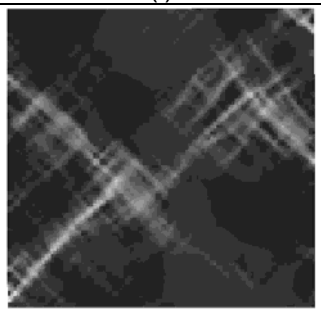 (j)
ε_a=2.0 %	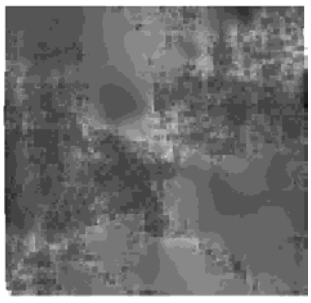 (c)	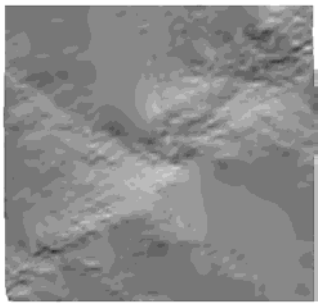 (g)	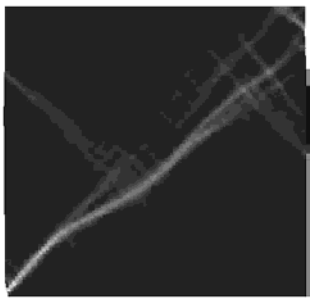 (k)
ε_a=5.0 %	 (d)	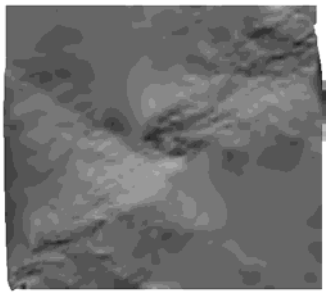 (h)	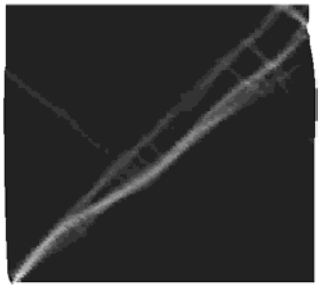 (l)

Figure 4.4 Strain localization in a medium with the large spatial correlation L/D=0.10, $\mu[e_0]$=0.9 and COV[e_0]=0.06: J_2 (2nd stress invariant) excess pore pressure, and shear strain. Initial void ratio field is presented in Figure 4.3a. Lighter regions indicate higher values.

- A localized shear zone is not apparent before yielding (Figure 4.4i).
- Several shear strain localizations are initiated at yielding (Figure 4.4j).
- During yielding, then the number of localized shear zones decreases gradually and shear strains prevail in a few bands (Figure 4.4k, l).

These observations are in agreement with experimental observations that show the beginning of strain localization at or before peak (Desrues, 1998).

Figure 4.5 show the initial void ratio distributions and the corresponding deformed shape and shear strain localization in the two strongest and the two weakest realizations identified in Figure 4.3a & b (L/D=0.10). Differences observed in strain localization patterns include:

- The shear bands are longer in the stronger media than in the weaker ones.
- There are fewer and clearer shear bands in the weaker media.

Figure 4.6 shows the initial void ratio distribution and the corresponding deformed shape and shear strain localization in the strongest and weakest realizations when media have a short correlation length (L/D=0.005; Figure 4.3c & d). Note that the zones where shear strains localize cannot be anticipated from a cursory observation of the initial void ratio field. The evolution of shear zone formation in media with short L/D is similar to processes in media with long L/D. However, fewer yet wider localized shear strain zones are observed in media with long L/D.

Case	Void ratio field	Shear strain field
Strongest #1 (Fig. 4.3b)	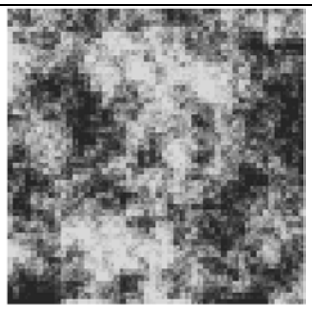 (a)	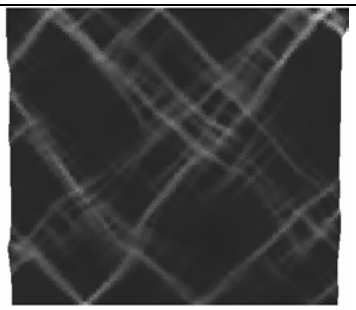 (e)
Strongest #2 (Fig. 4.3b)	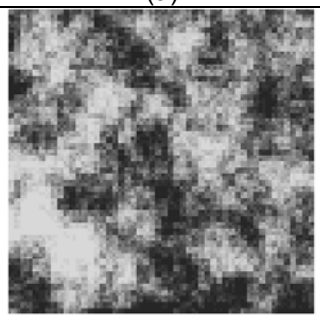 (b)	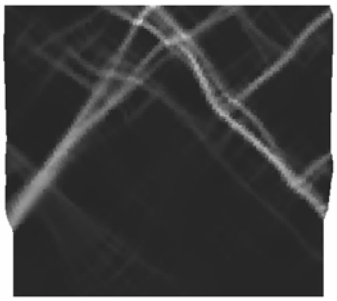 (f)
Weakest #1 (Fig. 4.3b)	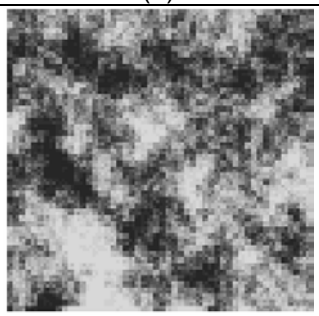 (c)	 (g)
Weakest #2 (Fig. 4.3b)	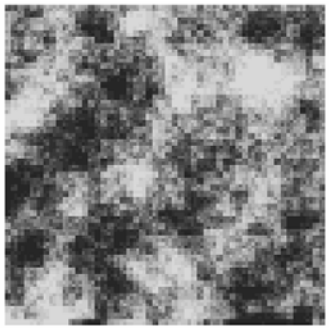 (d)	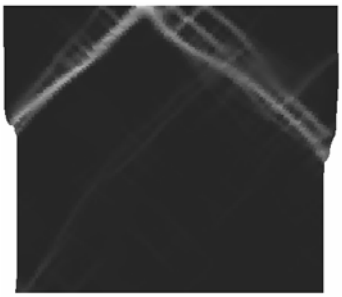 (h)

Figure 4.5 Strain localization in media with long correlation length. Void ratio fields and corresponding deformed shape and shear strain fields at a global vertical strain ε_z=0.05. Cases shown correspond to the strongest and weakest media with long correlation length (L/D=0.10; refer to Figure 4.3a and b). Lighter regions indicate higher values.

Case	Void ratio field	Shear strain field
Strongest (Fig. 4.3d)	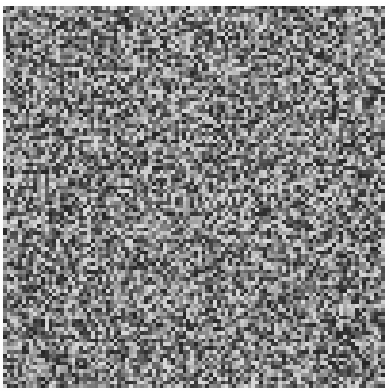 (a)	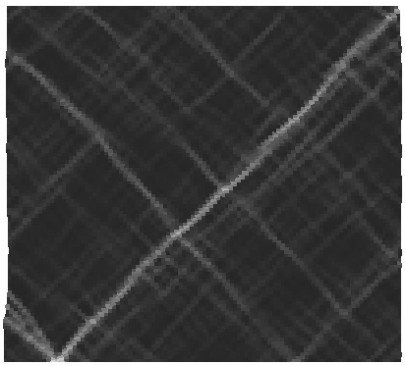 (b)
Weakest (Fig. 4.3d)	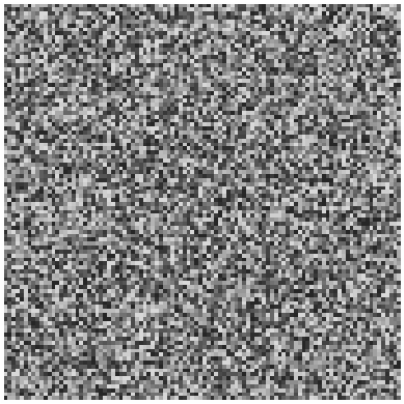 (c)	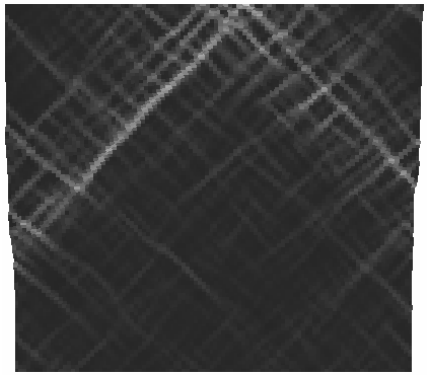 (d)

Figure 4.6 Strain localization in media with short correlation length. Void ratio fields and corresponding deformed shape and shear strain fields at a global vertical strain ε_z=0.05. Cases shown correspond to the strongest and weakest media with long correlation length (L/D=0.005; refer to Figure 4.3c and d). Lighter regions indicate higher values.

4.3.4 Influences of Variation in Initial Void Ratio Distribution

A parametric study is conducted to study the effect of initial void ratio variability COV[e_0] within the context of long correlated media (L/D=0.16). Numerical simulations are repeated twenty times for each case to obtain statistically meaningful results for correlated random media. It is assumed that the initial void ratio distribution is uniform, and that the soil behavior follows the critical state model. Figure 4.7a shows the mean normalized shear resistance and the three-sigma range versus COV[e_0]. The effective shear resistance decreases with the increase in COV[e_0] . Clearly, the connectivity of weak zones controls failure (See Griffiths et al., 2000 for similar results).

Figure 4.8 shows the mean shear resistance versus COV[e_0] and analytical mixture model predictions. The undrained shear strength corresponding to the mean void ratio overestimates the (mean) shear strength of random media with long relative correlation length. Furthermore, note that mixture strength is more sensitive than mixture stiffness to spatial variability.

4.3.5 Influences of Correlation Length in Spatial Distribution

The role of correlation length on the undrained shear strength is explored by varying the relative correlation length between L/D=0.005 and L/D=0.16 while keeping $\mu(e_0)$=0.9 and COV[e_0]=0.06 constant. Figure 4.9 shows the mean value and three sigma ranges for the normalized undrained shear strength versus L/D. Longer correlation lengths lead to weaker media and higher variance among different realizations in the ensemble.

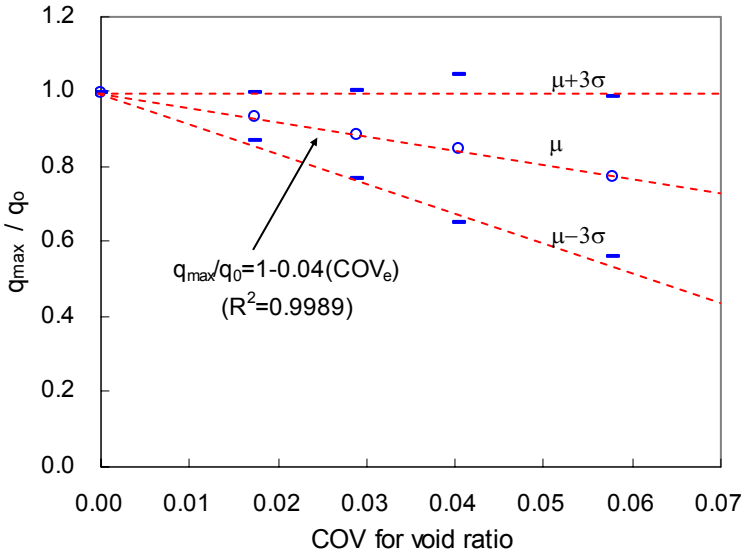

Figure 4.7 Ensemble averages of normalized maximum undrained shear resistances vs. COV for initial void ratio. The relative correlation length is constant L/D=0.16. Numerically computed shear strengths are normalized by the shear resistance of the homogeneous medium with the same mean void ratio. The mean trend and three sigma ranges of the numerical results are presented. The equation shown is the linear regression for the mean trend.

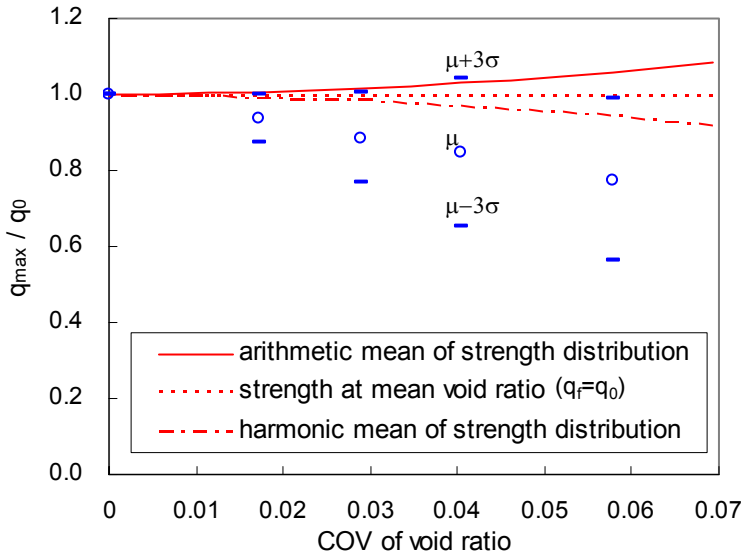

Figure 4.8 Comparison between ensemble average of numerical undrained shear strength determination and analytical mixture model predictions.

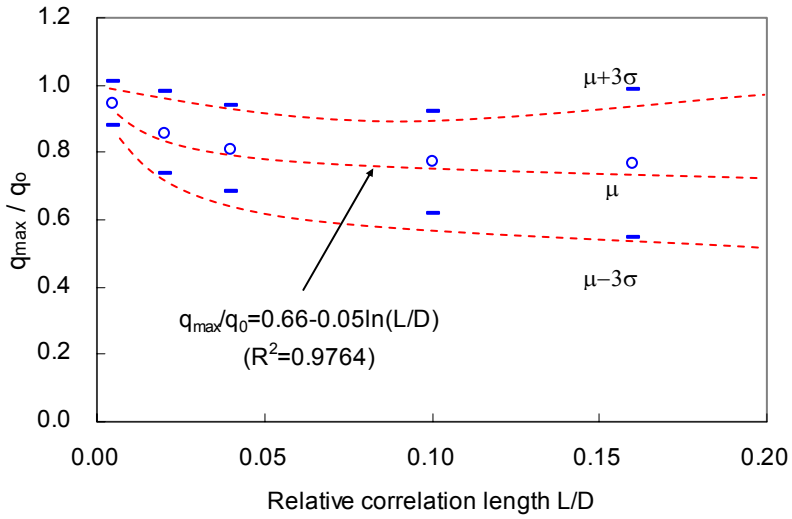

Figure 4.9 Ensemble averages of normalized undrained shear strength vs. relative correlation length. $\mu[e_0]$=0.9 and COV[e_0]=0.06. Numerically computed shear strengths are normalized by the shear resistance of the homogeneous medium with void ratio e_0=0.9. The mean trend and three sigma ranges of the numerical results are presented. The equation shown is the linear regression for the mean trend.

4.3.6 Analysis of Materials inside Localized Shear Zones

Several realizations are selected to analyze the materials that form shear zones (Figure 4.10). These include the weakest and strongest cases with the short and long correlation length (D/L=0.005 and 0.16). The variability of void ratio is constant COV[e_0]=0.3 in this study. The 5% most largely deformed elements are presumed to be part of localized shear zones. These elements are classified into twenty bins according to their initial void ratio. The resulting histogram for the four selected realizations are shown in Figure 4.10. The overwhelming presence of weak elements in shear zones confirms the role of weak elements in strain localization. Media with the highest global strength show a histogram closest to the uniform whole medium distribution.

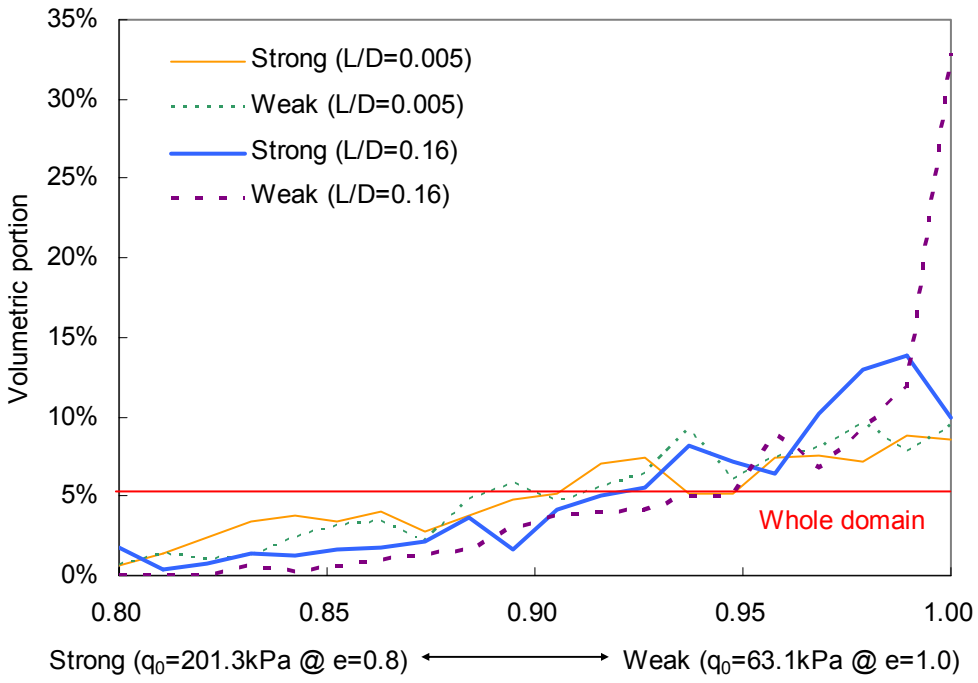

Figure 4.10 Void ratio histogram for elements presumed in shear zones during undrained deviatoric loading.

4.4 DRAINED RESPONSE STUDY

The section describes a numerical simulation study conducted to investigate the stress-strain response of correlated random media subjected to drained deviatory loading.

4.4.1 Drained Loading Response

Correlated random fields are realized for uniform distributed initial void ratio with mean $\mu(e_0)$=0.9; coefficient of variation COV[e_0]=0.03, and relative correlation length L/D=0.10. The modified Cam Clay model is used: λ= 0.174; κ=0.026; V_1=2.824 (where $V_1=1+e_0$ at 1kPa); M=1.0; ν_{1kPa} (Poisson's ratio at 1kPa)=0.3. The bulk of the medium is contractive. The square geometry is discritized into 100x 100 four-node plane strain elements. Figure 4.11 shows the evolution in the void ratio field (Figure 4.11a, b, c & d) and shear strain field (Figure 4.11e, f, g & h) for one realization of a correlated random field. It can be seen that:

- The weaker parts deform first causing shear strain localization and local volumetric contraction (Figure 4.11a, b, e & f).
- Volume contraction in weaker zones leads to a local shear strength increase, which reduces the spatial contrast in strength distribution and lessens shear strain localizations (Figure 4.11c & g).
- Locally sheared zones become homogenized with global conditions (Figure 4.11d & h).

Internal homogenization during shear of mostly contractive heterogeneous media is the most significant internal difference between drained and undrained cases. The macroscopic effect is very important. Figure 4.12a shows that the stress-strain response for homogeneous and random cases; the twenty random realizations have almost identical response due to internal homogenization after a global vertical strain $\varepsilon_z \approx 0.03$.

ε_a	Void ratio field (undeformed shape)	Shear strain field (deformed shape)
ε_a=0.01	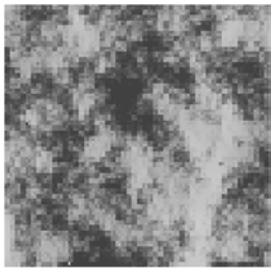 (a)	 (e)
ε_a=0.02	 (b)	 (f)
ε_a=0.04	 (c)	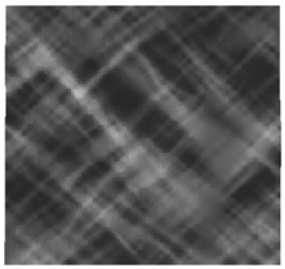 (g)
ε_a=0.08	 (d)	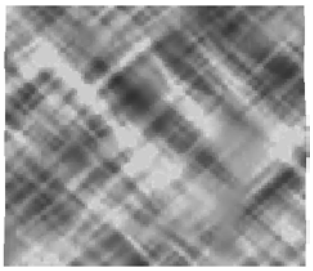 (h)

Figure 4.11 Void ratio field evolution during drained deviatoric loading and the corresponding shear strain field. Heterogeneous medium with $\mu[e_0]$=0.9, COV$[e_0]$=0.03, and relative correlation length L/D=0.10. Lighter regions indicate higher void ratios and shear strains (e=0.82~0.95; γ=0.01~0.10).

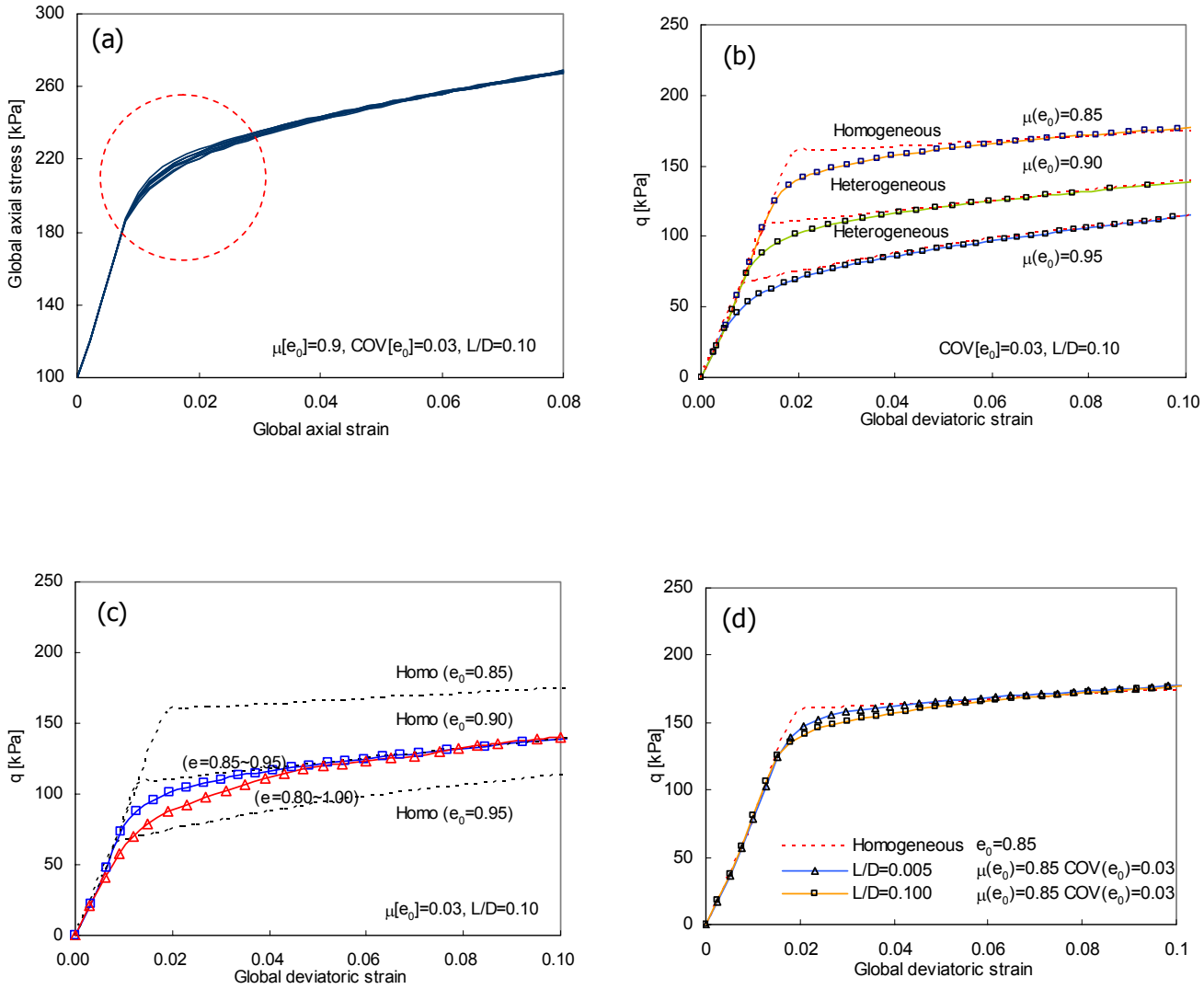

Figure 4.12 Drained stress-strain response in correlated random media. (a) Stress-strain response for 20 different random realizations with the same statistics. (b) Stress-strain response with respect to the mean initial void ratios. (c) Stress-strain response for different initial void ratio distribution ranges. (d) Stress-strain responses for different correlation lengths.

4.4.2 Influence of Internal Variability on Drained Shear Response

Additional simulations are conducted to study the influence of each statistical parameter on the drained shear response. Figure 4.12b shows the stress-strain responses for three different mean void ratios $\mu(e_0)$ with the same COV[e_0]=0.03 and same relative correlation length L/D=0.10. The three dotted curves are the corresponding homogeneous cases with the same mean initial void ratios. The stress-strain curves of the heterogeneous cases converge to the trend in homogenous cases when the global vertical strain reaches ε_z=0.03 to 0.04. Higher strain is required for media with lower $\mu(e_0)$ because a constant COV[e_0] implies higher strength variability at low void ratios.

Figure 4.12c & d show the influence of COV[e_0] and correlation length L/D in media with the same initial mean void ratio $\mu(e_0)$=0.9. Both figures show strain-driven homogenization. Random media with higher variability or longer correlation length require higher deformation to attain homogenization.

4.4.3 Analysis of Void Ratio Changes During Drained Shear

The realization in Figure 4.11 is selected to analyze void ratio changes during drained shear. All 10^4 elements are classified into thirty bins according to their void ratio (e=0.80~0.95). The resulting histogram is shown in Figure 4.13. The overwhelming deformation of weak elements and increasing kurtosis of void ratio distribution during drained shear confirms strain-induced internal homogenization. The void ratio evolution during drained deviatoric loading is schematically displayed in the critical state plane as shown in Figure 4.14.

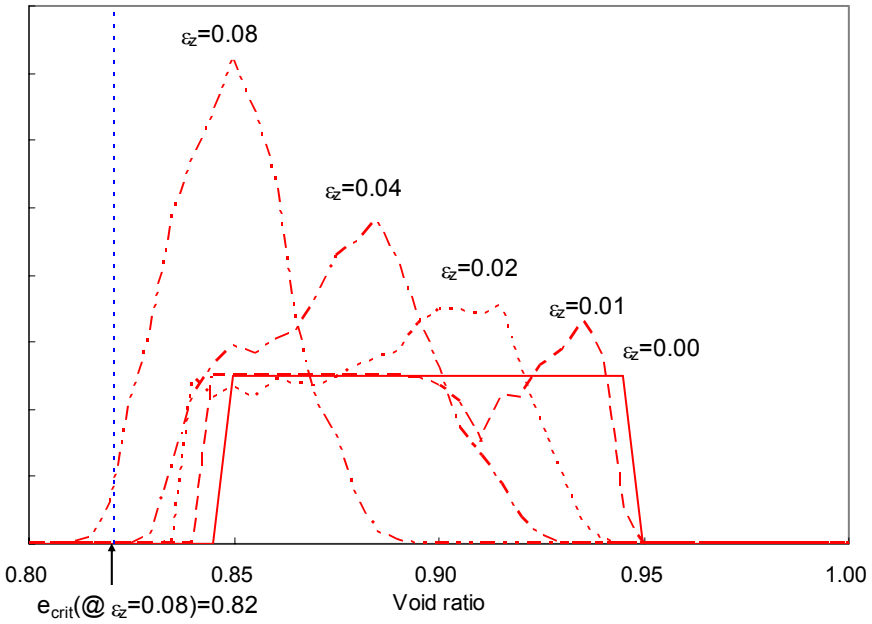

Figure 4.13 Void ratio histogram during drained shear.

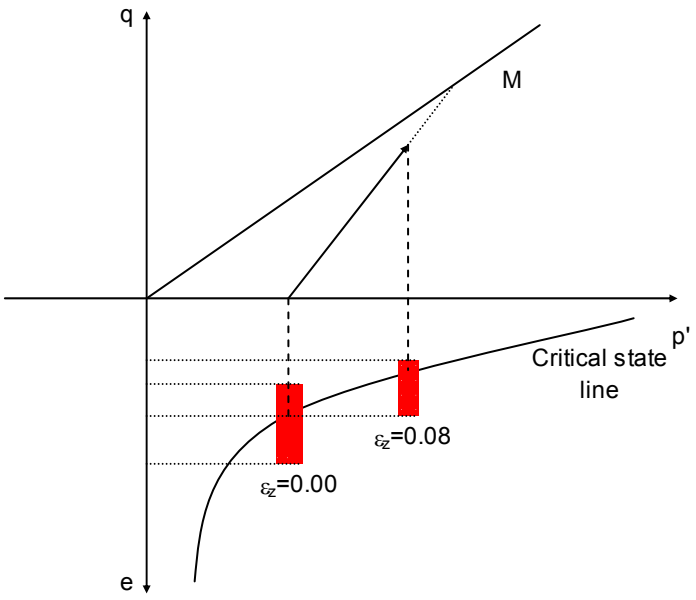

Figure 4.14 Schematic diagram of void ratio evolution in critical state space under drained deviatoric loading.

4.4 SUMMARY AND CONCLUSIONS

Spatial variability in strength-determining parameters have distinct manifestation in drained and undrained response. In this study, the initial void ratio is used as the single random variable that determines strength. The following conclusions can be drawn from numerical results.

- Shear strain localization due to percolating weak zones dominates the stress-strain response under undrained deviatoric loading.
- The global shear strength decreases with the increase in the variability of the initial void ratio distribution COV[e_0] because percolating weak zones become weaker as a larger number of weaker elements are included.
- Heterogeneous media with longer correlation length have lower undrained strength, fewer strong elements in the shear zone, and more locally developed shear bands.
- Drained deviatoric loading induces the local deformation of weak zones at first and leads to internal homogenization when the whole medium is primarily contractive. Internal heterogeneity becomes negligible at large strains and the stress-strain response is not affected by COV[e_0], range(e_0), or L/D.

CHAPTER V

ELASTIC WAVE PROPAGATION IN SPATIALLY VARYING MEDIA

Elastic wave propagation is often used to determine the small-strain stiffness of geomaterials. This study explores elastic wave propagation in spatially varying soils using numerical methods. Comparisons center on traveltimes. Results have important implications to laboratory testing and site characterization, including tomographic imaging.

5.1 INTRODUCTION

The propagation of elastic waves provides critical information about the medium. Therefore, various wave-based methods have been developed in geotechnical engineering. However, soil heterogeneity and anisotropy challenge the interpretation of elastic wave propagation. The purpose of this study is to "visualize" mechanical wave propagation in soils using numerical methods to simulate soil conditions at given scales. Several situations are considered, including vertical heterogeneity (with and without anisotropy), low velocity inclusions, and correlated random heterogeneity.

5.2 ELASTIC WAVE PROPAGATION IN HOMOGENEOUS MEDIA - SOURCES

Sources are the bottleneck in the development of seismic methods. Therefore, this first section addresses the initiation and propagation of elastic waves in homogeneous isotropic linear elastic media. Stability conditions in numerical simulations, and the effects of loading and boundary conditions are analyzed as well.

5.2.1 Stability and Sampling Criteria

The numerical simulation of wave propagation phenomena is affected by spatial and temporal discretizations. Numerical stability is established in terms of the Courant number p for the possible maximum phase velocity V in a linear elastic medium.

$$p\,(\text{Courant number}) = V \cdot \frac{\Delta t}{\Delta x} \tag{5.1}$$

Recommended criteria to avoid numerical dispersion are listed in Table 5.1. All criteria apply to numerical schemes with second order accuracy in time and fourth order in space. Note that spatial resolution is related to the minimum wavelength that can propagate through the finite mesh.

In this study, the maximum propagating frequency for shear waves is f=8 kHz, and the nominal shear wave velocity is V_s=120m/s; therefore, the corresponding minimum wavelength for shear waves is λ_s^{min}=1.5cm. The required element spacing should be less than Δx<0.25cm to guarantee less than 5% error in numerical solutions (Robertsson et al., 1994). The selected element spacing is Δx=0.15cm. The assigned calculation time interval

is Δt=5·10^{-6}sec. Then, the maximum phase velocity is V_p^{max}=300m/s following the stability criterion suggested by Valliappen and Murti (1984; Table 5.1).

Table 5.1 Stability and sampling criteria related to numerical dispersion of wave propagation solution

Criteria	condition	References
Stability criteria		
$p \le \sqrt{\frac{3}{8}}$	2D FDM	Abramowitz and Stegon (1964)
$p \le \frac{6}{7 \cdot \sqrt{D}}$ D = the dimension in space	FDM	Mitchell (1969)
$p \le 1$	2D FEM	Valliappan and Murti (1984; see Zerwer, 1999)
$p \le 0.606$	2D FDM	Levander (1988)
$p \le \sqrt{\frac{a_1}{a_2}}$ a_1 = sum of absolute values of weights of the finite difference operators for $\partial^2 u/\partial t^2$ a_2 = sum of absolute values of weights for the finite difference approximations to $\Box^2 u$.	FDM	Lines et al. (1999)
Sampling criteria		
$\Delta x \le \varsigma \cdot \lambda_s^{\min}$ ζ=0.25 for consistent mass assignment ζ=0.20 for irregular mass assignment	2D FEM	Valliappan and Murti (1984-see Zerwer, 1999)
$\Delta x \le \frac{\lambda_s^{\min}}{6}$	2D FDM	Robertsson et al. (1994)
$\Delta x \le \frac{\lambda_s^{\min}}{10}$	2D FDM	Moczo (1998)

Notations: Courant number $\mathrm{p} = V \cdot \frac{\Delta t}{\Delta x}$; V maximum phase velocity in the heterogeneous linear elastic medium; $\lambda_s^{\min}$ minimum wavelength of the propagating shear waves, $v_p^{\max}$ maximum compression wave velocity at maximum frequency traveling within the model.

5.2.2 Loading and Boundary Condition

Shear wave propagation is preferred to determine the skeletal stiffness in soils without the effects of the water bulk stiffness. Bender elements have become the most widely used transducers for laboratory applications (Santamarina et al., 2001; Lee, 2003). Bender elements generate shear waves in the longitudinal direction and compression waves on the sides. Similar radiation patterns are observed when impulse hammers are used as a source for crosshole seismic field testing (Figure 5.1).

Mechanical waves generated by vibrating bender elements are studied by applying a short-time impulse-type excitation in the vertical direction at a point. Infinite boundary elements are used to minimize reflections from boundaries. The propagating dynamic motion caused by a unidirectional impulse-type excitation in the medium consists of the vibrating motion and the long-term equivalent rigid-body motion. As an illustration, consider a quasi-static unit load applied in the x-direction at the center of an isotropic linear elastic medium (Figure 5.2a). Figure 5.2b shows the displacement contour in the x-direction. The contour shape is determined by Poisson's ratio (which also controls the ratio between shear modulus and constraint modulus in isotropic linear elastic media). The amount of the long-term equivalent rigid-body motion is actually estimated with a very long-term dynamic simulation. However, such rigid-body displacements are coupled with the vibrating motion and diminished by the energy loss at boundaries; therefore, it is difficult to separate these two motions. Time-derivatives of particle displacement remove the rigid body motion from the received signals. Figure 5.3 shows particle velocity and acceleration time histories.

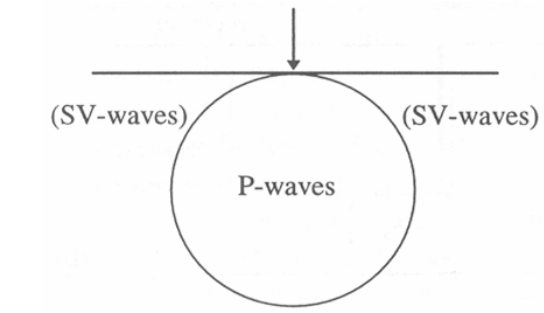

(a) Normal excitation

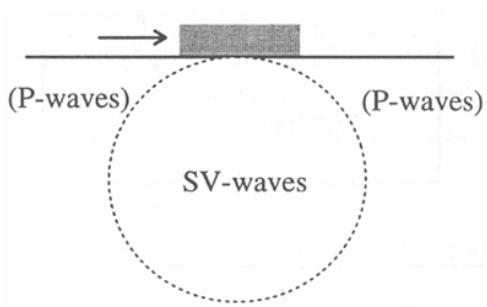

(b) Transverse excitation

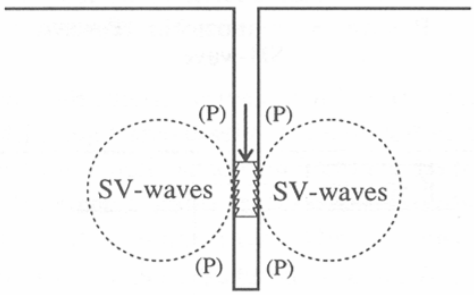

(c) Borehole shear source

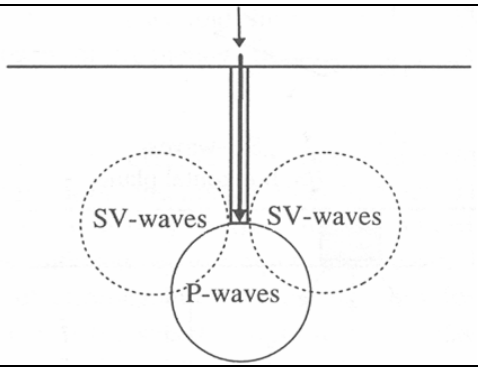

(d) Bottom source

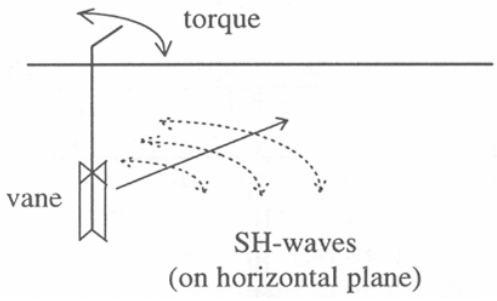

(e) Horizontally polarized shear source

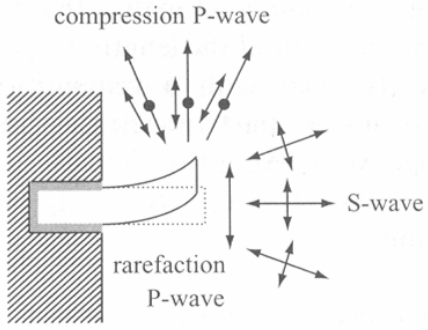

(f) Bender element vibration source

Figure 5.1 Directivity functions for common mechanical sources used in civil engineering (From Santamarina et al., 1998; Santamarina et al., 2001).

(a)

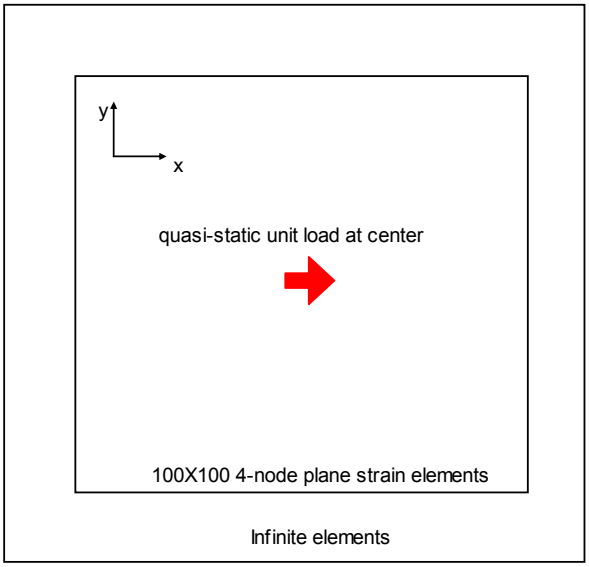

(b)

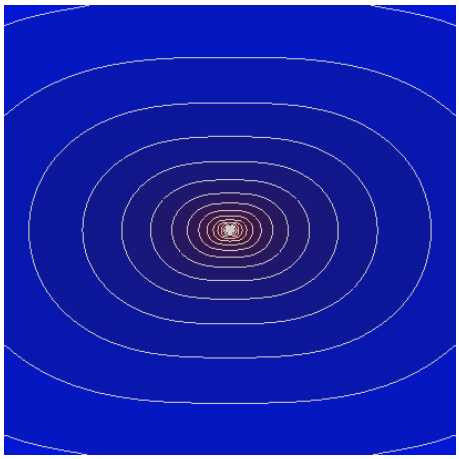

Figure 5.2 Displacement field that results from a unit force in the x-direction at the center of an isotropic linear elastic medium. (a) Loading and boundary conditions (Infinite elements are placed at all the boundary; Poison's ratio=0.2). (b) Contours of displacement in the x-direction. (The amplitude of displacements in the y direction is small and negligible when compared to the amplitude of displacements in the x-direction)

5.2.3 Directivity of Elastic Waves Initiated by a Point Seismic Source

The elastic wave characteristics of an isotropic medium have different manifestation along the different propagation directions. If the excitation is horizontal, the compression wave is prominent in the horizontal direction, and the shear wave is prominent in the vertical direction. Mechanical waves are generated by applying a short-time impulse-type excitation in the vertical direction at a point (Figure 5.3a and b). The corresponding displacement contours in the *x*- and *y*-directions are shown with shear-wave traveling time in Figure 5.4. Figure 5.5 show the particle velocity time-histories for different propagation directions from the source. These results suggest that the time-histories in a sole direction is insufficient to adequately assess the elastic properties of a material together with source characteristics. Note that multi-directional measurements can be decomposed into longitudinal and transverse propagations to enhance and clarify P-wave and S-wave propagation (Figure 5.5). However, if displacements are measured in only one direction, a careful alignment and arrangement of receivers is required to facilitate signal analysis.

Love (1944; See White, 1983) gives the particle displacement when a time varying force *g(t)* of magnitude *G* is applied. If the traveling distance is long enough to ignore near-field terms, the radiation of the displacement by a point force is (White, 1983):

$$\begin{aligned} u_r &= \frac{G\cos\phi}{4\pi\rho V_P^2 r} g\left(t - \frac{r}{V_P}\right) \\ u_\theta &= 0 \\ u_\phi &= -\frac{G\sin\phi}{4\pi\rho V_S^2 r} g\left(t - \frac{r}{V_S}\right) \end{aligned} \tag{5.2}$$

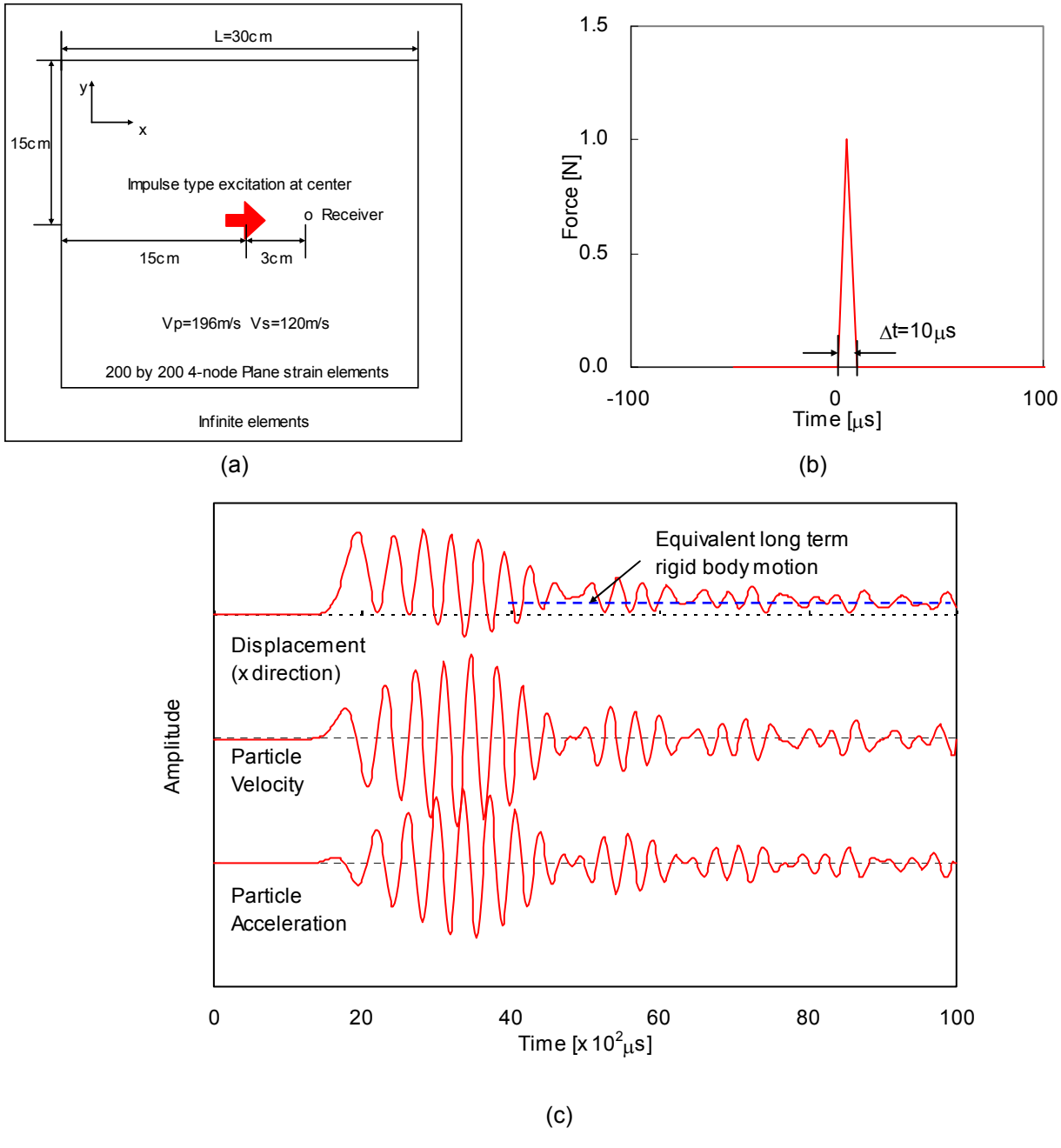

Figure 5.3 Particle displacement, velocity and acceleration at the receiver and equivalent long-term rigid body motion. (a) Loading and boundary conditions. (b) Applied impulse type load. (c) Time derivatives of particle displacements.

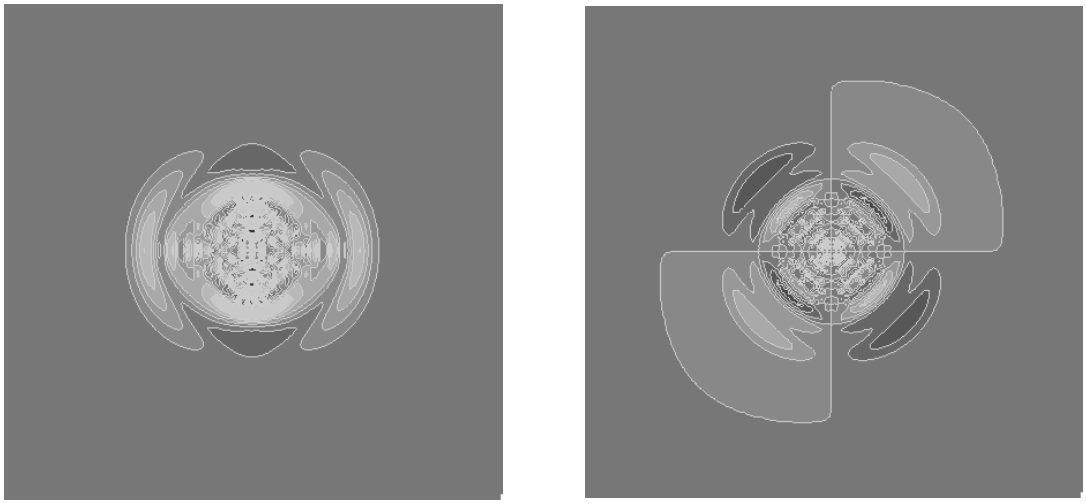

(a) U_x at t=0.30 T_0 (b) U_y at t=0.30 T_0

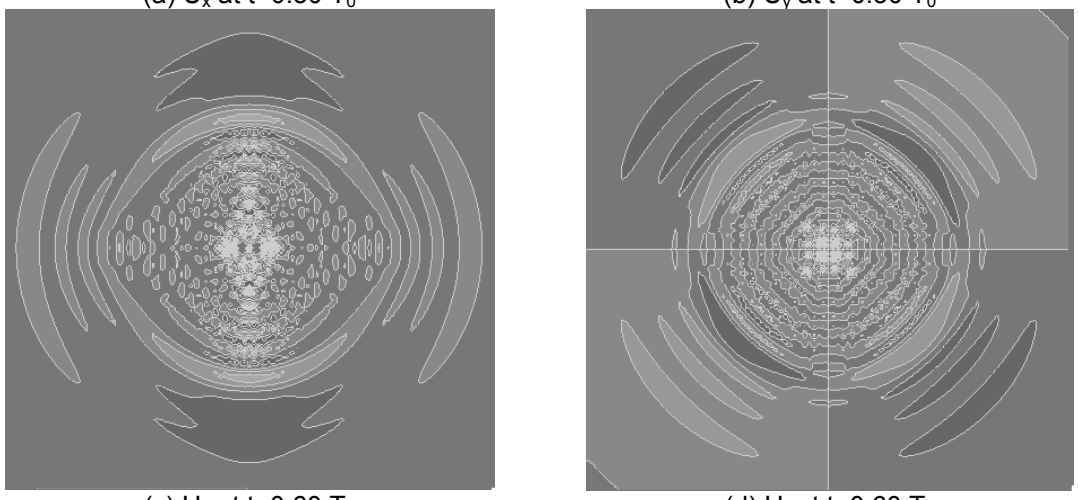

(c) U_x at t=0.60 T_0 (d) U_y at t=0.60 T_0

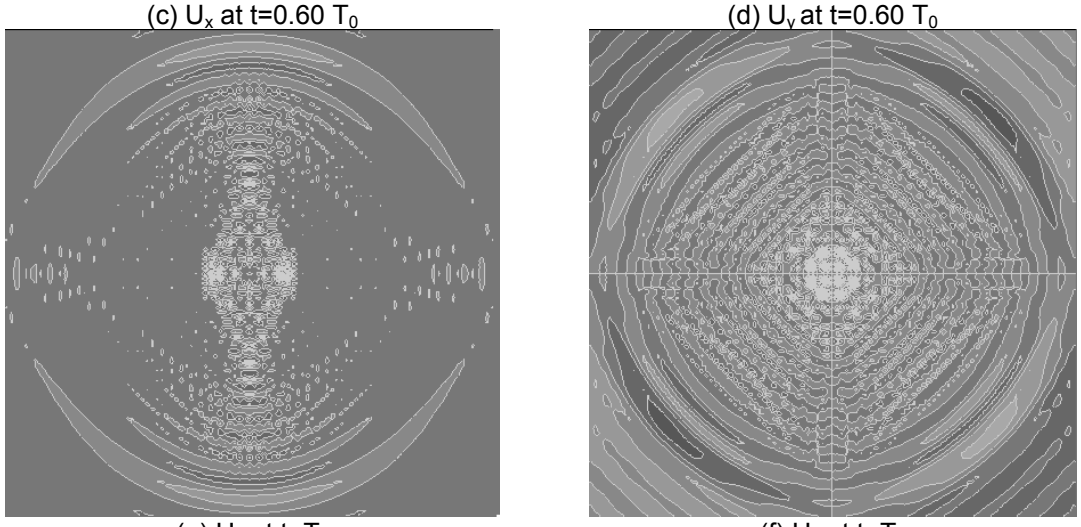

(e) U_x at t=T_0 (f) U_y at t=T_0

Figure 5.4 Elastic wave propagation triggered by a horizontal excitation in a homogeneous medium: Loading and boundary conditions are the same as in Figure 5.3a and b. The value $T_0=L/(2V_s)$ is the time for shear wave propagation from the center to the boundary.

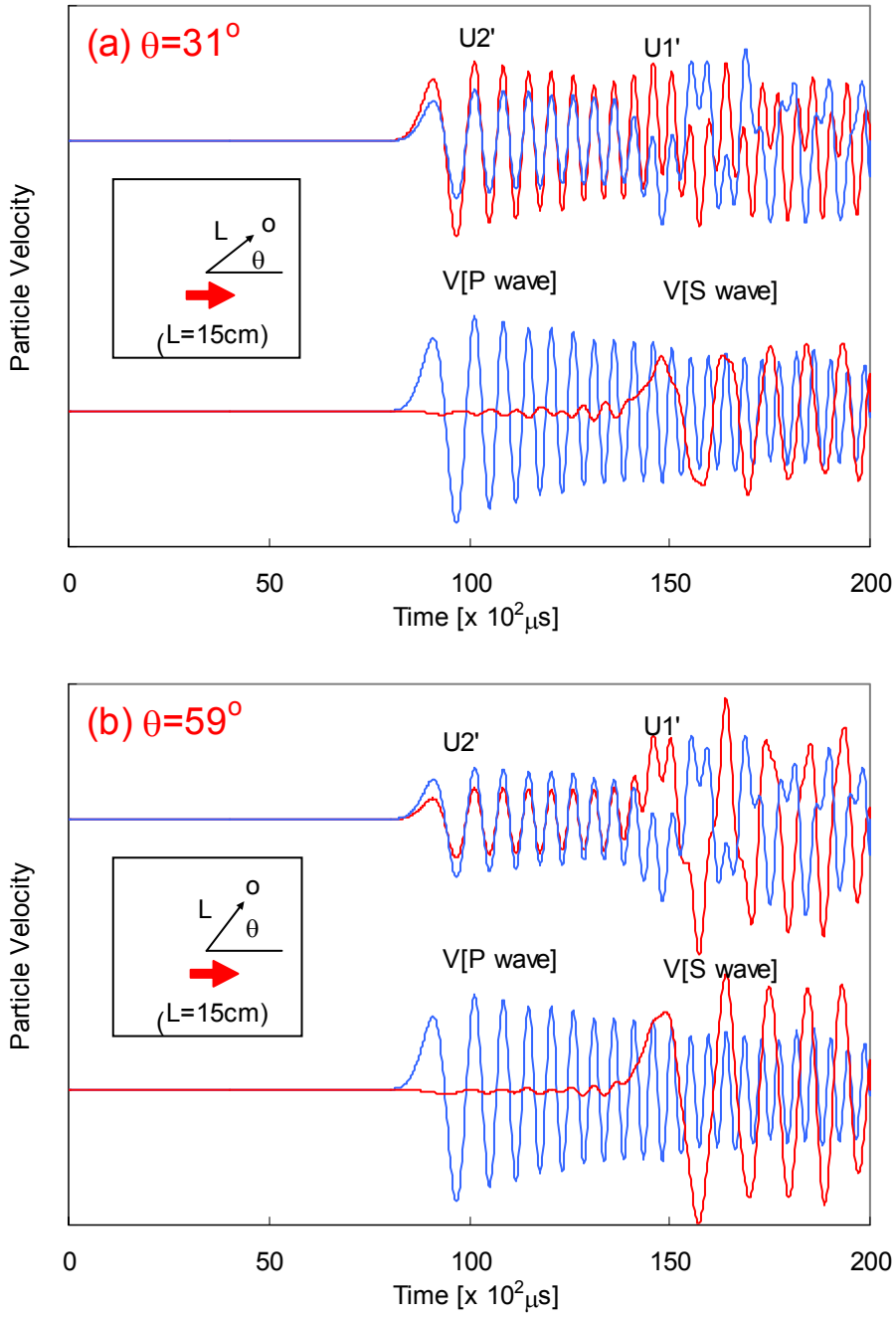

Figure 5.5 Particle velocities in the longitudinal and transverse directions. (a) Particle velocity time series at 31° from the horizontal line. (b) Particle velocity time series at 59° from the horizontal line.

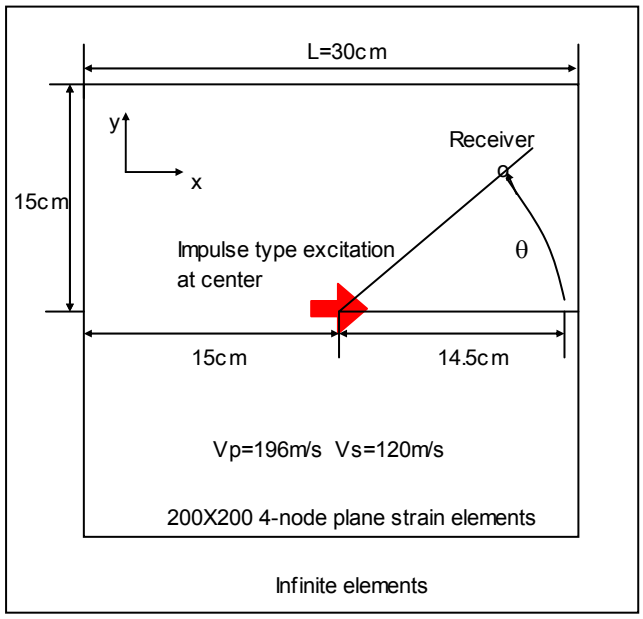

(a)

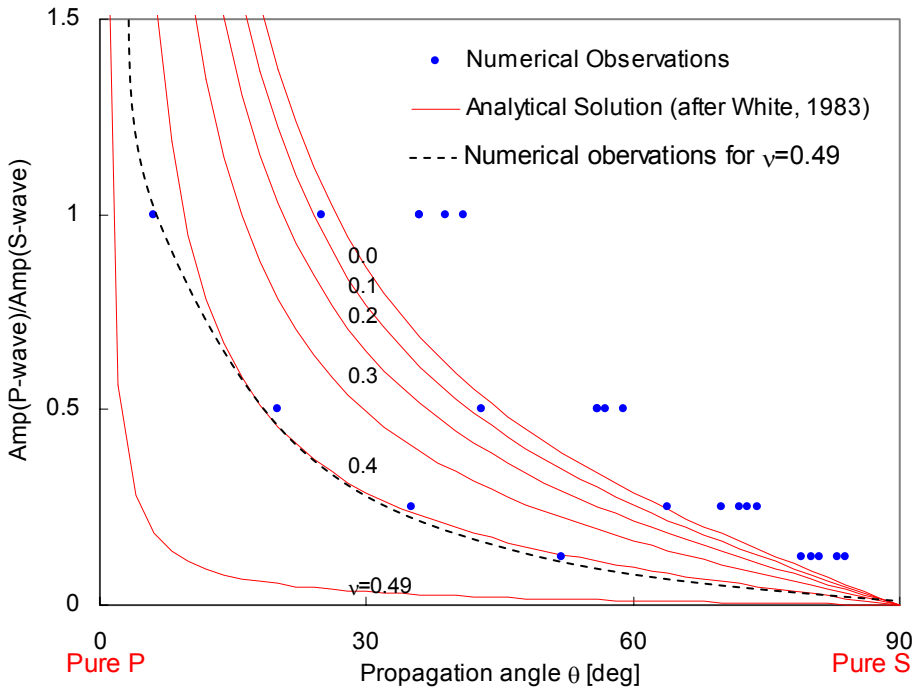

(b)

Figure 5.6 Relative directivity vs. propagation angle for different Poisson's ratios. (a) Loading and boundary conditions. (b) Comparison between analytical solution and numerical results.

where V_p is P-wave velocity, V_s is S-wave velocity, ρ is total mass density, and r is the radial distance from the origin. If an impulse-type unit force is applied at the origin, the ratio of the amplitude of radial displacement to the amplitude of tangential displacement, "relative directivity" can be computed as:

$$\left|\frac{u_r}{u_\phi}\right| = \frac{1}{|\tan\phi|}\frac{V_S^2}{V_P^2} = \frac{1}{|\tan\phi|}\frac{1-2\nu}{2(1-\nu)} \tag{5.3}$$

This parameter is computed for numerical simulations. Analytical and numerical results are plotted with respect to propagation direction for different Poisson's ratios in Figure 5.6. Results suggest that more complex time series should be expected between 30^o and 40^o when Poisson's ratio is small (dry or partially saturated soils). Therefore, the one-direction measurement configurations should take place only within $-20^o<\alpha<+20^o$ from the pure shear wave propagation direction, which allows the maximum displacement by compression wave to be less than 25% of the maximum displacement by the shear wave. Considerable differences between the numerical and analytical results show the effect of long-term rigid-body motion and the near-field components.

Comprehensive studies on radiation pattern by borehole seismic sources in isotropic media have been conducted by Lee and Balch (1982), Window (1991) and Gibson (1994), and by Dong and Toksöz (1995) in anisotropic media.

5.3 VERTICALLY HETEROGENEOUS, CROSS ANISOTROPIC LINEAR ELASTIC MEDIA

Stiffness anisotropy in soils results from anisotropic stresses (Roesler, 1979; Nikitin and Chesnokov, 1984; Lee and Stokoe, 1986; Rothenberg and Bathurst, 1989) and inherent depositional effects. In addition, the small strain shear modulus increases with confining stress, i.e., with depth. Therefore, real soils under K_0 condition are inherently vertically heterogeneous and anisotropic. Elastic wave propagation under these conditions is explored in this section

5.3.1 Analytical Solution of Ray Path in a Vertically Heterogeneous Cross Anisotropic Linear Elastic Medium

The effective stress profile is considered to be a linear function of depth, $\sigma_z' = \gamma' z$, and the lateral stress coefficient at rest K_0 is assumed constant. The shear wave velocity V_s is a power function of the state of effective stresses, $V_s = \alpha \sigma'^{\beta}$. The corresponding wave velocity profile is illustrated in Figure 5.7. The relationships between wave velocity and cross anisotropy material model are described in Appendix A.

The wave velocity field is herein simplified, assuming a locally linear velocity increase and weak anisotropy as:

$$
\begin{aligned}
&V_v(z) = a + bz = V(0^0, z) \\
&c = \frac{V_v}{V_h} = \frac{V(0^0, z)}{V(90^0, z)} \\
&V_\theta = V_v \cdot \sqrt{\frac{1 + c^2 \tan^2\theta}{1 + \tan^2\theta}}
\end{aligned}
\tag{5.4}
$$

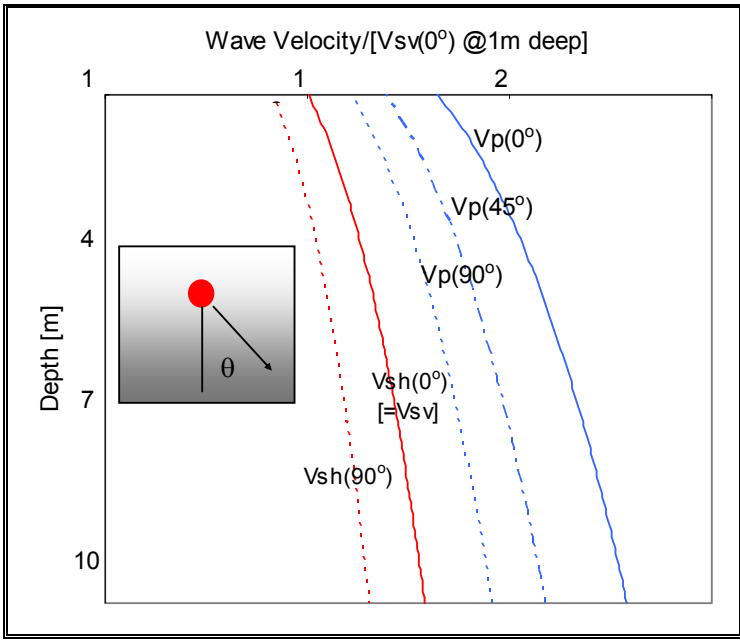

$$\sigma_v' = \gamma' z,\ \sigma_h' = K_0 \sigma_v'$$

$$V_{sv}(0^o) = V_{sv}(90^o) = V_{sh}(0^o) = \alpha_s \left(\frac{1+K_0}{2kPa} \sigma_v' \right)^{\beta}$$

$$V_{sh}(90^o) = \alpha_s \left(\frac{K_0}{1kPa} \sigma_v' \right)^{\beta}$$

$$V_p(0^o) = \alpha_p \left(\frac{\sigma_v'}{1kPa} \right)^{\beta}$$

$$V_p(90^o) = K_0^{\beta} \cdot V_p(0^o)$$

$$V_p(45^o) = \left(\frac{1+K_0}{2} \right)^{\beta} \cdot V_p(0^o)$$

$$\frac{V_p(0^o)}{V_{sv}(0^o)} = \sqrt{\frac{1-2\nu}{2(1-\nu)}}$$

$$\gamma' = 10\text{kPa},\ K_0 = 0.4,\ \beta = 0.25,\ \nu = 0.2$$

Figure 5.7 Stress-induced vertical heterogeneity and cross anisotropy in soils. Associated wave velocity profiles with depth.

where a, b and c are constant, and θ is the propagation direction. If the locations of the source and receiver are (x_s, z_s) and (x_r, z_r), the ray path z(x) is derived as a function of a, b and c (Santamarina and Cesare, 1994):

$$z(x) = \sqrt{\left(\frac{V_{vs}}{b} \right)^2 + (x - x_s) \left[\frac{V_{vr}^2 - V_{vs}^2}{b^2 (x_r - x_s)} + c^2 (x_r - x) \right]} - \frac{a}{b} \tag{5.5}$$

where V_{vr} and V_{vs} are the vertical propagation velocities at the source and the receiver locations. Pure shear wave propagation due to vertical displacement source corresponds to $\partial z(x)/\partial x\big|_{x=x_s} = 0$. Therefore, this equation can be reordered for $z(x_r)$:

$$z(x_r) = \frac{\sqrt{(a + bz_s)^2 - b^2 c^2 (x_r - x_s)^2} - a}{b} \tag{5.6}$$

5.3.2 Comparison between Numerical and Analytical Solutions

Figure 5.8 shows elastic wave propagation in vertically heterogeneous isotropic media. Mechanical waves are generated by applying a short-time impulse-type excitation in the vertical direction at a point near a boundary. There is no compression wave propagation in the direction of pure shear wave propagation when the medium is homogeneous. However, wave propagation in a vertically heterogeneous medium shows a compression wave propagation ahead the shear wave front in all directions. Thus, it is necessary to measure the direction in which the compression wave is propagating least. A parametric numerical study is conducted by varying parameters *a* and *b* in Equation 5.4. The lines are the analytical solutions and the dots are the numerical results in Figure 5.9 and 5.10. Figure 5.9 shows the numerical least compression wave propagating ray paths with different offsets in velocity profiles. The lower offset in velocity profiles produces the higher curvature. Figure 5.10 shows the least compression wave propagating rays with different velocity gradients. Higher gradient causes higher ray bending. Figure 5.9(c) shows the effects of anisotropy on the least compression wave propagation path. As K_0 is close to 1.0, anisotropy diminishes and ray curvature decreases.

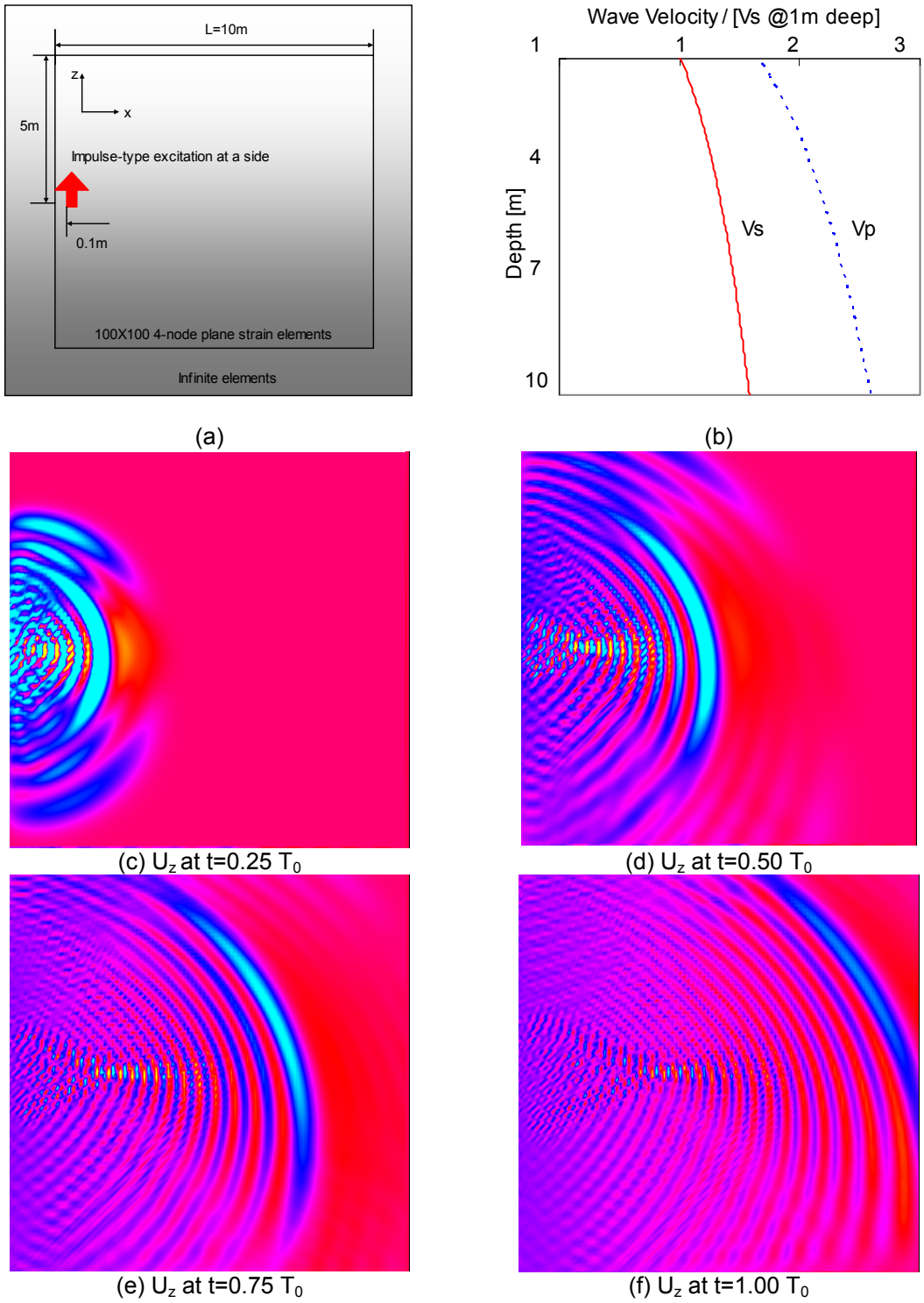

Figure 5.8 Elastic wave propagation in a vertically heterogeneous medium. $T_0=L/V_s$(at the source depth). (a) Loading and boundary conditions. (b) Wave velocity profile with depth

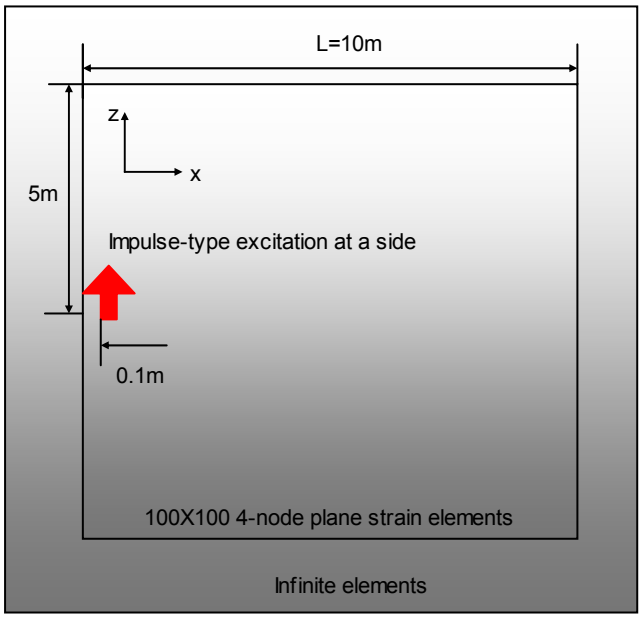

Load and boundary conditions

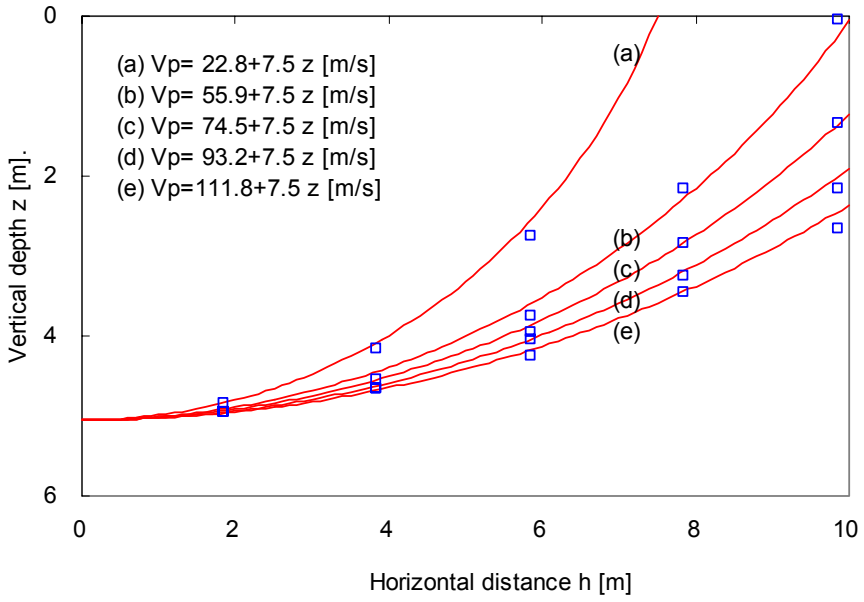

Figure 5.9 Shortest time P-wave propagation path for different offset velocities.

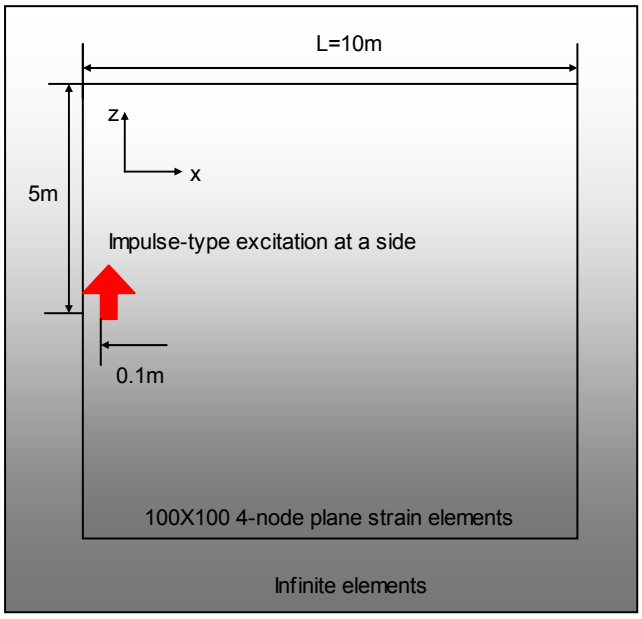

Load and boundary conditions

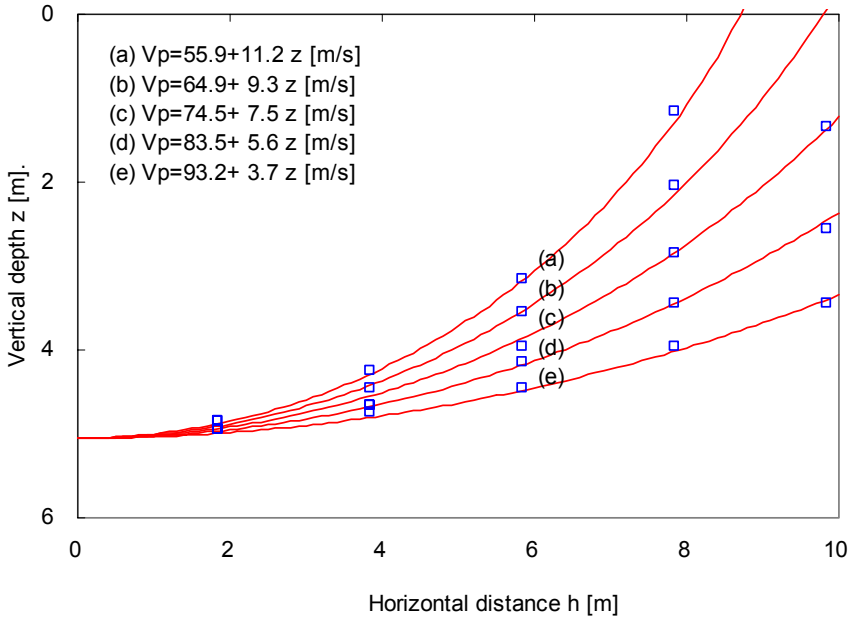

Figure 5.10 Shortest time P-wave propagation path for different velocity gradients.

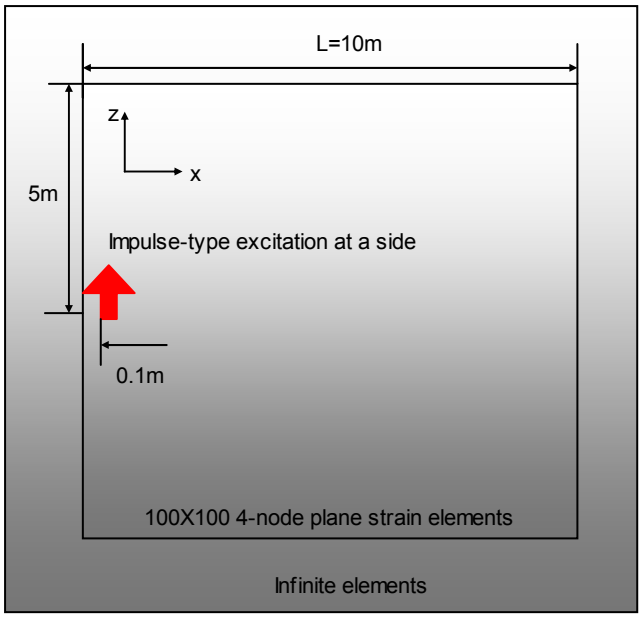

Load and boundary conditions

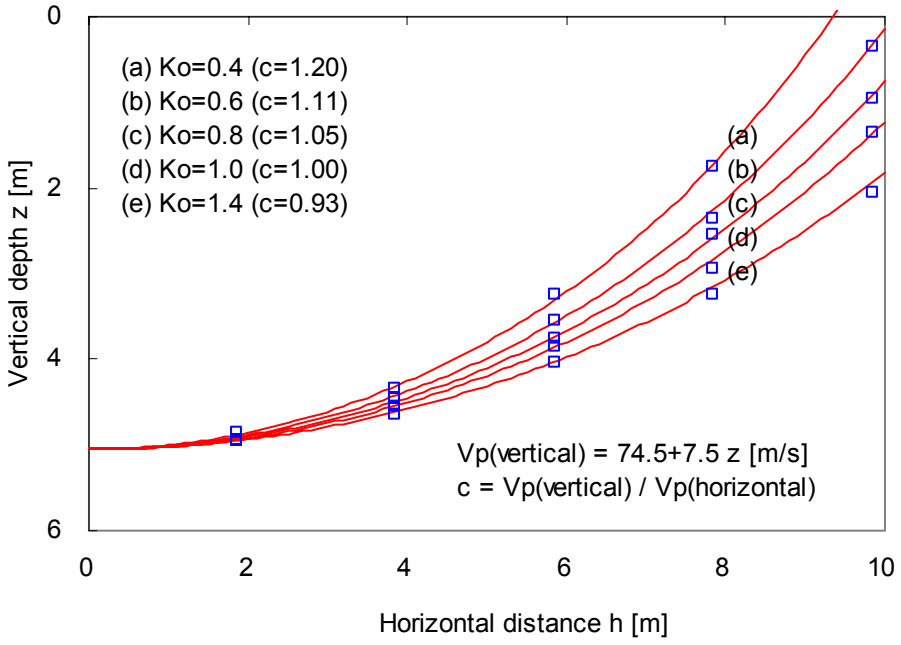

Figure 5.11 Shortest time P-wave propagation path for different anisotropy factors.

5.4 MEDIA WITH LOW VELOCITY INCLUSION

Wave propagation in a medium with low velocity inclusions has been studied to predict the effect of the local weakness such as cracks and cavities in structures in the context of nondestructive techniques (Wong, 1995; Llopis and Ballard, 1995; Sammon and O'Neill, 1997). Traveltime tomography using the straight ray assumption shows inherent disadvantages in geotechnical low velocity anomaly detection as follows (Tallin and Santamarina, 1992; Potts and Santamarina, 1993; Williamson and Worthington, 1993; Santamarina and Reed, 1994):

- The straight-ray tomography assumes the wave path thickness is infinitely narrow.
- The straight-ray assumption ignores the wavefront diffraction healing.
- There is a restriction for illumination directions in geotechnical applications.
- The anomalies inside the Fresnel's ellipsoid affect the traveltimes.

This study discusses the effects of low velocity inclusions on traveltimes and emergent phenomena such as diffraction healing using numerical simulations.

5.4.1 Shadow Effects

A numerical simulation of a plane wave propagation through a homogeneous medium with a low velocity cylindrical inclusion is conducted by applying a plane seismic source (Figure 5.12a). Figure 5.12(b) shows the node-displacement time-histories at different locations with the same direct distance from the source.

(a)

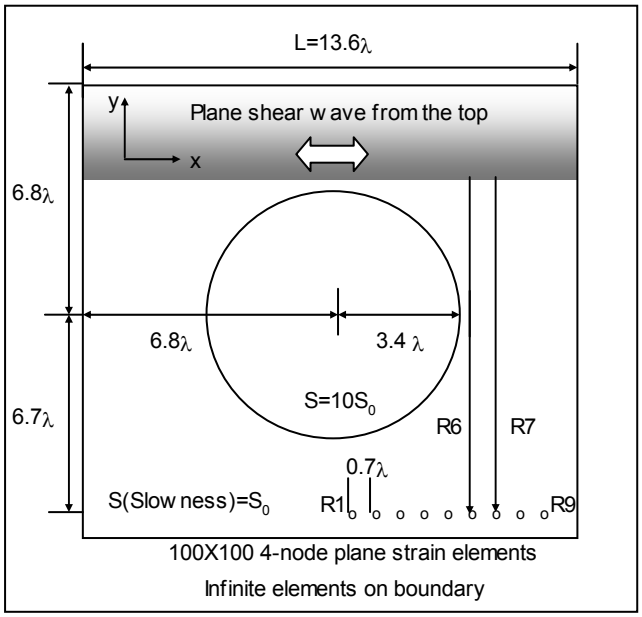

(b)

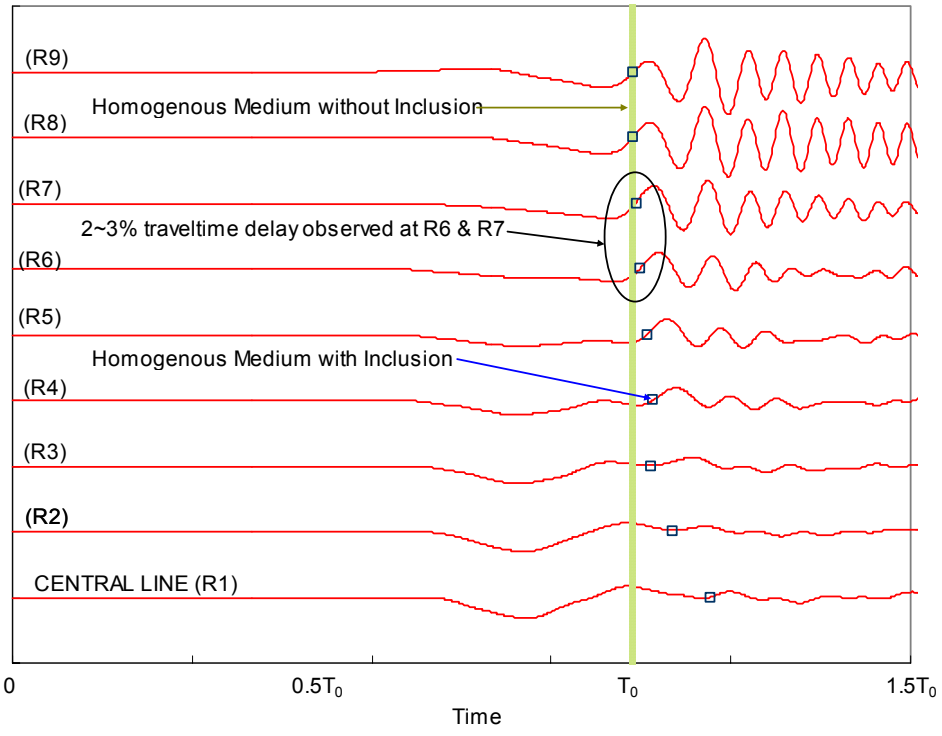

Figure 5.12 Shadow by low velocity inclusion. Straight rays R6 and R7 do not travel through the inclusion, but their traveltimes are affected by the low velocity inclusion. (a) Geometry and simulation details. (b) Particle displacement time series at receivers.

Points in the figure indicate the S-wave arrival times. Straight rays R6 and R7 travel close to the inclusion, but they do not "travel through" it. However, traveltimes are delayed by the presence of the low velocity inclusion.

A similar phenomenon is observed in a parallel experimental high-resolution shear-wave tomography study shown in Figure 5.13. Even if the straight ray paths #2 and #3 do not interact with the anomaly, the average ray wave-velocity is altered by the low velocity inclusion.

This phenomenon develops when the propagating wavelength is similar to the anomaly size. The characteristics of the arriving wave are determined by integrating within Fresnel's ellipse. An explicit solution for the multi-dimensional traveltime kernel to identify the first Fresnel's zone is presented by Dahlen et al. (2000). The maximum kernel width is shown about $\sqrt{\lambda L}$, where λ is the propagating wavelength and L is the direct travel distance. Therefore, the longer the wavelength, the wider the Fresnel's ellipse becomes (Figure 5.14; See Appendix B). This solution indicates that even if there are no obstacles along the direct wave path between a seismic source and a receiver, the traveltime is altered by the presence of anomalies within the Fresnel's ellipse.

5.4.2 P-wave Propagation: Diffraction Healing

It is difficult to detect the presence of low velocity inclusions using either signal duration, travel time, or power spectral density when the distance between receivers and a low velocity inclusion is longer than 4 to 6 diameters of inclusion size. This is called "diffraction healing" (Wielandt, 1987; Potts and Santamarina, 1993).

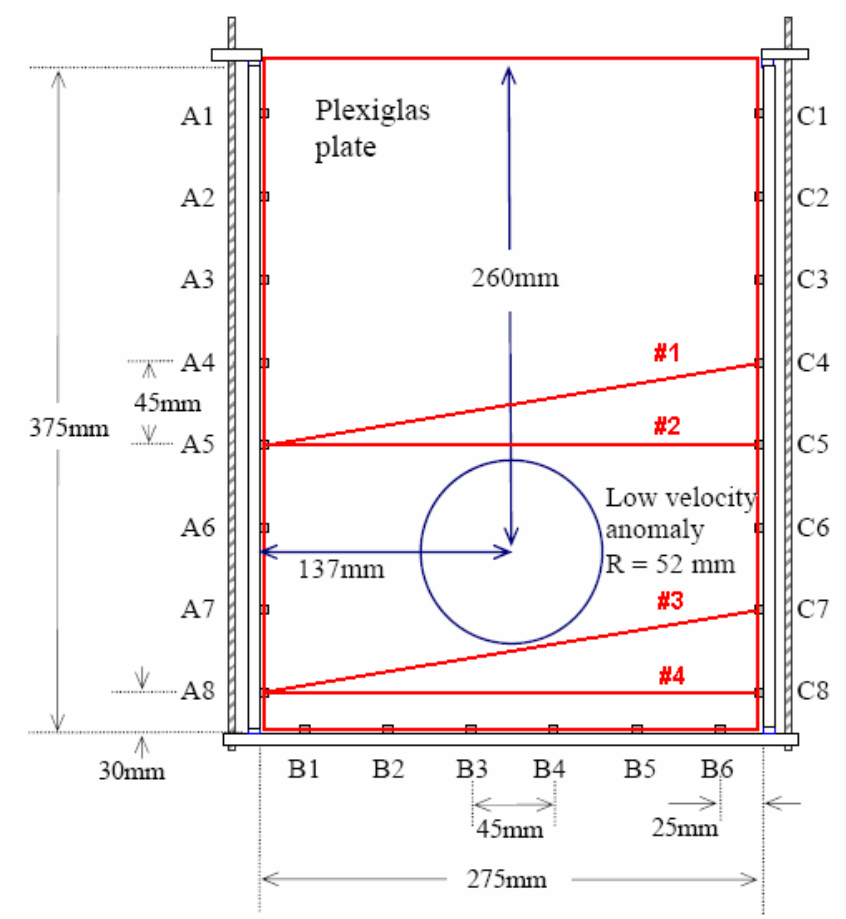

(a) Experimental setup

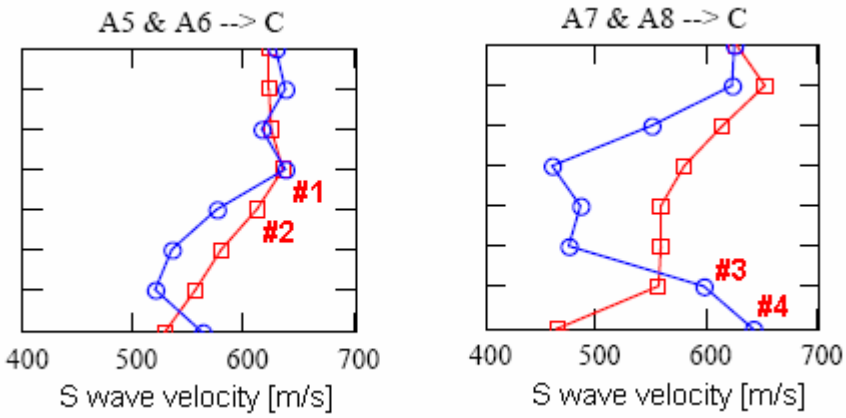

(b) Measured wave velocity with different rays

Figure 5.13 Shadows of average ray velocity. Rays (#1, #2, #3, #4) do not touch the low velocity inclusion. (a) Experimental setup (b) Measured wave velocity with different rays, Paths (#2, #3) close to the inclusion are delayed by the presence of the low velocity inclusion (data from Lee, 2003).

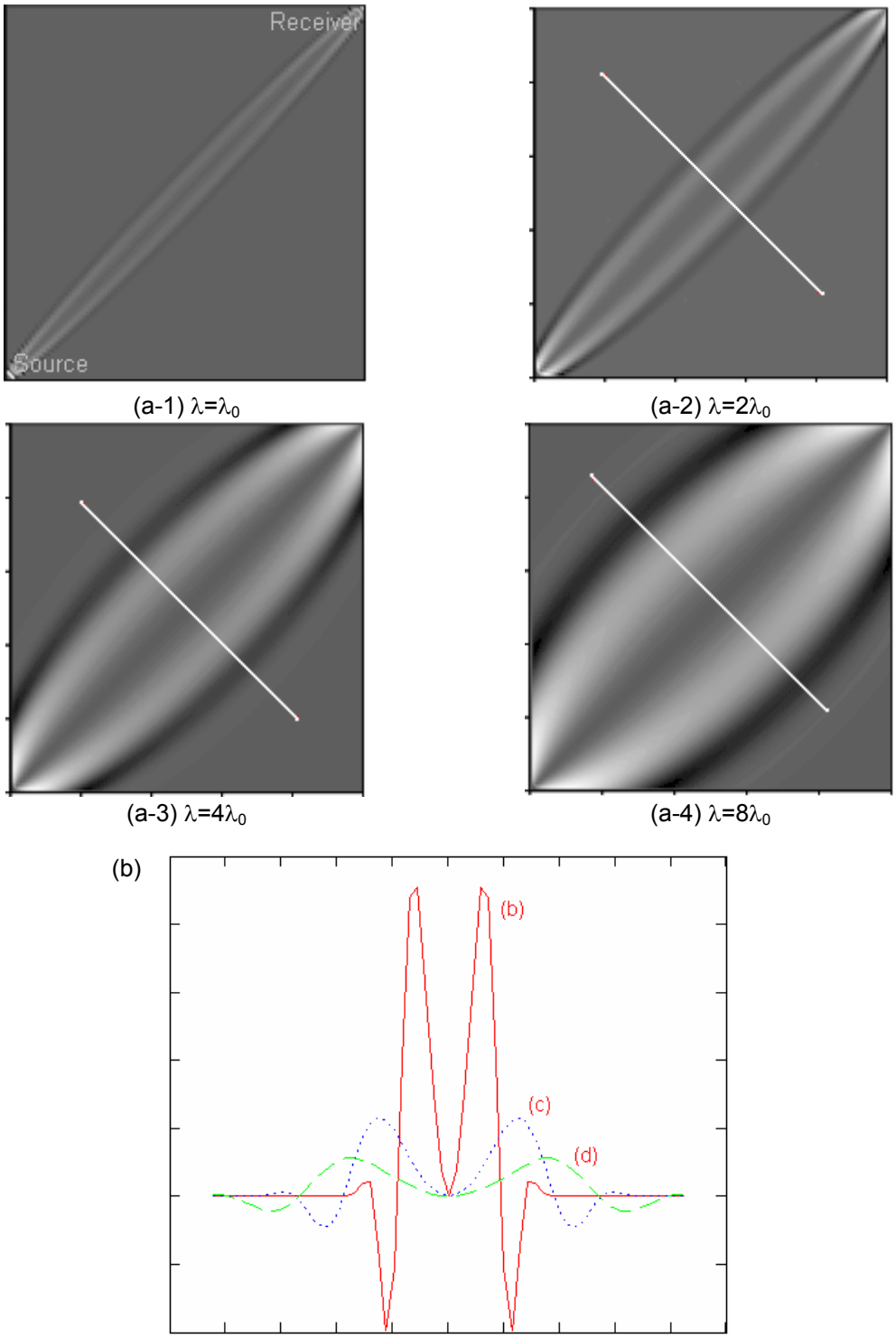

Figure 5.14 Multi-dimensional traveltime kernel used to identify the first Fresnel's zone. (a) Lighter regions indicate greater values in the kernel. (b) Cross-section of the traveltime kernel at the center between the source and the receiver (white lines).

A square low velocity inclusion with an impedance mismatch of 1/3 is considered next. The size D of the low velocity inclusion is about $D/\lambda \approx 3.9$, and the center of the inclusion is located 13.6λ away from the source. A plane compression wave is applied as a seismic source (Figure 5.15a). The first wave arrivals beyond the inclusion indicate that diffracted waves determine traveltimes. The interfacial "Stoneley wave" that travels along the interface between the host medium and the inclusion is slowed down by the presence of the lower stiffness anomaly (See also Achenbach, 1975). The ray paths that determine the first arrival traveltimes seem to curve some distance away from the inclusion.

Traveltimes are determined at various distances from the source. Figure 5.15b illustrates traveltimes normalized by the corresponding traveltimes in the homogeneous case. Values are plotted for different distance from the source. Figure 5.15b shows that the closest ray path estimation of traveltime is obtained using ray paths that curve about one wavelength around the interface that is $A \approx \lambda$ in Figure 5.15a.

Additional parametric studies indicate that regardless of the inclusion size, the one wavelength approximation is a valid assumption to estimate traveltimes for inclusions with stiffness contrast $\leq 1/10$ (Figure 5.16). It should be noted that in the case of small size inclusions (case a in Figure 5.16), the arrival of diffracted waves is almost concurrent with the arrival of the wave traveling directly through the low velocity inclusion, and the λ approximation becomes less relevant.

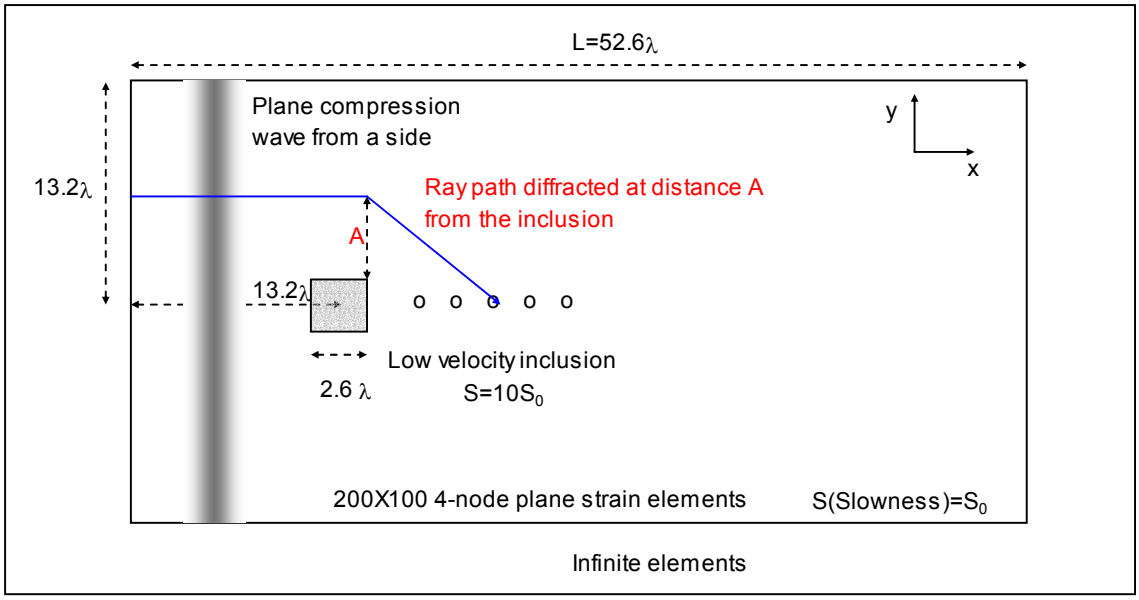

(a)

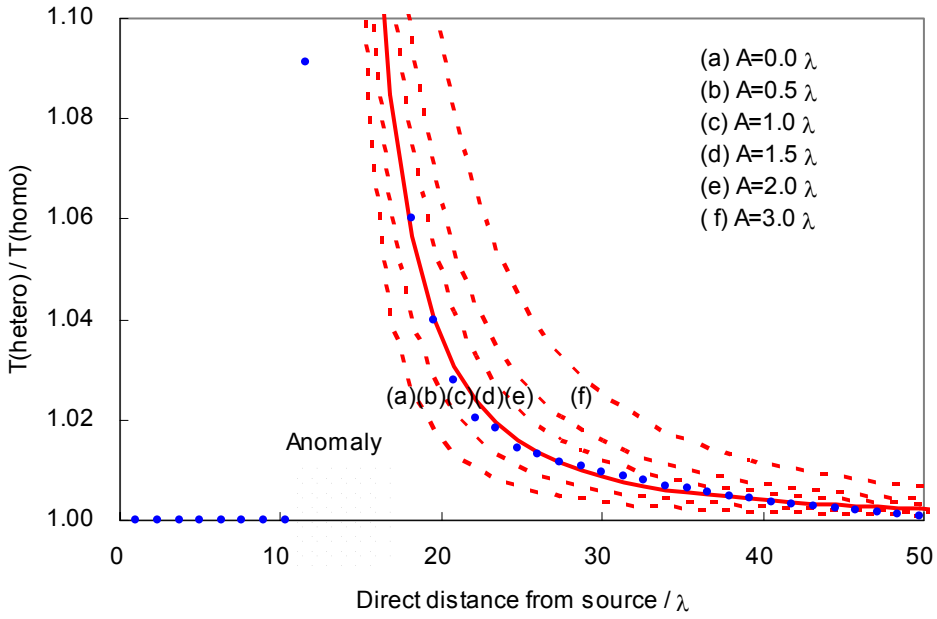

(b)

Figure 5.15 Normalized traveltimes in a medium with a low velocity inclusion with different ray path assumptions. (a) Loading and boundary conditions. (b) Normalized traveltime vs. direct distance from the source.

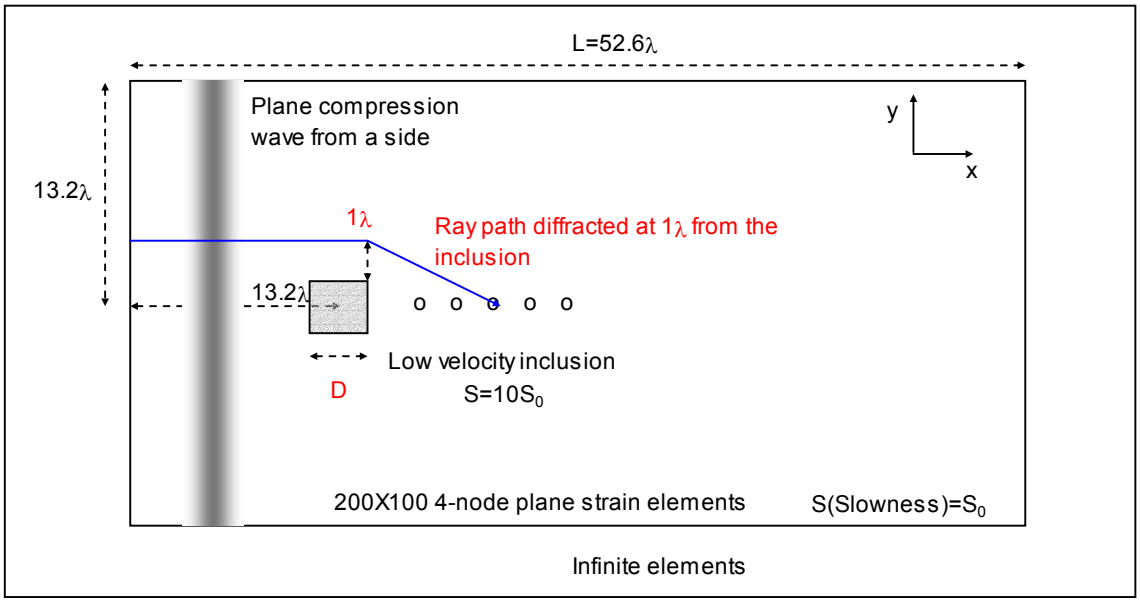

(a)

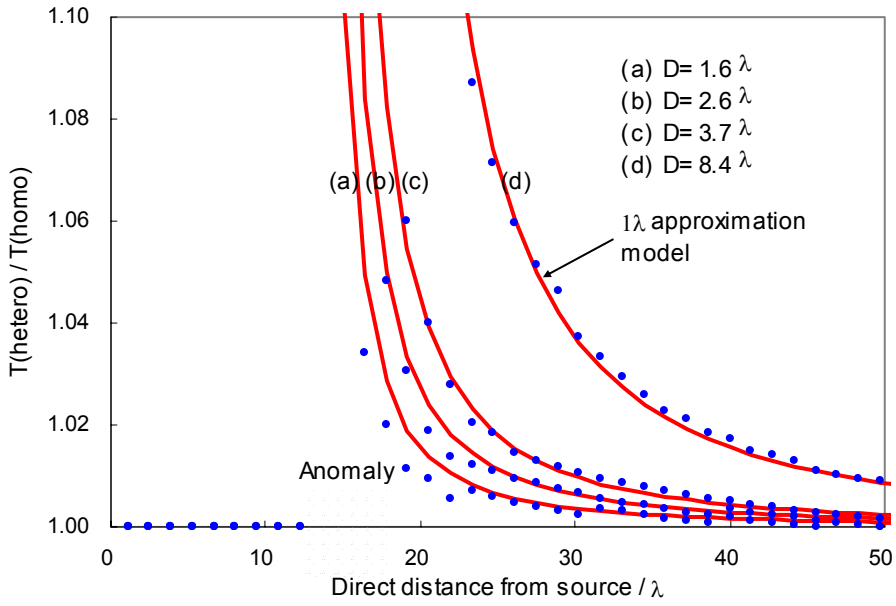

(b)

Figure 5.16 Normalized traveltimes in a medium with a low velocity inclusion with 1λ diffraction assumption. (a) Loading and boundary conditions. (b) Normalized traveltime vs. direct distance from the source.

5.4.3 S-wave Propagation: Mode Conversion around the Anomaly

Other phenomena are observed when shear waves travel through a medium with low velocity inclusions. Figure 5.17 shows a plane shear-wave propagating through a medium with a square low velocity inclusion (shown as a box in the figures). The wave that travels through the low velocity inclusion presents a head wave ahead of the diffracted waves inside the circle in Figure 5.17d. Such head waves are the result of mode conversion at interfaces between the host medium and the inclusion whereby fast traveling P-wave fronts are generated. The head waves affect the determination of the first arrival time for shear waves beyond the inclusion. However, it loses importance at a distance of 4 to 6 times the inclusion size D beyond the inclusion (Figure 5.17f). The amplitude of head waves depends on the inclusion size and stiffness contrast. Figures 5.18 and 5.19 show that, as the size of the inclusion or the stiffness contrast at the interface increases, the amplitude of head waves grows and exerts the greater influence on traveltime determinations.

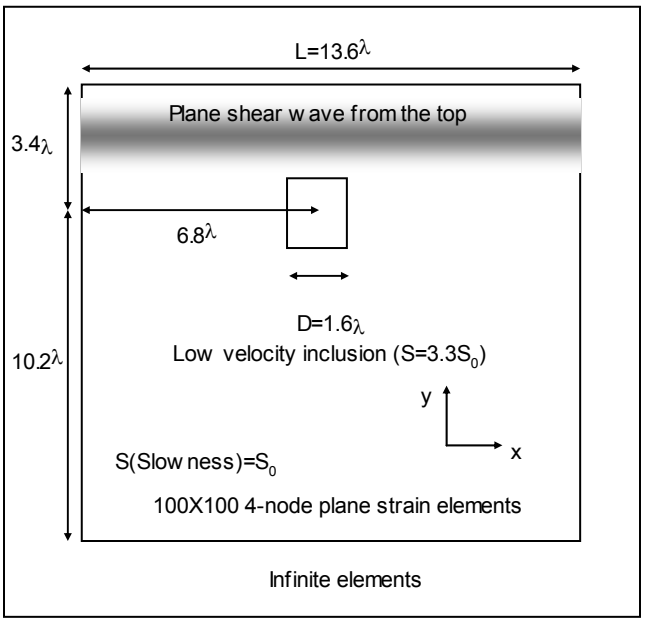

(a)

Figure 5.17 Plane shear wave propagation in a homogeneous medium with a low velocity inclusion: $T_0=L/V_{s0}$, and D (inclusion size≈1.6λ). (a) Loading and boundary conditions.

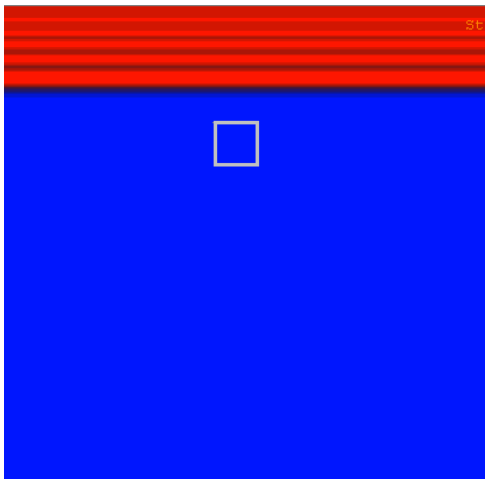

(b) t=0.17 T_0

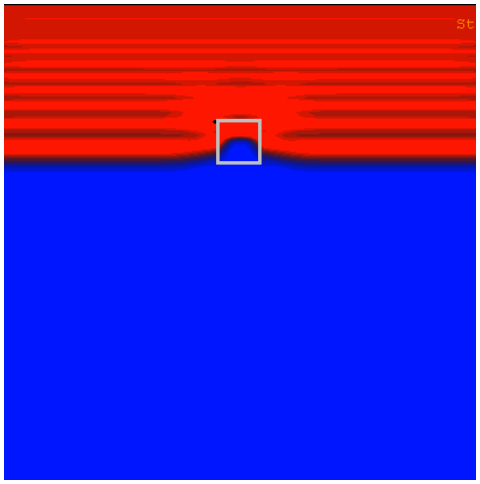

(c) t=0.33 T_0

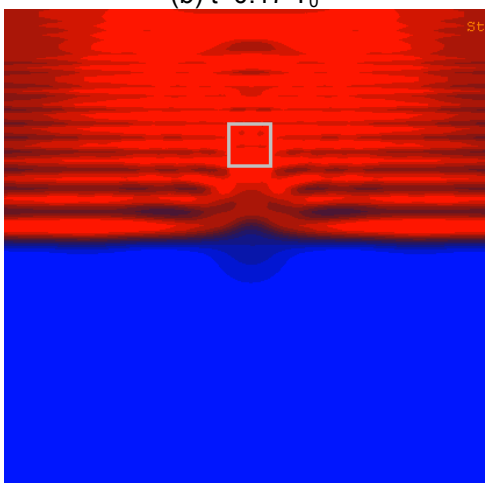

(d) t=0.50 T_0

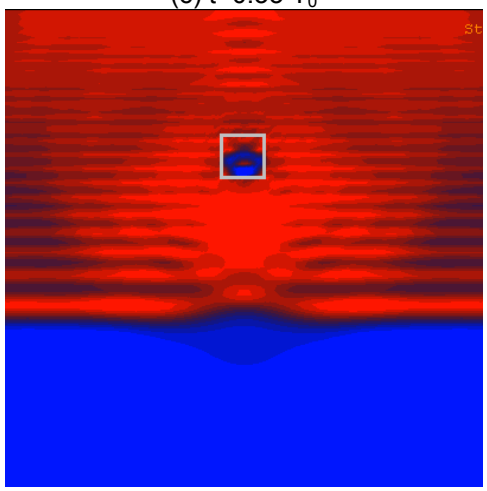

(e) t=0.67 T_0

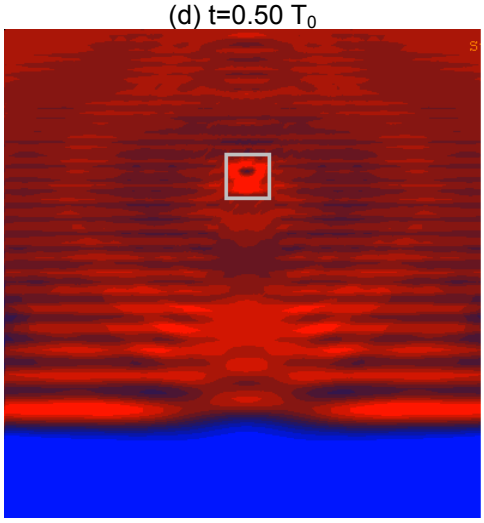

(f) t=0.83 T_0

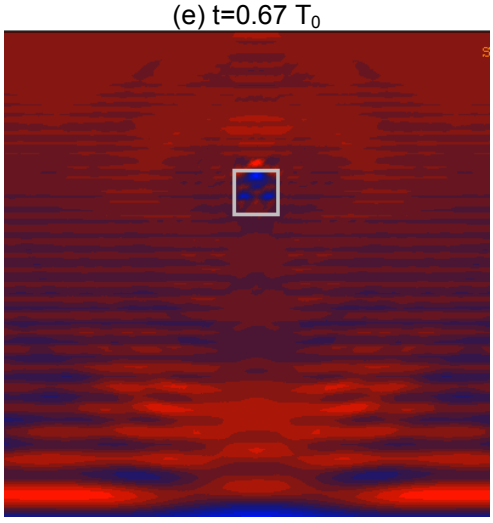

(g) t=1.00 T_0

Figure 5.17 (continued) Plane shear wave propagation in a homogeneous medium with a low velocity inclusion: $T_0 = L/V_{s0}$, the inclusion size $D \approx 1.6\lambda$, t=(traveltime).

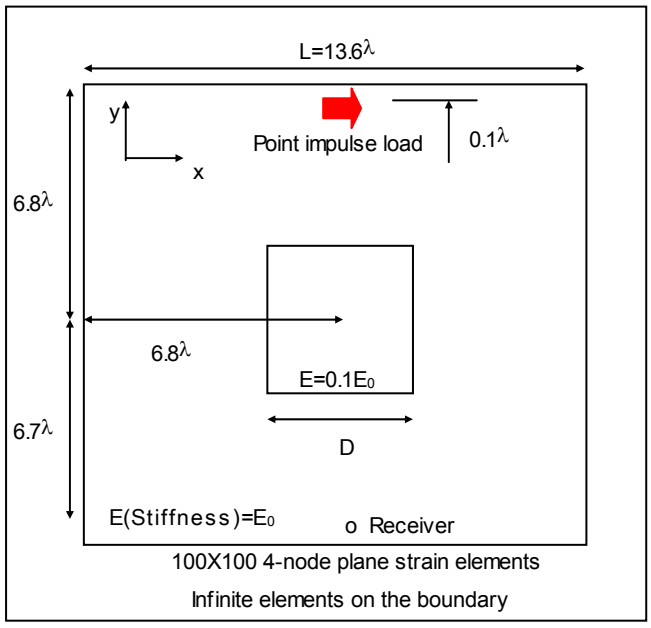

(a)

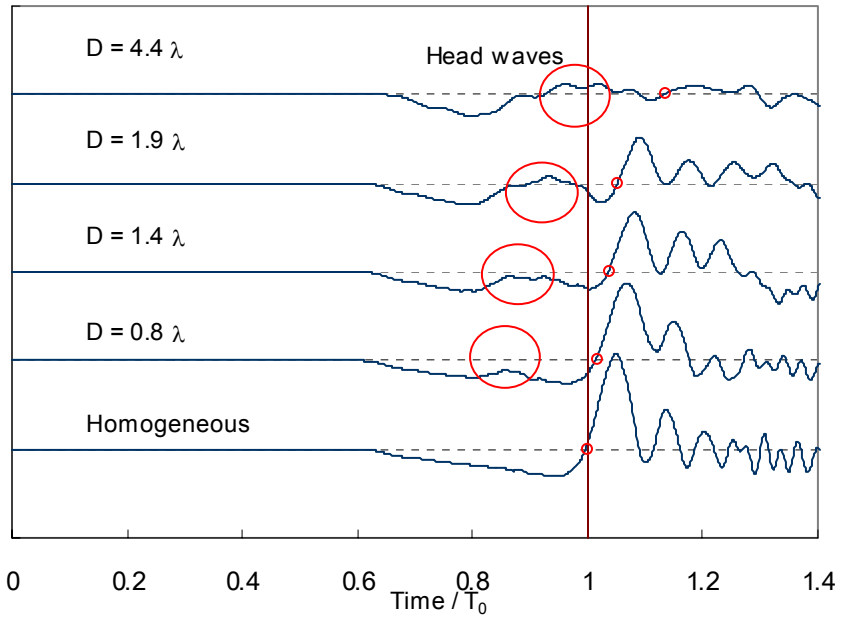

(b)

Figure 5.18 Effect of inclusion size D on shear wave propagation: $E_{inclusion}/E_0=0.1$. $T_0=L/V_{s0}$. (a) Loading and boundary conditions. (b) Head wave detection with different inclusion sizes.

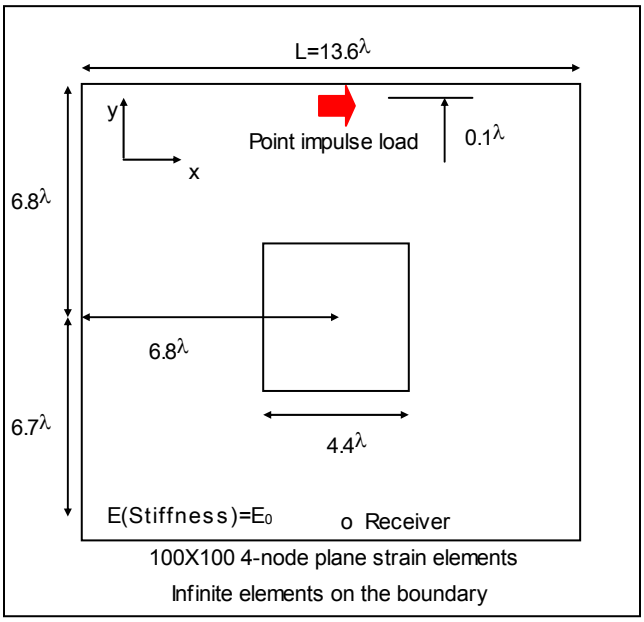

(a)

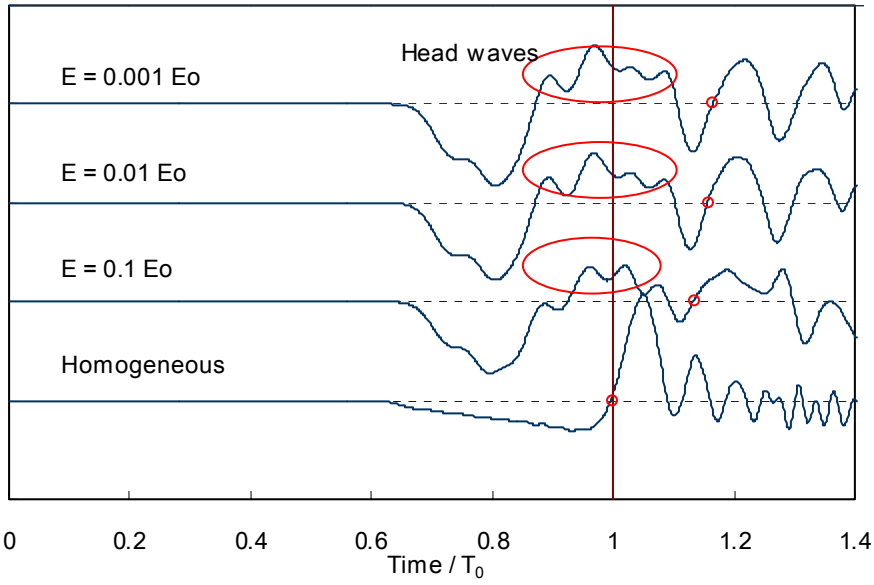

(b)

Figure 5.19 Effect of stiffness contrast $E_{inclusion}/E_0$ on shear wave propagation: The inclusion size D is D=3.2. Mass density ρ is constant. $T_0=L/V_{s0}$. (a) Loading and boundary conditions. (b) Head wave detection with different inclusion sizes.

5.5 RANDOMLY HETEROGENEOUS MEDIA

The medium behaves as an equivalent homogeneous medium when the propagating wavelength is much longer than the scale of heterogeneities. The acting propagating velocity can be obtained by effective media theory. Only waves with wavelengths longer than twice the layer thickness can travel through a stratified structure. The shorter wavelengths are filtered out, i.e. rejected by Brillouin's effect. Consider then, a long-wavelength (λ>>layer thickness), plane wave propagation normal to a one-dimensional layered media. The elastic wave velocity is approximated by the harmonic mean of the layer modulus (Buckus, 1962; Mukerji et al. 1995). The harmonic mean velocity is the lower bound of the wave velocity expectation.

On the other hand, if the propagating wavelength is much shorter than the layer thickness (λ<<layer thickness), the traveltime though the whole medium is the sum of traveltimes though each layer. The short wavelength (λ<<layer thickness) wave velocity is always faster than the long wavelength (λ>>layer thickness) wave velocity (Marion et al., 1994; Mavko et al, 1998).

The traveltime estimation becomes more complex in two-dimensional or three-dimensional random media. Traveltime can be estimated using ray theory. However, linearized ray theory is valid in the case of weakly heterogeneous media ($\Delta s/\mu_s$<0.2), when the propagation distance is much longer than the propagating wavelength and the wavelength is much longer than the internal scale of heterogeneity (Boyse, 1986). Wave propagation inside the first Fresnel's zone overcomes some of these limitations (Dahlen et

al., 2000; Hung et al, 2000, Zhao et al., 2000). The following numerical study explores elastic wave propagation in correlated random media.

5.5.1 Statistics of Traveltime in Randomly Heterogeneous Media

Compression and shear plane wave propagation in randomly heterogeneous media are simulated next with two different slowness variability COV_{SL}=0.025 and 0.20, and two different relative correlation lengths with respect to traveling distance *L/D*=0.005 and 0.1. The compression and shear wave velocities of unpertubated medium are 172m/s and 106m/s. The propagating distance from the source is 15cm, and the propagating wavelengths are λ_p=0.6cm for P-wave, and λ_s=1.3cm for S-wave.

As shown in Figure 5.20, first arrivals are often unclear due to the ballistic scattering which deteriorates the propagating waveforms. Such deterioration is aggravated when receivers are located close to or inside a very low-velocity or a very high-velocity zone. Indeed, stronger heterogeneities have high effect on traveltime determination because of the exacerbated multi-path arrivals (Spetzler and Sneider, 2001).

Two hundred wave arrivals for each case are monitored to assess the statistical distributions of first arrivals of compression (Figure 5.21a) and shear waves (Figure 5.21b). Several observations are common to both shear and compression wave propagations (See data summary in Table 5.2):

- Elastic wave arrivals occur earlier in random media with the strong heterogeneity (COV_{SL}=0.20) than in the random media with the weak heterogeneity (COV_{SL}=0.025).

- Elastic waves travel faster in the longer correlation length case than in the shorter correlation one.
- Both observations denote the wavefront ability to identify the fastest travel path (Fermat's principle), particularly inside the Fresnel's ellipse.

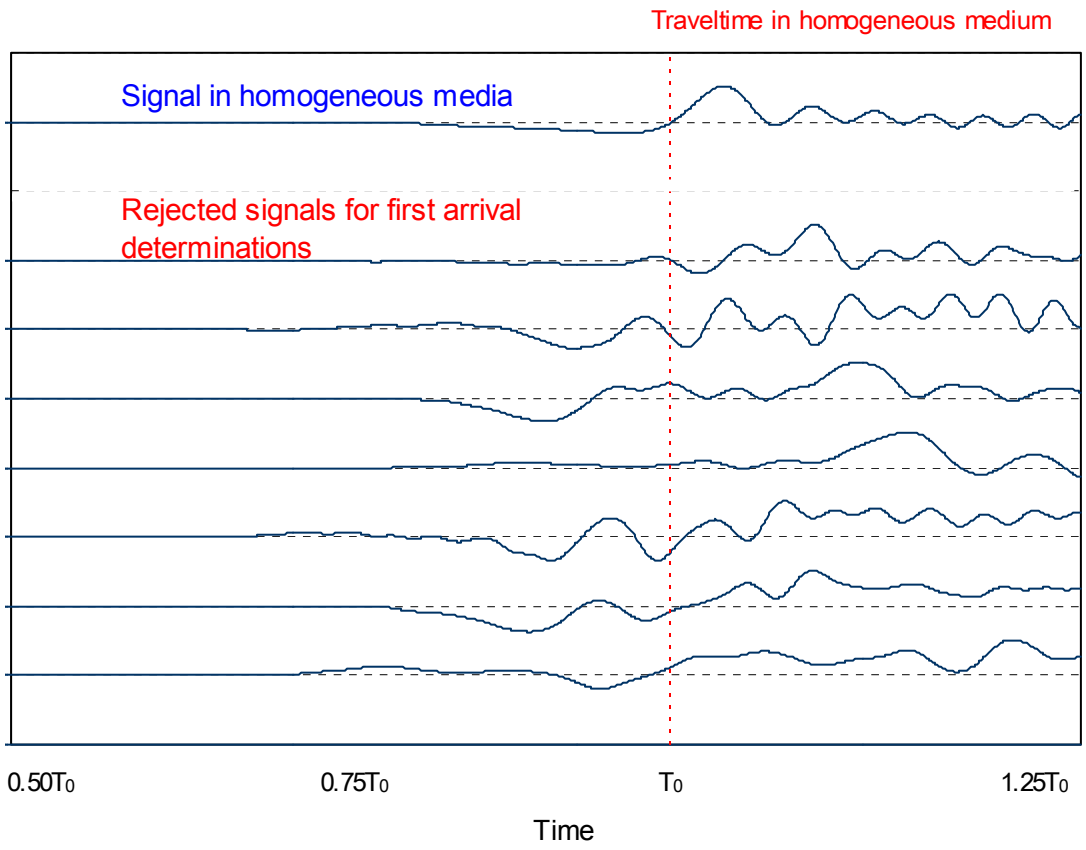

Figure 5.20 Particle displacement time-series. The first arrival of shear waves cannot be unequivocally selected.

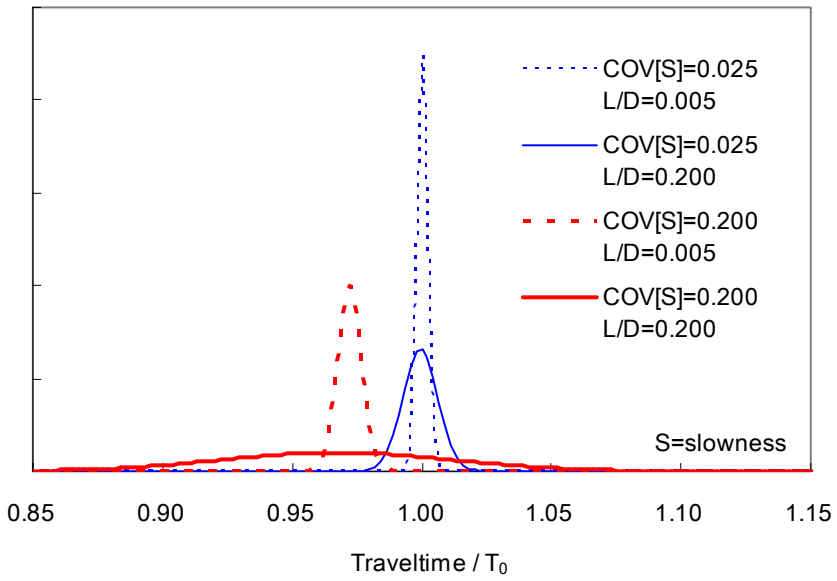

(a)

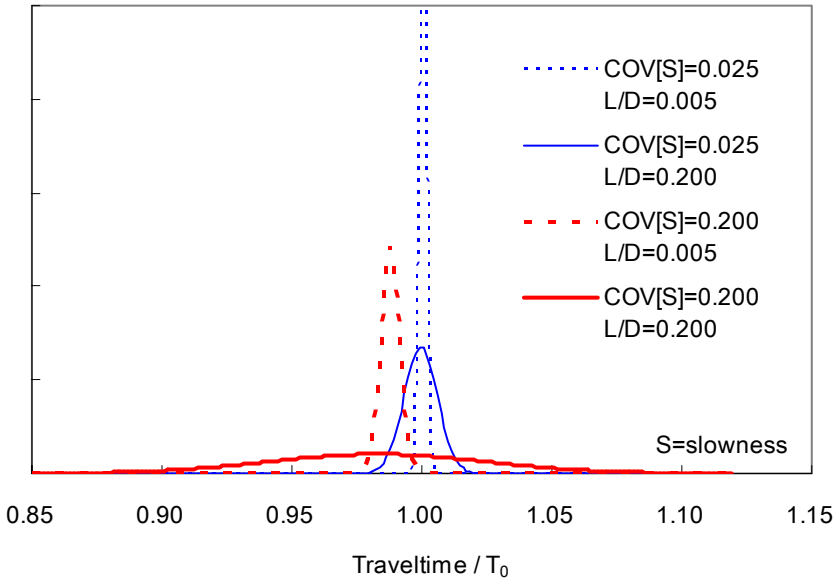

(b)

Figure 5.21 Statistical distributions of plane elastic wave traveltimes in randomly heterogeneous media: T_0 is the traveltime in a homogeneous medium. (a) Compression wave traveltimes. (b) Shear wave traveltimes.

Note that the S-wave wavelength is longer than that of the compression wave. Even if the same size of correlation length *L/D* is applied (where *D* is traveling distance), the effect of randomness on the first arrival time is different between shear wave propagation and compression wave propagation. In fact, the statistical distributions show that COV and skewness for P-wave traveltimes are greater than ones for S-wave traveltimes. Thus, it appears that the compression wave can find optimal travel paths more effectively than shear waves. This can be observed in longer tails due to earlier compression wave arrivals. The kurtosis of shear wave traveltimes is greater than the kurtosis of compression wave traveltimes because the propagation of waves with longer wavelength is not so affected as the propagation of waves with shorter wavelength. These results also suggest that Poisson's ratio inferred from V_p/V_s will be a function of the medium spatial variability.

Table 5.2 Statistical parameters of traveltime distribution in correlated random media

	2.5% COV in slowness				20% COV in slowness			
	L/D=0.005		L/D=0.1		L/D=0.005		L/D=0.1	
	S-wave	P-wave	S-wave	P-wave	S-wave	P-wave	S-wave	P-wave
T_{mean}/T_0	1.001	1.001	1.000	1.001	0.989	0.973	0.983	0.968
COV[%]	0.10	0.19	0.64	0.68	0.36	0.46	4.28	4.59
Skewness	0.256	0.101	-0.240	-0.504	-0.596	0.363	-0.111	-0.075
Kurtosis	-0.274	-0.496	-0.316	0.346	1.106	-0.728	0.957	0.515

5.6 SUMMARY AND CONCLUSIONS

This chapter explored elastic wave propagation in spatially varying soils using numerical methods. The study focused on emergent phenomena in relation to stress-induced vertical heterogeneity and cross anisotropy, low velocity inclusions, and correlated random heterogeneity. The following conclusions can be drawn:

- Stress-induced vertical heterogeneity and cross anisotropy are inherent in soils. Ray curvature in vertically heterogeneous media is aggravated by anisotropy.
- Velocity anomalies inside the Fresnel's zone alter traveltimes. In addition, diffraction healing and mode conversion take place around low velocity inclusions. The impact of these two phenomena vanishes at a distance of 4 to 6 times the inclusion size beyond the inclusion.
- Correlated random spatial heterogeneity affects traveltimes. The greater the variation in slowness distribution, the shorter the expected traveltime becomes.
- The length of spatial correlation functions act as a low-pass filter.
- When the wavelength approaches the scale of the correlation length, wave signatures are complex and reflect ballistic-type propagation and low-pass filtering.

CHAPTER VI

SAND-RUBBER MIXTURES

The mechanical behavior of granular mixtures is investigated in this chapter as an engineering application of "controlled" heterogeneous media. Emphasis is placed on the small-strain and intermediate-strain deformation of stiff sand and soft rubber chip mixtures.

6.1 INTRODUCTION: SAND-RUBBER MIXTURES

The number of wasted tires is astonishing: 279 million tires are disposed every year (EPA, 1991). Therefore, the potential reuse of wasted tires presents important economical and environmental benefits. Shredded rubber from wasted tires has been considered as highway embankment material (Bosscher et al., 1997), asphalt pavement material (Eleazer and Barlaz, 1992; Liang and Lee, 1996), lightweight fill material (Ahmed and Lovell, 1993; Masad et al., 1996; Lee et al., 1999), backfill material for retaining walls (Humphrey and Manion, 1992; Humphrey et al., 1993; Garga and O'shaughnessy, 2000) and subsurface drainage systems (Bressette, 1984).

Sand-rubber mixtures exhibit significant compressibility, low void ratio, and low friction angle (Humphrey et al., 1993; Edil and Bosscher, 1994; Foose et al., 1996; Masad et al., 1996; Wu et al., 1997; Gebhardt, 1997; Feng and Sutter, 2000; Yang et al., 2002). Additionally, the damping ratio of rubber particle specimens increases slightly with

confining stress probably because of enlarged rubber particle contacts (Zheng-Yi and Sutter, 2000).

6.1.1 Related Prior Research

The mass density of granular mixtures depends on the specific gravity of each component, their grain size distribution, and particle shapes. Related observations from previous studies show that (Youd, 1973; Guyon et al, 1987; German, 1989).

- Mixing two-size particles yields a system of lower porosity. The minimum porosity is reached for a volume fraction of small particles, usually around 30~40%.
- Lower mixture porosity and higher density are obtained with larger particle size ratios.
- The void ratio decreases with the increase in the coefficient of uniformity.
- The minimum and maximum void ratio increase as particles become more angular.

Therefore, if the composite consists of a mixture of two or more mono-sized spherical particles, the porosity of mixtures is dominated by the volume fraction of each particle and the particle size ratio.

Segregation is an inherent difficulty in granular mixtures. Segregation is triggered by differences in size, density, shape, stiffness, and roughness (Santamarina et al., 2001).

6.2 EXPERIMENTAL STUDY - MATERIALS AND DEVICES

Ottawa 50/70 sand and granulated rubber are the materials used in this study. Figure 6.1 shows the particle size distribution and a photograph of each material (sand particles: D_{50}=0.35mm, G_s=2.65; rubber particles: D_{50}=3.5mm, G_s=1.14). Note that rubber particles are angular while Ottawa sand particles are subrounded. Mixtures are prepared with volume fractions V_{rubber}=0.0, 0.1, 0.2. 0.3, 0.4, 0.5, 0.6, 0.7, and 1.0. Rubber particles are ten times larger than sand particles, and homogeneous mixtures cannot be attained for V_{rubber}=0.8 or 0.9. The selected rubber and sand particles show significant differences in particle size, shape, and specific gravity (Figure 6.1). Therefore, special precautions are implemented to prevent segregation; in particular, mixtures are not allowed to flow and are not vibrated.

Rubber-sand mixtures are tested in a modified oedometer cell that has simultaneous shear wave velocity measurement capacity using bender elements mounted on the top cap and the bottom plate of the cell. All shear wave signals are captured with a digital oscilloscope and recorded in a personal computer. Figure 6.2 shows details of the modified oedometer cell and peripheral electronics.

The general test procedure follows that of the conventional consolidation test. Vertical stress stages are: 10kPa, 19kPa, 36kPa, 70kPa, 140kPa, 278kPa, 556kPa, 833kPa and 1111kPa, followed by the reverse sequence of stages during unloading. Some mixtures show significant creep deformation as a result of the viscous deformation of rubber particles.

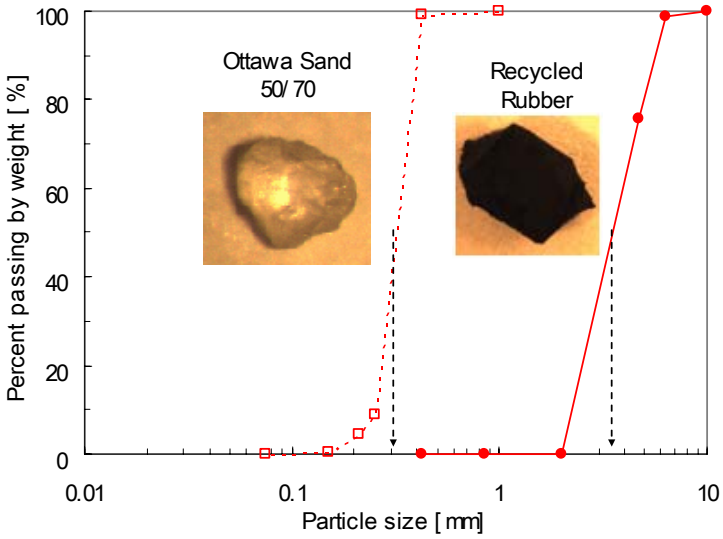

Figure 6.1 Particle size distribution and photographs of Ottawa 50/70 sand and recycled rubber particles.

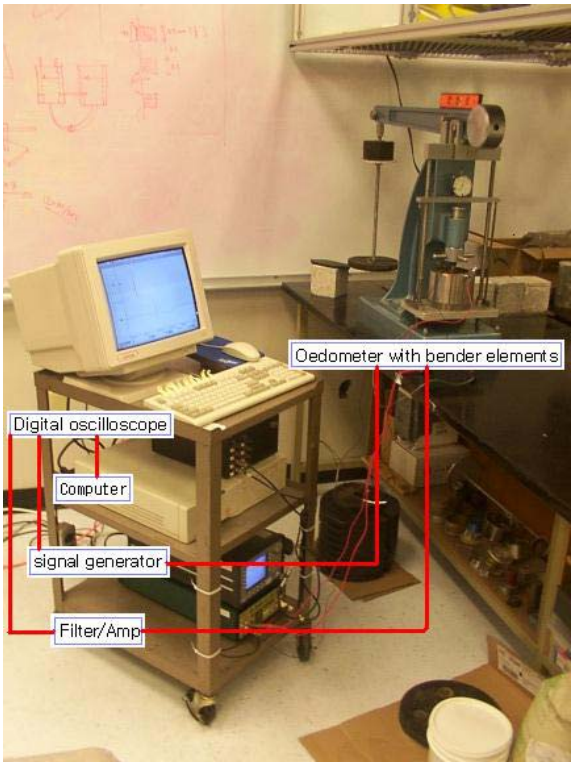

(a)

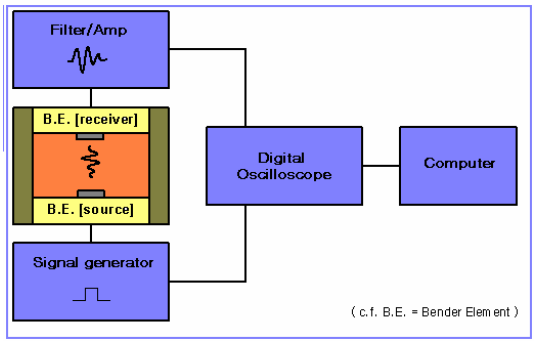

(b)

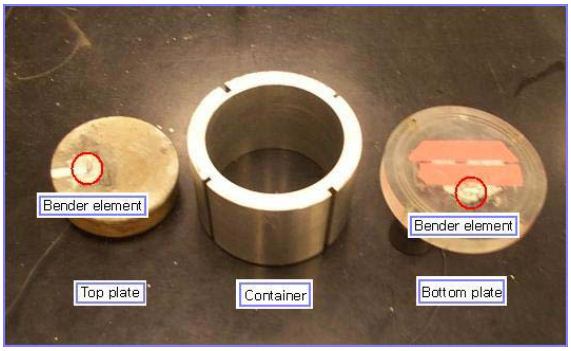

(c)

Figure 6.2 Experimental setup to measure the large strain and the small strain modulus of sand-rubber mixtures. (a) Testing device organization. (b) Schematic diagram of testing setup. (c) Engineering design of the modified oedometer cell.

Thus, the final deformation at each loading step is measured when the strain increment is negligible.

The shear wave is generated by applying a 10V step signal to the bender element in the bottom plate. Received signals are sampled at 500kHz. Stored signals are obtained by stacking 100 digital signals to increase the signal-to-noise ratio.

6.3 EXPERIMENTAL RESULTS

Mixture mass densities, intermediate strain load-displacement response and small-strain wave velocity for the sand-rubber mixtures are documented in this section.

6.3.1 Mass Density

Figures 6.3a & b show measured porosity and mass density versus the volume fraction of the large rubber particles. Values are shown at σ_v'=10kPa and 1111kPa. The analytical estimation shown in the figure is derived under the following assumptions:

- Voids between the large rubber particles are large enough to allow the random packing of small sand particles.
- Rubber packs with a void ratio e_{rubber}=0.9 due to the angular particle shape, while sand packs with a void ratio e_{sand}=0.7. These values are experimentally obtained.

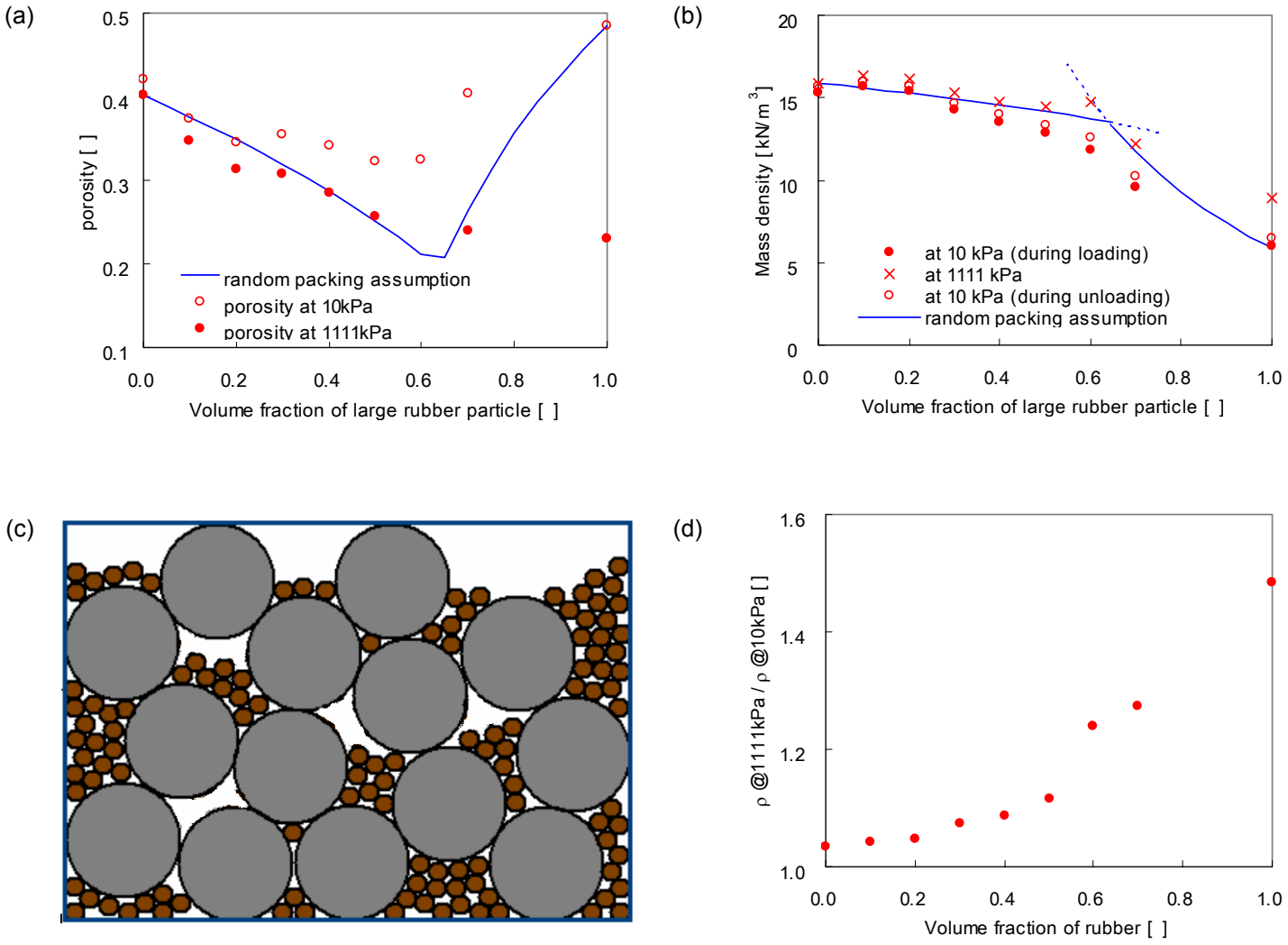

Figure 6.3 Packing of binary mixtures of different size particles. (a) Porosity of binary mixtures (b) Measured mass density of mixtures with respect to volume fraction of rubber particles and analytical expectation of the mass density. (c) Improper packing of binary particles due to differences in particle sizes (volume fraction of small particles: 20%, radii ratio: 6). (d) Ratios of mass density at σ_v'=1100kPa and σ_v'=10kPa versus volume fraction of rubber.

- Homogeneous mixtures cannot be made when $0.7<V_{rubber}<1.0$ because the volume of voids between large particles is too large and paticles fall by gravity within the porous network (Figure 6.3c).
- The effects of rubber particle deformation are not considered when calculating global void ratios.

Figure 6.3d shows the ratio between the densities measured at σ_v'=1111kPa and σ_v'=10kPa versus the volume fraction of rubber particles. The ratio increases significantly when the rubber volume fraction exceeds $V_{rubber}>0.5$ because rubber particles control the deformation of such mixtures.

6.3.2 Intermediate-Strain Compressibility and Swell

Figure 6.4 shows the stress-void ratio response for all mixtures. Figure 6.5 shows the evolution of the constraint modulus during loading for the V_{rubber}=0.1 mixture. The trend can be fit with a power function of the applied vertical stress

$$M = M_1 \cdot \left(\frac{\sigma_v}{1kPa} \right)^m \tag{6.1}$$

where M_1 is the constraint modulus at σ_v'=1kPa, and m captures the stress sensitivity of each mixture.

Figure 6.6b displays M_1 versus volume fraction of rubber. When $V_{rubber} \leq 0.2$, the mixture supports the load mainly through the sand skeleton.

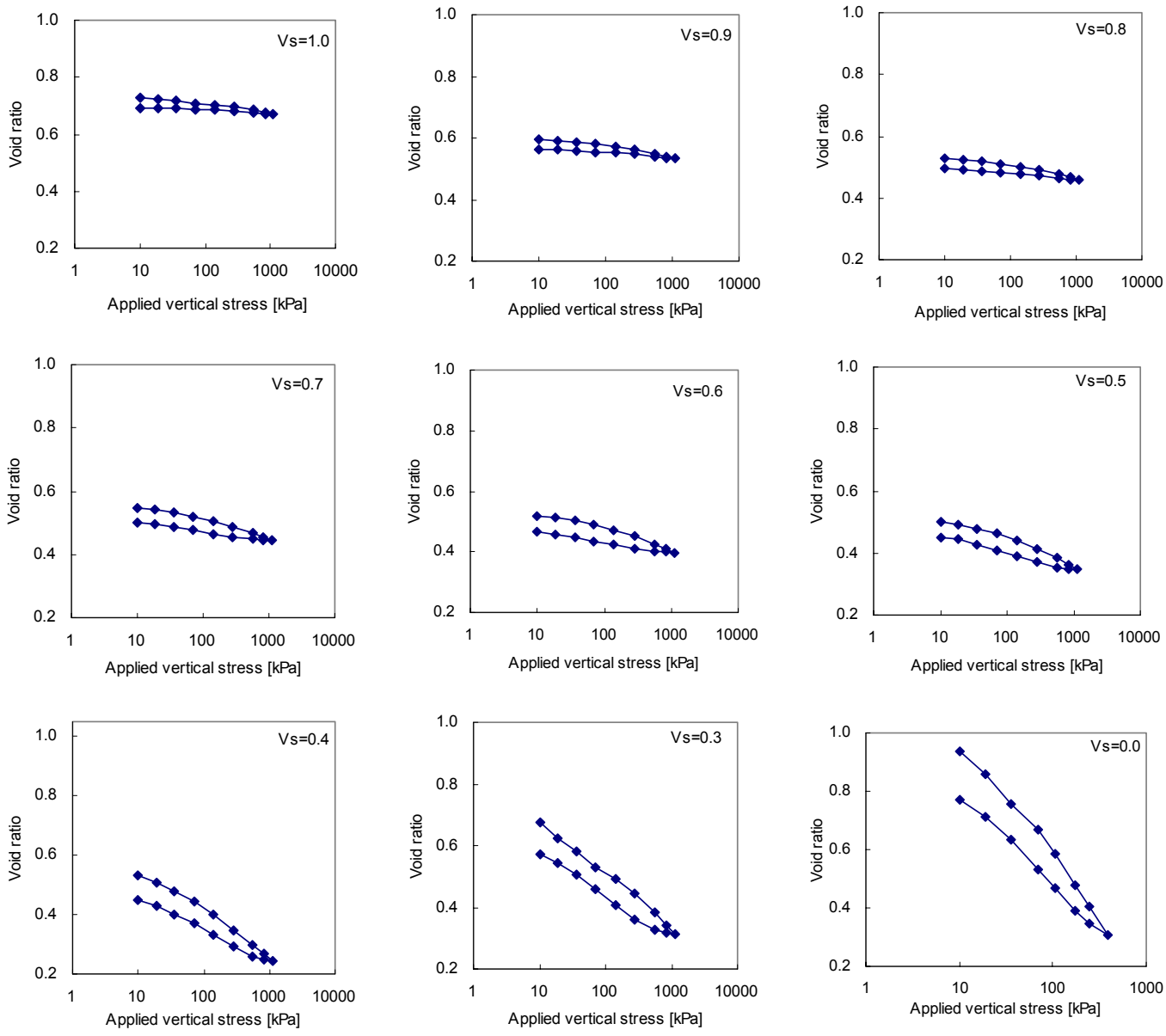

Figure 6.4 Load-displacement response for different sand-rubber mixtures: Loading and unloading sequences. V_s is the volume fraction of sand.

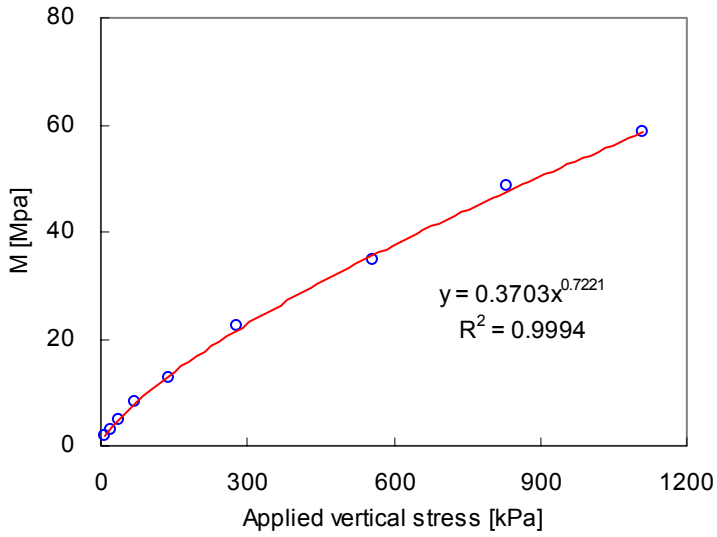

Figure 6.5 Constraint modulus evolution of a sand-rubber mixture during loading (V_{sand}=0.9).

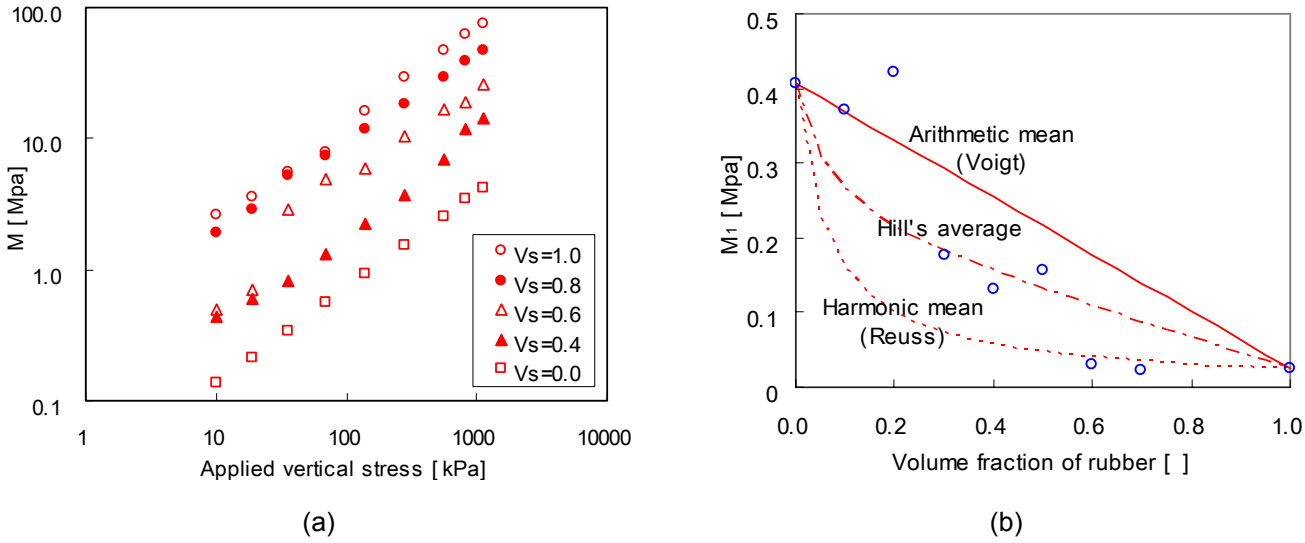

Figure 6.6 Constraint modulus in sand-rubber mixtures. (a) Constraint modulus vs. stress. (b) Constraint modulus number at 1kPa M_1 vs. volume fraction of rubber.

The global loss of sand particle contacts due to the presence of rubber particles gradually reduces the effective stiffness of mixture as the volume fraction of rubber particles increases.

Mixtures $0.3 \leq V_{rubber} \leq 0.5$ show a load-deformation behavior intermediate between rubber-dominant and sand-dominant; therefore, the effective constraint modulus can be estimated from Hill's average (the average of arithmetic mean and harmonic mean) in this mixture range. However, when $V_{rubber} \geq 0.6$, most of the applied load is transferred through rubber-to-rubber contacts, and the effective constraint modulus M_1 follows the Ruess lower bound (i.e., harmonic mean), which is very close to the Hashin-Strinkman lower bound.

Compressibility and swelling indices C_c and C_s are also calculated from e-logσ' trends (Figure 6.7). The values of C_c increase as the volume fraction of rubber increases. However, C_s shows the peak value at about 100kPa. When a vertical stress exceeds σ_v'>700kPa, the swelling index becomes little sensitive to the rubber volume fraction. The underlying mechanisms for these phenomena are not clear. Wall friction and stick-slip behavior are anticipated.

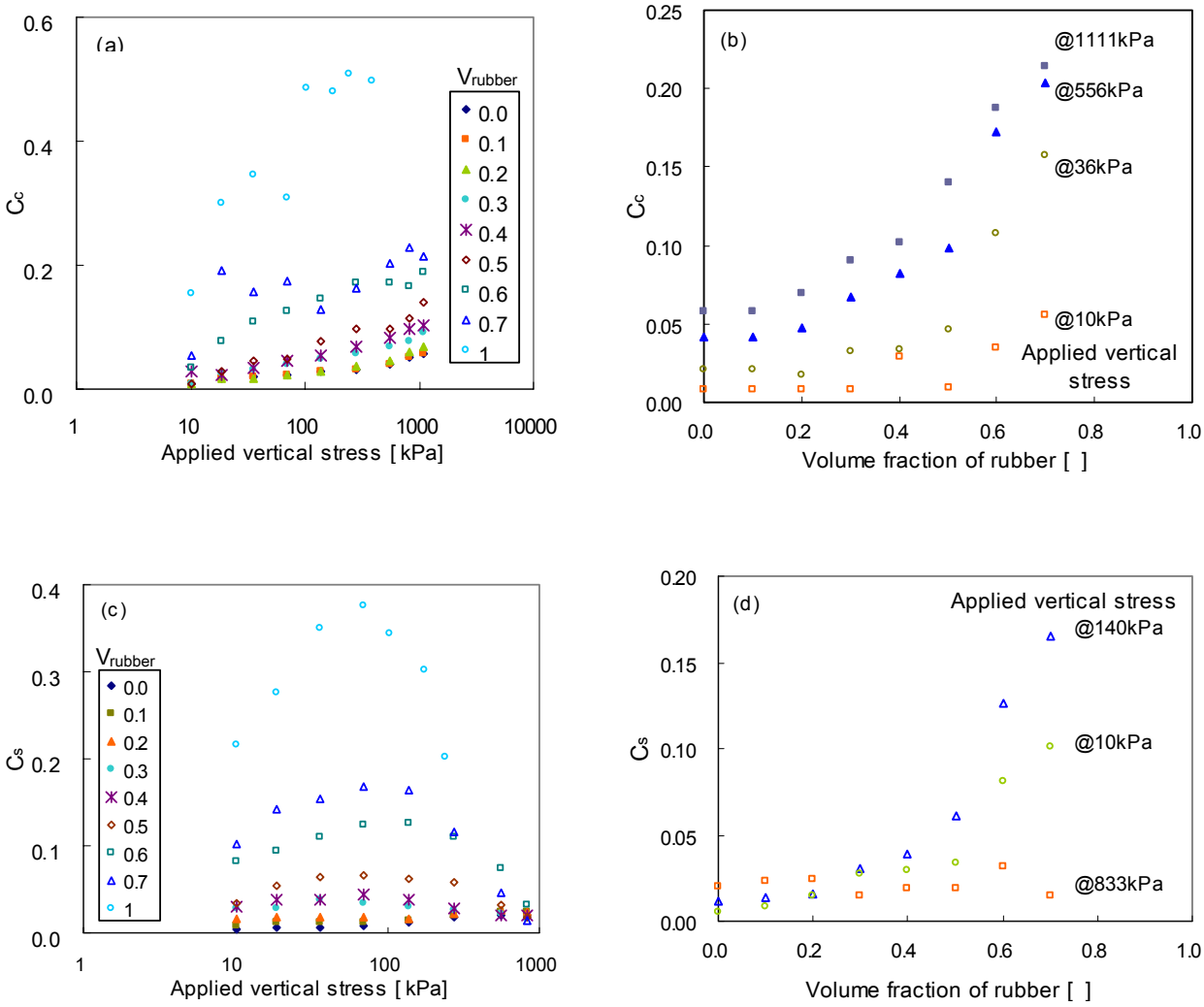

Figure 6.7 Compressibility index and swelling index of rubber-sand mixtures. (a) Compressibility index (b) Compressibility index versus volume fraction of rubber. (c) Swelling index. (d) Swelling index versus volume fraction of rubber.

6.3.3 Small-Strain Elastic Modulus

Shear wave signals for the V_{rubber}=0.3 specimen are shown in Figure 6.8 at the end of all loading stages. Figure 6.9a shows the evolution in shear-wave velocity with the applied vertical stress. Contrary to the constraint modulus, the shear wave velocity does not increase monotonically with the volume fraction of sand. Instead, the maximum shear wave velocity is observed in the V_{rubber}=0.2 mixture. The shear wave velocity decreases significantly when the rubber volume fraction $V_{rubber} \geq 0.3$.

The small-strain shear modulus G_{max} can be obtained from the measured shear wave velocities and corresponding mass densities (Note: G_{max} is more important than V_s for comparing mixtures with very different mass densities).

$$G_{\max} = \rho \cdot V_s^2 \tag{6.5}$$

The value of G_{max} can be expressed as a power function of mean effective stress σ_0' (Hardin and Black, 1968; Hardin and Drnevich, 1972; Saxena et al., 1988):

$$G_{\max} = A \cdot f(e) \cdot \left(\frac{\sigma_0'}{1kPa} \right)^{\beta^*} = A \cdot f(e) \cdot \left(\frac{1+K_0}{2} \right)^{\beta^*} \cdot \left(\frac{\sigma_v'}{1kPa} \right)^{\beta^*} = \alpha^* \left(\frac{\sigma_v'}{1kPa} \right)^{\beta^*} \tag{6.6}$$

where A and β^* are constants, and $f(e)$ is the function of void ratio. The factor $\alpha^* = A \cdot f(e) \cdot \left(\frac{1+K_0}{2} \right)^b$ is the reference shear modulus at 1kPa.

The value of α^* decreases with the increase in rubber volume fraction for V_{rubber}>0.3 in Figures 6.9c & d. This suggests that soft rubber particles promote effective stress focusing in the sand, causing an increase in local stiffness that overwhelms traveltime delays due to the torturous travel path. As the rubber volume fraction increases

above V_{rubber}>0.4, α^* decreases dramatically because rubber-to-rubber contacts dominate the global mixture stiffness.

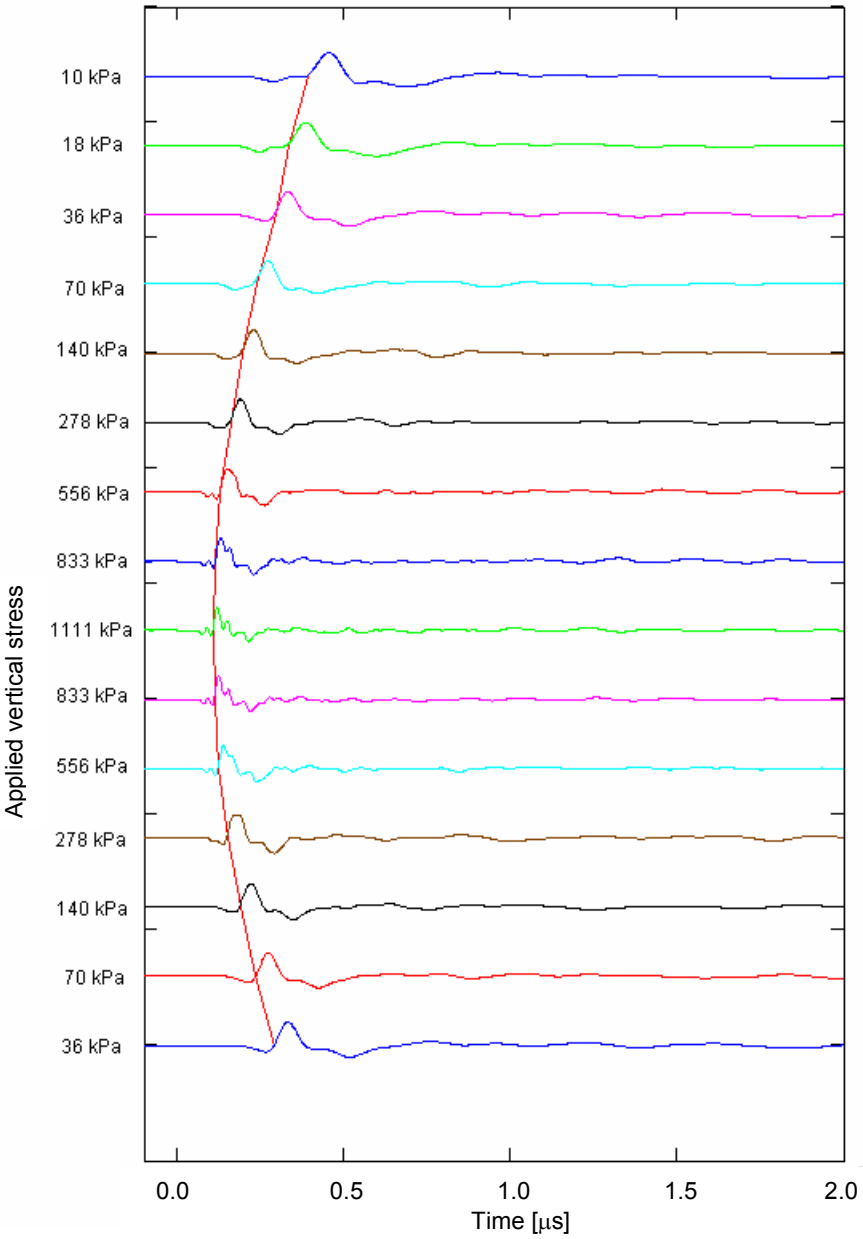

Figure 6.8 Received signals during K_0 loading and unloading (V_{rubber}=0.3).

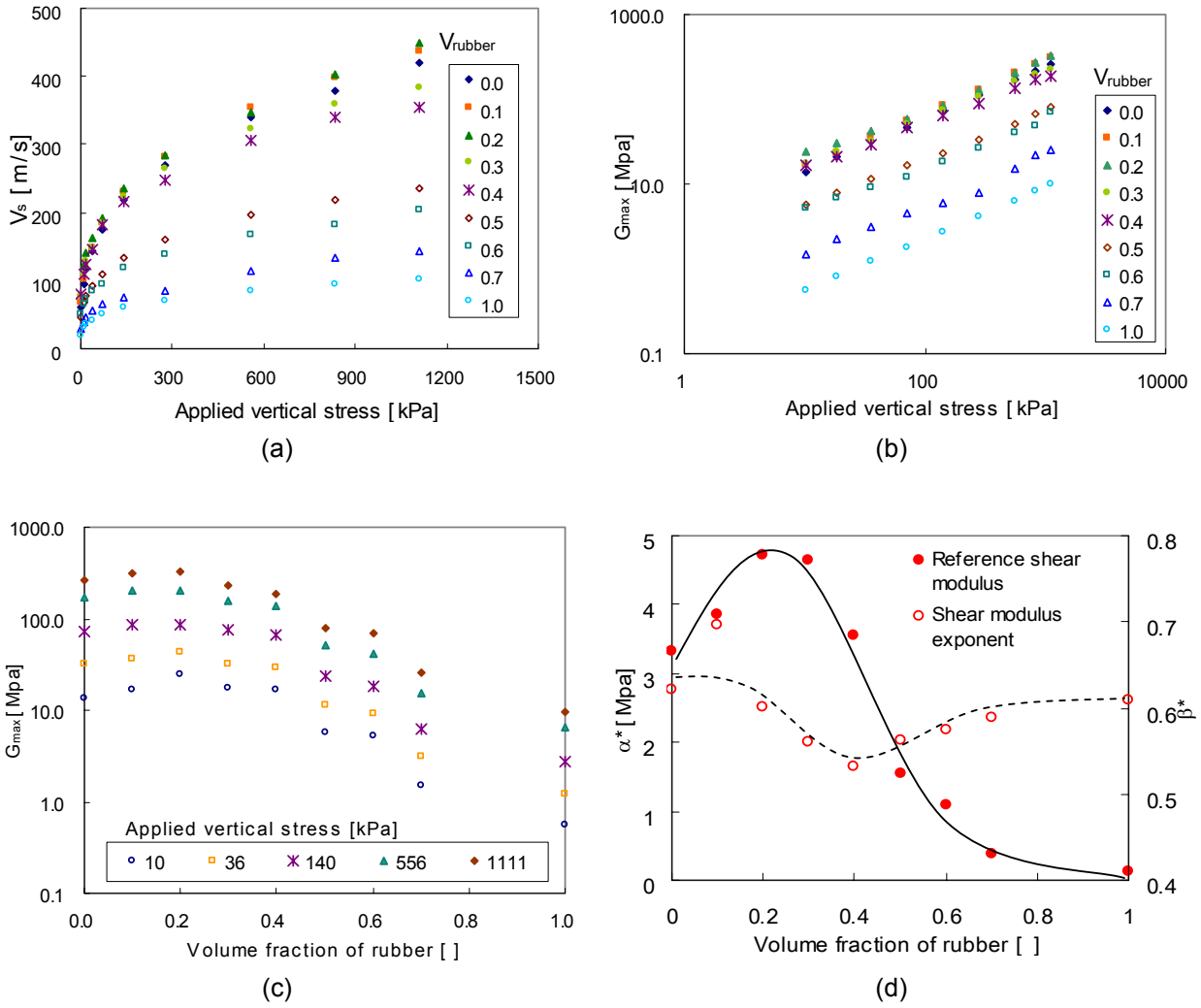

Figure 6.9 Shear wave velocity measurements in sand-rubber mixtures. (a) Shear wave velocity vs. applied vertical stress. (b) G_{max} vs. applied vertical stress. (c) G_{max} vs. volume fraction of rubber. (d) Reference shear modulus α^* exponent β^* and vs. volume fraction of rubber

6.4 NUMERICAL MODELING OF SAND-RUBBER MIXTURES

The experimentally observed nonlinear response of sand-rubber mixtures is further studied through numerical simulations. Because rubber particles are much larger than sand particles, sand is modeled as an equivalent non-linear continuum with rubber particles as soft inclusions.

6.4.1 Mixtures of Linear-Elastic Materials - Quasi-Static Loading

Numerical finite element simulations are conducted to estimate the mechanical behavior of two-phase linear elastic mixtures. The 100x 100 element mesh represents a plane-strain slice of a square body (four-node plane strain elements). Each element is randomly assigned as either a stiff material (E=1000kPa, ν=0.30) or a soft material (E=10kPa, ν=0.49) to satisfy preselected volume fractions.

The test simulation involves zero lateral displacement, and rigid cap and bottom plates. A 100kPa vertical stress is applied at the top. Figure 6.10 shows the captured effective constraint modulus with respect to the volume fraction of the soft material V_{soft}. The effective constraint modulus is close to the Hashin-Strinkman's upper bound when $V_{soft} \leq 0.3$, but it approaches the Hashin-Strinkman's lower bound or the harmonic mean when $V_{soft} > 0.7$. Mixtures $0.4 \leq V_{soft} \leq 0.6$ exhibit transitional mechanical behavior between the two bounds. Hashin-Strinkman's upper bound assumes that the stiff material wraps around the soft material; therefore, the stiff material properties are more important to assess the global mechanical behavior. The opposite is true for the lower bound.

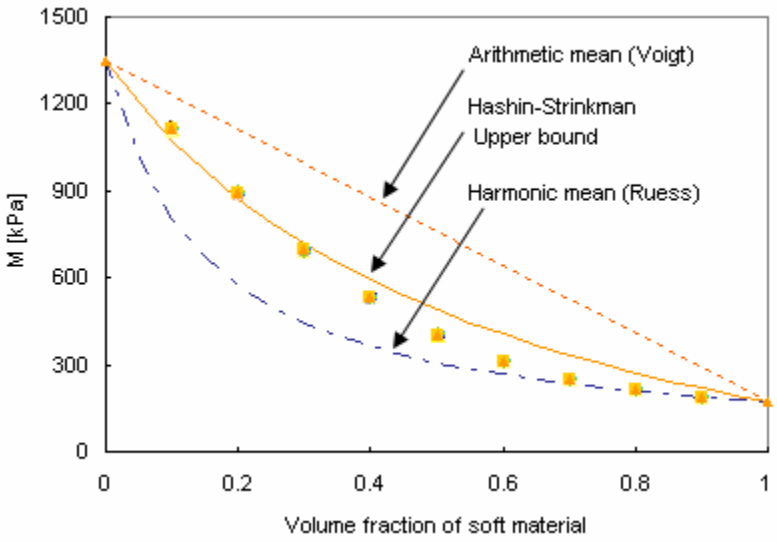

Figure 6.10 Effective constraint modulus of linear elastic two-phase material (numerical). Random mixture of soft and stiff materials.

6.4.2 Nonlinear Sand with Linear Elastic Rubber – Quasi-Static Loading

In this simulation, sand is modeled as a hypoelastic material by fitting the experimentally measured evolution of the constraint modulus in the oedometer cell (Figure 6.11). On the other hand, rubber is modeled as an isotropic linear elastic material (E=1020kPa, ν=0.49; see Table 6.1).

Table 6.1 Typical values of the elastic constants for various homogenous isotropic materials. (Walter and Clark, 1980)

Material	Young's modulus [kPa]	Shear modulus [kPa]	Bulk modulus [kPa]	Poisson's ratio
Steel	19.7×10^7	7.5×10^7	16×10^7	0.30
Glass	5.9×10^7	2.4×10^7	3.7×10^7	0.23
Lead	1.6×10^7	0.5×10^7	0.7×10^7	0.43
Epoxy	0.3×10^7	0.1×10^7	0.3×10^7	0.35
Rubber (nonreinforced)	1020	340	0.2×10^7	~ 0.50

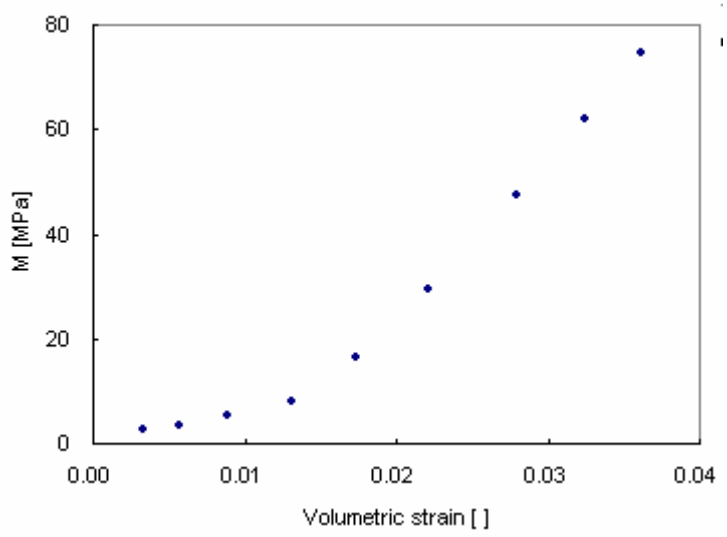

Figure 6.11 Constraint modulus of sand (V_{rubber}=0.0) vs. volumetric strain. Data used simulate the sand behavior in mixtures under K_0 loading.

A 100x 100, four-node plane-strain element mesh is used to study the deformation of a single cylindrical rubber particle in a sand-host medium subjected to vertical loading under zero-lateral strain conditions (Figure 6.12a).

Two interaction effects are observed. First, the soft rubber inclusion promotes vertical and horizontal stress concentration on the equatorial plane around the inclusion, and there is a corresponding stiffness increase in the sand (Figure 6.12b and c). Second, the soft rubber inclusion reduces the effective global stiffness. In fact, the larger the inclusion (V_{rubber}), the lower the effective constraint modulus (Figure 6.13). Figure 6.14 shows experimental and numerical e-log σ' results for different mixtures. Note that the numerical simulation presumes no rubber-to-rubber interaction; clearly, this assumption looses validity when $V_{rubber} \geq 0.3$.

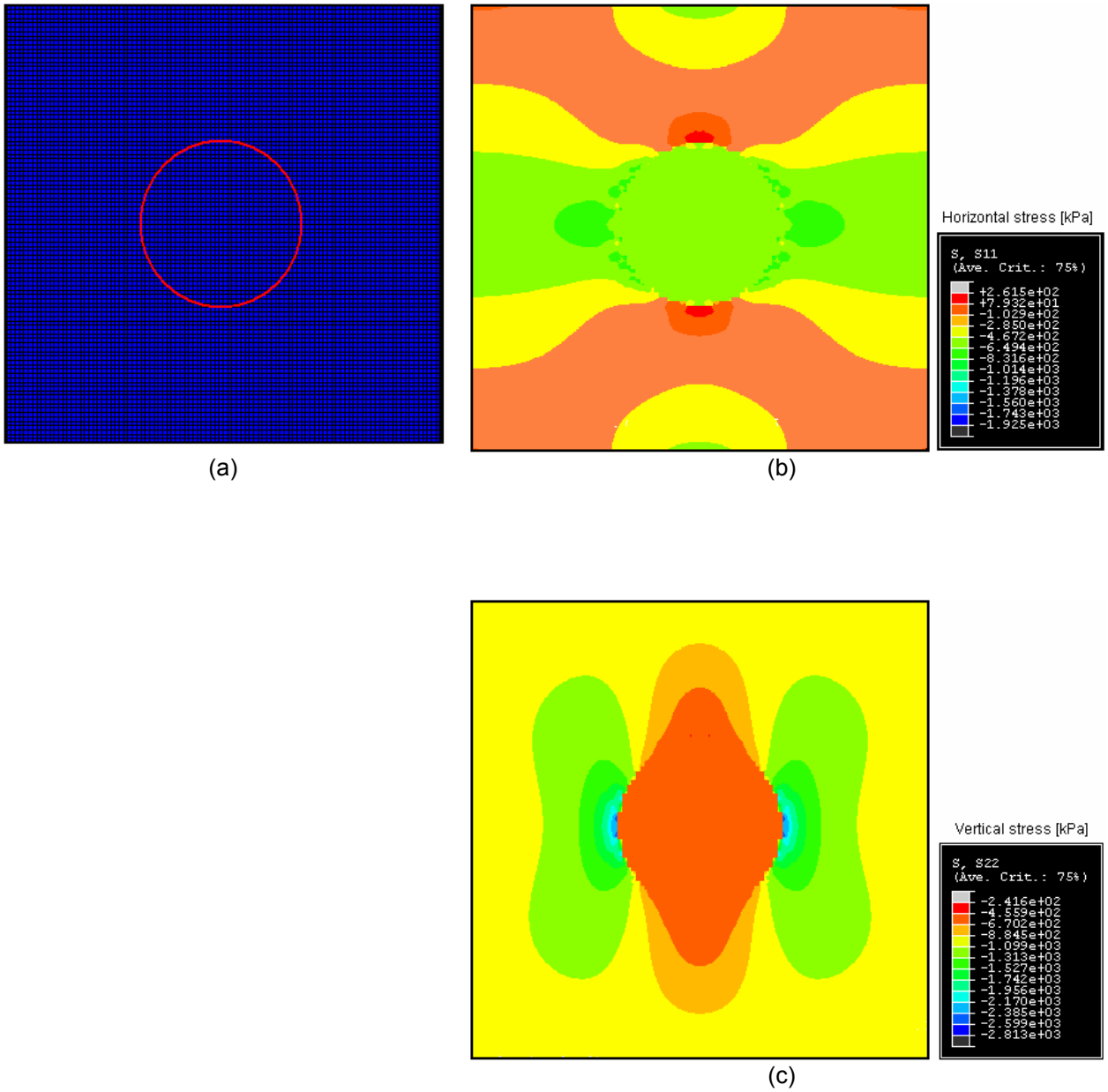

(a) (b) (c)

Figure 6.12 Nonlinear numerical simulation of sand with soft rubber inclusion. Stress field under K_0 loading condition. (a) Finite element mesh (b) Horizontal effective stress distribution for an applied 1000kPa vertical laod. (c) Vertical effective stress distribution for an applied 1000kPa vertical load.

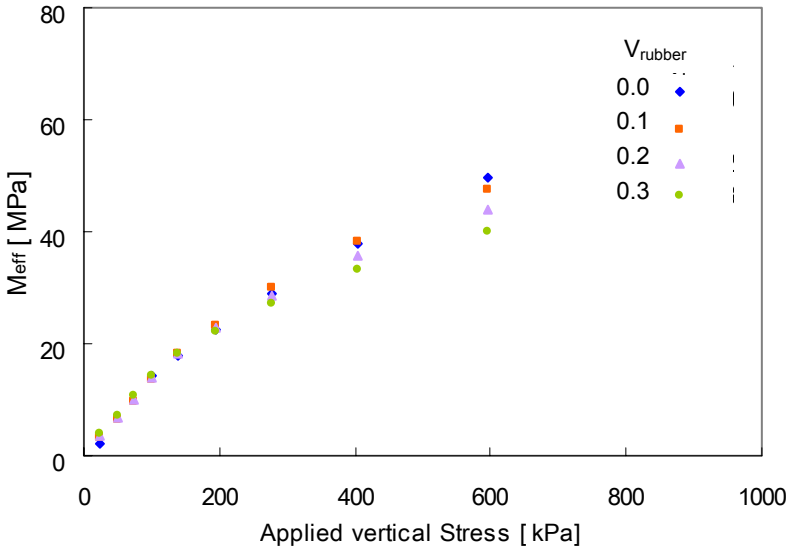

Figure 6.13 Numerical expectation of effective constraint modulus in mixtures for different applied vertical loads.

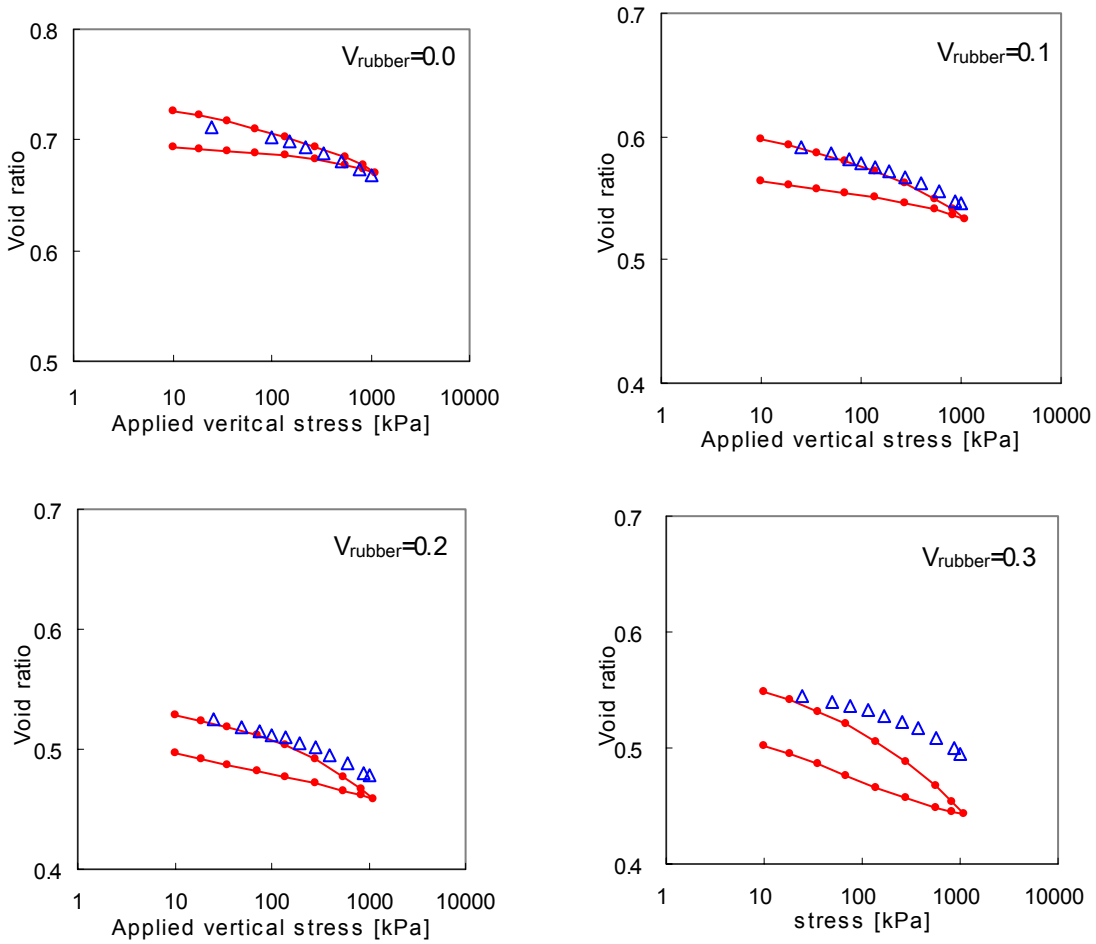

Figure 6.14 Load and displacement response comparison. Nonlinear numerical simulation results and experimental results (mixtures with small volume fraction of rubber): • experimental data; Δ numerical simulation.

6.4.4 Shear Wave Propagation in Mixtures

Experimental results show that shear waves propagate faster in mixtures with small volume fraction of soft rubber particles than in the pure sand (Figure 6.9). Numerical simulations are conducted to identify the underlying causal mechanisms. The simulated medium is described in Figure 6.15a. A single cylindrical rubber particle is located at the center of the host sand medium, and a plane shear wave is initiated from the top of the mesh. The size of the rubber particles is simulated to represent V_{rubber}=0.1 and V_{rubber}=0.2. Wave propagation data are gathered for a host medium without an inclusion (Figure 6.15b), a homogenous host medium with a soft inclusion (Figure 6.15c), and a host medium with an inclusion, including stress-induced elastic properties (Figure 6.15d) where the local values of the small-strain modulus are calculated from the previous static loading simulations with the nonlinear material model (Figures 6.12, 6.13, and 6.14).

Figure 6.16 shows time series at different locations for the V_{rubber}=0.1 case. Traveltimes where stress concentration effects are taken into consideration are clearly shorter than traveltimes without local effects, and even shorter than in the homogeneous sand without a soft inclusion. Figure 6.17 shows a summary of traveltimes for the different cases.

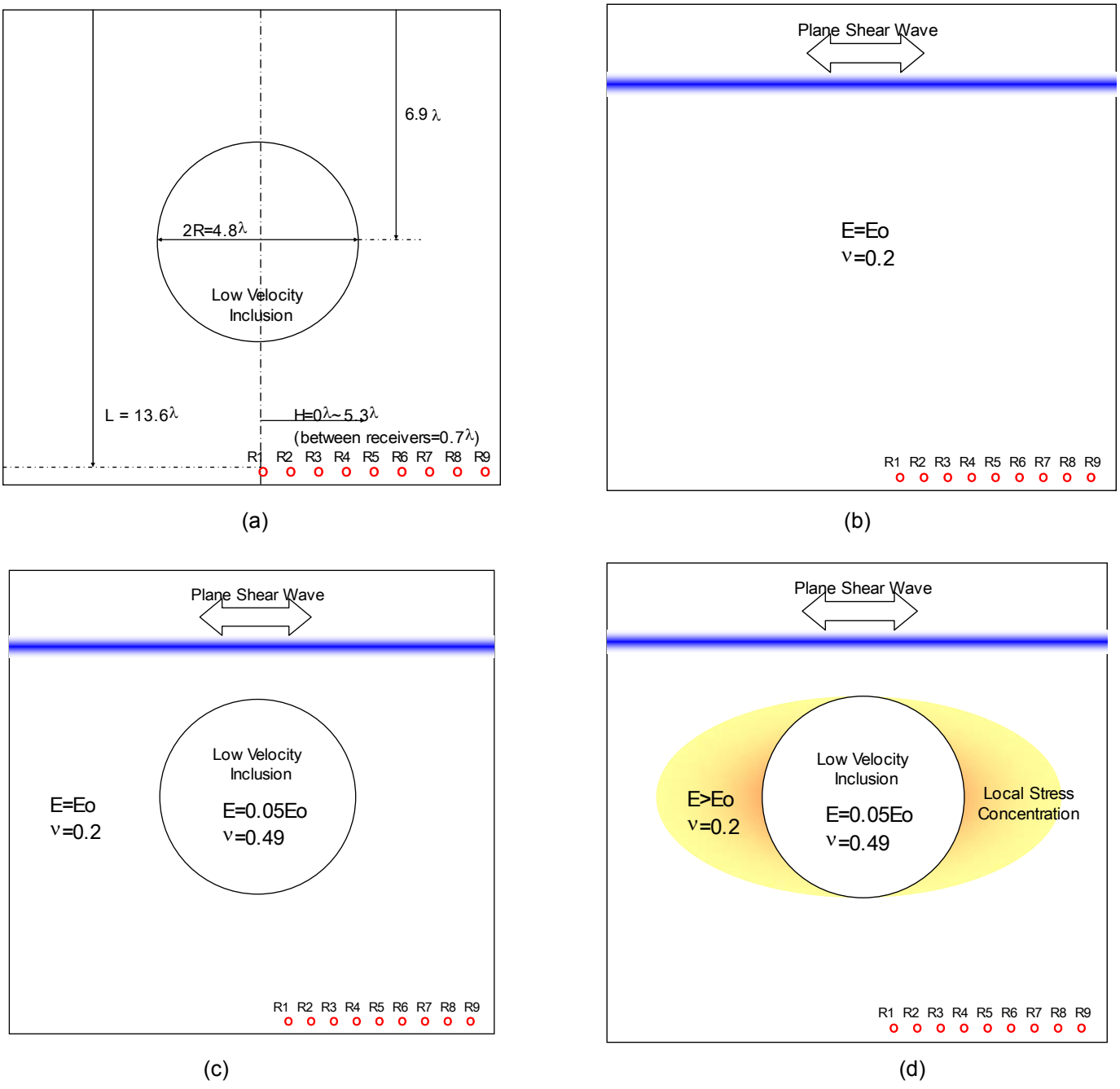

Figure 6.15 Numerical simulation of shear wave propagation in sand-rubber mixture. (a) Homogeneous medium without inclusion, (b) Homogeneous medium with low S-wave velocity inclusion, (c) Medium with low S-wave velocity inclusion and local stress concentration

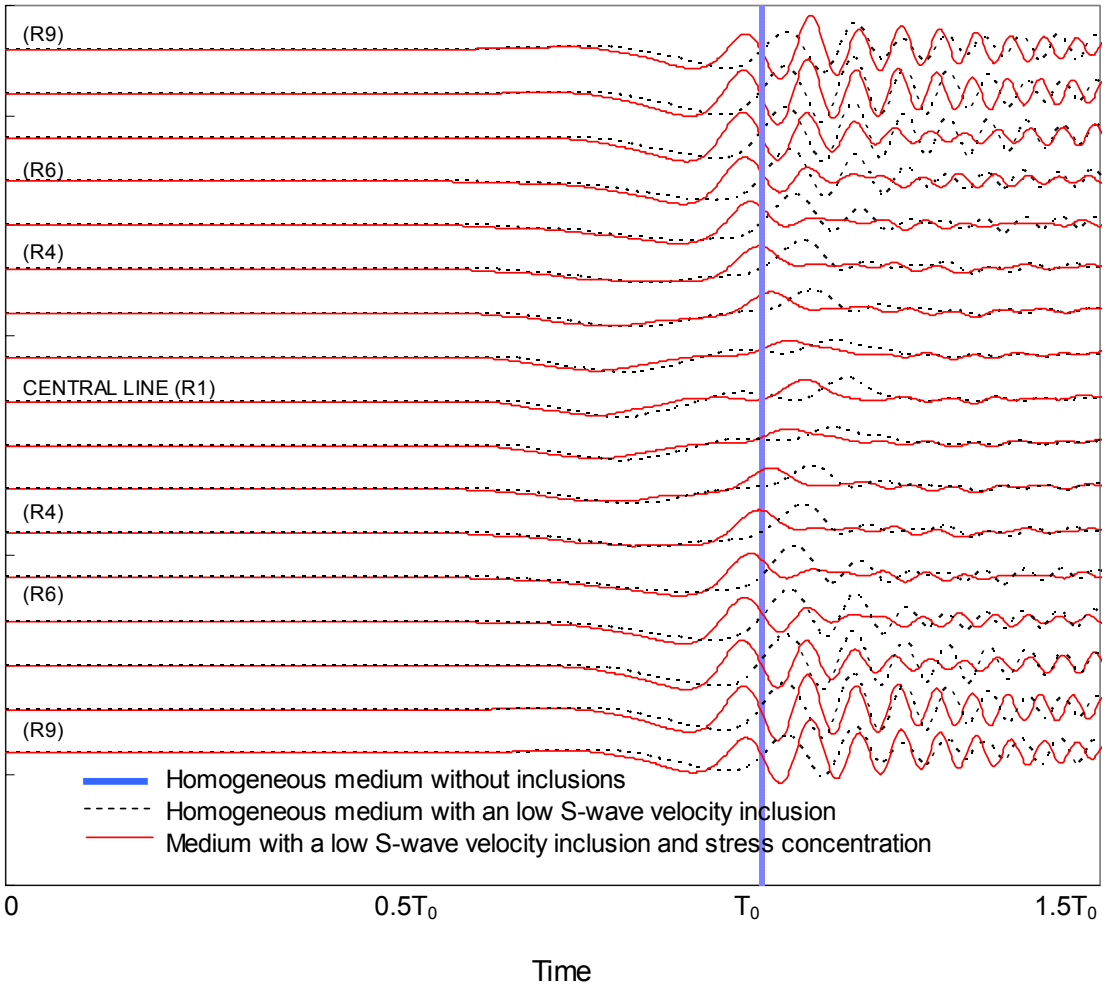

Figure 6.16 Time-series at different locations (Refer to Figure 6.15 – V_{rubber}=0.1)

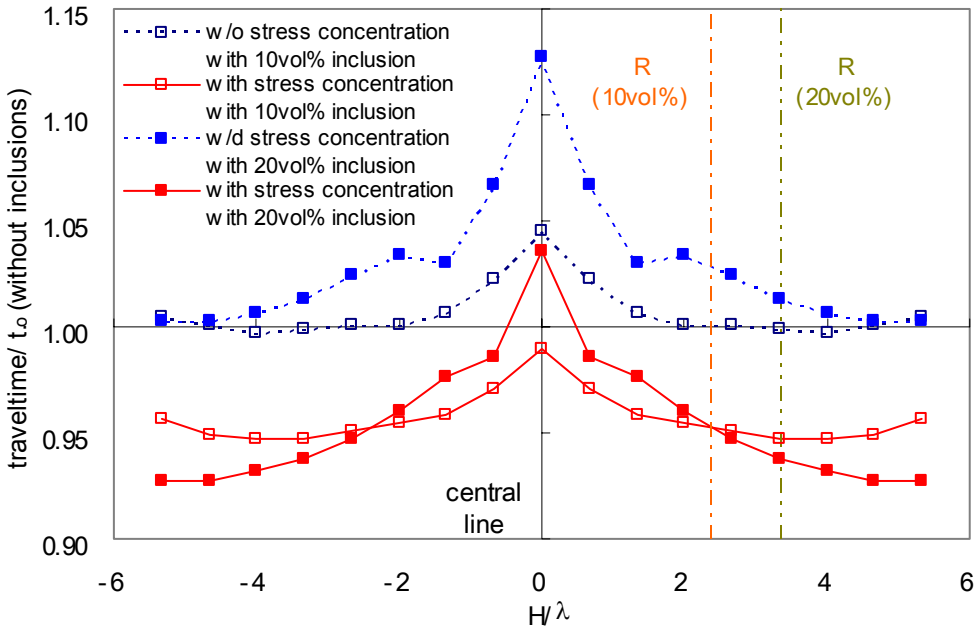

Figure 6.17 Summary of traveltimes (Refer to Figures 6.15 and 6.16). All spatial scales are normalized by the propagating wavelength, λ.

6.5 DISCUSSION

The significant difference in the particle size between rubber and sand ($D_{rubber}/D_{sand} \approx 10$) causes the following mechanisms that affect the mechanical behavior of sand-rubber mixtures when $D_{rubber} \gg D_{sand}$:

- Vertical loads arch around soft particles and increase the vertical stress in the sand (Figure 6.18).
- Incompressibility of rubber particles (ν~0.5). Once rubber particles deform and fill voids against sand particles, further vertical deformation must be accompanied by horizontal expansion into the sand. This produces an increase in local horizontal stress.
- Soft particle interaction. The decrease in global stiffness prevails when soft particles interact at high V_{soft}, This interaction overwhelms the local stiffness due to arching in the sand and lateral rubber expansion.

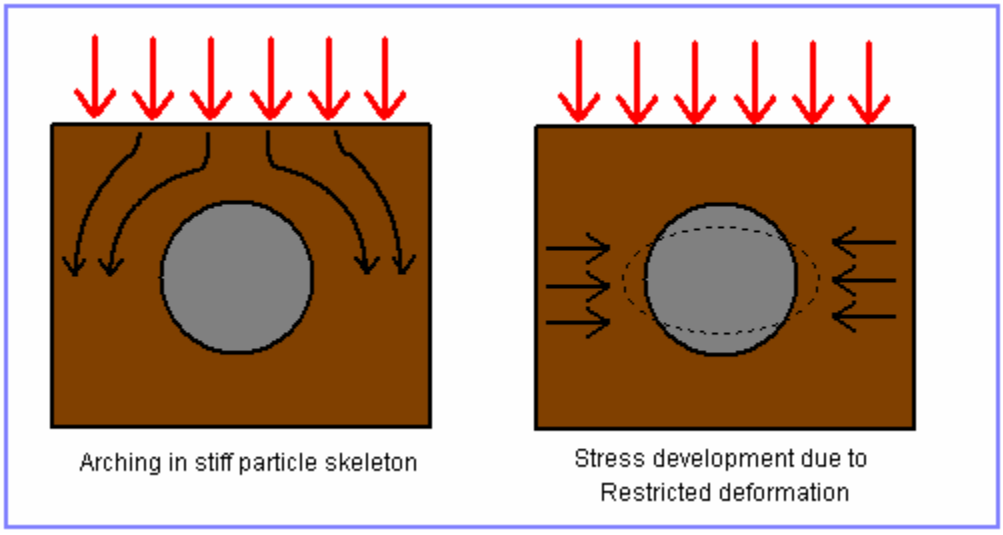

Figure 6.18 Mean stress increase due to arching around a soft inclusion and lateral expansion of an incompressible inclusion.

The wavelength λ of propagating perturbations must be considered in the analysis. In general, $\lambda \gg D$ (where D is particle size) implies equivalent continuum propagation while $\lambda \approx D$ must be analyzed as heterogeneous and ballistic propagation. Figure 6.19 shows the ratio of the propagating wavelength λ and D_{50} of rubber particles obtained from experimental results (wavelengths are calculated with the representative frequencies of the arriving front and the measured velocities). The wavelength seems to decrease with the increase in the applied stress σ_v', and it increases with the increase in the volume fraction of rubber V_{rubber}. Apparently, the interconnected rubber particles act as a low-pass filter (Brillouin effect).

As λ approaches the inter rubber-particle spacing, the traveling path becomes torturous, yet the increase in local stiffness by mean stress concentration ($\sigma_v'+\sigma_h'$) results in faster propagation in mixtures $V_{rubber} \approx 0.2$ than in pure sand. Eventually, ballistic propagation, scattering and global softening prevail as V_{rubber} increases further.

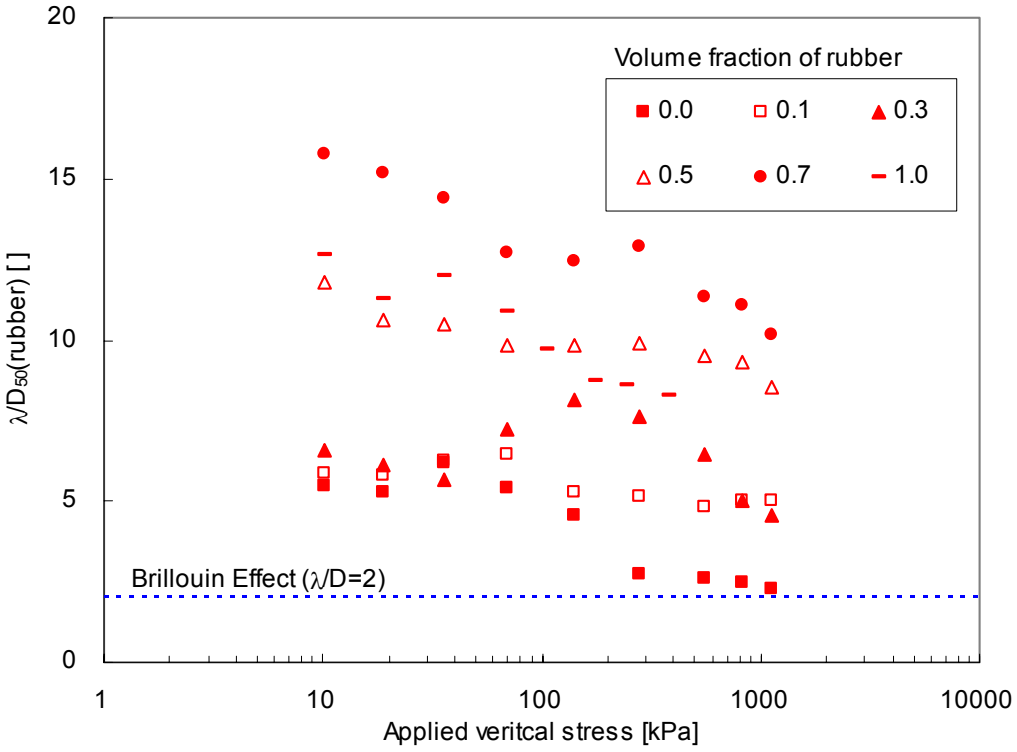

Figure 6.19 Wavelength of received shear waves normalized by the diameter of large rubber particles vs. applied vertical stress.

6.6 SUMMARY AND CONCLUSIONS

The mechanical behavior of granular mixtures made of stiffness-small grains and soft-large grains is studied as an engineering application of heterogeneous granular materials. Experimental and numerical results show:

- High contrast in particle size of binary granular mixtures (D_{large}/D_{small}~10) causes unavoidable segregation in mixtures V_{large}>0.7.
- The interaction among rubber particles dominates the global mechanical behavior when the volume fraction $V_{rubber} \geq 0.4$.
- The simple geometry of a single rubber particle in a host sand medium can simulate the small and intermediate strain behavior of sand-rubber mixtures V_{rubber}<0.3.
- Short wavelength propagation ($\lambda/D_{rubber} \approx 2$~10) shows higher propagation velocity in mixtures $0<V_{soft}<0.2$ than in pure sand ($V_{soft}=0$). This phenomenon is the result of high mean-stress development at the equatorial plane of soft particles. Soil arching (vertical stress increase) and incompressible rubber deformation (horizontal stress increase) contribute to this effect.
- Faster shear wave velocity does not necessarily imply the higher quasi-static small strain shear modulus in highly heterogeneous media.

CHAPTER VII

CONCLUSIONS

This research addressed the effect of spatial variability on the stiffness and strength of soils, identified new emergent phenomena, and provided the foundation to develop adequate guidelines for geotechnical design that takes into consideration spatial variability. The research methodology is based on Monte Carlo generation of realistic correlated random fields, simple yet robust constitutive models, and both linear and non-linear finite element simulations. The main conclusions are presented separately for each study.

Spatial variability and correlated random fields. The spatial variability in soil properties can be captured through three main statistical parameters: the actual trend, the deviation from the trend, and the correlation length. Realistic fields for geotechnical parameters can be generated using the matrix decomposition technique.

Stiffness in spatially varying media. The local stiffness variability affects internal processes and the external, global mechanical response. In particular:

- Load transfer in isotropic or K_0 loading concentrates along stiffer zones, leading to "stress-focusing". In particular, the stress field in cylindrical non-homogeneous specimen tends to decrease toward the center under isotropic loading.
- Stress focusing is enhanced in media with high variability in material stiffness.
- Stress-focusing reduces horizontal load transfer under K_0 loading.

- Stiffness-stress power relations lead to “stress-induced stiffness homogenization”.
- Higher stiffness variability lowers the global stiffness, while a larger relative correlation length results in a wider potential spread in the global constraint modulus.

Strength in spatially varying media. Local strength variability permits the percolation of weakness and conduces to shear strain localization.

- High strength variability and the long relative correlation length lead to both low and variable undrained shear strength.
- Undrained shear failure in heterogeneous media occurs along one or two percolating weak zones.
- The thickness of shear localization zones depends on the spatial correlation of variability.
- Fewer and clearer shear bands are observed in more variable media.
- Drained deviatoric loading causes higher deformation along percolating weak zones. When the whole mass is primarily contractive, it gradually homogenizes as it approaches the critical state.

Elastic wave propagation in spatially varying media. Spatial heterogeneity adds complexity to elastic wave propagation.

- Stress-induced vertical heterogeneity and cross anisotropy are inherent in natural soils. Vertical heterogeneity produces ray bending according to Fermat’s principle. This phenomenon is aggravated by anisotropy.

- Elastic waves traveling though low velocity anomalies experience wave front recovery beyond inclusions. Phenomena involved include “diffraction healing” and mode conversion.
- Velocity heterogeneity inside the Fresnel’s ellipse affects traveltimes and waveforms.
- The statistics of traveltime in correlated random media depend on three spatial scales: travel distance, correlation length, and wavelength.

Sand-Rubber mixtures. Large soft rubber particles buried in a sand host can be used as an “engineered fill”.

- There is high mean stress in the sand around the equatorial plane of soft particles.
- High particle size contrast in granular mixtures promotes low void ratio and high mass density, but can cause segregation.
- Mixtures may exhibit higher shear wave velocity than the host material, yet the quasi-static global stiffness is lower.
- The global stiffness of mixtures decreases dramatically when large rubber particles interact.

APPENDIX A

CROSS ANISOTROPIC LINEAR ELASTIC MATERIAL MODEL WITH SMALL STRAIN ELASTIC PROPERTIES.

1) Stress-induced anisotropy with power functions of elastic wave velocity (Kopperman et al., 1982 – See Santamarina et al., 2001; Yu and Richart, 1984; Santamarina and Cascante, 1996).

$$V_p\left(0^o\right)=\alpha_p\left(\frac{\sigma_v'}{1kPa}\right)^\beta$$

$$V_p\left(90^o\right)=\alpha_p\left(\frac{\sigma_h'}{1kPa}\right)^\beta=\alpha_p\left(\frac{K_0\sigma_v'}{1kPa}\right)^\beta=K_0^\beta\cdot V_p\left(0^o\right)$$

$$V_p\left(45^o\right)=\alpha_p\left(\frac{\sigma_v'+\sigma_h'}{\sqrt{2}kPa}\right)^\beta=\alpha_p\left(\frac{\sigma_v'+K_0\sigma_v'}{\sqrt{2}kPa}\right)^\beta=\left(\frac{1+K_0}{\sqrt{2}}\right)^\beta\cdot V_p\left(0^o\right)$$

$$V_{sh}\left(0^o\right)=V_{sv}\left(0^o\right)=V_{sv}\left(90^o\right)=\alpha_s\left(\frac{\sigma_v'+\sigma_h'}{2kPa}\right)^\beta=\alpha_s\left(\frac{\sigma_v'+K_0\sigma_v'}{2kPa}\right)^\beta=\left(\frac{1+K_0}{2}\right)^\beta\cdot\alpha_s\left(\frac{\sigma_v'}{1kPa}\right)^\beta$$

$$V_{sh}\left(90^o\right)=\alpha_s\left(\frac{\sigma_h'+\sigma_h'}{2kPa}\right)^\beta=\alpha_s\left(\frac{K_0\sigma_v'+K_0\sigma_v'}{2kPa}\right)^\beta=\alpha_s\left(\frac{K_0\sigma_v'}{1kPa}\right)^\beta=\left(\frac{2K_0}{1+K_0}\right)^\beta\cdot V_{sh}\left(0^o\right)$$

In those equations, 0^o is the vertical direction of propagation, and 90^o is the horizontal direction of propagation. Those five parameters are determined by four independent parameters with the assumption of K_0 loading condition and stress-induced small strain elastic properties.

2) Constitutive equation for cross anisotropy linear elastic media (Mavko et al, 1998).

$$\{\sigma\}=[D]\{\varepsilon\}$$

$$\begin{Bmatrix}\sigma_{11}\\ \sigma_{22}\\ \sigma_{33}\\ \sigma_{12}\\ \sigma_{13}\\ \sigma_{23}\end{Bmatrix}=\begin{bmatrix}D_{1111} & D_{1122} & D_{1133} & 0 & 0 & 0\\ D_{2211} & D_{2222} & D_{2233} & 0 & 0 & 0\\ D_{3311} & D_{3322} & D_{3333} & 0 & 0 & 0\\ 0 & 0 & 0 & D_{1212} & 0 & 0\\ 0 & 0 & 0 & 0 & D_{1313} & 0\\ 0 & 0 & 0 & 0 & 0 & D_{2323}\end{bmatrix}\begin{Bmatrix}\varepsilon_{11}\\ \varepsilon_{22}\\ \varepsilon_{33}\\ \varepsilon_{12}\\ \varepsilon_{13}\\ \varepsilon_{23}\end{Bmatrix}$$

3) Stiffness matrix D is constructed with the following components (1,2=horizontal direction; 3=vertical direction) (Mavko et al, 1998).

$$D_{1111} = \rho \cdot \left[V_p\left(90^o\right)\right]^2$$
$$D_{1122} = D_{1111} - 2\rho \cdot \left[V_{sh}\left(90^o\right)\right]^2$$
$$D_{2222} = D_{1111}$$
$$D_{1133} = -D_{3333} + \sqrt{4\rho^2\left[V_p\left(45^o\right)\right]^4 - 2\rho\left[V_p\left(45^o\right)\right]^2\left(D_{1111} + D_{3333} + 2D_{1212}\right) + \left(D_{1111} + D_{1212}\right)\left(D_{3333} + D_{1212}\right)}$$
$$D_{2233} = D_{1133}$$
$$D_{3333} = \rho \cdot \left[V_p\left(0^o\right)\right]^2$$
$$D_{1212} = \rho \cdot \left[V_{sh}\left(0^o\right)\right]^2$$
$$D_{1313} = D_{1212}$$
$$D_{2323} = \frac{1}{2}\left(D_{1111} - D_{1122}\right)$$

4) The wave velocities with the propagating direction are defined with the components of stiffness matrix (Mavko et al, 1998).

$$V_p(\theta) = \sqrt{\frac{D_{1111}\sin^2\theta + D_{3333}\cos^2\theta + D_{1212} + \sqrt{M}}{2\rho}}$$
$$V_p(\theta) = \sqrt{\frac{D_{1111}\sin^2\theta + D_{3333}\cos^2\theta + D_{1212} - \sqrt{M}}{2\rho}}$$
$$V_{sh}(\theta) = \sqrt{\frac{D_{2323}\sin^2\theta + D_{1212}\cos^2\theta}{\rho}}$$
$$M = \left[\left(D_{1111} - D_{1212}\right)\sin^2\theta - \left(D_{3333} - D_{1212}\right)\cos^2\theta\right]^2 + \left(D_{1133} + D_{1212}\right)^2\sin^2 2\theta$$

APPENDIX B

MATHGRAM OF TRAVELTIME KERNEL (Dahlen et al., 2000)

Location of seismic source (sx, sy); $sx := 0$ $sy := 0$

Location of seismic receiver (rx, ry); $rx := 101$ $ry := 101$

Wave period $\tau := 4$

Slowness of a medium $\sigma := 1$

Wavelength $\lambda := \frac{\tau}{\sigma}$ $\lambda = 4$

Traveltime kernel K

K=

for $x \in 1..100$

for $y \in 1..100$

$$A_{y,x} \leftarrow \frac{\sigma}{2\pi} \cdot \frac{\sqrt{(rx - sx)^2 + (ry - sy)^2}}{\sqrt{(x - sx)^2 + (y - sy)^2} \cdot \sqrt{(x - rx)^2 + (y - ry)^2}}$$

$$B_{y,x} \leftarrow \frac{\int_0^{\infty} \omega^3 \cdot \frac{(\omega \cdot \tau)^2}{2 \cdot \pi} \cdot e^{-\omega^2 \cdot \frac{\tau^2}{4\pi^2}} \cdot \sin\left[\omega \cdot \sigma \cdot \left[-\sqrt{(rx - sx)^2 + (ry - sy)^2} \ldots + \sqrt{(x - sx)^2 + (y - sy)^2} \ldots + \sqrt{(x - rx)^2 + (y - ry)^2}\right]\right]}{\int_0^{\infty} \omega^2 \cdot \left[\frac{(\omega \cdot \tau)^2}{2 \cdot \pi} \cdot e^{-\omega^2 \cdot \frac{\tau^2}{4 \cdot \pi^2}}\right] d\omega}$$

$K_{y,x} \leftarrow A_{y,x} \cdot B_{y,x}$

$K_{y,x} \leftarrow 100$ if $K_{y,x} > 100$

return K

If there is any perturbation in slowness field, $\delta\sigma$,

then the traveltime difference δT is computed as:

$$\delta T := \sum_{j=1}^{100} \sum_{i=1}^{100} \left(K_{i,j} \cdot \delta\sigma_{i,j}\right)$$

APPENDIX C

VERIFICATION OF MESH DISCRETIZATION

Twenty realizations are generated for each mesh resolution consisting of 400, 1600, 3600, 10000 or 19600 elements.

C.1 Linear elastic modulus

Boundary conditions correspond to those described in Section 3.4. Random fields are generated with a relative correlation length, L/D=0.1. The mean value and COV of the uniformly distributed Young's modulus are 10MPa and 0.2. The effective constraint modulus computed in each realization is plotted in Figure C.1. Meshes finer than 3600 elements (i.e. 60 by 60 mesh) show stable results.

C.2 Undrained deviatoric resistance

Boundary conditions correspond to those described in Section 4.2. Random fields are generated with a relative correlation length, L/D=0.1. The uniformly distributed void ratio has a mean value 0.9, and a COV=0.06. The maximum deviatory stress at a 100kPa confinement is numerically computed (Figure C.2). Meshes finer than 3600 elements (i.e. 60 by 60 mesh) show stable results.

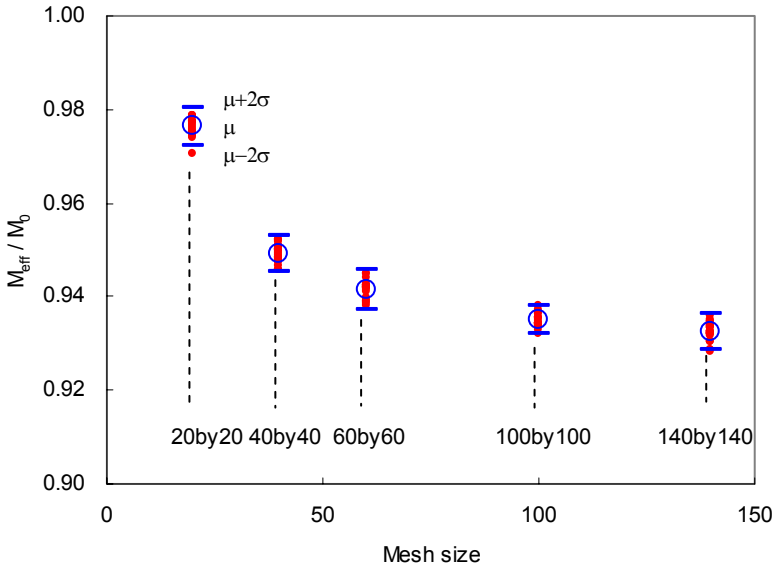

Figure C.1 Mesh discretization effects on effective constraint modulus

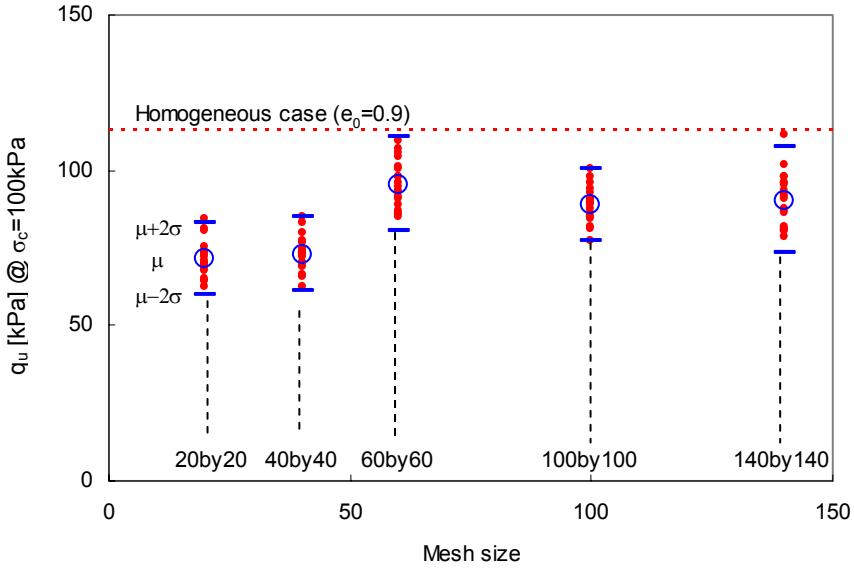

Figure C.2 Mesh discretization effects on maximum undrained deviatoric stress

APPENDIX D

THE INFLUENCE OF ASSUMED DISTRIBUTION

One hundred realizations of the cases explored in Section 3.4 and 4.2 are repeated for two different random variable distributions: uniform distribution and normal distribution (2σ range).

D.1 Linear elastic modulus

Boundary conditions correspond to those described in Section 3.4. The mean value of the Young's modulus is 10MPa and its COV is 0.2. The assumed relative correlation length is L/D=0.1. Results in Figure D.1 show that the increase in kurtosis causes an increase in effective stiffness.

D.2 Undrained deviatoric resistance

Boundary conditions correspond to those described in section 4.2. The mean void ratio 0.9, the COV=0.06 and relative correlation length L/D=0.1 are kept constant. The maximum deviatory stress at a 100kPa confinement is numerically computed (Figure D.2). The normal distribution shows higher kurtosis and shear resistance.

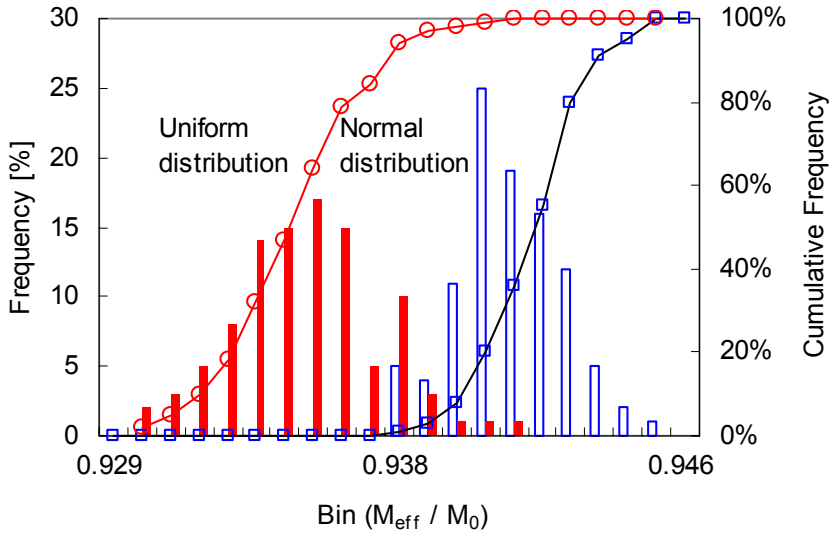

Figure D.1 Random variable distribution effects on effective constraint modulus

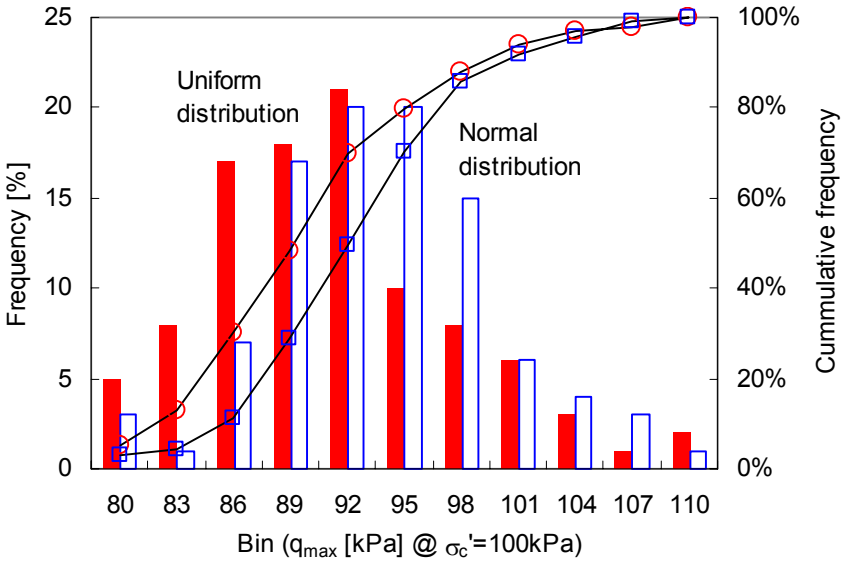

Figure D.2 Random variable distribution effects on the maximum undrained deviatoric stress

REFERENCES

ABAQUS/Standard User's Manual, Version 6.2 (2001), Habbit, Karlsson & Sorenson, Inc., Pawtucket, Rhode Island, U.S.A

AASHTO (2002), LRFD highway bridge design specifications, SI units. Washington, DC: American Association of State Highway and Transportation Officials.

Abramowitz, M. and Stegun, I.A. (1965), Handbook of mathematical functions, New York, Dover Publishing Co.

Achenbach, J.D. (1975), Wave propagation in elastic solids, Elsevier.

Ahmed, I. and Lovell, C.W. (1993), "Rubber soils as lightweight geomaterials", Lightweight artificial and waste materials for embankments over soft soils, Transportation Research Record, No. 1422, National Academy Press, Washington, DC, pp. 61-70

Ang, A.H.S. and Tang, W.H. (1975), Probability concept in engineering planning and design, Vol. 1, Wiley and Sons, New York.

Antonellini, M.A., Aydin, A., and Pollard, D.D. (1994), "Microstructure of deformation bands in porous sandstones at Arches National Park, Utah," Journal of Structural Geology, Vol .16, pp. 941-959

Antonellini, M.A., Aydin, A., Pollard, D.D. and D'Onfro, P. (1994), "Petrophysical study of faults in sandstones using petrographic image analysis and X-ray computerized tomography," Pure and Applied Geophysics, Vol. 143, pp. 181-201

Arthur, J.R.F., Dunstan, T., Al-Ani, Q.A.J.L. and Assadi, A. (1977), "Plastic deformation and failure in granular media," Geotechnique, Vol. 27, No. 1, pp. 53-74

Asaoka, A. and A-Grivas, D. (1982) "Spatial variability of the undrained strength of clays", Journal of the Geotechnical Engineering, Vol. 108, No. GT5, ASCE, New York, pp. 743-756

Atkinson, J. (1993), An introduction to the mechanics of soils and foundations through critical state soil mechanics, McGraw-Hill Co, London.

Aydin, A. (1978), "Small faults formed as deformation bands in sandstone," Pure and Applied Geophysics, Vol. 116, pp. 913-930

Backus, G. E. (1962), "Long-wave elastic anisotropy produced by horizontal layering", Journal of Geophysical Research, Vol. 67, pp. 4427-4440

Beacher, G. B. and Ingra, T. S. (1981), "Stochastic FEM in settlement predictions," Journal of Geotechnical Engineering, ASCE, Vol. 107, No. 4, pp. 449-463

Becker, D.E. (1996), "Limit states design for foundations. Part II: Development for national building code of Canada," Canadian Geotechnical Journal, Vol. 33, No. 6, pp. 984-1007.

Belytschko, T., Chiang, H. and Plaskacz, E. (1994), "High resolution two dimensional

shear band computations: imperfections and mesh dependence," Computational Methods of Applied Mechanics and Engineering, Vol. 119, pp 1-15

Berryman, J.G. (1995), "Mixture theories for rock properties," in A Handbook of Physical Constants, edited by Ahrens, T.J., American geophysical union, Washington, D.C., pp. 205-228

Borja, R.I, and Aydin, A. (2004), "Computational modeling of deformation bands in granular media. I. geological and mathematical framework," Computer Methods in Applied Mechanics and Engineering, Vol. 193, pp. 2667-2698

Borst, R. (1988), "Bifurcations in finite element models with a non-associated flow rule," International Journals of Numerical and Analytical Methods in Geomechanics, Vol. 12, pp. 99-116

Borst, R. (1991), "Simulation of strain localisation: a reappraisal of the Crosserat continuum," Engineering Computation, Vol. 8, pp. 317-332

Borst, R., Mühlhaus, H.B., Pamin, J., and Sluys, L.Y. (1992), "Computational modeling of localization of deformation," Proceeding of third international conference of computational plasticity, edited by Owen, D.R.J., Onate, E., and Hinton, E., pp. 483-508

Bosscher, P.J., Edil, T.B. and Kuraoka, S. (1997), "Design of highway embankments using tire chips," Journal of Geotechnical and Geoenvironmental Engineering, Vol. 123, No. 4, pp. 295-304

Box, G.E.P. and Muller, M.E. (1958), "A note on the generation of random normal deviates," The Annals of Mathematical Statistics, American statistical association, U.S.A., Vol. 29, pp. 610-613

Boyse, W.E. (1986), Wave propagation and inversion in slightly inhomogeneous media, PhD thesis, Stanford university.

Brandt, H. (1955), Chalk data, presented at workshop on effective media, Karlsruhe.

Bressette, T. (1984), "Used tire material as an alternative permeable aggregate," Report No, FHWA/CA/TL-84/07, Office of transportation laboratory, California department of transportation, Sacramento, CA.

Cambou, B. (1975), "Applications of first-order uncertainty analysis in the finite elements method in linear elasticity," Proceedings of Applications of Statistics and Probability in Soil and Structure Engineering, 2nd international conference, Aachen, Germany, pp 117-122.

Carter, J.P. (1982), "Predictions of the non-homogeneous behavior of clay in the triaxial test," Geotechnique, Vol. 32, No. 1, pp. 55-58

CEN (2001), Eurocode 7 Part I: Geotechnical design: General rules, Final Draft prEN 1997-1, Brussels: European Committee for Standardization (CEN).

Chaisson, P., Lafleur, J., Soulie, M. and Law, K.T. (1995), "Characterizing spatial variability of a clay by geostatistics", Canadian Geotechnical Journal, No.32, pp.1-10

Cho, G.C., Lee, J.S. and Santamarina, J.C. (2004), "Spatial variability in soils: high resolution assessment with electrical needle probe." Journal of Geotechnical and Geoenvironmental Engineering, ASCE. Vol. 130, No. 8, pp.843-850

Clark, I. (1979), Practical geostatistics, Applied Science Publisher Ltd., London.

Dagan, G. (1989), "Flow and transport in porous formations," Springer-Verlag, New York.

Dahlen, F.A., Hung, S.H, and Nolet, G. (2000), "Frȇchet kernels for finite frequency traveltimes-I. Theory," Geophysical Journal International, Vol. 141, pp. 157-174

DeGroot, D.J. and Baecher, G.B. (1993), "Estimating autocovariance of in-situ soil properties", Journal of Geotechnical Engineering, Vol. 119, No. 1, ASCE, New York, pp. 147-166

DeGroot, D.J. (1996), "Analyzing spatial variability of insitu soil properties," Uncertainty in the geologic environment, from theory to practice, Proceedings of Uncertainty '96, Geotechnical special publication No. 58, Madison, Wisconsin, pp. 210-238

Desrues, J. (1998), "Localization patterns in ductile and brittle geomaterials," Wiley-Intersciences, Europe.

Desrues, J. and Chambon, R. (2002), "Shear band analysis and shear moduli calibration," International Journal of Solids and Structures, Vol. 39, pp. 3757-3776

Desrues, j., Chambon, R., Monki, M. and Mazerolle, F., (1996), "Void ratio evolution inside shear bands in triaxial sand specimens studied by computed tomography," Geotechnique, Vol. 46, No. 3, pp. 529-546

Desrues, J., Lanier, J. and Stutz, P. (1985), "Localization of the deformation in tests on sand sample," Engineering Fracture Mechanics, Vol. 21, No. 4, pp. 909-921

Digby, P.J. (1981), "The effective elastic moduli of porous granular rocks", Journal of Applied Mechanics, Vol. 48, pp. 803-808

Dong, W. and Toksöz, M.N. (1995), "Borehole seismic-source radiation pattern in transversely isotropic media," Geophysics, Vol. 60, no.1, pp. 29-42

Duncan, J.M. and Chang, C.Y. (1970), "Nonlinear analysis of stress and strain in soils," Journal of the soil mechanics and foundations devision, ASCE, Vol. 96, No. SM5, pp.1629-1653

Dvorkin, J. and Nur, A. (1996), "Elasticity of high-porosity sandstones: Theory with the squirt and the Biot mechanisms", Geophysics, Vol. 58, pp.524-533

Edil, T.B. and Bosscher, P.J. (1994), " Engineering properties of tire chips and soil mixtures", Geotechnical Testing Journal, GTJODJ, Vol. 17, No. 4, Dec. 1994, pp. 453-464

Ehlschlaeger, C.R. and Goodchild, M.F. (1994), "Uncertainty in spatial data: defining, visualizing, and managing data errors," Proceedings of GIS/LIS 1994, Phoenix, Arizona, pp. 246-253

Einstein, H.H. and Baecher, G.B. (1982), "Probabilistic and statistical methods in engineering geology, I. Problem statement and introduction to solution," Rock Mechanics and Rock Engineering, Vol. 12, pp. 47-61

El-Kadi, A. I. (1986), "A computer program for generating two-dimensional fields of autocorrelated parameters," Ground Water, Vol. 24, No. 5, pp. 663-667

El-Kadi, A.I. and Williams, S.A. (2000), "Generating two-dimensional fields of auto-correlated, normally distributed parameters by the matrix decomposition technique," Ground Water, Vol. 38, No. 4, pp. 530-532

Eleazer, W.E. and Barlaz, M.B. (1992), "Technologies for utilization of waste tires in asphalt pavement", Utilization of waste materials in civil engineering : Proceedings, Material Engineering Division, ASCE, New York, edited by H. Inyang abd K. Bergeson, pp. 193-201

Feng, Z.Y. and Sutter, K.G. (2000), "Dynamic properties of granulated rubber and mixtures," Geotechnical Testing Journal, Vol. 23, No. 3, pp. 338-344

Fenton, G.A. and Griffiths, G.A. (1993), "Statistics of block conductivity through a simple bounded stochastic medium," Water Resources Research, Vol. 29, No. 6, pp. 1825-1830

Fenton, G.A., Paice, G.M. and Griffiths, D.V. (1996), "Probabilistic analysis of foundation settlement," Geotechnical special publication No. 58, pp. 657-665

Fernandez, A.L. (2000), Tomographic imaging the state of stress, PhD Thesis, Georgia Institute of Technology, Atlanta.

Finno, R.J, Harris, W.W., Mooney, M.A. and Viggiani, G. (1997), "Shear bands in plane strain compression of loose sand," Geotechnique, Vol. 47, No. 1, pp.149-165

Finno, R.J., Harris, W.W., Mooney, M.A. and Viggiani, G. (1996), "Strain localization and undrained steady state of sand," Journal of Geotechnical Engineering, Vol. 122, No. 6, pp. 462-473

Fisher, R.A. (1925), Statistical methods for research workers, Oliver and Boyd, Edinburgh.

Foose, G.J., Benson, C.H. and Bosscher, P.J. (1996), "Sand reinforced with shredded waste tires," Journal of Geotechnical Engineering, Vol. 122, No. 9, pp. 760-767

Garga, V.K. and O'Shaughnessy, V. (2000), "Tire-reinforced earthfill. Part I: Construction of a test fill, performance, and retaining wall design," Canadian Geotechnical Journal, Vol. 37, pp. 75-96

Gebhardt, M.A. (1997), Shear strength of shredded tires as applied to the design and construction of a shredded tire stream crossing, MS thesis, Iowa State University.

German, R.M. (1989), Particle packing characteristics, Metal powder industries federation, Princeton, NJ.

Gibson Jr., R.L.J. (1994), "Radiation from seismic sources in cased and cemented boreholes," Geophysics, Vol. 59, pp. 518-533

Griffiths, D.V. (2000), "Stability analysis of highly variable soils by elasto-plastic finite

elements," Course notes given at a Short Course on Advanced numerical applications and plasticity in geomechanics, International Centre for Mechanical Sciences, Udine, Italy

Griffiths, D.V. and Fenton, G.A. (2000), "Probabilistic geotechnical analysis: How difficult does it need to be?" Proceedings of the GeoDenver 2000 Symposium "Slope Stability 2000," GSP No. 101, ASCE, pp.184-193

Griffiths, D.V. and Fenton, G.A. (2001), "Bearing capacity of spatially random soil: the undrained clay Prandtl problem revisited," Geotechnique, Vol. 51, No. 4, pp. 351-359

Griffiths, D.V. and Lane, P.A. (1999), "Slope stability analysis by finite elements," Geotechnique, Vol. 49, No. 3, pp. 387-403

Griffiths, D.V., Fenton, G.A. and Tveten, D.E. (2002), "Probabilistic geotechnical analysis: How difficult does it need to be?" Keynote paper to be presented at the UEF Conference on Probabilistics in Geotechnics: Technical and economic risk estimation. To be held in Graz, Austria, Sept 15-19, 2002

Guyon, E., Oger, L. and Plona, T.J. (1987), "Transport properties in sintered porous media composed of two particles sizes," Journal of Applied Physics D; Applied Physics, Vol. 20, pp. 1637-1644

Hardin, B.O. and Black, W.L. (1968), "Vibration modulus of normally consolidated clay," Journal of Soil Mechanics and Foundations, ASCE, Vol. 89, SM2, pp. 353-369

Hardin, B.O. and Drnevich, V.P. (1972), "Shear modulus and damping in soils: measurement and parameter effects," Journal of soil mechanics and foundations division, Vol. 98, SM6, pp. 603-624

Harr, M. E. (1987), "Reliability based design in civil engineering," McGraw Hill, London, New York

Hashin, Z. and Shtrinkman, S. (1962), "A variational approach to the theory of effective magnetic permeability of multiphase materials," Journal of Applied Physics, Vol. 33, pp. 3125-3131

Hashin, Z. and Shtrinkman, S. (1963), "A variational approach to the elastic behavior of multiphase materials," Journal of Mechanics and Physics of Solids, Vol. 11, pp. 127-140

Hegazy, A.H., Mayne, P.M. and Rouhani, S. (1996), "Geostatistical assessment of spatial variability in piezocone tests," Uncertainty in the geologic environment, from theory to practice, Proceeding of Uncertainty '96, GSP 58, Madison, Wisconsin, pp. 254-268

Hicks, M. A. (1998), "Error estimation and mesh refinement for computations of localisation in geomaterials," Localization and bifurcation theory for soils and rocks, edited by Adachi, A., Oka, F. and Yashima, A., pp. 271-281

Hill, R. (1952), "The elastic behavior of crystalline aggregate", Proceeding of Physical Society, London, Vol. A65, pp. 349-354

Hill, R. (1965), "A self consistent mechanics of composite materials," Journal of Mechanics and Physics of Solids, Vol. 13, pp.213-222

Hoeg, K., Dyvik, R. and Sandbaekken, G. (2000), "Strength of undisturbed versus resonstituted silt and silty sand specimens," Journal of Geotechnical and Geoenvironmental Engineering, ASCE, Vol. 126, No. 7, pp. 606-617

Honjo, Y. and Kusakabe, O. (2002), "Proposal of a comprehensive foundation design code: Geo-code 21 ver.2," Proceedings of Foundation Design Codes and Soil Investigation in View of International Homogenization and Performance, 2002, Kamakura, Japan, pp. 95-103.

Humphrey, D.N. and Manion, W. (1992), "Properties of tire chips for lightweight fill", Grouting, Soil Improvement, and geosynthetics, ASCE, Geotechnical Spatial Publication, No. 30, pp. 1344-1355

Humphrey, D.N., Sandford, T.C., Cribbs, M.M. and Manion, W. P. (1993), "Shear strength and compressibility of tire chips for use as retaining wall backfill," Lightweight artificial and waste materials for embankments over soft soils, Transportation research record, No. 1422, National Academy Press, Washington, DC, pp. 29-35

Hung, S.H., Dahlen, F.A. and Nolet, G. (2000), "Frȇchet kernels for finite frequency traveltimes-II. Examples," Geophysical Journal International, Vol. 141, pp. 175-203

Hwang, D. and Witczak, M.W. (1984), "Multidimensional probabilistic consolidation," Journal of Geotechnical Engineering, Vol. 110, No. 8, pp. 1059-1078

Ishihara, K. (1993), "Liquefaction and flow failure during earthquakes," Geotechnique, Vol. 43, No. 3, pp. 351-415

Jang, D.J., Frost, J.D. and Park J.Y. (1999), "Preparation of epoxy impregnated sand coupons for image analysis," Geotechnical Testing Journal, Vol. 22, No. 2, pp. 147-158

Jones, A.L., Kramer. S.L. and Arduino, P. (2002), "Estimation of uncertainty in geotechnical properties for performance-based earthquake engineering," PEER report 2002/16.

Kolmogorov, A.N. (1941), "Interpolated and extrapolated stationary random sequences," Izvestya Akademiya Nauk SSSR, Seriya Matematicheskaya, Vol. 5, No. 1 (in Russian).

Kopperman, S.E., Stokoe, K.H. and Knox, D.P. (1982), "Effect of state of stress on velocity of low-amplitude compression waves propagating along principal stress directions in dry sand," Civil engineering department, University of Texas, Austin, Report GR82-22

Krige, D.G. (1966), "Two-dimensional weighted moving average trend surfaces for ore-evaluation," Journal of the South African Institute of Mining and Metallurgy, Vol. 66, pp. 13-38.

Kulhawy, F.H. and Phoon, K.K. (2002), "Observations on geotechnical reliability-based design development in North America," Proceedings of Foundation Design Codes

and Soil Investigation in View of International Homogenization and Performance, 2002, Kamakura, Japan, pp. 31-48

Kulhawy, F.H. (1992), "On evaluation of static soil properties", In Stability and performance of slopes and embankments II (GSP31), edited by Seed, R.B., and Boulanger, R.W., ASCE, New York, pp. 95-115

Kulhawy, F.H. and Phoon, K.K. (1996), "Engineering judgement in the evolution from deterministic to reliability-based foundation design", in Uncertainty in the geologic environment (GSP 58), edited by C.D. Shackelford, P.P. Nelson, and M.J.S. Roth . ASCE, New York, pp. 29-48

Kuster, G.T. and Toksöz, M.N. (1974), "Velocity and attenuation of seismic waves in two phase media," Geophysics, Vol. 39, pp. 587-618

Lacasse, S. and Nadim, F. (1996), "Uncertainties in characterizing soil properties", in Uncertainty in the geologic environment (GSP 58), edited by Shackelford, C.D., Nelson, P.P., and Roth, M.J.S., ASCE, New York, pp. 49-75

Ladd, R.S. (1974), "Specimen preparation and cyclic stability of sands," Journal of Geotechnical Engineering division, ASCE, Vol. 100, No. 10, pp. 1180-1184

Lapierre, C., Leroueil, S. and Locat, J. (1990), "Mercury intrusion and permeability of Louiseville clay," Canadian Geotechnical Journal, Vol. 27, No. 6, pp. 761-773

Lee, J.H., Salgado, R., Bernal, A. and Lovell, C.W. (1999), "Shredded tires and rubber-sand as lightweight backfill," Journal of Geotechnical and Geoenvironmental Engineering," Vol. 125, No. 2, pp. 132-141

Lee, J.S. (2003), High resolution geophysical techniques for small-scale soil model testing, PhD thesis, Georgia institute of technology, U.S.A.

Lee, M.W. and Balch, A.H. (1982), "Theoretical seismic wave radiation from a fluid-filled borehole," Geophysics, Vol. 47, pp. 1308-1314

Lee, S.H.H. and Stokoe, K.H.II (1986), "Investigation of low-amplitude shear wave velocity in anisotropic material," A report for United States Air Force office of scientific research.

Leroy, Y. and Ortiz, M. (1989), "Finite element analysis of strain localization in frictional materials," International Journal of Numerical and Analytical Methods in Geomechanics, Vol. 13, pp. 53-74

Levander, A.R. (1988), "Fourth-order, finite-difference P-SV seismogram," Geophysics, Vol. 53, pp. 1425-1436

Liang, R.Y. and Lee. S. (1996), "Short-time and long-term aging behavior of rubber modified asphalt paving mixture," Recycled rubber, aggregate, and fill in asphalt paving mixtures, Transportation research record, No. 1530, National academy press, Washington, DC, pp. 11-17

Lines, L.R., Slawinski, R. and Bording, R.P. (1999), "A recipe for stability of finite-difference wave-equation computations," Geophysics, Vol. 64, No. 3, pp. 967-969

Llopis, J.L. and Ballard, R.F. (1995), "Crosshole seismic methods to assess the seismic stability of earthen dams," Proceedings of the non-destructive evaluation of aging structures and dams, Oakland, CA, pp. 79-88

Loret, B. and Prevost, J.H. (1991), "Dynamic strain localization in fluid-saturated porous media," Journal of Engineering Mechanics, ASCE, Vol. 117, pp. 907-922

Love, A.E.H. (1944), "A treatise on the mathematical theory of elasticity, fourth edition," Dover, New York.

Lumb, P. (1966), "The variability of natural soils," Canadian Geotechnical Journal, Vol. 3, No. 2, pp. 74-97

Luset, N.M. (1989), "Vitesse et atténuation des ondes élastiques sonique et ultrasonique dans les roches sous pression de confinement," PhD thesis, Paris University

Mantoglou, A. and Wilson, J.L. (1982), "The Turning Bands Method for Simulating of Random Fields Using Line Generation by a Spectral Method," Water Resources Research, Vol.18, No. 5, pp.1379-1394

Marion, D., Mukerji, T. and Mavko, G. (1994), "Scale effects on velocity dispersion: from ray to effective medium theories in stratified media," Geophysics, Vol. 59, pp. 1613-1619

Masad, E., Taha, R., Ho, C. and Papagionnakis, T. (1996), "Engineering properties of tire/rubber mixtures as a lightweight fill material," Geotechnical Testing Journal, Vol. 19, No. 3, pp. 297-304

Mavko, G., Mukerji, T. and Dvorkin, J. (1998), "The rock physics handbook", Cambridge University Press. 329 pages

Mejia, J.M. and Rodriguez-Iturbe, I. (1974), "On the synthesis of random field sampling from the spectrum: an application to the generation of hydrologic spatial process," Water Resources Research, Vol.10, No. 4, pp. 705-711

Mercer, W.B. and Hall, A.D. (1911), "Experimental error of field trials," Journal of Agricultural Science, Cambridge, Vol. 4, pp. 107-132.

Mindlin, R.D. (1949), "Compliance of elastic bodies in contact", Journal of Applied Mechanics, Vol.16, pp. 259-268

Ministry of Transportation Ontario (1992), Ontario Highway Bridge Design Code and Commentary (OHBDC3), 3rd Edition, Downsview, Ontario.

Mitchell, A.R. (1969), "Computational methods in partial differential equations," John Wiley and Sons. Inc., 255 pages

Miura, S. and Yagi, K. (2002), "Mechanical behavior and particle crushing of volcanic coarse-grained soils in Japan," Proceedings of International Workshop on Characterization and Engineering Properties of Natural Soils, Singapore.

MOC (2002), Code for the design of building foundations, Beijing, Ministry of Construction.

Moczo, P. (1998), Introduction to modeling seismic wave propagation by the finite difference method, Lecture note, Kyoto University.

Mukerji, T., Mavko, G., Mujica, D. and Lucet, N. (1995), "Scale-dependent seismic velocity in heterogeneous media," Geophysics, Vol. 60, No. 4, pp 1222-1233

Mulilis, J.P., Chan, C.K. and Seed, H.B. (1975), The effects of method of sample preparation on the cyclic stress strain behavior of sands, EERC report, #75-18

Nash, J.C. (1979), Compact Numerical Methods for Computers; Linear Algebra and Function Minimization, John Wiley and Sons, New York.

Needleman, A. and Tvergaard, V. (1992), "Analysis of plastic flow localization in metals," Applied Mechanics Reviews, vol. 45, pp 3-18

Neuman, S.P. and Orr, S. (1993), "Prediction of steady state flow in nonuniform geometric media by conditional moments: Exact nonlocal formalism, effective conductivities, and weak approximation," Water Resources Research, Vol. 29, No. 2, pp. 341-364

Nikitin, L.V. and Chesnokov, E.M. (1984), "Wave propagation in elastic media with stress-induced anisotropy," Geophysical Journal of the Royal Astronomical Society, Vol.76, pp. 129-133

Nishimura, S.I., Shimada, K. and Fujii, H. (2002), "Consolidation inverse analysis considering spatial variability and non-linearity of soil parameters," Soils and Foundation, Vol. 42, No. 3, pp.45-61

Novak, R.C. and Bert, C.W. (1968), "Theoretical and experimental bases for more precise elastic properties of epoxy," Journal of Composite Materials, Vol. 2, pp. 506-508

Orchant, C.J., Kulhawy, F.H. and Trautmann, C.H. (1988), "Reliability based foundation design for transmission line structures: critical evaluation of in situ test methods," Electric power research institute, Palo Alto, California, Report EL-5507(2)

Paice, G.M., Griffiths, D.V. and Fenton G.A. (1996), "Finite element modeling of settlements on spatially random soil," Journal of Geotechnical and Geoenvironmental Engineering, ASCE, Vol. 122, No. 9, pp. 777-779

Phoon, K.K. (2004), Towards reliability-based design for geotechnical engineering, Special lecture for Korean Geotechnical Society, Seoul, Korea.

Phoon, K.K. and Kulhawy, F.H. (1999), "Characterization of geotechnical variability," Canadian Geotechnical Journal, Vol. 36, pp. 612-624

Phoon, K.K., Kulhawy, F.H. and Grigoriu, M.D. (1995), "Reliability-based design of foundation for transmission line structure," Report TR-105000, Electric Power Research Institute, Palo Alto.

Popescu, R. (1995), Stochastic variability of soil properties: data analysis, digital simulation, effects on system behavior, PhD thesis, Princeton University, Princeton, NJ.

Popescu, R., Prevost, J.H. and Deodatis, G. (1996), "Influence of spatial variability of soil properties on seismically induced soil liquefaction," Proceedings uncertainty in the geologic environment: from theory to practice, ASCE, Madison, WI, pp. 1098-1112.

Popescu, R., Prevost, J.H. and Deodatis, G. (2005), "3D effects in seismic liquefaction of stochastically variable soil deposits," Geotechnique, Vol. 55, No. 1, pp. 21-31.

Potts, B.D. and Santamarina, J.C. (1993), "Geotechnical tomography: the effects of diffraction," Geotechnical Testing Journal, Vol. 16, No. 4, pp. 510-517

Prada, J., Fratta, D. and Santamarina, J.C. (2000), "Tomographic detection of low-velocity anomalies with limited data sets (velocity and attenuation)," Geotechnical Testing Journal, Vol. 23, pp. 472-486

Press, W.H., Teukolsky, S.A., Vetterling, W.T. and Flannery, B.P. (1992) Numerical recipe in Fortran, Second Edition.

Qu, J. (2002), Micromechanics of composite materials, Lecture-note, Georgia Institute of Technology, Spring 2002.

Ramakrshnan, N. and Atluri, S.N. (1994), "Simulations of shear band formations in plane strain tension and compression using FEM," Mechanics of Materials, Vol. 17, pp 307-317

Ravi, V. (1992), "Statistical modeling of spatial variability of undrained strength", Canadian Geotechnical Journal, Vol. 29, pp. 721-729

Remakrishnan, N. and Atluri, S. N. (1994), "Simulations of shear band formations in plane strain tension and compression using FEM," Mechanics of Materials, Vol. 17, pp. 307-317

Resendiz, D. and Herrera, I. (1969), "A probabilistic formulation of settlement control design," Proceedings of 7 th ICSMFE, Vol.2, Mexico, pp.217-225

Robertsson, J.O.A, Blanch, J.O. and Symes, W.W. (1994), "Viscoelastic finite-difference modeling", Geophysics, Vol. 59, No. 9, pp.1444-1456

Roesler, S.K. (1979), "Anisotropy shear modulus due to stress anisotropy," ASCE Journal of Geotechnical Engineering, Vol. 105, pp 871-880

Roscoe, K.H. and Burland, J.B. (1968), "On the generalized stress-strain behavior of wet clay," in Engineering plasticity, edited by Heyman, J., and Leckie, F.A., Cambridge university press, London, pp. 535-609

Roscoe, K.H., Schofield, A. and Thurairajah, A. (1963), "Yielding of clays in state wetter than critical," Geotechnique, Vol. 13, No. 3, pp. 211-240

Roscoe, K.H., Schofield, A. and Worth, C.P. (1958), "On the yielding of soils," Geotechnique, Vol. 8, pp.22-53

Rothenburg, L. and Bathurst, R.J. (1989), "Analytical study of induced anisotropy in idealized granular materials," Geotechnique, Vol. 39, No. 4, pp. 601-614

Rubin, Y. and Gómez-Hernández, J.J. (1990), "A stochastic approach to the problem of upscaling of conductivity in disordered media: Theory and unconditional numerical simulations," Water Resources Research, Vol. 26, No. 4, pp. 691-701

Ruess, A. (1929), "Berechung der Fliessgrenzen von Mischikristallen auf Grund der Plastizitätsbedingung für Einkristalle," Zeitschrift für Angewandte Mathematik and Mechanik, Vol. 9, pp. 49-58

Samman, M.M. and O'Neill, M.W. (1997), "An exercise in seismic testing of drilled shafts for structural defects," Foundation Drilling, Vol. 36, No. 1, pp. 11-17

Santamarina, J.C. and Cascante, G. (1996), "Stress anisotropy and wave propagation – A micromechanical view", Canadian Geotechnical Journal, Vol. 33, pp. 770-782

Santamarina, J.C. and Cesare, M. (1994), "Velocity inversion in the near surface: vertical heterogeneity and anisotropy," Internal report, University of Waterloo, Canada

Santamarina, J.C. and Fratta, D. (1998), "Introduction to discrete signals and inverse problems in civil engineering," ASCE Press, Virginia.

Santamarina, J.C. and Reed, A.C. (1994), "Ray tomography: errors and error functions," Journal of Applied Geophysics, Vol. 32, pp. 347-355

Santamarina, J.C., Klein, K.A. and Fam, M.A. (2001), "Soils and waves," John Wiley and Sons, New York.

Saxena, S.K., Avramidis, A.S., and Reddy, K.R., (1988), "Dynamic moduli and damping ratios for cemented sands at low strains," Canadian Geotechnical Journal, Vol. 25, No. 2, 353-368.

Schneider J.A. and Mayne, P.W. (2000), "Soil liquefaction response In Mid-America evaluated by seismic piezocone tests," MAE report, No. CD-003.

Shuttle, D.A. and Smith, I.M. (1988), "Numerical Simulation of shear band formation in soils," International Journal of Numerical and Analytical Methods in Geomechanics, Vol. 12, pp. 611-626.

Soulie, M., Montes, P. and Silvestri, V. (1990), "Modelling of spatial variability of soil parameters", Canadian Geotechnical Journal, Vol. 27, pp. 617-630

Spetzler, J. and Sneider, R. (2001), "The effect of small-scale heterogeneity on the arrival time of waves," Geophysical Journal International, Vol. 145, pp. 786-796

Spry, M.J., Kulhawy, F.H. and Grigoriu, M.D. (1988), "Reliability based foundation design for transmission line structures: geotechnical site characterization strategy," Electric power research institute, Palo Alto, California, Report EL-5507(1)

Tallin, A.G. and Santamarina, J.C. (1992), "Digital ray tracing for geotomography," IEEE transactions on Geoscience and Remote Sensing, Vol. 30, No. 3, pp. 617-619

Tan, C.P., Donald, I.B. and Melchers, R.E. (1993), "Probabilistic slope stability analysis, State-of-Play," Proceedings of the conference on probabilistic methods in geotechnical engineering, Canberra, Australia, pp. 89-110

Tang, W. (1979), "Probabilistic evaluation of penetration resistance," Journal of Geotechnical Engineering, ASCE, Vol. 105, No. GT 10, pp. 1173-1191

Tejchman, J. and Bauer, E. (1996), "Numerical simulation of shear band formation with a polar hypoplastic model," Computers and Geomechanics, Vol. 19, No. 3, pp 221-244

Tejchman, J. and Wu, W. (1993), "Numerical study on shear band patterning in a biaxial compression tests," Mechanics Research Communications, Vol. 20, No. 1, pp. 61-74

Tejchman, J. and Gudehus, G. (2001), "Shearing of a narrow granular layer with polar quantities," International Journal for Numerical and Analytical Methods in Geomechanics, Vol. 25, pp. 1-28

Tejchman, J., Herle, I. and Wehr, J. (1999), "FE-studies on the influence of initial void ratio, pressure level and mean grain diameter on shear localization," International Journal for Numerical and Analytical Methods in Geomechanics, Vol. 23, pp. 2045-2074

Timoshenko, S. and Goodier, J.N. (1970), "Theory of elasticity," McGraw-Hill, New York.

Townsend, F.C. (1978), "A review of factors affecting cyclic triaxial tests," Dynamic Geotechnical Testing, ASTM STP 654, pp. 356-383

Treloar, L.R.G. (1975), "The physics of rubber elasticity," Oxford, Clarendon Press.

United States Army Corps of Engineers (USACE) (1995), "Appendix B – introduction to probability and reliability in geotechnical engineering," Engineering technical letter (ETL) 1110-2-547

Vaid, Y.P. and Sivathayalan, S. (2000), "Fundamental factors affecting liquefaction susceptibility of sands," Canadian Geotechnical Journal, Vol. 37, No. 3, pp. 592-606

Vaid, Y.P., Uthayakumar, M., Sivathayalan, S., Robertson, P.K. and Hofmann, B. (1995), "Laboratory testing of Syncrude sand," Proceedings of 48th Canadian geotechnical conference, Vancouver, Vol. 1, pp. 223-232

Valliappan, S. and Murti, V. (1984), "Finite element constraints in the analysis of wave propagation problem," UNICV report No. R-218, the University of New South Wales, The school of civil engineering

Vanmarcke, E.H. (1977), "Probabilistic modeling of soil profiles," Journal of Geotechnical Engineering, Vol. 103, No. GT11, ASCE, New York, pp. 1227-1246

Vanmarcke, E.H. (1984), "Random fields: Analysis and synthesis," MIT press, Cambridge, MA.

Vardoulakis, I. (1980), "Shear band inclination and shear modulus of sand in biaxial tests," International Journal of Numerical and Analytical Mechanics and Geomechanics, Vol. 4, pp. 103-119

Wackernagel, H. (1995), Multivariate geostatistics: an introduction with applications, Springer, New York.

Walter, J. D. and Clark, S. K. (1980), "Cord reinforced rubber," Mechanics of pneumatic tires, edited by Clark, S. K., U.S. Department of Transportation, National highway traffic safety administration, Washington D.C.

Walton, K. (1987), "The effective elastic moduli of a random packing of spheres", Journal of Mechanics and Physics of Solids, vol.35, pp. 213-216

Webster, R. and Oliver, M. (2001), Geostatistics for environmental scientists, John Wiley and Sons, New York.

White, J.E. (1983), "Underground sound: Application of seismic waves," Elsevier, New York.

Wielandt, E. (1987), "On the validity of ray approximation for interpreting delay times," Seismic Tomography, G.D. Nolet, Ed., Reidel publishing Co., Boston, pp. 85-98

Williamson, P.R. and Worthington, M.H. (1993), "Resolution limits in ray tomography due to wave behavior: numerical experiments," Geophysics, Vol. 58, No. 5, pp. 727-735

Winbow, G.A. (1991), "Seismic sources in open and cased boreholes," Geophysics, Vol. 56, pp. 1040-1050

Wong, J. (1995), "Crosshole Seismic Tomography across a masonry dam," Proceedings of the Non-destructive evaluation of aging structures and dams, Oakland, California, pp. 58-66

Wood, D.M. (1990), "Soil behaviour and critical state soil mechanics," Cambridge university press, UK.

Wu, T.T. (1966), "The effect of inclusion shape on the elastic moduli of a two-phase material," International Journal of Solids and Structures, Vol. 2, pp. 1-8

Wu, W.Y., Benda, C.C. and Cauley, R.F. (1997), "Triaxial determination of shear strength of tire chips," Journal of Geotechnical and Geoenvironmental Engineering, Vol. 123, No. 5, pp.479-482

Yang, S., Lohnes, R.A. and Kjartanson, B.H. (2002), "Mechanical properties of shredded tires," Geotechnical Testing Journal, Vol. 25, No.1, pp. 44-52

Yoshida, T., Tatsuoka, F., Siddiquee, M.S.A., Kamegai, Y. and Park, C.-S. (1993), "Shear banding in sands observed in plane strain compression," Proceedings of the third international workshop localization and bifurcation theory for soils and rocks, Grenole, pp. 165-179

Youd, T.L. (1973), "Factors controlling the maximum and minimum densities of sands", Evaluation of relative density and its role in geotechnical projects involving cohesionless soils, ASTM special technical publication 523, Edited by Selig and Ladd, American Society for Testing and Materials, Philadelphia, pp. 98-112

Youden, W.J. and Mehlich, A. (1937), "Selection of efficient methods for soil sampling," Contributions of the Boyce Thompson institute for plant research, Vol. 9, pp. 59-70.

Yu, P. and Richart, F.E.Jr. (1984), "Stress ratio effects on shear modulus of dry sands," Journal of Geotechnical Engineering, Vol. 110, No. 3, pp. 331-345

Zeitoun, D.G. and Baker. R. (1992), "A stochastic approach for settlement predictions of shallow foundations," Geotechnique, Vol. 42, No. 4, pp. 617-629

Zerwer, A. (1999), "Near surface fracture detection in structural elements: investigation using Rayleigh waves", PhD thesis, University of Waterloo.

Zhang, L.M. and NG, A.M.Y. (2005), "Probabilistic limiting tolerable displacements for serviceability limit state design foundations," Geotechnique, Vol. 55, No. 2, pp. 151-161.

Zhao, L., Jordan, T.H. and Chapman, C.H. (2000), "Three-dimensional Frѐchet differential kernels for seismic delay times," Geophysical Journal International, Vol. 141, pp. 558-576

Zheng-Yi, F. and Sutter, K.G. (2000), "Dynamic properties of granulated rubber/sand mixtures," Geotechnical Testing Journal, Vol. 23, No. 3, pp. 338-344